Solid-state synthesis and pulsed laser deposition of electroceramic materials

Thesis submitted in accordance with the requirements of the University of Liverpool for the degree of Doctor in Philosophy by:

Christos Tzitzeklis

May 2018

Supervised by

Professor M. J. Rosseinsky

Dr J. B. Claridge

Abstract

The work presented in this thesis is related to two different families of technological materials: optoelectronics and multiferroics. Our focus on these categories of materials was largely driven by an interest in growing highly crystalline epitaxial films by the Pulsed Laser Deposition technique and the anticipated thin film properties of smart materials, suitable for miniaturized electronic and energy devices.

The thesis is structured in two parts. In the first part, the experimental investigation of $SrZn_{1-x}Li_xO_2$ as an optically transparent *p*-type material is discussed. Our work in this area was initially motivated by computational studies by Gupta et al.[i] on $SrZnO_2$ as a host for *p*-type carrier and first-principles doping-dependent calculations indicating Li as the most promising *p*-type dopant. A range of dopants were experimentally tested by the conventional solid-state reaction and strictly anaerobic conditions and the successful substitution of Li^+ for Zn^{2+} has been confirmed by combined PXRD and ICP studies. High quality ceramic samples of $SrZn_{1-x}Li_xO_2$ ($0 < x < 0.06$) were isolated and their structural, compositional and physical properties have been investigated.

The *p*-type behaviour of $SrZn_{1-x}Li_xO_2$ was validated by thermopower and variable-pO_2 resistivity measurements and found to be maintained for 40 days after storage in dry air, confirming the long-term stability of our *p*-type compounds. The synthesized $SrZn_{1-x}Li_xO_2$ samples were also found to retain the optical transparency of the parent $SrZnO_2$ having a band gap of 4.27 eV, measured by UV-visible spectroscopy, in agreement with Gupta's calculations predicting a band gap of 3.80 eV[i]. It is worth noting here that this value supersedes the only previous report of $SrZnO_2$ band gap of 3.41 eV[ii]. Attempts to grow single-phase $SrZnO_2$ films under variable growth conditions by PLD were unsuccessful. The main results of this work are currently under submission.

In the second part of this thesis, our attention was focused on $(1-x)BiTi_{(1-y)/2}Fe_yMg_{(1-y)/2}O_3-xCaTiO_3$ (BTFM-CTO), a single-phase room temperature multiferroic stabilized at the morphotropic phase boundary between the rhombohedral [111]p and orthorhombic [001]p phases. The material exemplifies a doping strategy has been developed by Rosseinsky's group towards a lead-free and ambient-pressure bismuth-based phase demonstrating a long-range

[i] C.A Tzitzeklis, J.K. Gupta et al. *Inorg. Chem*., 2018, 57 (19), 11874
[ii] Manavbasi et. al., *J. Lumin.* **79**, 2005, 129

polarization along both the rhombohedral [111]p and orthorhombic [001]p phases. Investigating the room temperature properties of the x = 0.15 and y = 0.75 composition, Mandal et al[iii] succeeded to measure polarization of 66 μC/cm^2, a saturated magnetization of 0.0097 μ_B per Fe and a linear magnetoelectric susceptibility of 0.19(1) ps/m.

In this thesis, our work was focused on the epitaxial growth of $0.85BiTi_{0.1}Fe_{0.80}Mg_{0.1}$ - $0.15CaTiO_3$ thin films on single crystal substrates of $SrTiO_3$ and the investigation of their ferroelectric and magnetic properties.

The multi-cation nature of the targeting compound required the precise control of the deposition process and the epitaxial growth of morphotropic $(1-x)BiTi_{(1-y)/2}Fe_yMg_{(1-y)/2}O_3-xCaTiO_3$ was only possible in a narrow window of growth conditions, identified by the combined use of elemental analysis (EDX/SEM) and structural (XRD) studies. Small deviations from this optimum set of growth conditions resulted in impurity phases. The coexistence of the two-phase regime in the as-deposited films was initially observed as a peak splitting of their out of plane $(00l)_{PC}$ pseudocubic reflections and later verified by detailed rocking curve measurements revealing the presence of two well-distinct crystalline phases. Reciprocal space maps confirm the coherent morphotropic film growth along different in plane crystallographic directions and their in-plane stretching to the $SrTiO_3$ substrate.

The crystalline structure of BTFM-CTO films was also found to be sensitive to epitaxial constraints. A higher lattice mismatch between ultra-thin (20 nm) BTFM-CTO films and the $LaAlO_3$ substrate resulted in the growth of a single tetragonal-like phase, relaxed to a mixture of tetragonal and morphotropic (O+R) phases at higher thickness.

To study the electrical properties of BTFM-CTO films parallel-plate capacitors were fabricated with the growth of a $SrRhO_3$ buffer layer as bottom electrode and sputtered with Pt acting as top electrode. Dielectric measurements have shown the insulating (~ 1.6 GΩ) and low losses nature of BTFM-CTO films. Room-temperature *PE* hysteresis loops measurements revealed the ferroelectric properties of BTFM-CTO films with a remanent $\boldsymbol{P}_{\boldsymbol{max}}^{(\boldsymbol{001})_{\boldsymbol{PC}}}$ polarization exceeding 130 μC/cm^2 under an applied voltage up to 25 V. These values were found to be much larger than those measured on bulk BTFM-CTO as a result of the preferential film orientation. The dielectric and ferroelectric properties of BTFM-CTO films were also found to

[iii] P. Mandal et al., *Adv. Funct. Mater.* **26**, 2016, 2523

depend on the morphotropic nature of the deposited films and samples failed to grow in the phase transition region have shown a shown a lossy, non-ferroelectric behaviour.

Temperature dependent *M(T)* magnetisation and isothermal field-dependent magnetization *M(H)* measurements showed a substantially different magnetic behaviour of BTFM-CTO films to that of bulk samples with a strongly magnetized ferromagnetic iron-based impurity dominating the overall magnetic response of the films and hindering the weak ferromagnetic response of BTFM-CTO films.

Acknowledgements

Firstly, I would like to thank my primary supervisor Prof Matt Rosseinsky for the opportunity he has given me to work in his group and for his interest in this work. I would also like to thank my secondary supervisor Dr. John Claridge for his assistance. My deep gratitude also goes out to my assessors, Prof Paul Chalker (University of Liverpool) and Dr. David Payne (Imperial College London) for their constructive and insightful comments and suggestions.

During my PhD I worked together with many people whose advice and input greatly improved my work and whom I would like to thank here: Dr. Troy D. Manning, Dr. Matthew S. Dyer, Dr. Michael J. Pitcher, Dr. Marita O'Sullivan and Dr. George R. Darling.

I would like especially to thank Dr. Christophe Didier for his generous assistance and valuable input in solid-state synthesis and powder diffraction analysis as well as Jyoti K. Gupta for her help on the computational aspects of the $SrZnO_2$ project of my thesis. Thanks go also to Dr. Stanislav Savvin for his help on discussing the impedance electrical measurements in chapter 4 and to Dr. Jonathan Alaria for his help on organizing the synchrotron measurements performed at Diamond Light Source and the discussions we have had on the BTFM-CTO project. Speaking about the BTFM-CTO project, many thanks go, of course, to Dr. Pranab Mandal for his collaboration and his helpful suggestions.

The list is long. I could not forget here to thank Dr. Marco Zanella for his continued assistance on EDX measurements. Also, Dr. Liam O'Brien for his fruitful discussions on the magnetic measurements of BTFM-CTO. I would also like to express my deep appreciation to Dr. Hongjun Niu for his invaluable help on many, many phases of this work.

During my PhD time I was lucky enough to meet and collaborate closely with Dr. Paritosh Wadekar and Dr. Davide Innocent, who helped me to develop my understanding on thin film science and to whom I owe a special debt of gratitude for their friendship and their generosity of time and engagement.

Finally, I would like to thank my family, Christina and friends for their support, tolerance and good company outside the lab.

Table of Contents

Chapter 1: Transparent conductive oxides

1.1 Basics on transparent conductive oxides theory

Transparent conductive oxides (TCOs) represent a class of materials demonstrating high optical transparency and high electrical conductivity. This is an odd combination of properties given that the conductive materials are usually opaque to visible light whereas insulating and semiconducting materials are transparent due to their large band gaps.

TCOs are usually doped metal oxides of poly/amorphous nature with a transmittance to incident light greater than 70% and a resistivity lower than 10^{-3} Ω.cm. In order to combine these properties, TCOs materials should possess an energy band gap larger than 3 eV for not absorbing the visible light and a high density of free carriers (electrons or holes) of at least 10^{19} cm^{-3} with a mobility greater than 1 cm^2/Vs [1].

TCOs were initially used as aircraft de-icing heaters during WW2 and later as low-emission windows that could reflect the IR radiation while allowing the visible light to pass. Today, TCOs are used in a variety of technological applications including solar photovoltaics, electromagnetic shielding materials, liquid crystal devices, flat panel displays, oxide based thin film transistors and other opto-electronic devices[1].

Among the most studied TCOs material are: indium oxide (In_2O_3), tin oxide (SnO_2) and zinc oxide (ZnO), with tin-doped indium oxide (ITO) being the most widely used TCO in technological applications as it combines the highest available conductivity together with the highest transmissivity in visible light[2].

TCOs are still attracting a lot of attention in the scientific community, partly due to their significantly increased use in architectural (window) and flat panels applications and partly because of their resource scarcity (especially indium in indium tin oxide, ITO). Over the last fifteen years, research into developing new TCOs has been revitalized and a number of binary compounds such as aluminium-doped zinc oxide (AZO), fluorine doped tin oxide (FTO) and doped zinc oxide (FZO) have been extensively studied as potential low-cot alternatives to ITO [1,2,3].

Table 1. 1: Best reported electrical properties of common polycrystalline TCOs films taken from[2].

	Optical Bandgap (eV)	**Conductivity** ($S.cm^{-1}$)	**Carrier concentration** (cm^{-3})	**Mobility** ($cm^2 V^{-1} s^{-1}$)
In_2O_3	3.75	10,000	$> 10^{21}$	35
ZnO	3.35	8,000	$> 10^{21}$	20
SnO_2	3.6	5,000	$> 10^{20}$	15

1.2 Types of electronic materials

According to the band theory, when the atomic orbitals of separated atoms are combined together they are forming bands of molecular orbitals with comparable energy levels. Similar to the quantized shell model of atoms (Bohr atomic model), the electronic structure of solids consists of discrete allowed energies bands with a filled valence band and an empty conduction band at higher energies.

The energy barrier between these bands is defining the electronic behaviour of solid materials and their insulating, semiconducting or metallic character, as illustrated in **Figure 1. 1**.

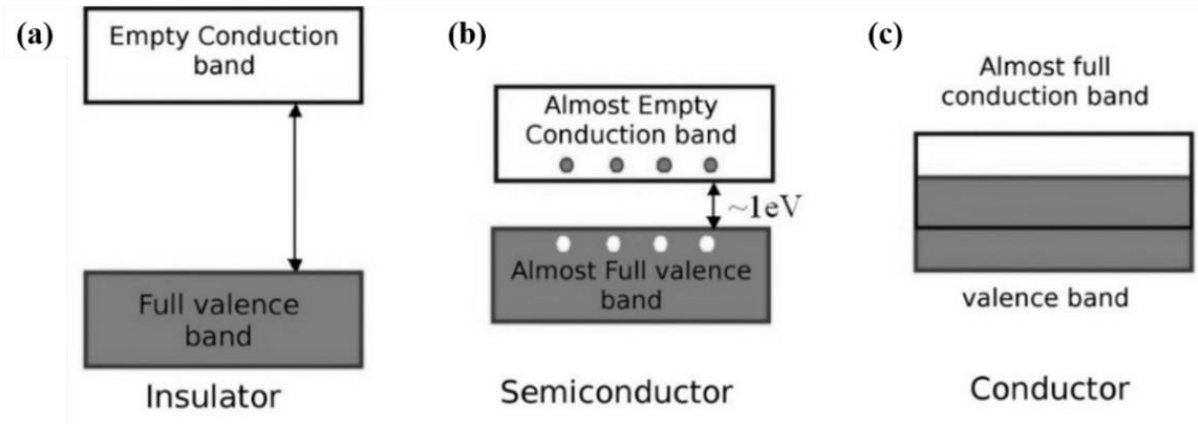

Figure 1. 1: Band structure of insulating, semiconducting or metallic materials. Taken from[4].

Materials with a metallic behaviour have overlapped valence and conduction bands without an energy gap separating them and therefore charge carriers are relatively free to move between the bands. As temperature is increased, the mobility of charge carriers decreased due to collisions among them and thus the conductivity of metals.

Materials showing an insulating behaviour, demonstrate a clear energy separation between their valence and conduction bands (> 9 eV) with the charge carriers being tightly bound to individual atoms (or bonds between them) and their move between bands being limited.

Semiconductors represents an intermediate class of materials between metallic and insulating materials, in which a certain number of valence electrons can reach the conduction band

(**Figure 1. 1b**). Although insulators at temperatures close to absolute zero, semiconductors will see their conduction band being thermally populated by valence band electrons at higher temperatures (according to Fermi-Dirac statistics) and accordingly a thermally-induced (intrinsic) conductivity is observed[5,6].

Table 1. 2: Typical values of electronic conductivity of materials, taken from[5].

	Electronic conductivity ($S.cm^{-1}$)
Metals	$10^{-1} – 10^{5}$
Semiconductors	$10^{-5} – 10^{-2}$
Insulators	$< 10^{-2}$

The conductivity of semiconductors can further be increased with the inclusion of extrinsic impurity atoms which can increase the number of charge carriers of the host semiconductor, a process known as doping.

From the band structure point of view, *n*-type doping forms an impurity band of negative charge carriers (e') below the conduction band while *p*-type doping forms an acceptor impurity band of positive holes ($h^{\bullet}$) above the valence band, as shown in **Figure 1. 2**. In both cases a new band will be formed between the valence and the conduction band, thereby reducing the band gap of the host semiconductor and increasing its conductivity.

In addition, the non-stoichiometric deviation of a solid compound, according to the rules of equilibrium defect chemistry, can also induce extra charge carriers and thus change the conductivity of the compound.

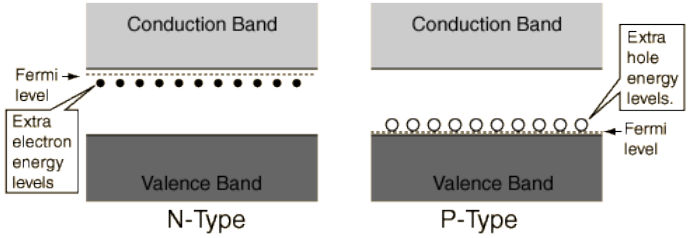

Figure 1. 2: Schematic band diagram for (a) *n*-type, and (b) *p*-type semiconductors at thermal equilibrium conditions, taken from[7].

This is the case, for example, when oxygen can be found in exchange with its gas-phase in a aliovalently doped divalent metal oxide: $M^{I}M^{II}O_{1-x}$ (where M^{I} = monovalent ion and M^{II} = divalent dopant ion), according to the defect equilibrium equations of:

(i) dissolving $M_2^I O$ O in $M^{II}O$:

$$M_2^I O \rightarrow \ 2M_{M^{II}}^{I\,/} + \ O_o^x + V_o^{\cdot\cdot} \qquad \textbf{(Eq 1. 1)}$$

where $M_{M^{II}}^{I\,/}$ are negatively charged monovalent ions sitting on a M^{II} divalent ion that needs $V_o^{\cdot\cdot}$ positive counterions to balance electroneutrality and

(ii) intake of gaseous oxygen from the gas phase:

$$\frac{1}{2}O_{2\,(g)} + \ V_o^{\cdot} \rightarrow \ O_o^x + 2h^{\cdot} \qquad \textbf{(Eq 1. 2)}$$

Resulting to:

$$M_2^I O + \frac{1}{2}O_{2\,(g)} \rightarrow \ 2M_{M^{II}}^{I\,\prime} + \ 2O_o^x + 2h^{\cdot} \qquad \textbf{(Eq 1. 3)}$$

which shows that the aliovalent doping of a divalent metal oxide under oxygen excess conditions increases the *p*-type conductivity of the doped compound.

1.3 Electrical and optical properties of TCOs

1.3.1. Electrical properties of TCOs

The conductivity of TCOs, ranging between 10^{-6} to 10^{4} Sm^{-1}, can be described as the product of the density of materials charge carriers (n), their mobility (μ) and the elementary charge (e). ranging between 10^{-6} to 10^{4} Sm^{-1}

$$\sigma = \frac{1}{\rho} = n\,\mu\,e \qquad \textbf{(Eq 1. 4)}$$

with the mobility of charge carriers given by the formula:

$$\mu = \frac{e\tau}{m^*} \qquad \textbf{(Eq 1. 5)}$$

where m^* is the effective carrier mass and τ is the mean free time between collisions of charge carriers along their path. The effective carrier mass m^*, usually given in terms of free electron mass as: m^*/m_o, is a specific parameter for each crystal lattice environment and, once known, the motion of carriers into the lattice can be calculated according to classical mechanics.

The electrical resistance of films can also be expressed as a quantity associated with the thickness of the measured film for a given square surface area of measurement (typically by the four-point probe method), called as sheet resistance, R_s:

$$R_S = \rho\,\frac{L}{A} = \rho\,\frac{L}{L\,d} = \rho\,/d \qquad \textbf{(Eq 1. 6)}$$

where ρ is the bulk resistivity (Ω cm) and d is the film thickness. The value of the sheet resistance R_s is independent of the square area of measurement and dimensionally equal to an Ohm as the quotient of the resistivity divided by the film thickness, as illustrated in **Figure 1. 3**. Another unit notation of sheet resistance, also encountered in the literature, is: "ohms per square", denoted as "Ω/sq" or "Ω/□ ", which is referred to the square surface area of the measurement.

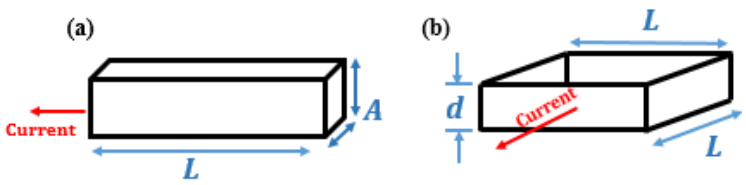

Figure 1. 3: Geometrical definition of (a) resistance and (b) sheer resistance.

With the conductivity of semiconductors being proportional to the product of carrier's mobility and density, there is a point where further increase of doping level leads to a reduction of carriers mean path and the conductivity. **Figure 1. 4** is qualitatively showing the resistivity dependence of TCOs on the doping concentration: at low doping levels, a limited number of available charge carriers is resulting to a high resistivity. The increase of doping level will initially introduce additional carriers into system that will reduce its resistance up to a point where further increase of doping will also increase the scattering rate of carriers resulting in a low mobility and a decreased resistivity.

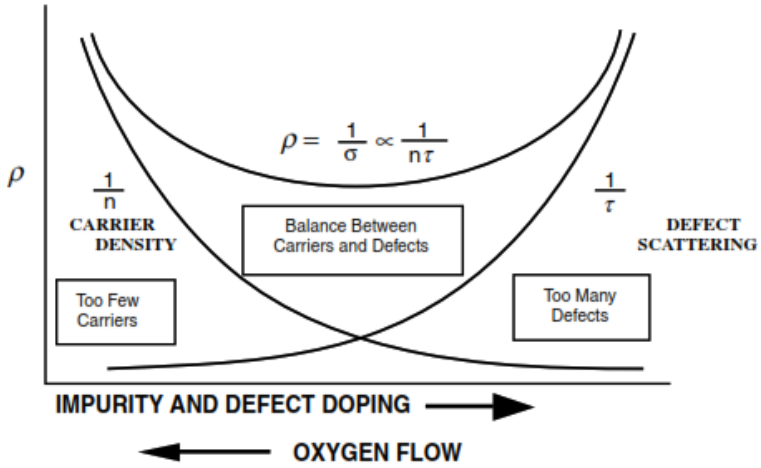

Figure 1. 4: Qualitative TCO doping model. Taken from[8].

More precisely, the effective mobility of TCOs can be described by an approximation formula where all the different scattering mechanisms are summarized according to the Matthiessen's rule:

$$\frac{1}{\mu} = \sum_i \frac{1}{\mu_i} \qquad \textbf{(Eq 1. 7)}$$

with μ_i accounting for different contributions to the sum of (1.4) including the scattering effects of doped ionized impurity atoms (μ_{imp}), phonons (μ_p), grain boundaries (μ_{gb}), neutral impurities (μ_n), carrier-carrier scattering ($\mu_{car\text{-}car}$)[9]. In fact, with the TCOs films being grown or annealed at temperatures higher than 200 °C, the ionized impurities are the dominant scattering mechanism.

The total carrier mobility of semiconductors shows a strong dependence on the doping densities with higher doping levels resulting in higher ionized impurity scattering rates. Nevertheless,

the hole mobility of TCOs is significantly lower than that of electrons due to different band structure topologies and range of interactions with the crystal lattice[8]. An example of calculated carrier mobilities as a function of doping density for silicon is shown in **Figure 1. 5**.

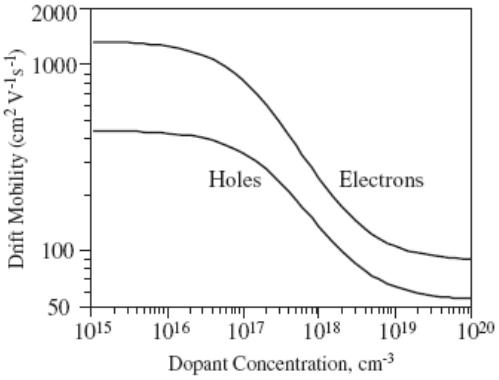

Figure 1. 5: Calculated electron and hole mobilities as a function of doping density for silicon. Taken from[10].

1.3.2. Optical properties of TCOs

As it can be seen in the optical spectra of ZnO in **Figure 1. 6**, the TCOs response in the incident electromagnetic wave is characterized by a transmission window (~70 %) in the visible range of spectra.

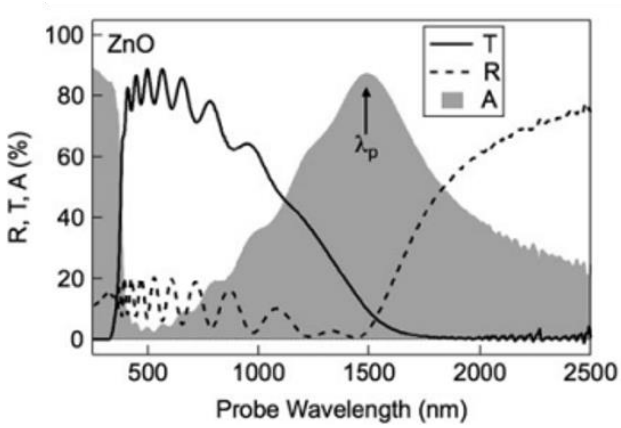

Figure 1. 6: Optical spectra of ZnO. Taken from[1].

At energies higher than the band-gap energy of TCOs, in the near and deep UV spectrum, the electromagnetic wave has enough energy to stimulate band excitations from the VB to the CB of the TCO and the incident ultraviolet light is absorbed from them[1].

In contrast, at energies lower than the transmission limit, in the in the (near) IR spectrum, the incident light is electronically reflected according to the classical Drude free-electron model. According to the Drude free-electron theory, the charge carriers can be conceived as a plasma that is set into motion by the electric field component of the electromagnetic field[11,12].

In the classical Drude theory, the plasma-resonance frequency is directly proportional to the density of carriers as[11,13]:

$$\omega_p = \sqrt{\frac{ne^2}{m^*\varepsilon_r\varepsilon_o}}$$

where m^* is the effective carrier mass, $\varepsilon_r\varepsilon_o$ is the permittivity of the material, n the density of charge carriers and e the elementary charge of carriers, and λ_p the corresponding plasma wavelength.

The transmission of TCOs in the visible range of the electromagnetic wave spectrum is an intrinsic material property which is associated with their band bap structure. The band gap of a semiconductor can be direct or indirect depending whether the CB minimal-energy state and the VB maximal-energy state are characterized by the same or different crystal momentum (k-vector) in the Brillouin zone, as depicted in **Figure 1. 7**.

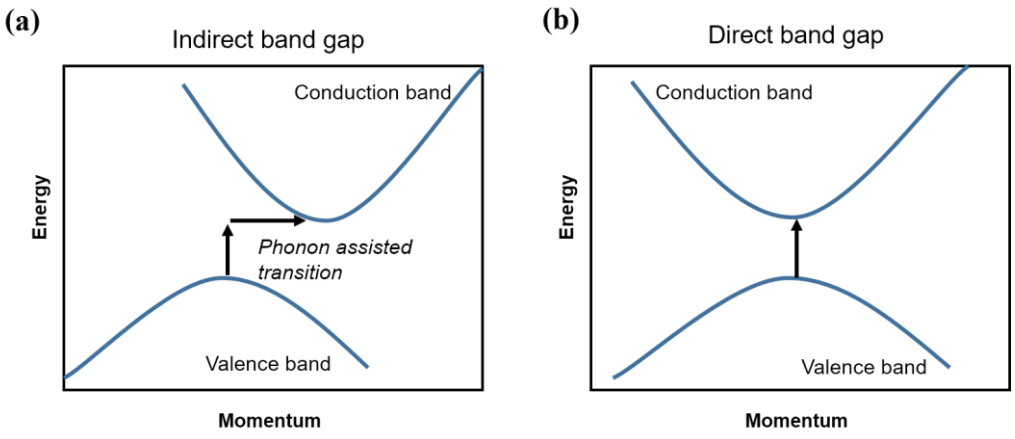

Figure 1. 7: (a) Indirect (photon assisted excitation) and (b) direct band gap. Adapted from[14].

The relation of the incident phonon energy (hv) with the absorption coefficient of excited carriers, whether they are reaching the CB (electrons) or leaving the VB (holes), is given by:

$$(ahv)^{1/n} = A_n(hv - E_g) \quad \textbf{(Eq 1. 8)}$$

where A_n is a constant independent of energy and E_g the bandgap of the material while exponent n defines the transition type of carrier excitation and varies between n = 1/2, 2, 3/2, 3 for allowed direct, allowed indirect, forbidden direct and forbidden indirect transitions.

Over the years, different equations have been developed to quantify and compare the transparency of TCOs[11]. In an early attempt, Haacke[15] defined a figure of merit where the optical transmittance (T) and sheet resistance (R_s) of TCOs films were correlated according to:

$$\Phi_H = \frac{T^q}{R_s} = T^q \cdot \sigma \cdot d \quad \textbf{(Eq 1. 9)}$$

with q (> 1) being an exponent defining the required film transmittance, usually set at q=10 for 90% transmittance. Higher quality TCOs films possess a higher Φ_H merit.

Later, Iles and Soclof[16] developed a figure of merit which is independent of film thickness:

$$\Phi_{IS} = R_S(1 - T) = \frac{\alpha}{\sigma} \quad \textbf{(Eq 1. 10)}$$

where a is the absorption coefficient, σ the conductivity of the film while lower values of Φ_{IS} corresponds to higher quality TCOs films.

Even more detailed expressions of the figure of merit for TCOs have been recently derived by correlating the films transmittance with the optical and dc conductivity film components as well as the substrate interference[11].

1.4 *P*-type TCOs: progress and challenges

Most of the well-known and commercially available TCOs films are *n*-type such as the In_2O_3, SnO_2 and ZnO. The abundance of *n*-type metal oxides is correlated to the s character of their conduction band which reduces the effective mass of their electron carriers[17]. A number of doped binary metal oxides have already found their way on a wide range of electrical applications combining high carrier mobilities, greater than 20 - 35 $cm^2V^{-1}s^{-1}$, and a doping-induced high carrier density.

At the same time, the realization of *p*-type TCOs with a similar performance is largely impeded by their much inferior conductivity, typically smaller by a factor of 500 to 1000 (in the range of 1 – 20 Scm^{-1}). As extensively discussed in topic reviews[18], only a few candidates have until now demonstrated electrical and optical properties that allow them to be considered reliable *p*-type materials. Among them are the Cu^+ ($3d^{10}$) and Cr^{3+} ($3d^3$) -based materials, the layered oxychalcogenides, spinel oxides (nd^6), lone pair based oxides (ns^2) as well as nickel oxide (NiO), probably the currently most widely used *p*-type material in electrical applications.

The difficulty of obtaining *p*-type doped TCOs is related to the different band structure topologies of *n*- and *p*-type materials. Due to the ionic character of metal oxides, the O 2*p* orbitals are lying lower in energy than the valence orbit of metallic atoms and the generated holes are found strongly localized around the oxygen atoms and with low mobilities[19]. Other difficulties on stabilizing *p*-type doping are related to the relatively low solubility of acceptors and the strong compensation effects between native defects and the introduced acceptors. In a number of TCOs systems, the instability and degradation of *p*-type response was found to be associated with their strong photoconductive nature[20] or the inclusion of reactive (interstitial) donor defects that act as acceptor- trapping centres[21, 22, 23].

Although various *p*-type TCOs systems have been developed so far, one of the biggest challenges towards their integration in device applications remains their inferior electrical performance as compared to *n*-type TCOs. In a broader perspective, the inferior electrical properties of TCOs (*n*- and *p*-type) to those of III-V semiconductors, is also attributed to their polycrystalline or amorphous nature and therefore the epitaxial growth of high-quality TCOs will allow the development of films with superior properties.

Finally, the temperature specifications of plastic substrates for flexible and transparent electronic applications set additional requirements on the crystal quality and the electric properties of TCOs films grown at even lower process temperatures (< 200 °C)[8].

1.4.1 Strategies towards *p*-type TCOs

To overcome the intrinsically ionic character of most TCOs, Kawazoe et al.[24]of the Tokyo Institute of Technology suggested in 1997 a new designing strategy called "Chemical Modulation of the Valence Band", as illustrated in **Figure 1. 8**.

They focused their attention on *d* orbital metal ions, which lie energetically closer to the O 2*p* orbitals, and investigated the effect of an increased hybridization in the metal-oxygen bonding of TCOs on the resulting hole mobility of the system[17,19]. According to their approach, an anticipated higher degree of covalency in the metal-oxygen bond was expected to result in a dispersion of the oxide valence band and, thus, increased delocalization of hole carriers (away from the O 2*p* orbitals) and an improvement in their mobility.

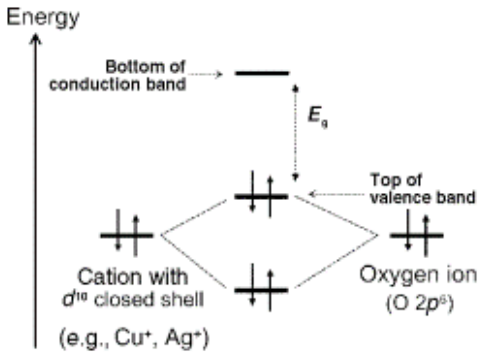

Figure 1. 8: Diagram of the Chemical Modulation of the Valence Band concept proposed by Kawazoe et al. Taken from[25].

Their initial work on empty d^o orbital valence metals has shown a coloration due to *d-d* transition[19] and soon they directed their focus on cations with a closed electronic configuration ($d^{10}s^0$). They started with Cu_2O, a native *p*-type material with a small bandgap of 2.17 eV[26], and they explored the optical properties of the resulting $CuAlO_2$ delafossite compound by the incorporation of Al. In $CuAlO_2$, the three-dimensional interactions of neighbouring Cu^+ ions of the cubic Cu_2O are giving their place to a two-dimensional configuration of Cu ions located between AlO_6 octahedral layers, as shown in **Figure 1. 9**, while the structure retains the "covalent" character of the Cu_2O valence band[24,27]. Under these principles, Kawazoe et al.[24]

succeeded to grow transparent (3.5 eV) *p*-type $CuAlO_2$ thin films by PLD with a room-temperature conductivity up to 1 Scm^{-1}.

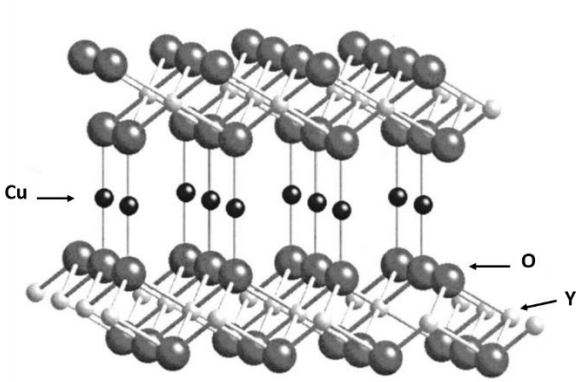

Figure 1. 9: Delafossite structure of $CuAlO_2$. Taken from[28].

Following the discovery of $CuAlO_2$, several other $CuM^{III}O_2$ compounds were investigated, such as $CuGaO_2$[29], $CuInO_2$[30], $CuScO_2$[31,32], $CuCrO_2$[33], $CuBO_2$[34] and also $AgM^{III}O_2$[28]. In the following years, a number of *p*-type delafossite films were also studied such as $CuAl_{1-x}Mg_xO_2$[35], $CuCr_{1-x}Mg_xO_2$[33], $CuCr_{1-x}Zn_xO_2$[36], $CuY_{1-x}Ca_xO_2$[37], $CuSc_{1-x}Mg_xO_2$[38]. However, in most of the cases the resulting compounds did not show an electrical performance better than $CuAlO_2$[19]. Exceptions to this trend were the polycrystalline growth of $CuScO_{2+x}$ films under oxygen-rich conditions[39] and a high conductivity of 30 Scm^{-1} and the divalent Mn^{2+} doping of $CuCrO_2$ films resulting to a record conductivity of 220 Scm^{-1} together with high optical transparency (70%)[33,40].

With the hole densities and carrier mobilities of *p*-type doped copper-based delafossites being substantially low, due to the high oxygen electronegativity, the concept of chemically modulate the valence band of metal oxides was extended to the chalcogen p orbital of S, Se and Te. According to Hosono et al.[41], the close energy levels of Cu 3*d*- and Ch *p*- orbitals could possibly increase the valence band dispersion in chalcogen p orbital Cu-based compounds (Cu_2Ch, Ch = S, Se, Te). To anticipate the intrinsically small band-gap of Cu_2Ch, these compounds were further modified by the incorporation of oxide layers into a MCuOCh structure (oxychalcogenides) [1,17,42,43].

In line with this direction, the conductivity of LaCuOS films displayed a value of 0.26 S cm^{-1} [44]. Interestingly, however, Mg doped LaCuOSe films were found to reach a record high *p*-type

conductivity of 910 S cm^{-1} even if their band gap was shifted below the visible range (at 2.8 eV)[45].

Promising results were also obtained in copper-based chalcogenide fluorides (BaCuQF, with Q=S, Se) that have a similar structure to LaCuOCh[46,47]. Doping with potassium these fluorides have seen the bulk conductivities of these compounds increased by three orders of magnitudes to 82 and 43 Scm^{-1}. Even more promising was, however, the growth of BaCuSF films at temperatures as low as 100 °C having a *p*-type conductivity of 260 S cm^{-1} and an optical band gap of 1.8 eV. H_2O treatment of these films resulted in even higher conductivities of 800 S cm^{-1} although the optical transparency of the as-treated films was further reduced to 1.5 eV.

1.5 ZnO

Zinc oxide (ZnO) consists a well-studied material that has been integrated in a broad range of applications. Having a wide direct bandgap (3.37 eV[48]), a relatively high thermal/chemical stability, sufficient mechanical strength and piezoelectric response, ZnO is considered an attractive candidate for a wide range of applications, from transparent electronics and solar cells to piezoelectric transducers and acousto-electric devices.

ZnO crystallizes in the hexagonal wurtzite, cubic zinc blende, and cubic rocksalt structure as shown in **Figure 1. 10**. At ambient conditions, is met in the hexagonal wurtzite-type structure. The zinc-blende structure of ZnO is a metastable phase can only be obtained by growth on cubic structure substrates while the rocksalt structure is obtained at relatively high pressures.

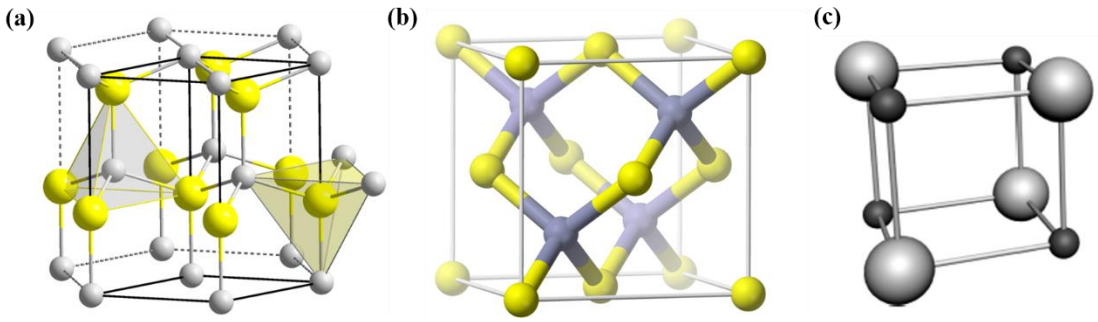

Figure 1. 10: The (a) hexagonal wurtzite, (b) zincblende and (c) rock salt structures of ZnO. In subfigures (a) and (b) O atoms are depicted as yellow spheres and Zn atoms as grey spheres. In subfigure (c) O atoms are depicted as white spheres and Zn atoms as black spheres. Taken from[49].

In the hexagonal wurtzite phase, each Zn^{2+} ion is surrounded by four O^{2-}, a typical tetragonal arrangement favouring an sp^3 covalent bonding. However, the Zn-O bond has also a strong ionicity, resulting in a bond between ionic and covalent character. In addition, the tetrahedral coordination of the wurtzite structure is also giving rise to polar symmetry (along the hexagonal axis), responsible for the piezoelectricity and spontaneous polarization of ZnO.

ZnO is a II-VI semiconductor compound, with a resistivity that can be tuned from insulating to semimetallic. It also exhibits a large excitation binding energy (60 meV) and a high electron mobility (> 200 cm^2/Vs [50]), together with an enhanced luminescence efficiency and high transparency over the whole visible range[51]. It can be easily synthesized and processed under different chemical treatments, especially regarding the toxicity of ITO ($0.01mg/m^3$)[92], and as

such it represents a promising TCO candidate[17]. A lot of research on doping ZnO has been carried out over the past decades focusing on tuning its direct wide band gap[52,53] and its conductivity[18] over a wide range of applications.

The as-grown ZnO, in single crystal or film form, exhibits an intrinsic n-type conductivity, the origin of which has been debated during the 2000s. Up to the early 2000s, the prevailing interpretation was that its intrinsic *n*-type conductivity should be attributed to native defect points of oxygen vacancies (V_o) and zinc interstitials (Zn_i). However, first principle calculations, as well as experimental results, have later shown that Zn_i, although shallow donors, are possessing a high formation energy and therefore are unstable at room temperature [54,55,56,57] while V_o are eventually deep donors although their lower formation energy [58,59]. Finally, the native *n*-type conductivity of ZnO was found to be related to the unintentional incorporation of hydrogen which can be found in most of the process routes of ZnO synthesis[60]. Computational DFT studies by Van der Walle, in 2000[61] showed that hydrogen can be incorporated in interstitial sites and thus act as a shallow donor, a finding which later was also confirmed by experimental observations[62,63].

With the donor (electron) carrier concentrations of native point defects do not exceeding 10^{18} cm^{-3}, highly degenerate n-type ZnO can only be obtained after doping with group-III metals such as Al, Ga, B, or In. Several different growth techniques have been utilized for the growth of *n*-type ZnO films, including molecular beam epitaxy, sputtering, spray pyrolysis, sol-gel, chemical vapour and pulsed laser deposition [64] and the obtained resistivities of the as-grown films were found to lie, regardless of the deposition method or dopant element, in the range of 1.4 to 2×10^{-4} Ω.cm. According to many researchers[65,66,67] improved physical properties and electrical properties have been reported for ZnO films deposited by PLD when compared with other techniques.

Among the different *n*-type dopants, strongly oriented Al-doped (1 wt%) ZnO films, deposited at 300 °C, have been reported to show the lowest recorded resistivity of 1.4×10^{-4} Ω.cm together with a carrier concentration of 10^{21} cm^{-3} and a transmittance of 90% for wavelengths higher than 380 nm[49,68,69,70].

Attempts to reduce further the resistivity of ZnO have also been focused on increasing the carrier mobility of epitaxially grown doped ZnO films at higher temperatures (up to 700 °C), where the detrimental role of grain boundaries and dislocations is expected to be less

pronounced, without nevertheless any significant improvement on the obtained conductivities[49,71,72,73].

Despite the intense research on the electrical properties of ZnO over the last 30 years, the development of ZnO-based optoelectronic applications, p-n junctions and ultimately transparent electronics is largely hindered by the low performance and chemically unstable nature of *p*-type doped ZnO. Over the years, the growth of *p*-type zinc oxides films has been examined with different deposition techniques such as molecular beam epitaxy, metal-organic chemical vapour deposition, sputtering, chemical vapour and pulsed laser deposition[49,64].

Work on *p*-type zinc oxides films has mainly focused on acceptor dopants of group-I (Li, Na and K) and group-V elements (N, P and As). Although group-I elements were found to be shallower dopants than group-V elements[74], their small atomic radii allow their atoms to occupy interstitial (rather than substitutional) sites and thus act as donor sources, a development that is further enhanced by the spontaneous formation of V_o compensation defects[60,64].

Computational studies on the formation energy of group-I substitutional impurities have shown that the inclusion of "acceptor-killer" defects can effectively be supressed under oxygen-rich conditions[75,76] and/or the introduction of hydrogen-acceptor complexes[77]. Furthermore, the successful growth by PLD of *p*-type Na-H co-doping ZnO films under a mixture of O_2/NH_3 atmosphere provided experimental evidences on these predictions[78].

In the case of group-V dopants, the large bond lengths of Zn-P and Zn-As initially suggested the unstable *p*-type nature of phosphorus- and arsenic- doped ZnO due to the unintentional anion anti-site doping, (A_{Zn}). On the contrary, the nitrogen dopant, having a bond length closer to the ideal Zn-O bond of 1.93 Å[79] and a smaller ionization energy[80], appeared at first to be a better dopant candidate. As a result, a lot of work on *p*-type zinc oxides was originally focused on nitrogen, although the as-grown *n*-doped ZnO films were only found to demonstrate a weak and unstable *p*-type nature and this under the condition that the used N-source was NO_2 or NO[81].

Differently, however, to the calculated doping energies of group V dopants, several publications reported the realization of *p*-type zinc oxides films using phosphorus and arsenate. These experimental results have later been supported by computational studies that showed acceptors of the form $A_{Zn} - 2V_{Zn}$ are having lower formation energies and can be shallower acceptor dopants than A_{Zn}[64,82].

In an alternative route, the growth of *p*-type zinc oxides films was investigated by applying the concept of co-doping method, where the ionization energy of dopants (for example nitrogen) is attempted to be lowered with the use of reactive co-dopants. Following the established literature on GaN and AlN[83], Yamamoto et al.[84,85] examined computationally the stability of ZnO:(Ga, 2N) supercells and found an enhancement of acceptor incorporation and stability on the system. Soon, experimental evidence of those results have been presented by Joseph et al.[86] and later several other groups have reported *p*-type co-doping of ZnO with a combination of different dopants complexes such as N-Al, N-Ag, N-P, N-Mg, P-In etc[64].

Lastly, the spinels ZnM_2O_4 (M = Co, Rh, Ir) are the only ternary zinc oxide compounds that have been so far investigated for *p*-type doping. Observing the "quasi-closed" d^6 configuration of Co^{3+}, Rh^{+3} and Ir^{3+} transition metals (resembling the closed d^{10} configuration of Cu), Mizoguchi et al.[87] from the group headed by H. Hosono were the first to report *p*-type conductivity on $ZnRh_2O_4$ thin films while they have also confirmed the low spin state of Rh $4d^6$ by magnetic susceptibility measurements. Following the discovery of $ZnRh_2O_4$, the growth of polycrystalline and epitaxial $ZnCo_2O_4$ and $ZnIr_2O_4$ thin films confirmed the identification of a new class of non-d^{10} *p*-type zinc-based oxides which however are characterized by small optical band gaps (< 3 eV)[18]. Theoretical studies confirmed later the intrinsic *p*-type conductivity of ZnM_2O_4 oxides, arising from acceptor-like antisite defects (Zn_M) and Zn vacancies (V_{Zn}), as well as the small mobilities of these compounds due to their large hole effective masses.

1.6 $SrZnO_2$

1.6.1 A comparison of $SrZnO_2$ and ZnO

In contrast to ZnO, which adopts the hexagonal wurtzite structure of three-dimensional corner sharing ZnO_4 tetrahedra, $SrZnO_2$ has a two-dimensional orthorhombic structure with layers of corner-sharing ZnO_4 tetrahedra separated by Sr^{2+} ions which are coordinated by seven oxide ions as seen in **Figure 1. 11**. It has a reported experimental band-gap of 3.41 eV[88], similar to that of ZnO (3.37 eV)[89], and has been used as a phosphor host. However, no published data on the conductivity and band structure of $SrZnO_2$ have been so far published.

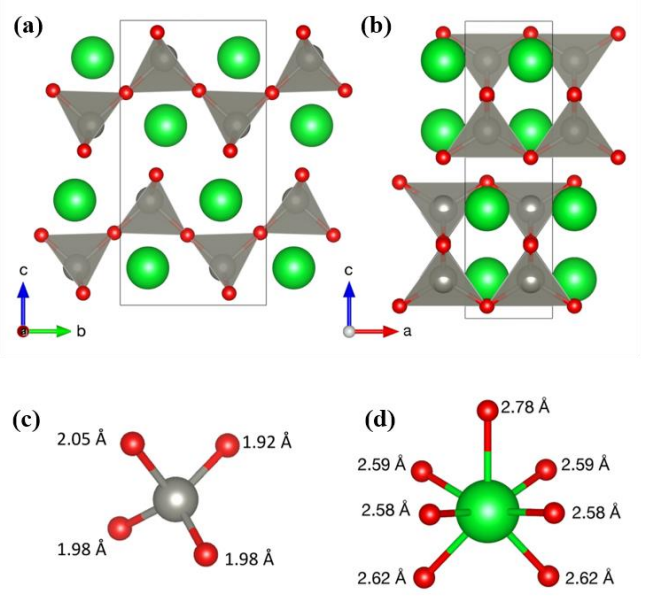

Figure 1. 11: Structure of SrZnO2 with Sr^{2+} ions being located between the corner-sharing ZnO_4 tetrahedra viewed a) along the a-axis, b) along the b-axis, c) the ZnO_4 tetrahedra with the Zn-O bond lengths indicated and d) the SrO_7 environment with the Sr-O bond lengths. Taken from[90].

Electronic structure calculations on $SrZnO_2$, performed by Gupta et al.[90] from Rosseinsky's group, using the HSE06 hybrid functional have shown a band gap of 3.80 eV and thus being transparent to the visible range of the electromagnetic spectrum. This value was found higher that the previously reported computed value of 3.41 eV[88] and closer to the experimental value of 4.27 eV, measured in lab by UV-visible spectroscopy on our samples. We should note here that the HSE06 calculated band gap of $SrZnO_2$ was found to be underestimated compared to the experimental value, similarly to what was been observed in other reports of HSE06 ZnO

calculations due to strong interaction between the p and d bands[90]. In addition, band structure calculations using the PBE functional have also shown a $SrZnO_2$ hole effective mass of $m^* = 0.67\ me$, a value smaller than the ZnO hole effective mass of 0.95 *me*, suggesting a larger hole mobility of $SrZnO_2$ compared to that of ZnO[90].

As can also be seen on the HSE06 calculations of **Figure 1. 12**, the nature of the valence and conduction band edges of $SrZnO_2$ are similar to those of ZnO. The top of the valence band in $SrZnO_2$ (between 0 and -3.7 eV) was found to be dominated by the O 2*p* states with some contribution from the Zn 3*d* states while the bottom of the valence band is mainly formed by Zn 3*d* states with some contribution from O 2*p* states, as in ZnO. Finally, the conduction band of $SrZnO_2$ is associated with the delocalized Zn 4*s* states with only a minor contribution from Zn 4*p* and Sr 5*s* states[90], again similar to ZnO.

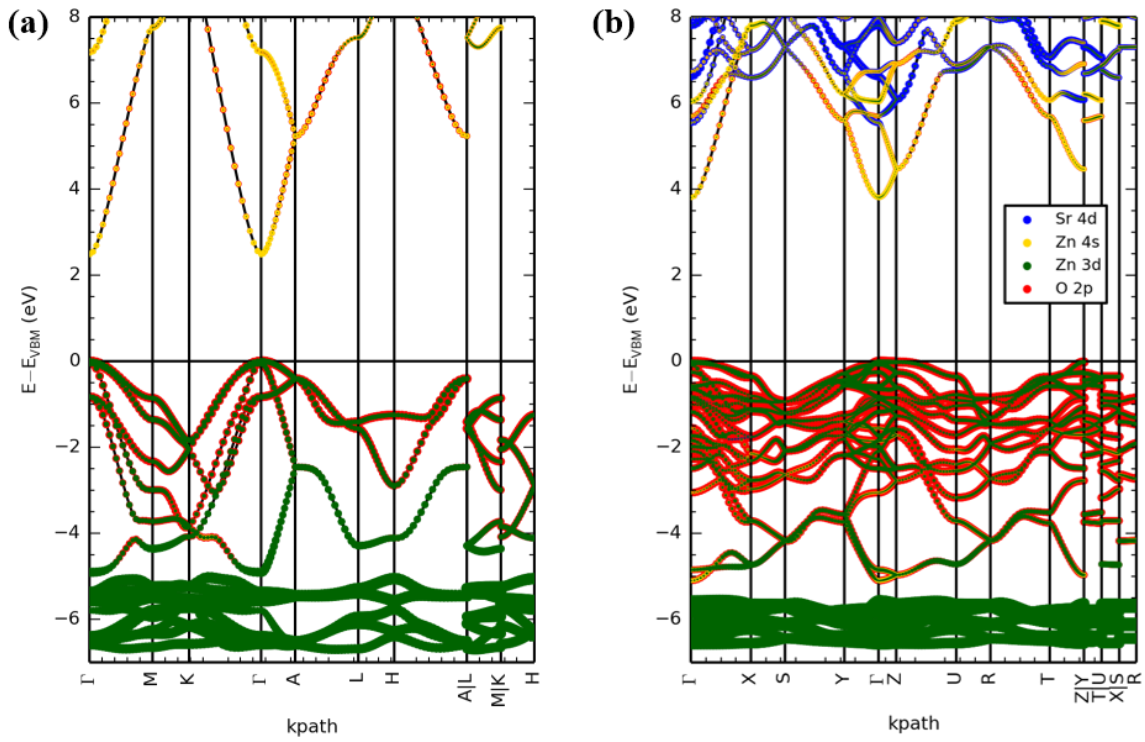

Figure 1. 12: Computed band structures of: (a) ZnO and (b) $SrZnO_2$ from HSE06 calculations. The radius of symbols represents the extent to which different atomic orbitals contribute to the electronic states. Projections are only shown for those atomic orbitals with a major contribution. Taken from[90].

1.6.2 Substitution calculations for *p*-type doping of $SrZnO_2$

P-type conductivity in $SrZnO_2$ was investigated by Gupta et al.[90] with the aliovalent substitution of 1^+ cations at either the Sr^{2+} or Zn^{2+} site, as summarized in **Table 1. 3**. The energy above the convex hull (ΔE) of all the different doping systems, presented in **Table 1. 4** calculated using the Python Materials Genomics (pymatgen) package and $SrZn_{(1/32)}Li_{(31/32)}O_2$ was found to be the only candidate lying closest to $SrZnO_2$ convex hull with an energy of 7 meV/per functional unit (f.u.), thus Li incorporation in the Zn sites is the most likely of all the screened candidates.

The free energy analysis of the doped compounds was calculated using the configurational entropy (S_{mix}), as described in **(Eq. 1. 11)** and **(Eq. 1. 12)**, where x is the dopant concentration, k_B is the Boltzmann constant, T is the temperature (in Kelvin) and ΔE is the energy change of substituting one atom in the super cell:

$$S_{mix} = -k_B\,(x \ln x + (1-x)\ln(1-x)) \qquad \textbf{(Eq 1. 11)}$$

$$\Delta G\ (\mathrm{eV/f.u.}) = x\,\Delta E - T\,\Delta S_{mix} \qquad \textbf{(Eq 1. 12)}$$

Table 1. 3: Ionic radii of selected *p*-type dopants for the substitution of Zn^{2+} and Sr^{2+} within $SrZnO_2$, with the corresponding coordination environments according to[91]. Taken from[90].

Ion	Coordination no.	Ionic Radius (Å)	Dopant ion	Ionic Radius (Å)	Difference in radii (Å)
Zn^{2+}	4	0.60	Li^+	0.59	-0.01
			Ag^+	1.00	0.40
Sr^{2+}	7	1.21	Na^+	1.12	-0.09
			K^+	1.46	0.25
			Ag^+	1.22	0.01

Table 1. 4: Energies above the convex hull of the doped $SrZnO_2$ materials. Taken from[90].

Compound	Competing Phases	Energy above convex hull (ΔE, meV/ fu)
$SrZnO_2$	–	0
$SrLi_{(1/32)}Zn_{(31/32)}O_2$	$\frac{31}{32}\ SrZnO_2 + \frac{1}{32}\ SrO + \frac{1}{64}\ Li_2O_2$	7
$Sr_{(31/32)}Na_{(1/32)}ZnO_2$	$\frac{31}{32}\ SrZnO_2 + \frac{1}{96}\ ZnO + \frac{1}{96}\ NaO_2 + \frac{1}{96}\ Na_2Zn_2O_3$	15
$Sr_{(31/32)}K_{(1/32)}ZnO_2$	$\frac{31}{32}\ SrZnO_2 + \frac{1}{48}\ ZnO + \frac{1}{96}\ K2ZnO_2 + \frac{1}{96}\ KO_2$	11
$SrAg_{(1/32)}Zn_{(31/32)}O_2$	$\frac{31}{32}\ SrZnO_2 + \frac{5}{192}\ SrO + \frac{1}{192}\ SrAg_6O_4 + \frac{1}{64}\ O_2$	24
$Sr_{(31/32)}Ag_{(1/32)}ZnO_2$	$\frac{185}{192}\ SrZnO_2 + \frac{7}{192}\ ZnO + \frac{1}{192}\ SrAg_6O_4 + \frac{1}{128}\ O_2$	33

Gupta et al work on finite temperature effects, in **Figure 1. 13**, has also shown that the formation of $Sr_{1-x}Na_xZnO_2$ and $Sr_{1-x}\ K_xZnO_2$ are thermodynamically favoured only at high temperatures while the stability of $Sr_{1-x}K_xZnO_2$ is extended in a relatively broader composition range (0.015 – 0.03)[90]. Doping Ag into $SrZnO_2$ on either the Sr^{2+} or Zn^{2+} site, was found thermodynamically unstable over the calculated conditions. On the other hand, the formation of $SrZn_{1-x}Li_xO_2$ was seen to be stable at temperatures as low as 800 K and a broader composition range. In addition, the partial density of states (PDOS) of the screened doped compound has been calculated showing the formation of unoccupied states above the Fermi energy for all the group I elements, in **Figure 1. 14** and **Appendix A**.

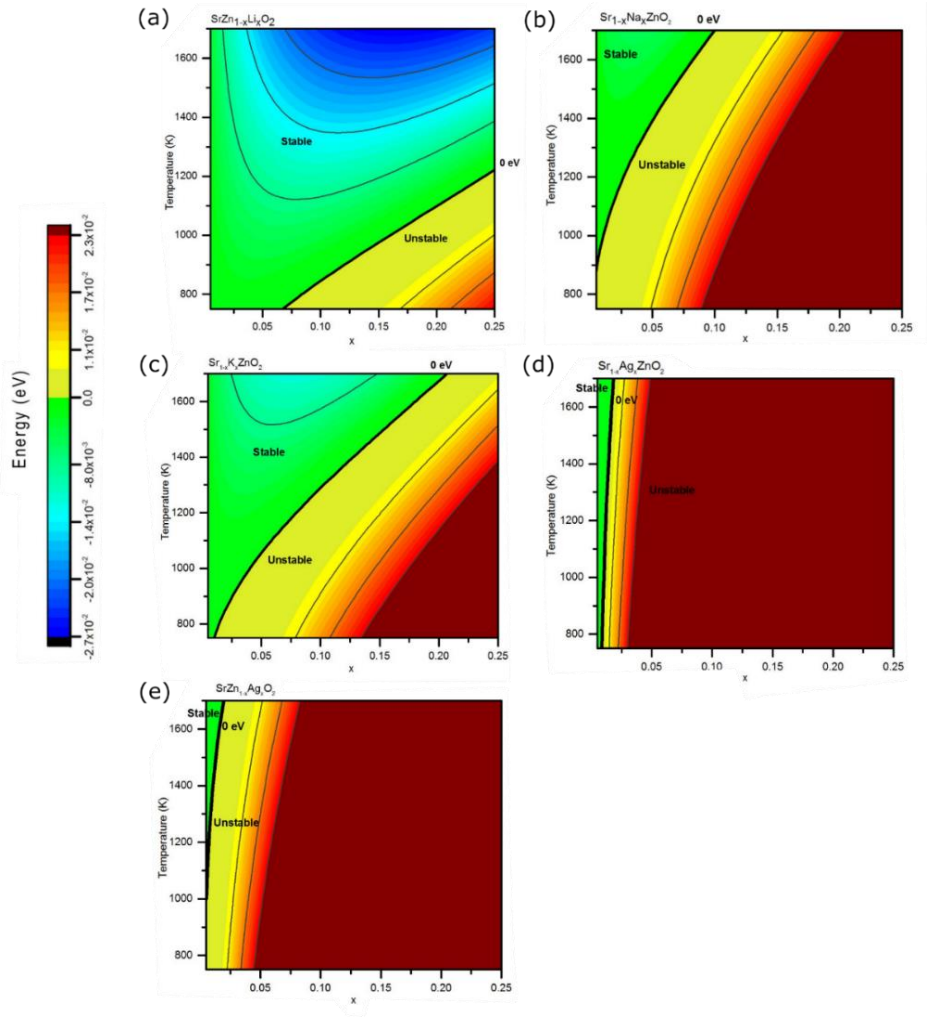

Figure 1. 13: Free energy analysis (in eV) of a) $SrZn_{1-x}Li_xO_2$, b) $Sr_{1-x}Na_xZnO_2$, c) $Sr_{1-x}K_xZnO_2$, and d) $Sr_{1-x}Ag_xZnO_2$, and e) $SrZn_{1-x}Ag_xO_2$ with the bold black line representing the boundary between the thermodynamic stability and instability of the respective compounds. Taken from[90].

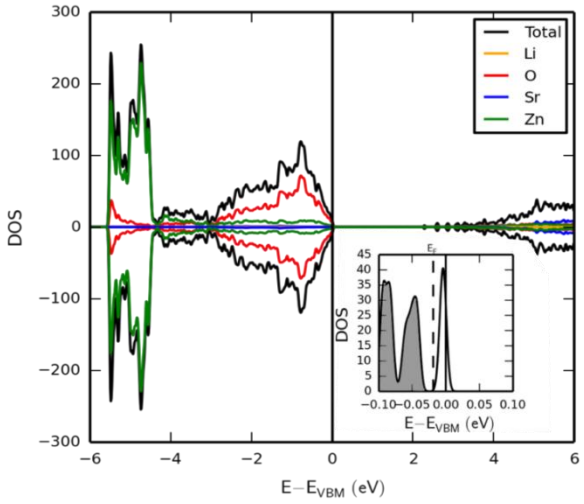

Figure 1. 14: Partial density of states (PDOS) of $SrZn_{1-x}Li_xO_2$ (x = 1/32). The insert in the bottom right focuses around the VBM with the dashed line indicating the E_F. The occupied states shaded in grey while the remaining unoccupied states were left unshaded. The presence of the empty states, above the E_F, is indicative of *p*-type doping. Taken from[90].

In summary, Gupta et al.[90] work over the substitution energetics and the finite temperature effects on many $SrZnO_2$ dopants have suggested $SrZn_{1-x}Li_xO_2$ as the most favourable *p*-type candidate compound.

1.7 Aim of the project

Ternary zinc oxides containing a second electropositive cation may offer an alternative route to stabilize acceptor impurities: apart from the option of substitute dopants, they can also provide the opportunity of exploring additional doping sites. As was already discussed, the only ternary *p*-type zinc oxides that have been reported so far in the literature are the spinels M_2ZnO_4 (M = Co, Rh, Ir).

In this thesis we considered the wide band-gap oxide $SrZnO_2$. The conceptual backbone of the project lies in band gap and hole mobility calculations, conducted by Gupta[90], investigating the electronic structure of $SrZnO_2$ to ZnO and identifying $SrZnO_2$ as a potential host for *p*-type carriers. Furthermore, first-principles doping-dependent calculations highlighted Li as the most promising *p*-type dopant for $SrZnO_2$.

Experimentally, the work of this thesis was focused on exploring different *p*-type dopants by (i) the conventional solid-state route and (ii) strictly anaerobic conditions (of more reactive reagents). Our aim will be the isolation of phase pure doped $SrZnO_2$ samples, the characterization of the structural and optical properties of the doped samples as well as the assessment of their electrical performance. Finally, we will also investigate the growth of $SrZnO_2$ thin films by means of PLD.

References

[1] D.S. Ginley, H. Hosono, D.C. Paine, *Handbook of transparent conductors*, Springer, 2011

[2] J. F. Wager, D.A. Keszler, R.E. Presley, *Transparent Electronics*, Springer, 2008

[3] A. Stadler, *Materials* **5**, 2012, 661

[4] *Fundamentals of Semiconductor physics*, at: http://www.optique-ingenieur.org

[5] A.R. West, *Basic Solid-State Chemistry*, John Wiley & Sons, 1996

[6] Rao, C.N.R., Raveaus, B., *Transition Metal Oxides: Structure, Properties and Synthesis of Ceramics Oxides*, John Wiley & Sons, 1998

[7] R. Nave, *Bands for Doped Semiconductors*, http://hyperphysics.phy-astr.gsu.edu

[8] A. Facchetti, T.J. Marks (eds.), *Transparent Electronics: From Synthesis to Applications*, John Wiley & Sons, 2010

[9] S. Kasap, P. Capper (eds.), *Springer Handbook of Electronic and Photonic Materials*, Springer, 2006

[10] C. Jacoboni, C. Canali, G. Ottaviani, A.A. Quaranta, *Solid-State Electron*., *vol. 20*, **77**, 1977

[11] K. Ellmer, *Nat. Photonics* **6**, 2012, 809

[12] I. Luciu, (2012). *RF plasma synthesis and characterization of thin films for transparent conductors*, PhD Thesis, University of Trento

[13] Y. Lee, B.O. Park, *Thin Solid Films* **510**, 2006, 154

[14] C. Hamaguchi, *Basic Semiconductor Physics*, Springer, 2001

[15] G. Haacke, *J. Appl. Phys*. **47**, 1976, 4086

[16] I. Luciu, *RF plasma synthesis and characterization of thin films for transparent conductors*, PhD Thesis, University of Trento, 2012

[17] H. Hosono, *Thin Solid Films* **515**, 2007, 6000

[18] K.H.L. Zhang, K. Xi, M.G. Blamire, R.G. Egdell, *J. Phys.: Condens. Matter* **28**, 2016, 383002

[19] A.N. Banerjee, K.K. Chattopadhyay, *Prog. Cryst. Growth & Charact* **50,** 2005, 52

[20] D.C. Look, *Semicond. Sci. Technol*. **20**, 2005, S55

[21] T.M. Barnes, K. Olson, C.A. Wolden, *Appl. Phys. Lett*. **86**, 2005, 112112

[22] W.J. Li, C.Y. Kong, G.P. Qin, H.B. Ruan, L. Fang, *J. Alloy. Compd*. **609**, 2014, 173

[23] H. Zhang, C. Kong, W. Li, G. Qin, H. Ruan, M. Tan, *J Mater Sci: Mater Electron* **27**, 2016, 5251

[24] H. Kawazoe, M. Yasukawa, H. Hyodo, M. Kurita, H. Yanagi, H. Hosono, *Nature* **389**, 1997, 939

[25] H. Kawazoe, H. Yanagi, K. Ueda, H. Hosono, *MRS Bulletin* **25**, 2000, 28

[26] J.P. Dahl, A.C. Switendick, *J. Phys. Chem. Solids* **27**, 1966, 931

[27] H. Yanagi, S. Inoue, K. Ueda, H. Kawazoe, H. Hosono, N. Hamada, *J. Appl. Phys*. **88**, 2000, 4159

[28] R. Nagarajan, N. Duan, M.K. Jayaraj, J. Li, K.A. Vanaja, A. Yokochi, A. Draeseke, J. Tate, A.W. Sleight, *Int. J. Inorg. Mater*. **3**, 2001, 265

[29] K. Ueda, T. Hase, H. Yanagi, H. Kawazoe, H. Hosono, H. Ohta, M. Orita, M Hirano, *J Appl Phys*. **89**, 2001, 1790

[30] H. Yanagi, T. Hase, S. Ibuki, K. Ueda, H. Hosono, *Appl. Phys. Lett*. **78**, 2001, 1583

[31]Y. Kakehi, K. Satoh, T. Yoshimura, A. Ashida, N. Fujimura, *Vacuum* **84**, 2009, 618

[32] Y.-H. Chuai, H.Z. Shen, Y.-D. Li, B. Hu, Y. Zhang, C.-T. Zheng, Y.D. Wang, *RSC Advances* **5**, 2015, 49301

[33] R. Nagarajan, A. D. Draeseke, A. W. Sleight, J. Tate, *J. Appl. Phys.* **89**, 2001, 8022

[34] M. Snure and A. Tiwari, *Appl. Phys. Lett.* **91**, 2007, 092123

[35] Y.S. Zou, H.P. Wang, S.L. Zhang, D. Lou, Y.H. Dong, X.F. Songa, H.B. Zeng, *RSC Adv*. **4**, 2014, 4129

[36] Y.H. Chuai, X. Wang, H.Z. Shen, Y.D. Li, C.T. Zheng, Y.D. Wang, *J. Mater. Sci*. **51**, 2016, 3592

[37] M.K. Jayaraj, A.D. Draeseke, J. Tate, A.W. Sleight, *Thin Solid Films* **397**, 2001, 244

[38] H. Yanagi, S. Park, A.D. Draeseke, D.A. Keszler, J. Tate, *J. Solid State Chem*. **175**, 2003, 34

[39] N. Duan, A. W. Sleight, M. K. Jayaraj, J. Tate, *Appl. Phys. Lett.* **77**, 2000, 1325

[40] P. L. Popaa, J. Crêpellière, P. Nukala, R. Leturcq, D. Lenoble, *Applied Materials Today* **9**, 2017, 184

[41] K. Ueda, S. Inoue, S. Hirose, H. Kawazoe and H. Hosono, *Appl. Phys. Lett*.**77**, 2000, 2701

[42] M. Ono, S. Webster, S. Ito, and H. Hosono, *Proc. SID.* '**06**, 2006, 1642

[43] D.O. Scanlon, J. Buckeridge, C.R.A. Catlow, G.W. Watson, *J. Mater. Chem. C* **2**, 2014, 3429

[44] K. Ueda, S. Inoue, H. Hosono, N. Sarukura, M. Hirano, *Appl. Phys. Lett*. **78**, 2001, 2333

[45] M. Buchammagari, Y. Toda, M. Hirano, H. Hosono, D. Takeuchi, K. Osakada, *Org. Lett*. **9**, 2007, 4287

[46] M. Palazzi, *C. R. des Acad. Sci*. *Ser. I*. **292**, 1981, 789

[47] H. Hiramatsu, K. Ueda, H. Ohta, M. Hirano, T. Kamiya, H. Hosono, *Appl. Phys. Lett*. **82**, 2003, 1048

[48] J. Nishino, S. Ohshio and K. Kamata, *MRS Proc*. **363**, 1994, 219

[49] C. Jagadish, S. Pearton, *Zinc oxide bulk, thin films and nanostructures: processing properties and applications*, Elsevier, 2006

[50] D.C. Look, D.C. Reynolds, J.R. Sizelove, R.L. Jones, C.W. Litton, G. Cantwe, W.C. Harsch, *Solid State Communications* **105**, 1998, 399

[51] D.J. Rogers, F.H. Teherani, *Encyclopaedia of Materials: Science and Technology*, Elsevier, 2010

[52] D.C. Reynolds, D.C. Look, B. Jogai, C.W. Litton, G. Cantwell, W.C. Harsch, *Phys. Rev. B* **60**, 1990, 2340

[53] F. Y. Mao, H. Deng, L.P. Dai, J.J. Chen, Z.L. Yuan, Y. Li, *Chinese Science Bulletin* **53**, 2008, 2582

[54] A. Janotti, C.G. Van de Walle, *J. Cryst. Growth* **287**, 2006, 58

[55] A. Janotti and C.G. Van de Walle, *Phys. Rev. B* **75**, 2007, 165202

[56] D.C. Look, J.W. Hemsky, and J.R. Sizelove, *Phys. Rev. Lett*. **82**, 1999, 2552

[57] H. Noor, P. Klason, O. Nur, Q. Wahab, M. Asghar, M. Willander, *J. Appl. Phys*. **105**, 2009, 123510

[58] A. Janotti, C.G. Van de Walle, *Appl. Phys. Lett*. **87**, 2005, 122102

[59] L.S. Vlasenko, G.D. Watkins, *Phys. Rev. B* **71**, 2005, 125210

[60] A. Janotti, C.G. Van de Walle, *Rep. Prog. Phys*. **72**, 2009, 126501

[61] C.G. Van de Walle, *Phys. Rev. Lett*. **85**, 2000, 1012

[62] D.M. Hofmann, A. Hofstaetter, F. Leiter, H.Z., F. Henecker, B.K. Meyer, S.B. Orlinskii, J. Schmidt, P.G. Baranov, *Phys. Rev. Lett*. **88**, 2002, 045504

[63] S.F.J. Cox, E.A. Davis, S.P. Cottrell, P.J.C. King, J.S. Lord, J.M. Gil, H.V. Alberto, R.C. Vilão, J. Piroto Duarte, N. Ayres de Campos, A. Weidinger, R.L.Lichti, S.J.C. Irvine, *Phys. Rev. Lett*. **86**, 2001, 2601

[64] J.C. Fan, K.M. Sreekanth, Z. Xie, S.L. Chang, K.V. Rao, *Prog. Mater. Sci*. **58**, 2013, 874

[65] A. Suzuki, T. Matushita, N. Wada, Y. Sakamoto, M. Okuda, *Jpn. J. Appl. Phys*. **35**, 1996, L56

[66] G.A. Hirata, J. McKittrick, J. Siqueiros, O.A. Lopez, T. Cheeks, O. Contreras, J.Y. Yi, *J. Vac. Sci. Technol. A* **14**, 1996, 791

[67] M. Hiramatsu, K. Imaeda, N. Horio, M. Nawata, *J. Vac. Sci. Technol. A* **16**, 1998, 669

[68] K. Matsubara, P. Fons, K. Iwata, A. Yamada, K. Sakurai, H. Tampo, S. Niki, *Thin Solid Films* **431–432**, 2003, 369

[69] A.V. Singh, R.M. Mehra, N. Buthrath, A. Wakahara, A. Yoshida, *J. Appl. Phys*. **90**, 2001, 5661

[70] B. Bayraktaroglu, K. Leedy, R. Bedford, *Appl. Phys. Lett*. **93**, 2008, 022104

[71] H. Kim, J.S. Horwitz, S.B. Qadri, D.B. Chrisey, *Thin Solid Films* **420-421**, 2002, 107

[72] M. Karger, M. Schilling, *Phys. Rev. B* **71**, 2005, 075304

[73] M. Kumar, R.M. Mehra, A. Wakahara, M. Ishida, A. Yoshida, *J. Appl. Phys*. **93**, 2003, 3837

[74] C.H. Park, S.B. Zhang, S.H. Wei, *Phys. Rev. B* **66**, 2002, 073202

[75] Y.F. Yan, S.H. Wei, *Phys. Stat. Sol.(b)* **245**, 2008, 641

[76] R. Vidya, P. Ravindran, H. Fjellvåg, *J. Appl. Phys.* **111**, 2012, 123713

[77] E.C. Lee, K.J. Chang, *Phys. Rev. B* **70**, 2004, 115210

[78] S.S. Lin, H.P. He, Y.F. Lu, Z.Z. Ye, *J. Appl. Phys*. **106**, 2009, 093508

[79] Ü. Özgür, Ya. I. Alivov, C. Liu, V. Avrutin, A. Teke, M. A. Reshchikov, S. Doğan, S.-J. Cho, H. Morkoç, *J. Appl. Phys*. **98**, 2005, 041301

[80] C.H. Park, S.B. Zhang, S.H. Wei, *Phys. Rev. B* **66**, 2002, 073202

[81] X. Li, Y. Yan, T.A. Gessert, C. DeHart, C.L. Perkins, D. Young, T.J. Coutts, *Electrochem. Solid-State Lett.* **6**, 2003, C56

[82] S. Limpijumnong, S.B. Zhang, S.H. Wei, C.H Park, *Phys. Rev. Lett*. **92**, 2004, 155504

[83] J. Zhang, K. Tse, M. Wong, Y. Zhang, J. Zhu, *Front. Phys*. **11**, 2016, 117405

[84] T. Yamamoto, H. Katayama-Yoshida, *Jpn. J. Appl. Phys*. **38**, 1999, 166

[85] T. Yamamoto, *Thin Solid Films* **420**, 2002, 100

[86] M. Joseph, H. Tabata, T. Kawai, *Jpn. J. Appl. Phys*. **38**, 1999, L1205

[87] H. Mizoguchi, M. Hirano, S. Fujitsu, T. Takeuchi, K. Ueda, H. Hosono, *Appl. Phys. Lett*. **80**, 2002, 1207

[88] A. Manavbasi, J. C. LaCombe, M. Batzill, U. Diebold, *J. Lumin.* **79**, 2005, 129

[89] J. Nishino, S. Ohshio, K. Kamata, *MRS Proc*. **363**, 1994, 219

[90] C.A Tzitzeklis, J.K. Gupta, M.S. Dyer, T.D. Manning, M.J. Pitcher, H.J. Niu, S. Savvin, J. Alaria, G.R. Darling, J.B. Claridge, M.J. Rosseinsky, *Inorg. Chem*., 2018, 57 (19), 11874

[91] R.D. Shannon, *Acta Crystallogr*. *Sect. A* **32**, 1976, 751

[92] E.M. Bomhard**,** *Environ Toxicol Pharmacol.* **45**, 2016, 282

Chapter 2: Multiferroic materials

2.1 Ferroelectricity

2.1.1 Basic considerations on ferroelectricity

Based on their ability to conduct current, materials can be classified as *conductors*, *insulators* and *semiconductors*. In the class of insulating materials, *dielectrics* are of great technological interest due to their ability to be polarized when an electric field is applied.

While all the materials are polarized under an applied electric field, the atomic arrangement of ions in some of them will produce a naturally occurring spontaneous polarization. *Piezoelectrics* is a certain subclass of non-centrosymmetric (polar) dielectrics, capable to be polarized when subjected to an external mechanical stress (direct piezoelectric effect) or get strained under an external applied electric field (inverse, indirect piezoelectric effect).

In the case of *pyroelectrics*, a subset of piezoelectrics, a spontaneous and reversible polarization will emerge when the materials are heated and subsequently cooled. Contrary, though, to other piezoelectrics, their polarization can also be preserved in the absence of electric field or mechanical stress.

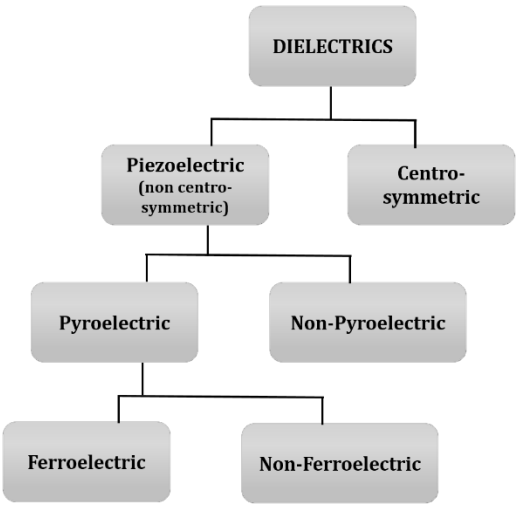

Figure 2. 1: Classification of dielectric materials.

Ferroelectrics, also demonstrate a spontaneous polarization in the absence of external electrical field or mechanical stress as pyroelectric and piezoelectric materials do. In the case of the ferroelectrics, however, their spontaneous polarization can also be easily switched under an applied electric field[92].

For reasons related to nonuniform strains, microscopic defects and the thermal/electrical history of the material, the spontaneous polarization of a ferroelectric crystal is not usually uniformly directed along the whole crystal. Instead, the formation of ferroelectric domains leads to a reduction of the electrostatic energy and the elastic energy of the system. The type of domains walls that emerge are associated to the crystal symmetry of the phases along the ferroelectric transition (paraelectric-ferroelectric phase transition)[93].

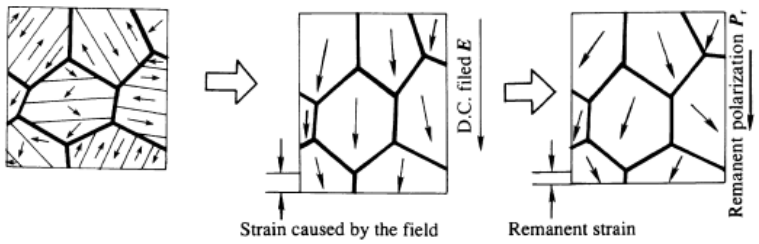

Figure 2. 2: Schematic illustration of the poling process. Taken from[94].

A single domain will be obtained only when a sufficiently high electric field is applied and re-orientate the different domains by moving their domain walls, a process known as *poling*. As can be seen in **Figure 2. 2**, the phase difference between the externally applied electrical field and the induced domain alignment will give rise to the observed ferroelectric *P-E* hysteresis loop, in **Figure 2. 3**.

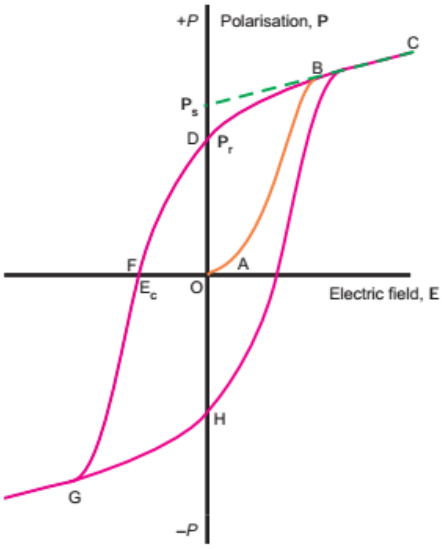

Figure 2. 3: A typical *P-E* hysteresis loop of polarization, *P*, versus the applied electric field, *E*, of a ferroelectric material. Taken from[92].

A number of points can be made from the hysteresis loop of a material regarding its ferroelectric response. To begin with, as the strength of the applied electric field is increased in **Figure 2. 3**, the different domains of the ferroelectric are gradually switched over the direction of the external field until a single domain material will be obtained with a saturated polarization at its higher value. As the field is then reduced, the ferroelectric material will be depolarized and only a fraction of the domains maintained their initial direction at zero applied field, resulting to a sample of a net remanent polarisation ***Pr***. In order to pole the ferroelectric material in the opposite direction, a reversed field of the same magnitude will be required while the field to reduce the polarisation *P* to zero is called the coercive field strength ***Ec***.

The induced polarization P_i of a ferroelectric material during this process is given by:

$$P_i = x_{ij} E_j \qquad \textbf{(Eq. 2. 1)}$$

where x_{ij} is the dielectric susceptibility of the material and E_j the externally applied field[95].

An important feature of the ferroelectrics in relation to their technical applications is also their insulating character, allowing them to sustain large applied voltages without degradation or becoming conducting[96]. The insulating character of ferroelectrics can be quantified based on the energy losses of dielectric measurements performed over a range of frequencies.

The dielectric loss are typically calculated by the equation:

$$tan\ \delta = \frac{\varepsilon''}{\varepsilon'} \quad \textbf{(Eq. 2. 2)}$$

where ε' is the real part of the permittivity, which is constant in the static limit and decreases as the frequency is increased. In non-time variable electromagnetic fields is given by:

$$\varepsilon' = \frac{C}{C_o}\frac{d}{A} \quad \textbf{(Eq. 2. 3)}$$

where Co is the capacitance of an identical capacitor in a vacuum, d the distance and A the surface area of capacitor's plates, respectively.

The imaginary part of the dielectric permittivity, ε'', describes the lag between the phase of the input field and the phase of the output field due to bound charge and dipole relaxation phenomena.

2.1.2 Ferroelectricity in the morphotropic phase boundary (MPB)

One of the most interesting features of ferroelectrics is the enhanced electro-mechanical properties in the vicinity of morphotropic phase boundary of ferroelectric solid solutions. Lead zirconate titanate (PZT), of the chemical formula $xPbZrO_3$-$(1-x)PbTiO_3$ is an archetypal material in this class of materials.

Above *Tc*, PZT adopts the perovskite structure with titanium and zirconium atoms randomly occupying B-sites while lead atoms are placed at the corners of the unit cell, as shown in **Figure 2. 4**. The ferroelectricity of PZT is originated from the displacement of the B-site (Ti^{4+} and Zr^{4+}) cations.

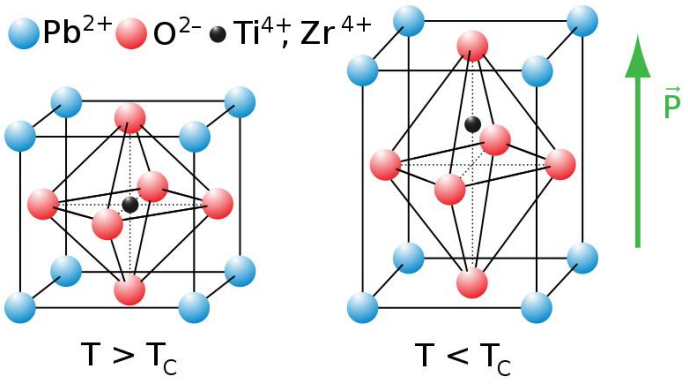

Figure 2. 4: Schematic of PZT crystalline lattice and the origin of permanent dipole in tetragonal lattice. Taken from[97].

$PbTiO_3$ crystallizes in a cubic paraelectric phase at high temperatures and undergoes a phase transition to a tetragonal ferroelectric phase at around 490 °C. On the other hand, $PbZrO_3$ is demonstrating a cubic-paraelectric to an orthorhombic-antiferroelectric phase transition at 230 °C.

While PZT is cubic over the whole range of compositions above the Tc, it crystallizes in two ferroelectric phases at temperatures below Tc, depending the composition ratio of $PbZrO_3/PbTiO_3$. A morphotropic phase boundary (MPB) is dividing the ferroelectric region on a tetragonal (Ti-rich) phase and a rhombohedral (Zr-rich) phase with the boundary of the phases laying, in room temperature, at Zr/Ti = 52/48. The phase diagram of PZT as a function of the composition ratio of the two constituted binary oxides, $PbZrO_3$ and $PbTiO_3$ is presented in **Figure 2. 5**.

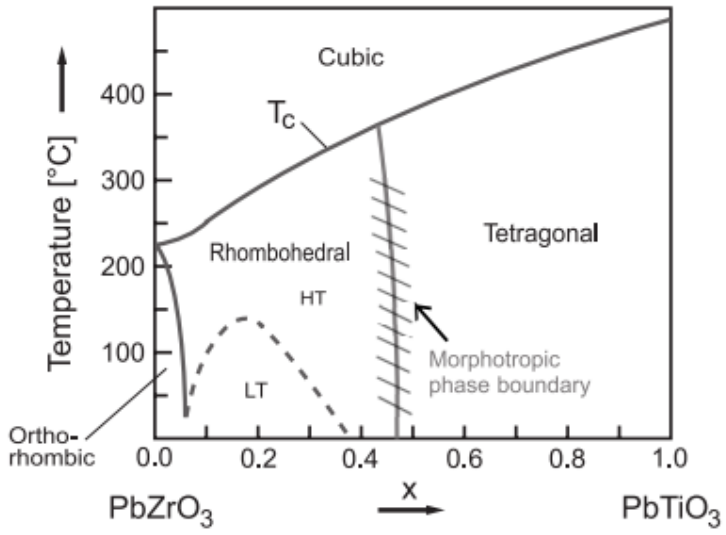

Figure 2. 5: Phase diagram of $xPbZrO_3$ - $(1-x)PbTiO_3$, PZT. Taken from[98].

As a result of the coexistence of the two-phase around the MPB region, the transition from tetragonal to rhombohedral phase is bridged by a monoclinic phase[99]. As it shown in **Figure 2. 6**, close to the MPB, a great enhancement on the dielectric and piezoelectric properties of PZT is observed attributed to the multiplicity of polarization rotations driven by monoclinic structural distortions[100].

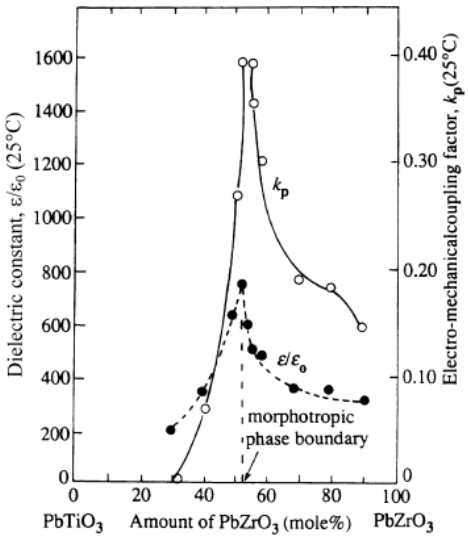

Figure 2. 6: Dielectric and piezoelectric properties of the PbTiO3-PbZrO3 solid solution. Taken from[101].

Although the unique piezoelectric properties of PZT credited as a material of significant technological importance there are still however some major drawbacks related to its use.

From technical point of view, the low T_c (below 400 °C) of PZT is limiting the range of the technical applications where it could be utilized. To tackle this constraint, a variety of dopants have till now been studied to effectively tune the piezoelectrics properties of PZT to higher temperatures, with the topic remaining still active.

However, the biggest concern with the use of PZT is related to its environmental impact due to the toxic effects of the contained lead. In front of restrictions on its use researchers have focused their attention on developing alternative lead-free piezoelectric materials to replace lead-based materials. Among other candidates, $BiFeO_3$, a multiferroic material with a high Tc (825 °C) has attracted a considerable attention as a possible lead-free, environmentally friendly, piezoelectric. In this direction, the discovery of a Bi-based MPB system with electromechanical properties comparable to PZT represents a research field of great interest.

2.2 Magnetism

2.2.1 Basic considerations on magnetism

Since magnetism is originated from the motion of charged particles, all particles of matter should experience magnetism associated with their orbital magnetic momentum, $m_{orbital}$, and their intrinsic spin magnetic moment, m_{spin}.

According to the theory of magnetism, the total magnetic dipole moment of an atom is given by[92]:

$$m_{atom} = g_J \mu_B \sqrt{J(J+1)} \quad \textbf{(Eq. 2. 4)}$$

where g_J is the $Lande\ g-factor$ that is given by:

$$g_J = 1 + \frac{J(J+1)-L(L+1)+S(S+1)}{2J(J+1)} \quad \textbf{(Eq. 2. 5)}$$

with *L*, *S* and *J* are respectively describing the orbital angular momentum, the intrinsic angular (spin) momentum and the total angular momentum quantum number of an atom, while μ_B is the magnetic dipole moment of a spinning electron, the $Bohr\ magneton$, given by:

$$\mu_B = \frac{eh}{4\pi m} \quad \textbf{(Eq. 2. 6)}$$

with *e* the charge of the electron, *h* the Planck's constant and *m* the electron's mass.

The magnetic response of a material to an external field of *H* strength can be defined as the magnetic susceptibility, χ:

$$\chi = \frac{M}{H} \approx \frac{\mu_o M}{B} = \frac{\mu_o \mu^2}{3k_B T} \quad \textbf{(Eq. 2. 7)}$$

where μ_o the permeability of free space, k_T the Boltzmann constant, *M* is the magnetic moment per unit volume of the material, *H* the strength of the applied magnetic field, *B* the magnetic flux density, which is related to the applied field *H* by the relationship $B = \mu_o(H + M)$.

2.2.2 Overview of magnetic materials

Macroscopically, the interaction between the magnetic moments on neighbouring atoms is giving rise to different type of long-range arrangements.

Materials in which their atoms do not exhibit elementary magnetic dipoles (ie, the orbital shells of the atoms are filled) are called diamagnetic. When subjected to an external magnetic field, a weak magnetization of opposite direction to the imposed magnetic flux density, B, will emerge. As a result, their magnetic susceptibility is negative (as also temperature independent).

On the contrary, paramagnetic materials are these in which some of the atoms will demonstrate a permanent magnetic dipole moment due to their unpaired electron configuration. In the absence of an external field the elementary magnetic moments of their atoms do not interact with each other and macroscopically do not display any net magnetization. However, in the presence of an external field, a partial alignment of their atomic magnetic dipoles towards the field's direction will be developed, resulting in a positive (parallel to H) magnetization and an increased field strength inside the solid material. The paramagnetic materials possess temperature-dependent (positive) susceptibility as thermal motion effects increase the disorder of their magnetic dipoles that follows the Curie-Weiss law:

$$\chi_m = \frac{C}{T} \qquad \textbf{(Eq. 2. 8)}$$

where χ_m is the mass susceptibility (m^3/Kg) and C is a material-specific constant (Curie constant).

In the case of ferromagnetic materials (also antiferromagnetic and ferrimagnetic), the magnetic dipoles of their atoms are aligned over a considerable area under an external magnetic field (parallel or antiparallel, as illustrated in **Figure 2. 7**) even when the magnetic field is withdrawn, a phenomenon called hysteresis.

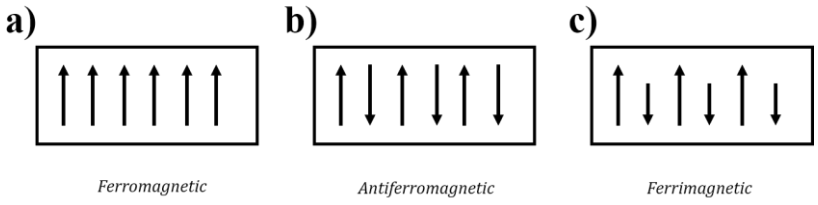

Figure 2. 7: Different long-range magnetic orders: ferromagnetism, antiferromagnetism, ferrimagnetism.

Above a certain temperature, defined as the *Curie temperature* T_c for ferromagnetic and *Neel temperature* T_N for antiferromagnetic materials, the thermal energy of these atoms is becoming bigger than their magnetic energy and consequently their long-range magnetic order is disrupted. This phase transition is reversible and all the magnetic materials will regain their magnetic orientation as temperature is again decreased. The magnetic susceptibility of these materials is following the Curie-Weiss law:

$$\chi_m = \frac{C}{T-\theta} \quad \textbf{(Eq. 2. 9)}$$

where θ is the Curie-Weiss constant (positive for ferromagnetic, negative for antiferromagnetic materials) and C the Curie constant.

At the macroscopic level, the long-range order of magnetic materials will result in the formation of domains of different sizes. While short-range exchange interactions of electrostatic nature tend to align magnetic spins in an ordered way, long-range dipole-dipole contributions to the total magnetic energy of the particles start to prevail as the distance of dipoles is increased. The development of magnetic domains emerges as a balance between these two components as the system is trying to reduce its overall energy.

It is because of the random alignment of these magnetic domains that even soft ferromagnetic materials do not show a net magnetic moment in the absence of an external magnetic field. When, however, an external magnetic field is applied, a magnetization process will take place, involving the growth of domains favourably oriented to the external field and rotations of domains magnetization towards the direction of the field as showing in **Figure 2. 8**.

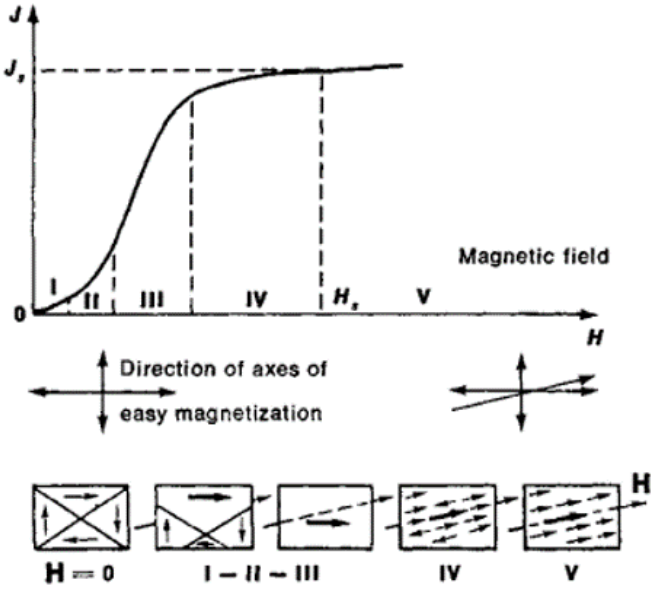

Figure 2. 8: Magnetic domain morphology of a ferromagnetic material. Taken from[102].

2.2.3 Crystal field and Exchange Interactions

Some interesting magnetic phenomena are observed on atoms with *d* electrons. In these atoms, contrary to the anticipated electron configuration predicted by Hund's rules to lower their total energy, interactions with neighbouring atoms lead to an orbital quenching of their *d* orbitals and the rise of "crystal field" effects allowing other possible configurations[92].

This way, the formerly degenerate *3d* orbitals of the transition ions will be seen to split into subgroups when subjected to electrostatic interactions with their neighbour ligand orbitals. For instance, when a transitional metal ion is found in a perovskite octahedral environment of 6 surrounding oxygens, its closest to the neighbouring O^{2-} ions orbitals (d_{z^2} *and* $d_{x^2+y^2}$) will raise their energy while the orbitals further away of the ligands (d_{xy} , d_{xz} , d_{yz}) will lower their energy.

As a result, the *3d* transition metal ions with electron configuration between $3d^4$ and $3d^7$ can be found in two spin states: high spin (HS) and low spin (LS), as seen in **Figure 2. 9**. The width of the crystal field splitting depends on the cation - anion interactions and can be stronger or weaker. For example, Fe^{3+} with a $3d^5$ electron configuration is possible to have five unpaired spins or only one depending on its local environment [92].

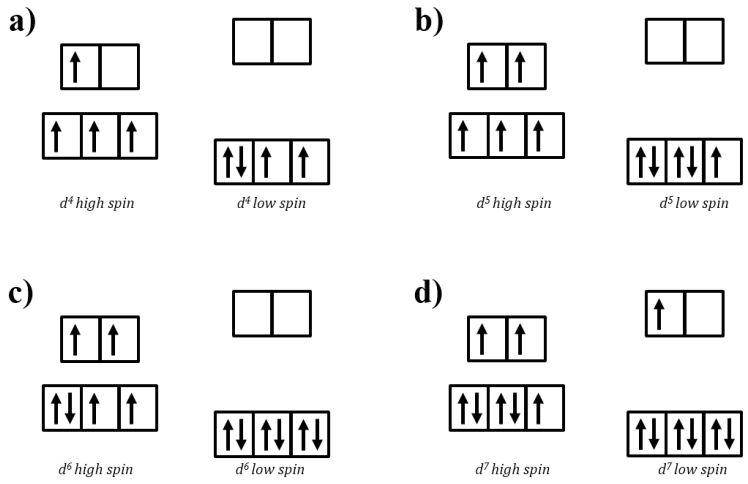

Figure 2. 9: The two possible electron configurations of high spin (HS) or low spin (LS) for d^4 – d^7 cations in an octahedral crystal field.

The long-range order of atomic magnetic moments arise through exchange interactions. These interactions describe the interplay of electrons on neighbouring magnetic ions and can be direct (direct exchange), when the electron orbitals of neighbouring atoms are overlapping, or indirect (superexchange, double exchange, Dzyaloshinskii–Moriya interaction, etc) when the coupling of magnetic ions occurs through intermediate ions.

For example, as can be seen in **Figure 2. 10** the spin moments of Fe^{3+} (d^5) ions in an octahedral environment will overlap with neighbouring oxygen 2p orbitals, leading to an anti-parallel alignment and an antiferromagnetic coupling, a mechanism known as super-exchange.

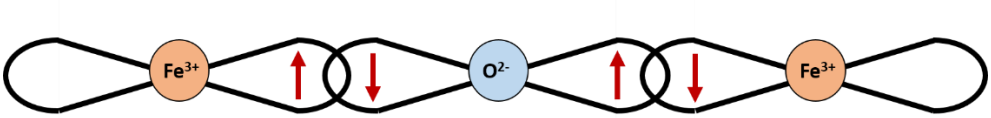

Figure 2. 10: Antiferromagnetic coupling of spins of *d* electrons on Fe^{3+} ions through *p* electrons of O^{2-}.

The Dzyaloshinskii–Moriya interaction (DM-interaction) is a type of exchange interaction occurring in low-symmetry structures via a strong spin orbit coupling rather than the intermediate oxygen ion of the superexchange interaction[103].

It appears in the case of *3d* transition metal oxides ABO_3 where differences in the size of A and B -ions introduce a tilt of the oxygen octahedra and bend the B-O-B bond from the ideal angle of 180 degrees. This distortion (bending) will induce the Dzyaloshinskii–Moriya interaction as a relativistic correction to the superexchange between magnetic B ions[104] and will induce a spin spiral formation.

For given S_i and S_j spins of two neighbouring B-ions, this asymmetric exchange interaction can be written microscopically as:

$$\varepsilon_D = \sum_{i,j} D_{i,j}(S_i \times S_j) \qquad \textbf{(Eq. 2. 10)}$$

where $S_{i,j}$ are the spins on the atomic sites *i, j* and D_{ij} is the Dzyaloshinskii vector and its orientation given by the relation: $D_{ij} \propto r_i \times r_j = r_{ij} \times x$, lying perpendicular to the plane of the three involved ions, as seen in **Figure 2. 11**.

The Dzyaloshinskii–Moriya interactions have contributed on clarifying the origin of an observed net magnetic moment on antiferromagnet systems resulting in weak ferromagnetism. They have also an important role on understanding the magnetically induced electric polarization in type II class of multiferroics.

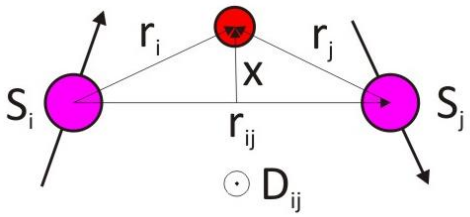

Figure 2. 11: Orientation of the Dzyaloshinskii-Moriya vector from the local geometry. Taken from[105].

Finally, in many (conductive) ferromagnetic ferrites, such as the Fe_3O_4, the long-range order of Fe ions is occurred through a double exchange mechanism, where the coupling between Fe ions (Fe^{2+} and Fe^{3+} ions located in octahedral sites) is accomplished by an electron transfer through adjacent O^{2-} ions, as illustrated in **Figure 2. 12**.

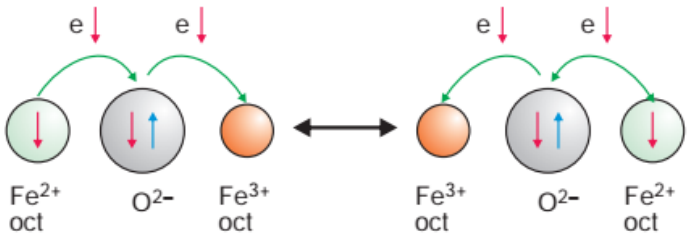

Figure 2. 12: Double exchange interactions between Fe^{2+} and Fe^{3+} leading to a ferromagnetic alignment of dipoles in the case of Fe_3O_4 Taken from[92].

2.2.4 Superparamagnetic materials

Ferrite spinels of the general chemical formula MFe_2O_4, where M can be a divalent metal ion, are materials of great technological interest because of their stability in high temperatures and their low magnetic and electric losses.

An interesting aspect of these materials is the tuneability of their magnetic ordering, from ferrimagnetic or antiferromagnetic, depending on the distribution of cations on tetrahedral (A) and octahedral (B) sites of their structure (normal, inverse or intermediate) and the nature of the metal ions. Examples of this category of materials are the normal spinels of $FeCr_2O_4$, Mn_3O_4, $FeCr_2S_4$, $ZnAl_2S_4$ with general formula: $(M^{2+})[Fe_2^{3+}]BO_4$ and the inverse spinels of: Fe_3O_4, $CoFe_2O_4$, and $NiFe_2O_4$ with the formula: $(Fe^{3+})[M^{2+}Fe^{3+}]\ BO_4$, where elements in round and square brackets represent the position of ions in tetrahedral and octahedral sites, as seen in **Figure 2. 13**.

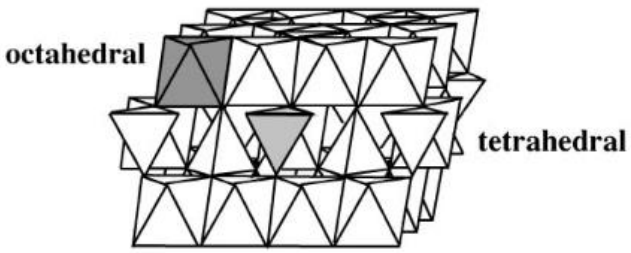

Figure 2. 13: Crystal structure of spinels. Taken from[106].

Another property of the magnetic spinels, with significant technological importance, is their ability to display a very specific magnetic order, known as superparamagnetism, when their size approaches the nanoscale.

To start with, an important feature of the magnetic nanoparticles that needs to be recalled is that below a critical size they are only containing one domain, as seen in **Figure 2. 14a**, a well-known phenomenon related to the relative stability of single- and multi-domain particles and the competition between magnetostatic and domain-wall energies of the systems[107].

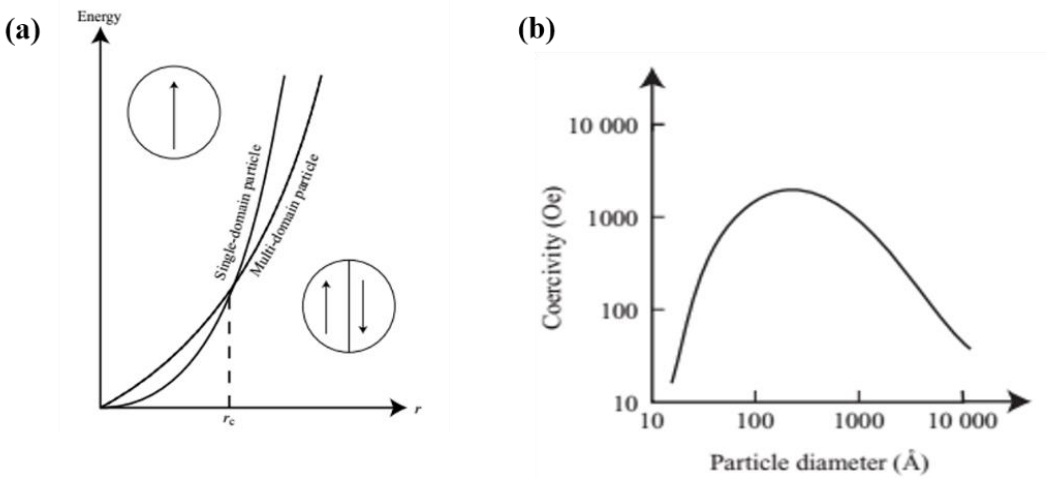

Figure 2. 14: (a) Relative stability of single- and multi-domain particles and (b) coercivity as a function of particle size. Taken from[107].

This single-domain state of nanoparticles has also an effect on their magnetization mechanism. When an external field is applied opposite to the nanoparticles' easy direction, where a small applied magnetic field is sufficient to reach the saturation magnetization, it forces the particles (in the absence of domain walls) to re-orientate their magnetic moments through their hard direction. This rotation, however, has a high energy cost due to the strong anisotropy forces that keep magnetization on the easy axis and therefore the coercivity of single-domain nanoparticles is seen to increase as the size of the particles is reduced. As the size of the nanoparticles continuing to decrease, their anisotropy energy will start to decrease according to their anisotropy constant (K) and their volume (V). As illustrated in **Figure 2. 15**, below a critical size, D_C, the magnetization flip of nanoparticles does not have any more to overcome strong anisotropic forces which become comparable to the thermal energy, $k_B T$. With the anisotropy of nanoparticles tending to zero their coercivity will be seen to be significantly reduced and the magnetic moments of each particle will start pointing at any direction, similar to the paramagnetic state[107].

A simple model to describe the magnetic behaviour of a group of nanoparticles can be derived by the Langevin function based on the paramagnetic theory:

$$M(H) = N\, m\, L(a) \qquad \textbf{(Eq. 2. 11)}$$

where N is the density of atoms (number of atoms per unit volume), m their magnetic moment and L is the Langevin function:

$$L(x) = 1/\tanh(a) - 1/x \quad \textbf{(Eq. 2. 12)}$$

with $x = \mu_o H \mu / T k_B$.

In the case where the anisotropy of the particles is non-zero, the magnetic moments of the particles appear to be quantized (with two allowed orientations) and their magnetization will be described by the Brillouin function[107]:

$$M(H) = N\, m\, tanh(a) \quad \textbf{(Eq. 2. 13)}$$

As has been already pointed out, superparamagnetism is also a temperature-dependent phenomenon. There is, therefore, a critical temperature (T_b, the blocking temperature) above which the thermal energy of the nanoparticles is becoming high enough to start randomly moving their magnetic dipole moments and the material is losing macroscopically its preferred magnetization direction. Under an applied magnetic field, the blocking temperature of a uniaxial materials can be expressed as[108]:

$$T_b(H) = \frac{K_u V}{k_B \ln(\tau_m / \tau_o)} \left[1 - \left(\frac{H}{H_k}\right)\right]^2 \quad \textbf{(Eq. 2. 14)}$$

where V is the volume of the nanoparticles, K_u is the anisotropy constant, τ_m is the average length of time for a magnetization reversal to occur, τ_0 is a characteristic material time constant, H is the applied filed and H_K is the anisotropy field.

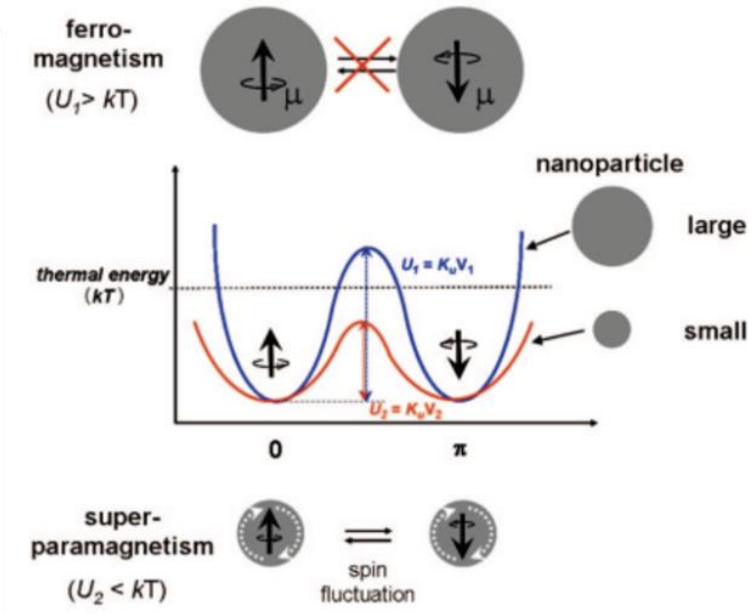

Figure 2. 15: Energy diagram of nanoscale transition for magnetic nanoparticles from ferromagnetism to superparamagnetism. The size of the magnetic nanoparticles is defining the barrier between their magnetic anisotropy energy of spin fluctuations and their thermal energy. Taken from[109].

There are a few more remarks worth adding on the superparamagnetic behaviour of nanoparticles. Despite the similarities of superparamagnetic and paramagnetic materials with respect to their randomly fluctuated magnetic moments and zero net magnetization, there are also significant difference between them. Perhaps more importantly, the superparamagnetic nanoparticles, once magnetized, demonstrate a significantly higher magnetic susceptibility, due to the quantum mechanical nature of their dipole exchange forces[110,111], whereas the magnetic moments of paramagnetic materials are acting independently and thus their susceptibility is substantially lower.

With a higher magnetic moment per particle, *m*, than that of the paramagnetic materials, the superparamagnetic materials can be saturated even at relative small fields while they do not show a hysteresis behaviour or coercivity -features of great importance in technological applications (such as biomedical application)[108]. However, as temperature is decreasing below the blocking temperature, the superparamagnetic nanoparticles will not possess enough thermal energy anymore to overcome their spin orientation towards the applied field and a hysteresis loop will eventually be observed, as illustrated in **Figure 2. 16**[107].

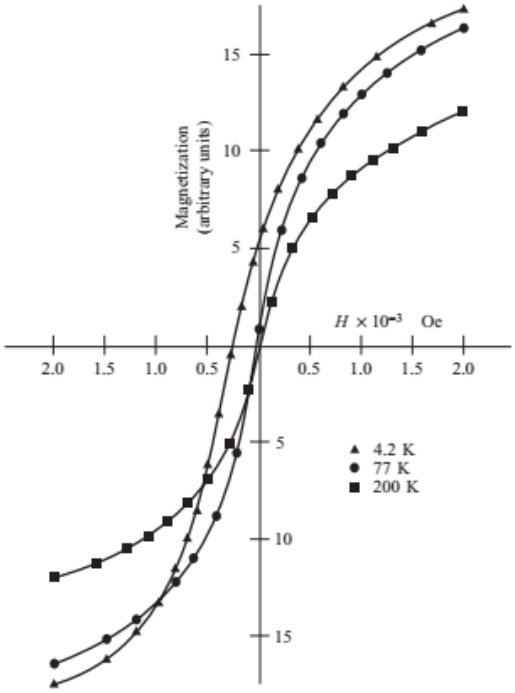

Figure 2. 16: Magnetization curves of iron particles above and below the superparamagnetic transition temperature. Taken from[112].

2.3 Multiferroic materials

2.3.1 Introduction

Ferroelectric materials, demonstrating a reversible polarization *P* of two stable states of opposite sign upon the application of an external electric field, have been widely used over the past decades as actuators and transducers, ferroelectric random-access memories (FeRAMs), dynamic random-access memory (DRAM) capacitors, ferroelectric liquid crystal display (FLCD), ferroelectric photovoltaics etc[113]. Ferromagnetic materials, on the other hand, exhibiting a switchable spontaneous magnetization *M* under an external magnetic field, have been also greatly employed in the data-storage industry of magneto-electronics, magnetic random-access memories (MRAMs), spintronics etc [114, 115, 116].

Despite, however, the wide applications of ferroelectricity and ferromagnetism in broad technological fields, the potentials of combining different ferroic orders in the same phase material have intensified research efforts over the last twenty years for a new generation of applications. Driven by the stimulus of smart materials for miniaturized devices and high-density data storage, multiferroics have received a great attention as a new class of materials where the coexistence of different ferroic orders could allow an additional degree of freedom in the design of four-state memories and sensing-actuating devices.

The term of "multiferroics" was originally used to describe single-phase compounds possessing simultaneously at least two of the primary ferroic properties: ferroelectricity (*FE*), ferromagnetism (*FM*) and ferroelasticity[117]. Soon, however, their definition was extended to include also the antiferroic orders[118].

Whilst the most distinct feature of multiferroic materials is the strong magnetoelectric coupling among different ferroic orders, the difference between magnetoelectric (*ME*) and multiferroic (*MF*) materials should not be misunderstood. Magnetoelectrism is referred to the cross-coupling between an applied electric (or magnetic) field and the induced magnetization (or polarization) of a material[119,120,121] and in the broadest case it may be demonstrated in a variety of systems without restriction on the nature of their electrical and magnetic ferroic orders, as illustrated in **Figure 2. 17**. Characteristic examples that elucidate the differences between these materials are: Cr_2O_3, a linear magnetoelectric but not ferroelectric material and $YMnO_3$, a ferroelectric and antiferromagnetic multiferroic but not magnetoelectric material.

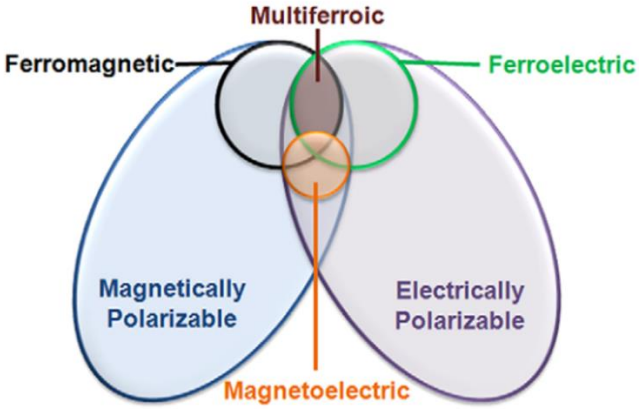

Figure 2. 17: Relationship between multiferroic and magnetoelectric materials. Taken from[122].

2.3.2 Magnetoelectric effect

In 1888[123], before the notion of magnetoelectric coupling being fully grounded, Röntgen was demonstrating its effect when a dielectric material becomes magnetized once moved inside an electric field. Soon after, the opposite response was also observed, with a moving dielectric inside a magnetic field becoming polarized[121,124]. In the meanwhile, Pierre Curie was already pointing out on his seminal work on "Symmetry in physical phenomena" in 1894 that the symmetries of the causes are to be found in the effects [125].

However, it was only later, in 1958[126], that Lev Landau and Evgeny Lifshitz addressed the theoretical description of magnetoelectrism by showing the coupling between the electric and magnetic properties of materials. In line with Landau's theory, magnetoelectric coupling can be derived by the expansion of the free energy functional, i.e.

$$F(\vec{E},\vec{H}) = F_o - P_i^S E_i - M_i^S H_i - \frac{1}{2}\varepsilon_o\varepsilon_{ij}E_iE_j - \frac{1}{2}\mu_o\mu_{ij}H_iH_j - a_{ij}E_iH_j - \frac{1}{2}\beta_{ijk}E_iH_jH_k - \frac{1}{2}\gamma_{ijk}H_iE_jE_k - \ldots$$ **(Eq. 2. 15)**

with $\vec{E}$ and $\vec{H}$ are, respectively, the electric and magnetic field.

Differentiating the equation of free energy with respect to the electric field (E) is giving the polarization (P):

$$P_i(\vec{E},\vec{H}) = -\frac{\partial F}{\partial E_i} = P_i^S + \varepsilon_o\varepsilon_{ij}E_j + a_{ij}H_j + \frac{1}{2}\beta_{ijk}H_jH_k + \gamma_{ijk}H_iE_j + \ldots$$ **(Eq. 2. 16)**

while the derivative of free energy to the magnetic field (H) gives the magnetization (M):

$$M_i(\vec{E},\vec{H}) = -\frac{\partial F}{\partial H_i} = M_i^S + \mu_o\mu_{ij}H_j + a_{ij}E_i + \beta_{ijk}E_iH_j + \frac{1}{2}\gamma_{ijk}E_jE_k + \ldots \quad \textbf{(Eq. 2. 17)}$$

where $\overrightarrow{P^S}$ and $\overrightarrow{M^S}$ are the spontaneous polarization and magnetization, ε and μ are respectively the electrical and magnetic susceptibilities, a_{ij} the linear magnetoelectric susceptibility tensor and β_{ijk} , γ_{ijk} represent higher-order (quadratic) magnetoelectric coefficients.

The coefficient a_{ij} is generally expressed as $a = \frac{\Delta E}{\Delta H}$ and called the ME voltage coefficient with units of s/m in the SI system or mV/cmOe. With the parameters β and γ being usually much smaller in magnitude than a_{ij} the equations (2.2) and (2.3) can be simplified to:

$$P_i(\vec{E},\vec{H}) = -\frac{\partial F}{\partial E_i} = a_{ij}H_j \quad \textbf{(Eq. 2. 18)}$$

and

$$M_i(\vec{E},\vec{H}) = -\frac{\partial F}{\partial H_i} = a_{ij}E_i \quad \textbf{(Eq. 2. 19)}$$

Furthermore, it can be shown that the linear magnetoelectric susceptibility is been constrained by the relation [127] :

$$a_{ij}^2 < \chi_e\chi_m \quad \textbf{(Eq. 2. 20)}$$

where χ_e and χ_m are the electrical and magnetic susceptibilities.

According to the equation (2.6), a large linear magnetoelectric effect should be expected on multiferroic materials where both the electrical and magnetic susceptibilities are non-zero.

2.3.3 Symmetry considerations and chemistry limitations

The distinction between magnetoelectric and multiferroic materials can also be understood by symmetry considerations, as depicted in **Figure 2. 18**.

The emergence of an electrical dipole in a multiferroic material suggests that its structure is non-centrosymmetric and as such its spatial inversion symmetry (J) is broken. On the other side, the appearance of a magnetic moment can be understood as a charge in a closed orbit whose direction is only changed by a time inversion symmetry (T).

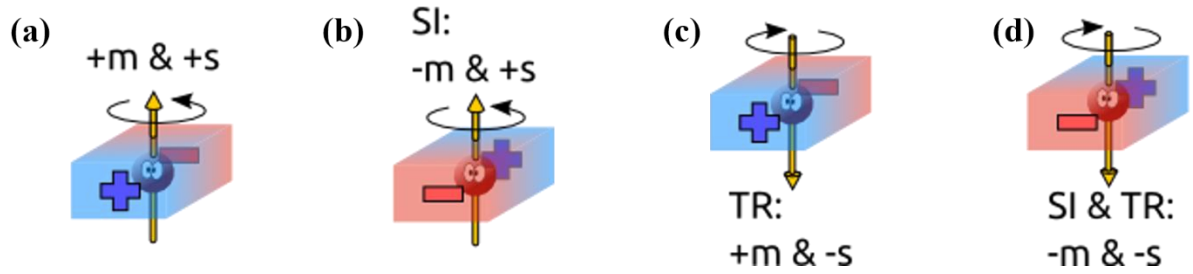

Figure 2. 18: Spatial inversion (SI) and time reversal (TR) symmetry effects on the electrical dipole (m) and magnetic moment (s) of a material. The spatial inversion of magnetic moment, in (b), will leave its direction unchanged. Taken from[128].

Although these symmetry operations can also be met on a linear magnetoelectric (*ME*) material, multiferroic and magnetoelectric materials are differentiated on the base of the product of those two symmetries. For a *ME* material both symmetries, *J* and *T*, should be broken while the product *JT* is conserved and, thus, consecutive applications of time reversal and spatial inversion will return back to the initial state. In contrast, in real multiferroics not only *J* and *T* should be broken but also their product *JT* [129]. These remarks underline the differences between multiferroic and magnetoelectric materials and highlight the reasons for the scarcity of single-phase multiferroic materials as was outlined by Nicolas Spaldin's seminal article in 2000[130].

The scarcity of single-phase multiferroics, especially at room temperature, can also be understood by chemistry considerations upon the competing electronic requirements of ferroelectricity and ferromagnetism.

The emergence of electric dipole moment in most ferroelectric materials is produced by the off-centre displacement of transition metal (TM) ions forming strong covalent bond with their neighbouring oxygen which, in turn, requires empty *d*-states of d^n TM ions to be hybridised with the *p* orbitals of the surrounding oxygen anions[107,131,132]. An archetypal example of this type of ferroelectricity is barium titanate ($BaTiO_3$). On the contrary, magnetic ions are encountered with partially filled *d*-shells since the filled orbits do not contribute to the orbital magnetic moment[92].

Different strategies have been developed to anticipate these chemistry limitations and incorporate ferroelectric (*FE*) and ferromagnetic (*FM*) orders in a single-phase multiferroic material. One of the first attempts was to explore mixed multiferroic systems (Type I: mixed systems) where both d^0 and d^n ions coexist such as $Pb(Fe_{2/3}W_{1/3})O_3$ [121],

$Pb(Fe_{0.5}Nb_{0.5})O_3$ [133], $Pb(Co_{0.5}W_{0.5})O_3$ [133] and $(1-x)Pb(Fe_{2/3}W_{1/3})O_3 - xPb(Mg_{1/2}W_{1/2})O_3$ [134], the first reported multiferroic solid solution.

The discovery of weak antiferromagnetism and room temperature spontaneous polarization in $BiFeO_3$ of the ABO_3 perovskite structure by Smolensky's group in early 1960s[135,136], draw the attention to the stereochemical activity of A-site ions (lone pair electrons) allowing the B-site cations to be occupied by partially filled *d*-shells cations. Characteristic examples of this type of multiferroic materials (*Type-I, lone pairs*) are the Bi^{3+} ($BiFeO_3$, $BiMnO_3$[137,138]) and Pb^{2+} ($PbVO_3$[139]) compounds.

2.3.4 Type of multiferroics

2.3.4.1 Single-phase multiferroics

Based on the microscopic source of magnetoelectric coupling, multiferroics materials can be distinguished in two groups: *Type-I* where ferroelectricity and magnetism are existing independently and *Type-II* where ferroelectricity is appearing as an effect of magnetic ordering. In both types, different sub-categories can be distinguished depending on the exact nature of ferroic coupling mechanism.

In *Type-I*, multiferroics can be classified according to the origin of ferroelectricity into: *mixed-systems*, *lone-pairs*, *geometric-FE* and *FE due to charge ordering* [140].

As already discussed in **section 2.3.3**, much of the initial attention on multiferroic was focused on *mixed-systems* and *lone-pair* materials where the emerged polarization is associated with a polar structural ordering caused by electronic pairing (proper ferroelectrics). Later, attention was also directed to the two other subfamilies of *geometric FE* and *FE due to charge ordering* where the developing ferroelectric order, although still independent of the emerging magnetization, is the result of a lattice distortion (improper ferroelectrics) and not the electronic arrangement of individual cations [141].

In the case of *geometric FE (multiferroic)* of rare earth hexagonal manganites, with $RMnO_3$ and *R*=Ho-Lu and Y, the ferroelectricity is caused by the tilt of manganese-oxygen bipyramids towards a closer packing driven by the smaller size *R* ions [142,143]. Other examples of this type of ferroelectric multiferroics are met on the $BaMF_4$ (*M* = Mn, Fe, Co, Ni) family of alternating MF_6 octahedra rotations [144].

Ferroelectricity can also be induced in materials where a non-centrosymmetric distribution of charges is emerged due to the coexistence of inequivalent side- and bond-centred charge orderings[145], usually in transition metal compounds of different oxidation states. Examples of this class of materials are perovskite manganites of the type (PrCa)MnO_3 and strongly ferroelectric frustrated $LuFe_2O_4$[146].

Finally, a lot of attention has recently been focused on *Type-II* multiferroic materials, also called magnetic multiferroics, where a broken inversion symmetry and a spontaneous polarization is induced by magnetic order[147]. Examples of these materials are the $TbMnO_3$[148] and $TbMn_2O_5$[149] oxides where ferroelectricity is induced by spiralling magnetic phases and Ca_3CoMnO_6 where polarization is emerged due to more complicate phenomena such as exchange striction mechanisms.

Although the direct coupling of ferroelectricity with a specific magnetic phase appears promising for technological application, the poor ferroelectric polarization and the low Neel temperatures of current *Type-II* multiferroics are obstacles that need to be resolved[150].

2.3.4.2 Thin film magnetic phenomena

The past 20 years have seen a resurgence of interest on multiferroics materials driven by the advances of new thin film deposition techniques allowing the precise control of high quality materials. Much of the work on single-phase multiferroic thin films has been mainly focused on bismuth- and lead-based perovskites and hexagonal manganites

Different physical and chemical vapour deposition techniques, including plasma and ion beam sputtering (PSD and IBSD), pulsed laser deposition (PLD), molecular beam epitaxy (MBE) and metalorganic vapour phase deposition (MOVPE), have been initially employed to investigate the growth of ferroelectric films and later multiferroic and complex layered heterostructures, as summarized in the reviews by Ramesh et al [151], Dawber et al [152] and Martin et al[122].

The advances on new thin film deposition techniques allowed the growth of high quality thin films and exploited the opportunity of stabilizing non-equilibrium material phases as well as strain-engineering of already existing materials[122,153,154]. A series of pioneering works in the early 2000s elucidated how epitaxial strains can give rise to interesting phenomena such as the room temperature ferroelectricity in under other conditions paraelectric $SrTiO_3$[155] or the

increase of ferroelectric Curie temperature (by almost 500 °C) and the remanent polarization (by 250%) of $BaTiO_3$ with respect to the corresponding bulk values[156].

The effect of stabilizing non-equilibrium material phases and amplifying directional signals in thin film structures (otherwise cancelled out on polycrystalline or poly-domain single crystals), is especially instructive in the case of $BiFeO_3$. As Wang et al.[157] demonstrated on their work, $BiFeO_3$ was initially found showing a 10-times larger remanent polarization ($P_s = 60$ μC/cm^2) when stabilized in a strain-induced thin film tetragonal phase[157,158] in comparison with early bulk orthorhombic samples. Theoretical calculations[159] and measurements on high quality single-crystals[160] samples later confirmed this intrinsically large ferroelectric polarization of $BiFeO_3$ (over $P_s = 100$ μC/cm^2 [161]).

Even more elucidating, however, is the weak ferromagnetic behaviour and the strong magnetoelectric coupling of epitaxial $BiFeO_3$ thin films. Bismuth ferrite, a G-type antiferromagnet with a weak iron spin canting due to Dzyaloshinskii-Moriya interactions which, however, are cancelled out by a ferroelectrically induced spin cycloid (of 62 nm) that averages out the local canted magnetism[162]. Wang et al's[157] have shown that this cycloidal ordering of $BiFeO_3$ can be destabilized in strained films and lead to finite magnetization.

Besides of $BiFeO_3$, thin films of $BiCrO_3$ have been grown on $LaAlO_3$ (001), $SrTiO_3$ (001), and $NdGaO_3$ (110) substrates and found to be room temperature ferroelectric and weak antiferromagnetic below 120 K[163].

The epitaxially-strained growth of $BiMnO_3$ thin films[138] on $SrTiO_3$ (001) by PLD led to the stabilization of a metastable monoclinic $BiMnO_3$ phase, obtained otherwise only under a high-temperature/high-pressure synthetic protocol during conventional bulk synthesis, which exhibits ferroelectricity below 450 K and ferromagnetism at 105 K[164]. Although $BiMnO_3$ is one of the few existing ferromagnetically-ordered multiferroic materials, its low temperature magnetic order has been a major obstacle on technological applications of tunnel junctions[165]. $GaFeO_3$, a ferroelectric and ferrimagnetic material, has been proposed as an alternative candidate option. Orthorhombic $GaFeO_3$ films grown on STO (111) and YSZ (001) substrate by PLD have demonstrated a large room temperature ferroelectric polarization[166]. Its ferrimagnetic Curie temperature was found to increase by almost 100 degrees, compared to that of $BiMnO_3$, at 200 K[167], while studies on single-crystal $Ga_{2-x}Fe_xO_3$ samples have shown that an increase of Fe content can raise the Curie temperature of the $Ga_{2-x}Fe_xO_3$ compound up to 350 K (for x = 1.4)[168].

In $PbVO_3$, similarly to $BiFeO_3$, multiferroicity should be driven by the 6*s* lone pair of Pb^{2+} and the d^1 electrons on V^{4+} [169]. $PbVO_3$ films were grown on $LaAlO_3$, $SrTiO_3$, $NdGaO_3$, and $LaAlO_3$/Si substrates and were found to display a transition from a polar-only 4mm state to a polar and magnetic state below 130 K[170]. However, the highly distorted tetragonal structure of $PbVO_3$ is leading to a loss of its polar symmetry upon heating above 573 K and making difficult its use in applications.

The antiferromagnetic hexagonal $YMnO_3$ was one of the first ("geometric") multiferroic thin film, obtained in 1996[171], exemplifying how intrinsic strains on epitaxial thin films can stabilize a hexagonal phase, approached otherwise only by a high-temperature/high-pressure synthetic protocol. Hexagonal $YMnO_3$ has a paraelectric / ferroelectric phase transition at around $T_c \sim 900$ K and an antiferromagnetic transition at $T_N \sim 70$ K. Over the next years, a lot of research was directed on a wide range of hexagonal-$RE$$MnO_3$ systems (RE = Nd, Ho, Tm, Lu, Yb, Tb, Dy, Gd and Sm[137,172,173,174,175]) in an attempt to tune their antiferromagnetic ordering temperature closer to room temperature. The relative low however magnetoelectric coupling of these compounds is limiting the prospects of technological applications[145].

The work conducted on lead-based solid solution perovskites (SSPs) provided an alternative route of synthesising single-phase solid solutions materials towards room temperature multiferroic materials [176]. Initially synthesised with the method of chemical solution deposition, single-phase polycrystalline films of $(PbZr_{0.53}Ti_{0.47}O_3)_{0.8}$-$(PbFe_{0.67}W_{0.33}O_3)_{0.2}$ (0.8PZT/0.2PFW) were found to demonstrate a room-temperature multiferroicity. The growth, later, of highly oriented $PbZr_{0.53}Ti_{0.47}O_3)_{0.60}$-$(PbFe_{0.5}Ta_{0.5}O_3)_{0.4}$ (0.6PZT/0.2PFT) films on $La_{0.67}Sr_{0.33}CoO_3$-coated MgO substrates by PLD have also shown to display a near room temperature multiferroic relaxor behaviour[177,178,179].

2.3.4.3 Composite multiferroics films

The scarcity of single-phase multiferroic materials showing a strong ferroelectric and magnetic coupling at room-temperature has shifted research focus on the development of composite materials where the coupling of the two ferroic orders could be achieved at multiferroic hetero-interfaces[180,181].

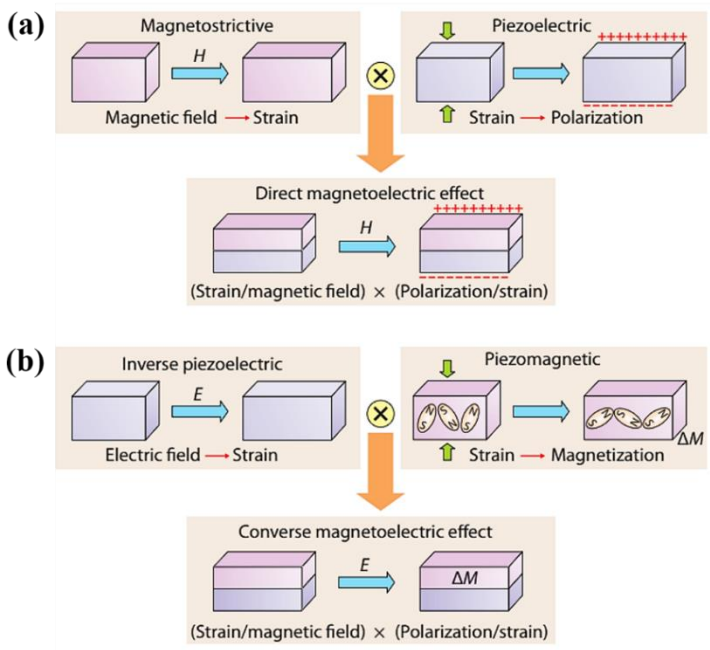

Figure 2. 19: Schematic illustration of the strain-mediated ME effect in a composite layered (2-2 horizontal) heterostructure. Taken from[182].

The strain-mediated magnetoelectric (ME) effect, as illustrated in **Figure 2. 19**, exemplifying the concept of new functionalities in multiferroic composites systems[164,182]. Under this approach, an external in-plane magnetic field is inducing a strain response in the magnetic component of a composite layered heterostructure while in a second step, a dielectric polarization is obtained via the piezoelectric effect to the ferroelectric component of the system. In the reverse direction, an external electric field is possible to induce a strain via the inverse piezoelectric effect in the ferroelectric component of a composite system which will mechanically transferred to the magnetic component and introduce magnetization change[182].

The ME effect can therefore be understood as the cross interaction of two distinct phenomena on two different phases: the magnetostrictive effect in the magnetic phase and the electrostrictive effect in the electrical phase as follows:

$$Direct\ ME\ effect = \frac{Magnetic}{Mechanical} \times \frac{Mechanical}{Electric}$$

and

$$Converse\ ME\ effect = \frac{Electric}{Mechanical} \times \frac{Mechanical}{Magnetic}$$

The various ME composites nanostructures that have been addressed so far can be categorized in three types according to the complex component geometries in: 2-2 horizontal heterostructures, 1-3 vertical nanostructures, and 0-3 nanoparticle embedded films[183].

In the *2-2 horizontal heterostructures*, alternating ferroelectric and magnetic layers of thin films heterostructures have shown great potentials for device applications with an obtained ME coefficient ranging from 3 to 4680 mV/cm Oe[122,184]. Examples of ferroelectric-ferromagnetic composites which have been explored so far are: $Pb(Zr_{0.4}Ti_{0.6})O_3 - Ni_{0.8}Zn_{0.2}Fe_2O_4$[185,186] PZT - - Ni-ferrite[187], PZT - $CoFe_2O_4$ [186], PZT - $La_{0.7}Sr_{0.3}MnO_3$ and PZT-$La_{0.7}Ca_{0.3}MnO_3$ [188]. On a slightly different route, heterostructures of epitaxially grown PZT films on $La_{1.2}Sr_{1.8}Mn_2O_7$ single crystal substrates have shown a ME coefficient as high as 600 mV/cmOe[189].

To address the constraint effect of substrate clamping on the piezoelectric response of grown films (calculated to restrain the magnetoelectric coefficient of composite systems by a factor up to five[190]) Zheng et al.[191] have also explored the *vertical columnar* arrangement of composites systems. Taking advantage of the natural separation between the perovskite and spinel phases, they found that the ferromagnetic $CoFe_2O_4$ can be embedded in the form of nanopillars inside a $BaTiO_3$ (ferroelectric) matrix resulting to an increased interface-to-volume ratio and a strong magnetoelectric coupling[122]. One of the most significant drawbacks, however, of this architecture is the high leakage current of the resulting composite structure due to the continuous paths of the low resistance ferrite phase[192]. Since this first publication, several other nanopillar composites of ferroelectric perovskite and ferromagnetic spinel (or corundum) phases have been synthesised, such as: $PbTiO_3$-$CoFe_2O_4$ [193], PZT-$CoFe_2O_4$ [194], PZT-$NiFe_2O_4$ [195], $BiFeO_3$-$NiFe_2O_4$ [196], $BiFeO_3$−$CoFe_2O_4$ [197].

In a variation of the vertical nanostructure method, Wan et al[194] have employed a sol-gel route of growing a PZT matrix containing dispersed CoFe2O4 nanoparticles in what was called a "*0-3 nanoparticle embedded film system"*. He was followed by Zhong et al.[198] synthesizing a ferroelectric $Bi_{3.15}Nd_{0.85}Ti_3O_{12}$ film encapsulating $CoFe_2O_4$ nanoparticles. In both cases, the complex composites retained their ferroic behaviour and demonstrated a measurable ME coefficient. Ryu et al[199] starting from two sintered semicircular disks of PZT and $NiFe_2O_4$, have investigated the growth of (100)-oriented PZT/$NiFe_2O_4$ composite films by PLD and found that the $NiFe_2O_4$ nanoparticles were randomly dispersed in the PZT matrix. The measured magnetoelectric voltage coefficient α_E of the complex was found comparable, although lower, to than reported of bulk PZT-$NiFe_2O_4$ particulate composites[200].

2.4 $BiFeO_3$

$BiFeO_3$ (BFO) crystallizes at room temperature in the rhombohedral *R3c* space group as it cools down from a high temperature cubic perovskite structure. It can be described as two distorted perovskite cells (ABO_3) connected along their pseudocubic [111] body diagonal, in **Figure 2. 20**. Within this configuration, the two oxygen octahedra of the neighbouring blocks adopts an antiferrodistortive distortion as they rotate along the [111] direction in opposite directions by ±13.8◦, whereas the Fe ions are shifted by 0.135 Å away from the centre of the oxygen octahedra and along the same direction.

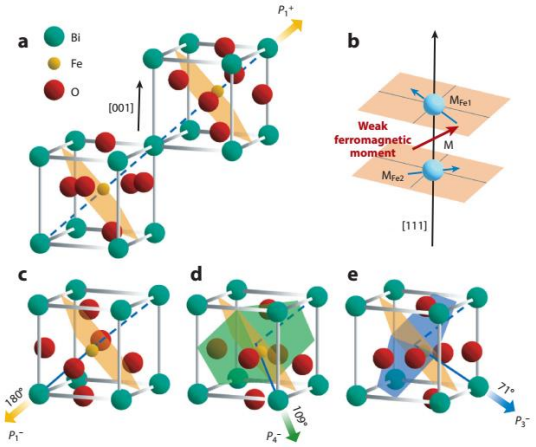

Figure 2. 20: Schematic representation of (0 0 1)-oriented $BiFeO_3$ crystal structure and the ferroelectric polarization (bold arrows) and antiferromagnetic plane (shaded planes). (a) Polarization with an up out-of-plane component before electrical poling, (b) the formation of the weak ferromagnetic moment. Ferroelectric polarization switching of: (c) 180°, (d) 109°, (e) 71°. Taken from[201].

Initially studied as a promising lead-free candidate for next-generation piezoelectric devices, BFO was later extensively explored as a potential magnetoelectric spintronic material following the discovery of enhanced multiferroic properties in thin film form. BFO is an antiferromagnetic ferroelectric at room temperature with a large polarization along the polar $\langle 111 \rangle_{PC}$ direction. It has both high antiferromagnetic (T_N = 640 K) and ferroelectric (T_C = 1100 K) transition temperatures and it is of great interest, among other multiferroics, for high-temperature applications due to its single-phase, room temperature multiferroic properties.

BFO demonstrates a G-type antiferromagnetic order with each of its iron spin being surrounded, in the 3D space, by six antiparallel next nearest iron spins. The

non-centrosymmetric structure of BFO induces a small antisymmetric spin-canting of antiferromagnetic Fe^{3+} ions via the Dzyaloshinskii–Moriya interaction, in **Figure 2. 21**. Neutron diffraction studies on bulk BFO[202,203] have also revealed a long-range, ferroelectrically-induced incommensurate spin cycloid order of the antiferromagnetic Fe spins with a 62 nm period and a propagation vector along the [110] direction[204].

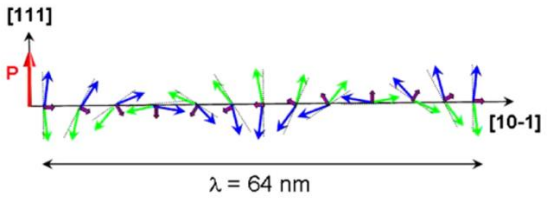

Figure 2. 21: Antisymmetric spin-canting of $BiFeO_3$. The spin-canted antiferromagnetic coupling (in blue and green arrows) give rise to an incommensurate cycloid spin structure of 62 nm period (with purple). Taken from[205].

The presence of this incommensurate spin cycloid in bulk BFO cancels any linear magnetoelectric (ME) coupling between polarization (*P*) and magnetization (*M*), allowing only higher orders of couplings, as can be seen in **Figure 2. 22**. Hence, the linear magnetoelectric effect can only be obtained in bulk BFO when high magnetic fields destabilize the cycloidal order and retrieve the Fe spin-canting order together with the corresponding BFO remnant magnetization[205].

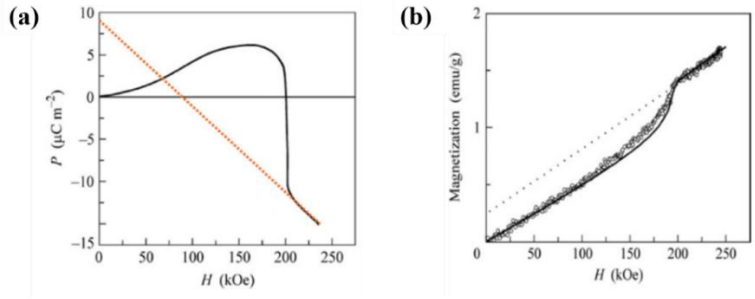

Figure 2. 22: Magnetoelectric (ME) coupling between polarization (P) and magnetization in BiFeO3. The linear magnetoelectric (ME) coupling is only displayed in high magnetic fields. Taken from[205].

In a highly influential paper published from Ramesh's group in 2003, Wang et al.[157] reported enhanced room-temperature polarization (up to ~90 μC/cm^2) and magnetization (of ~70 emu cm^{-3}) together with a magnetoelectric coefficient of about 3 V/(cm.Oe) in heteroepitaxially constrained, tetragonal-like, BFO films as summarized in **Figure 2. 23**.

While a number of following publications confirmed the reported large ferroelectric polarization of BFO in high quality single crystals[160] and ceramics[206], the magnitude of the reported magnetization sparked a long-running debate on the exact nature of BFO magnetic properties. First principles studies [Spaldin[207], Bea[208], Lebeugle[160,209]] confirmed the presence of a weak ferromagnetism due to DM interactions between canted antisymmetric Fe^{3+} spins although the calculated remanent magnetization was found to be substantially lower (~8 emu cm^{-3}) than that measured by Wang et. al.

The anomalously large magnetic moment of strained BFO films by Wang et al. was initially attributed by other groups to secondary magnetic phases (such as γ-Fe_2O_3) and the detrimental role of paramagnetic impurities of low concentrations (for example $Bi_{25}FeO_{39}$)[209] at reducing growth conditions. More recently, however, additional experimental results have unambiguously proven the magnetoelectric coupling of BFO at room temperature as well as a giant magnetoelectric effect of 24 V/(cm Oe) in composite multilayer BFO-based heterostructures[210], results which were afterwards supported by theoretical studies[211].

In the aftermath of Wang's publication on the magnetoelectric properties of BFO, a rejuvenation of interest in thin film multiferroic has been sparked over a wide range of research areas including atomic-level layering routes of material design and [210,212,213,214,215,216,217,218] and coupling phenomena (exchange coupling, exchange bias etc) at multilayer ferromagnet - antiferromagnetic heterostructure interfaces such as $Co_{0.9}Fe_{0.1}/BiFeO_3$ [169], $CoFe_2O_4/BiFeO_3$, $La_{0.7}Sr_{0.3}MnO_3/BiFeO_3$ [219,220].

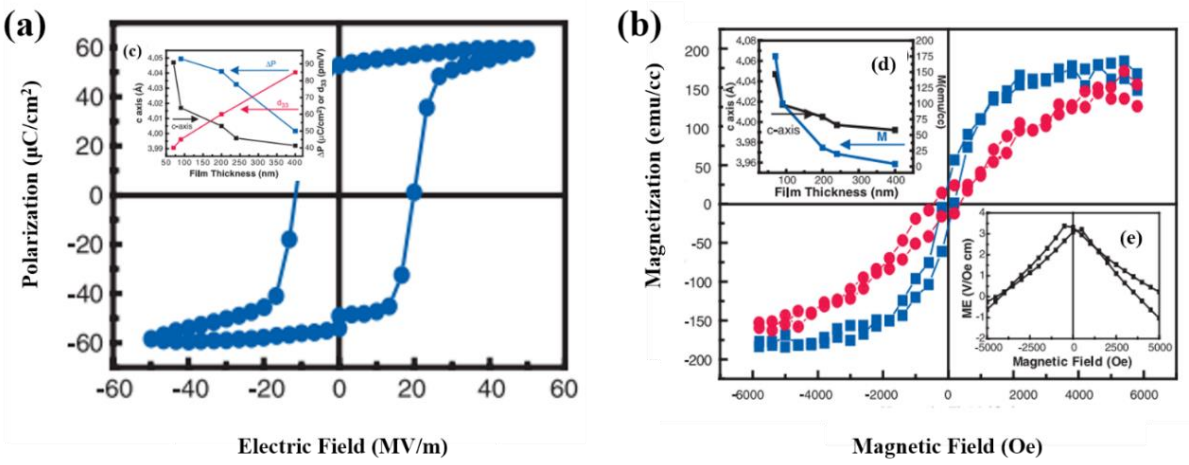

Figure 2. 23: (a) Ferroelectric P-E hysteresis loop of epitaxial BFO thin film at 15 kHz. Inset (c): summary of thickness dependent evolution of out-of-plane lattice parameter, polarization, and d_{33}, (b) Magnetic hysteresis loops for a 70-nm-thick BFO film. Inset (d): thickness dependence of saturation magnetization and inset (e) ME measurement showing a maximum value of 3 V(cm.Oe) and hysteresis of about 200 Oe. Taken from[157].

2.4.1 Bulk doping strategies

If $BiFeO_3$ is to succeed in device fabrications, specific limitations related to its metastable nature in air and compositional impurities need to be addressed. Oxygen vacancies have been shown to be detrimental in leakage currents leading to dielectric losses[221,222] and compromising the accuracy of the measured magnetoelectric (ME) coupling coefficient[214]. The presence of paramagnetic Fe^{3+} impurities and mixed valence states of Fe^{2+} and Fe^{3+} [223] (favoured by oxygen-deficient growth conditions) have shown to have a decisive factor on BFO films' functional properties and the artificial enhancement of its remnant magnetization[205,224,225.]

To overcome these obstacles, different A- and B-site doping strategies have been evolved to improve the compositional stability, the leakage resistance and the overall multiferroic performance of BFO[226,227,228]. Interesting doping effects have been observed in the structural and physical properties of the parent BFO and are summarized in the review literature[229]. Atomic substitutions, in both sites, can reduce the leakage current of BFO thin films by 1-3 orders of magnitude due to the formation of defect complexes or the suppression of oxygen vacancies[230,231,232] . Substitution of Bi^{3+} with lanthanides (La [233,234], Nd [227], Sm [235], Gd [236], Ce [237], Dy [238]) or alkaline metals[239] (Sr [240], Ba [241,242,] Ca [243]) has shown to improve the BFO dielectric/ferroelectric properties and even its magnetic properties trough the perturbation of the parent spiral spin structure via magnetoelectric interactions[244]. The substitution of Fe in B-site is usually resulting in the deterioration of the ferroelectric and piezoelectric response of parent BFO while the direct or even indirect substitution (in the form of addition to the stoichiometric BFO powder) of magnetic elements, such as Co and Ni can even increase the remanent magnetization via ferromagnetic super-exchange interactions of the form: Fe^{3+}-O-Ni^{2+} [245].

A solid-solution approach has also been investigated where additive ABO_3 oxides or mixture of them are introduced to form a single-phase solution. The $BaTiO_3$[246] and $PbTiO_3$[247,248] are two of the most studied oxides in this direction. The resulting solid-solution phases can undergo a gradual structural transition from the parent rhombohedral phase to a different phase where improvements on the piezoelectric and ferroelectric properties of BFO are reported. According to this route, a giant remnant polarization of $2P_r \sim 198.3$ $\mu C/cm^2$ and decreased leakage current were reported in $(1-x)BiFeO_3$-$x(Bi_{0.50}Na_{0.50})TiO_3$ single-phase solid-solution thin films of

(111) orientation where the incorporation of $Bi_{0.50}Na_{0.50})TiO_3$ into BFO led to a change in the lattice dimension of the BFO unit cell[249].

In general, ferroelectric and magnetic properties of BFO thin films are expected be improved by introducing ABO_3 additives and the stabilization of a strongly discontinuous transition to a morphotropic phase boundary. Although the notion of a multiferroic phase boundary has attracted a lot of attention as a promising approach towards single-phase, room temperature multiferroics BFO-based system, little progress has however been made towards a conclusive study of multiferroicity on such compounds (including for example magnetoelectric measurements). Among them, stand out the lead-based ternary systems of $BiFeO_3$-$PbTiO_3$-$BaTiO_3$[250] and $BiFeO_3$-$BiMnO_3$-$PbTiO_3$[251] where a reported enhanced room-temperature ferroelectricity, canted ferromagnetism and magnetoelectric coupling have been associated with the presence of a morphotropic phase boundary (MPB) between multiferroic polymorphs of monoclinic and tetragonal symmetries.

2.5 The morphotropic BTFM-CTO

One of the biggest obstacles in obtaining a bismuth-based and lead-free morphotropic system is the difficulty of stabilizing at ambient pressure a bismuth phase with a polarization direction other than the $[001]_p$[252].

To meet these challenges a multiple A and B-site doping strategy has been developed by Rosseinsky's group. They have focused their attention on $BiTi_{3/8}Fe_{2/8}Mg_{3/8}O_3$ (BTFM), a polar rhombohedral $R_{[111]}$ structure, where Bi cations demonstrate locally correlated $[110]_p$ displacements in addition to the long-range ordered $[111]_p$ displacements. To stabilize a long-range polarization along the $[110]_p$ direction, they have explored different solid solutions of BTFM with $LaFeO_3$ and $CaTiO_3$, noting that the Ti cations of $CaTiO_3$ increase the possibility of locking local Ti displacements on BTFM in directions other than the primary $[110]_p$ [253,254].

Solid solutions of $(1-x)BiTi_{3/8}Fe_{2/8}Mg_{3/8}O_3–xCaTiO_3$ $(0.0 < x \leq 0.40)$ at the morphotropic phase boundary between the rhombohedral $[111]_p$ and orthorhombic $[001]_p$ phases were successfully synthesized and found to demonstrate enhanced piezoelectric properties and high depolarization temperatures[252]. However, with the Ti^{4+} and Mg^{2+} content of the examined compositions kept high enough to minimize dielectric loss, the Fe content of the synthesised compounds was constrained below the threshold of a long-range magnetic order.

An increase of Fe content in the MPB system of BTFM-CTO along with an optimized synthetic protocol to eliminate the presence of a spinel (ferrimagnetic) impurity phase have finally led to a single-phase, room temperature multiferroic $(1-x)BiTi_{(1-y)/2}Fe_yMg_{(1-y)/2}O_3$-$xCaTiO_3$ [252,255]. The bulk perovskite was found to demonstrate a ferroelectric and a weakly ferromagnetic ordering together with a magnetoelectric coupling at room temperature. When Rosseinsky et al. focused their attention on the composition with x = 0.15 and y = 0.75, they succeeded to measure a saturated magnetization of 0.0097 μ_B per Fe, a linear magnetoelectric susceptibility of 0.19(1) ps m^{-1}, and a polarization of 66 μC cm^{-2} at room temperature.

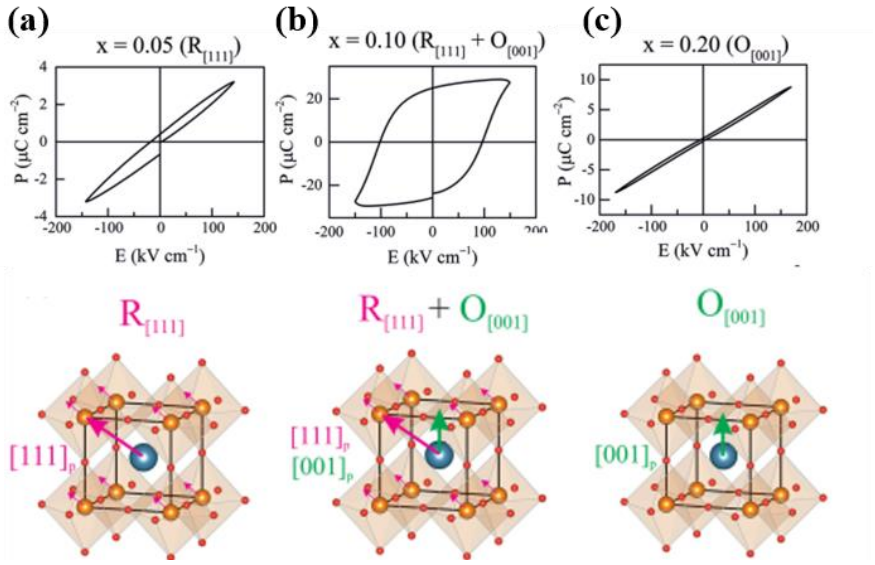

Figure 2.24: P(E) loops under comparable measurement fields for: (a) R[111] (x = 0.05), (b) R[111] + O[001] (x = 0.10) and (c) O[001] (x = 0.20) BTFM-CTO materials. Taken from[252].

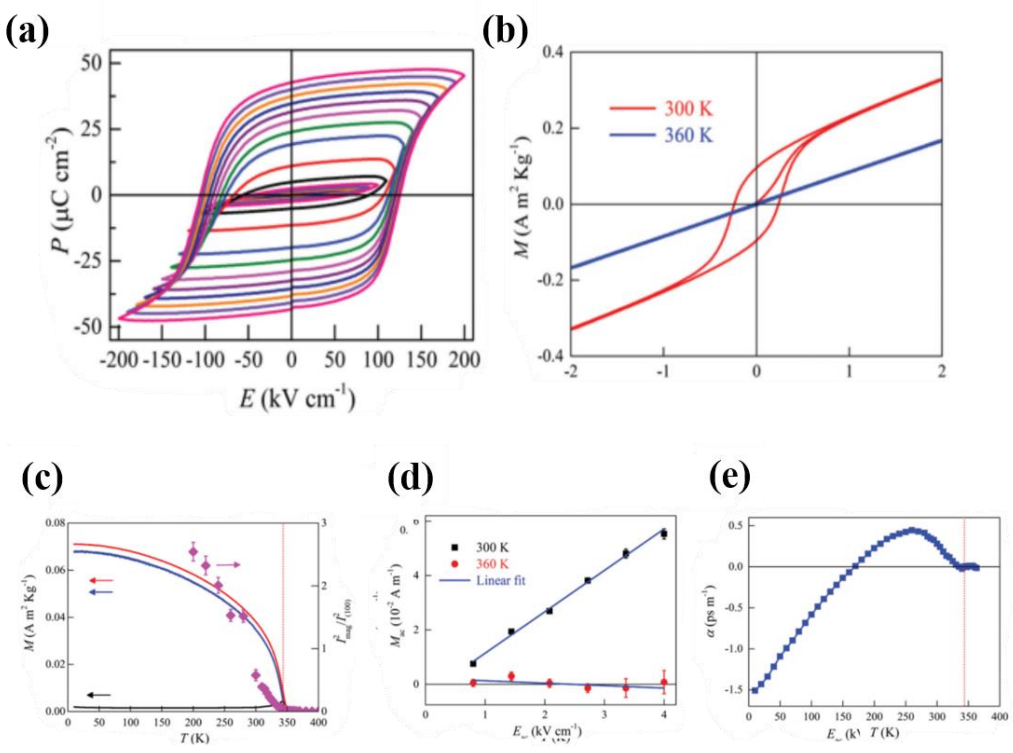

Figure 2.25: Multiferroic behaviour of phase-pure 0.85BiTi0.125Fe0.75Mg0.125O3-0.15CaTiO3 (x = 0.15, y = 0.75) at room temperature: (a) *P(E)* hysteresis loop at increasing electric fields at 10 Hz. (b) Magnetic isotherms at 300 K (red, < T_N) and 360 K (blue, > T_N) confirming the presence of a single magnetic phase. (c) Temperature dependent magnetisation, *M(T)*, (d) Linear magnetoelectric effect at 300 K (black squares) and 360 K (red circles), (e) Temperature dependence of the linear magnetoelectric coefficient *(α)*. Taken from[255].

During the time of writing up this thesis, another group[256] have claimed that they grew epitaxial BTFM-CTO films on $SrTiO_3$ substrate on a conductive $La_{0.7}Sr_{0.3}MnO_3$ buffer layer. They reported room temperature ferroelectricity and a ferromagnetic-like saturated $M-H$ hysteresis loops with switchable magnetization as high as 145.3 emu.cm^{-3}. However, their assessment on the magnetic purity of the reported films was far from conclusive as they omit reporting any magnetoelectric coupling or temperature dependent magnetisation data.

2.6 Aim of the project

In **section 2.5**, we outlined how the bulk $(1-x)BiTi_{(1-y)/2}Fe_yMg_{(1-y)/2}O_3–xCaTiO_3$ represents a novel room-temperature single-phase multiferroic with a linear magnetoelectric response emerged by the chemical modification of $BiFeO_3$ cycloid spin structure.

The work of this thesis is focused in the epitaxial growth of $(1-x)BiTi_{(1-y)/2}Fe_yMg_{(1-y)/2}O_3–xCaTiO_3$ films in the morphotropic phase boundary region. Given the close proximity of the interplanar distances of the pseudocubic 001_{PC} planes for the two morphotropic phases and the structural complexity of the studied multi-cation compound, the deposition of single-oriented films will be assessed by detailed elemental analysis and structural characterization.

The deposition of the bulk $(1-x)BiTi_{(1-y)/2}Fe_yMg_{(1-y)/2}O_3–xCaTiO_3$ would allow us to directionally amplify the multiferroic signals of thin film structure while substrate-induced lattice strain effects would add an extra degree of freedom in the functional properties of the studied system.

References

[92] R. Tilley, *Understanding Solids: The Science of Materials*, John Wiley & Sons, 2005

[93] Ashish Garg, *Ferroelectric Domains*, 2012, at: http://nptel.ac.in/courses/113104005/ lecture28/28_2.htm

[94] Y. Xu, *Ferroelectric Materials and Their Applications*, North Holland, 1991.

[95] D. Damjanovic, *Rep. Prog. Phys.* **61**, 1998, 1267

[96] P.S. Halasyamani, *Noncentrosymmetric Inorganic Oxide Materials: Synthetic Strategies and Characterisation Techniques*. In: D.W. Bruce, D. O'Hare, R.I. Walton (eds.), *Functional Oxides*, John Wiley & Sons, 2010

[97] Wikipedia, "Lead zirconate titanate", <https://en.wikipedia.org/wiki/Lead_zirconate_titanate>

[98] R. Waser, U. Böttger, *Polar Oxides: Properties, Characterization and Imaging*, Wiley, 2005

[99] B. Noheda, J.A. Gonzalo, L.E. Cross, R. Guo, S.E. Park, D.E. Cox, G. Shirane, *Phys. Rev. B* **61**, 2000, 8687

[100] R. Guo, L.E. Cross, S.E. Park, B. Noheda, D.E. Cox, G. Shirane. *Phys. Rev. Lett.* **84**, 2000, 5423

[101] B. Jaffe, W.R. Cook, H. Jaffe, *Piezoelectric Ceramics*, Academic Press, 1971

[102] S.V. Vonsovskii, *Magnetizm*, Great Soviet Encyclopedia, 1971

[103] T. Moriya, *Phys. Rev.* **120**, 1960, 91

[104] S. Dong, J.M. Liu, *Single-Phase type-ii Multiferroics: Frustrated Magnetism-triggered Ferroelectricity*. In: J. Wang ed. *Multiferroic Materials: Properties, Techniques, and Applications*, CRC Press, 2016

[105] Wikipedia, "*Antisymmetric exchange*", at: https://en.wikipedia.org/wiki/Antisymmetric_exchange

[106] Y. Suzuki, *Annu. Rev. Mater. Res*. **31**, 2001, 265

[107] N.A.Spaldin, *Magnetic Materials: Fundamentals and Device Applications*, Cambridge University Press, 2003

[108] R. Díaz-Pardo, R. Valenzuela, *Characterization of Magnetic Phases in Nanostructured Ferrites by Electron Spin Resonance*. In: S.O Bashir (ed.), *Advanced Electromagnetic Waves*, InTech, 2015, 210

[109] Y. Jun, J. Seo, J. Cheon. *Acc Chem Res.*, **41**(2), 2008, 179

[110] H. Kim, *Magnetoelectric Effect and Magnetodielectric Effect in Magnetic Nanoparticles*, PhD thesis, University of California, Los Angeles, 2013

[111] Anandh Subramaniam, *Magnetism in Nanomaterials*, 2013, at: http://home.iitk.ac.in/~anandh /MSE694/courseMSE694/

[112] C.P. Bean, I.S. Jacobs, *J. Appl. Phys.* **27**, 1958, 1448

[113] J.F. Scott, *Science* **315**, 2007, 954

[114] Applications of Ferromagnetism. < http://hyperphysics.phy-astr.gsu.edu/hbase/Solids/ferro.html#c6 >

[115] A. Goldman (ed.), *Handbook of Modern Ferromagnetic Materials*, Kluwer Academic Publishers, 1999

[116] M. Ziese, M.J. Thornton eds. *Spin Electronics*, Springer, 2001

[117]H. Schmid, *Ferroelectrics* **162**, 1994, 317

[118] W. Eerenstein, N.D. Mathur, J.F. Scott, *Nature* **442**, 2006, 759

[119] C.N.R. Rao, A. Sundaresan, R. Saha, *J. Phys. Chem. Lett.* **3,** 2012, 2237

[120] J.F. Scott, *J. Mater. Chem* **22**, 2012, 4567

[121] M. Fiebig, *J. Phys. D: Appl. Phys*. **38**, 2005, R123

[122] L.W. Martin, S.P. Crane, Y.H. Chu, M.B. Holcomb, M. Gajek, M. Huijben, C.H. Yang, N. Balke, R. Ramesh, *J. Phys.: Condens. Matter* **20**, 2008, 434220

[123] W.C. Rontgen, *Ann. Phys*. **35**, 1888, 264

[124] H. A. Wilson, *Phil. Trans R. Soc. A* **204**, 1905, 121

[125] P. Curie, *Journal de Physique* **3**, 1894, 393

[126] L.D. Landau, E. Lifshitz, *Quantum Mechanics: Non-Relativistic Theory: Volume 3*, Course of Theoretical Physics, 1958

[127] W.F. Brown, R.M. Hornreich, S. Shtrickman, *Phys. Rev.* **168**, 1968, 574

[128] R. Lobo, *Types of Multiferroics*, 2013, at: https://www.lpem.espci.fr/ocg/res_mf_types.html

[129] D.I. Khomskii, *Coupled electricity and magnetism in solids: multiferroics and beyond*. In: J. Wang (ed.), *Multiferroic Materials: Properties, Techniques, and Applications*, CRC Press, 2016

[130] N. Hill, *J. Phys. Chem. B* **104**, 2000, 6694

[131] R.E. Cohen, *Nature* **358**, 1992, 136

[132] D. Khomskii, *J. Magn. Magn. Mater.* **306**, 2006, 1

[133] D. Khomskii, *Coupled electricity and magnetism: multiferroics and beyond*, 2014, at: http://sadovski.iep.uran.ru/RUSSIAN/LTF/Kourovka_35/Khomskii/Khomskii.pdf

[134] G.A. Smolenskii, V.A. Isupov, N.N. Krainik, A.I. Agranovskaya, *Izv. Akad. Nauk SSSR* **25**, 1961, 1333

[135] N.Y. Venevtsev, G. Zhdanov, S. Solovév, *Sov. Phys. Crystallogr*. **4**, 1960, 538

[136] G.A. Smolenskii, V. Yudin, E. Sher, *Sov. Phys. JETP* **16**, 1963, 622

[137] A.M. d. Santos, S. Parashar, A.R. Raju, Y.S. Zhao, A.K. Cheetham, C.N. Rao, *Solid, State Commun*. **122**, 2002, 49

[138] A.M. d. Santos, A.K. Cheetham, W. Tian, X. Pan, Y. Jia, N.J. Murphy, J. Lettieri, D.G. Schlom, *Appl. Phys. Lett.* **84**, 2004, 91

[139] L.W. Martin, Q. Zhan, Y. Suzuki, R. Ramesh, M. Chi, N. Browning, T. Mizoguchi, J. Kreisel, *Appl. Phys. Lett.* **90**, 2007, 062903

[140] D. Khomskii, *Physics* **2**, 2009, 20

[141]A.P. Levanyuk, D.G. Sannikov, *Sov. Phys. Usp*. **17**, 1974, 199

[142] B.B. Van Aken, T.T.M. Palstra, A. Filippetti, N.A. Spaldin, *Nature Mater.* **3**, 2004, 164

[143] C.J. Fennie, K.M. Rabe. *Phys. Rev. B* **72**, 2005, 100103

[144] E. Claude, N.A. Spaldin, *Phys. Rev. B* **74**, 2006, 020401(R)

[145] D. Khomskii, *Transition Metal Compounds*, Univ. Köln, 2014

[146] J. Van den Brink, D. Khomskii, *J. Phys.: Condens. Matter* **20**, 2008, 434217

[147] J. Hwang, *Magnetoelectric and Multiferroic Properties in Layered 3D Transition Metal Oxides*, PhD thesis, The Florida State University, 2012, at: http://fsu.digital.flvc.org/ islandora/object/fsu%3A183257

[148] T. Kimura, T. Goto, H. Shintani, K. Ishizaka, T. Arima, Y. Tokura. *Nature* **426**, 2003, 55

[149] S. W. Cheong and M. Mostovoy. *Nature Materials* **6**, 1997, 13

[150] T. Aoyama, K. Yamauchi, A. Iyama, S. Picozzi, K. Shimizu, T. Kimura, *Nature Communications* **5**, 2014, 4927

[151] R. Ramesh, S. Aggarwal, O. Auciello, *Materials Science and Engineering: R.* **32**, 2001, 191

[152] M. Dawber, K.M. Rabe, J.F. Scott, *Rev. Mod. Phys*. **77**, 2005, 1083

[153] D.G. Schlom, J.H. Haeni, J. Lettieri, C.D. Theis, W. Tian, J.C. Jiang, X.Q. Pan, *Materials Science and Engineering: B* **87**, 2001, 282

[154] C. Ederer and N.A. Spaldin, *Phys. Rev. Lett*. **95**, 2005, 257601

[155] J.H. Haeni, P. Irvin, W. Chang, R. Uecker, P. Reiche, Y.L. Li, S. Choudhury, W. Tian, M.E. Hawley, B. Craigo, A.K. Tagantsev, X.Q. Pan, S.K. Streiffer, L.Q. Chen, S.W. Kirchoefer, J. Levy, D.G. Schlom, *Nature* **430**, 2004, 758

[156] K.J. Choi, M. Biegalski, Y.L. Li, A. Sharan, J. Schubert, R. Uecker, P. Reiche, Y.B. Chen, X.Q. Pan, V. Gopalan, L.Q. Chen, D.G. Schlom, C.B. Eom, *Science* **306**, 2004, 1005

[157] J. Wang, J.B. Neaton, H. Zheng, V. Nagarajan, S.B. Ogale, B. Liu, D. Viehland, V. Vaithyanathan, D.G. Schlom, U.V. Waghmare, N.A. Spaldin, K.M. Rabe, M. Wuttig, R. Ramesh, *Science* **299**, 2003, 1719

[158] C. Tabares-Muñoz, J.P. Rivera, A. Bezinges, A. Monnier, H. Schmid, *Jpn. J. Appl. Phys*. **24**, 1985, 1051

[159] J.B. Neaton, C. Ederer, U.V. Waghmare, N.A. Spaldin, K.M. Rabe, *Phys. Rev. B* **71**, 2005, 014113

[160] D. Lebeugle, D. Colson, A. Forget, M. Viret, *Appl. Phys. Lett*. **91**, 2007, 022907

[161] K.Y. Yun, D. Ricinschi, T. Kanashima, M. Noda, M. Okuyama, *Jpn. J. Appl. Phys*. **43**, 2004, L647

[162] G. Catalan, J.F. Scott, *Adv. Mater.* **21**, 2009, 2463

[163] M. Murakami, S. Fujino, S.H. Lim, C.J. Long, L.G. Salamanca-Riba, M. Wuttig, I. Takeuchi, *Appl. Phys. Lett.* **88**, 2006, 152902

[164] L.W. Martin, Y.H. Chu, R. Ramesh, *Materials Science and Engineering R.* **68**, 2010, 89

[165] M. Gajek, M. Bibes, A. Barthélémy, K. Bouzehouane, S. Fusil, M. Varela, J. Fontcuberta, A. Fert, *Phys. Rev. B* **72**, 2005, 020406(R)

[166] S. Song, H.M. Jang, N. S. Lee, J. Y. Son, R. Gupta, A. Garg, J. Ratanapreechachai, J. F. Scott, *NPG Asia Materials* **8**, 2016, e242

[167] M. Trassin, N. Viarta, G. Versini, J.L. Loison, J.P. Vola, G. Schmerber, O. Crégut, S. Barre, G. Pourroy, J.H. Lee, W. Jo, C. Mény, *Appl. Phys. Lett.* **91**, 2007, 202504

[168] T. Arima, D. Higashiyama, Y. Kaneko, J.-P. He, T. Goto, S. Miyasaka, T. Kimura, K. Oikawa, T. Kamiyama, R. Kumai, Y. Tokura, *Phys. Rev. B* **70**, 2004, 064426

[169] L.W. Martin, *Engineering Multiferroic Materials and New Functionalities in Materials*, PhD thesis, University of California, Berkeley, 2008

[170] A. Kumar, L.W. Martin, S. Denev, J.B. Kortright, Y. Suzuki, R. Ramesh, V. Gopalan, *Phys. Rev. B* **75**, 2007, 060101(R)

[171] N. Fujimura, T. Ishida, T. Yoshimura, T. Ito, *Appl. Phys. Lett.* **69**, 1996, 1011

[172]A.A. Bosak, A.A. Kamenev, I.E. Graboy, S.V. Antonov, O.Y. Gorbenko, A.R. Kaul, C. Dubourdieu, J.P. Senateur, V.L. Svechnikov, H.W. Zandbergen, B. Hollander, *Thin Solid Films* **400**, 2001, 149

[173] K. Suzuki, K. Nishizawa, T. Miki K. Kato, *Jpn. J. Appl. Phys.* **43**, 2004, 6613

[174] J.H. Lee, P. Murugavel, H. Ryu, D. Lee, J.Y. Jo, J.W. Kim, H.J. Kim, K.H. Kim, Y. Jo, M.H. Jung, Y. H. Oh, Y.W. Kim, J.G. Yoon, J.S. Chung, T.W. Noh, *Adv. Mater.* **18**, 2006, 3125

[175] K.R. Balasubramaniam, S. Havelia, P.A Salvador, H. Zheng, J.F. Mitchell, *Appl. Phys. Lett.* **91**, 2007, 232901

[176] A. Kumar, G.L. Sharma, R.S. Katiyar, J.F. Scott, R. Pirc, R. Blinc, *J. Phys. Condens. Matter* **21**, 2009, 382204

[177] D. Lee, Y.A. Park, S.M. Yang, T.K. Song, Y. Jo, N. Hur, J.H. Jung, T.W. Noh, *J. Phys. D: Appl. Phys*. **43**, 2010, 455403

[178] D. Lee, S.M. Yang, Y. Jo, T.K. Song, *J. Korean Phys. Soc*. **57**, 2010, 1914

[179] D. Sanchez, A. Kumar, N. Ortega, R.S. Katiyar, J.F. Scott, *Appl. Phys. Lett*. **97**, 2010, 202910

[180] P. Yu, Y.H. Chu, R. Ramesh, *Phil. Trans. R. Soc. A* **370**, 2012, 4856

[181] N. Ortega, A. Kumar, J.F. Scott, R.S. Katiyar, *J. Phys.: Condens. Matter* **27**, 2015, 504002

[182] Y. Wang, J. Hu, Y. Lin, C.W. Nan, *NPG Asia Mater.* **2**(2), 2010, 61

[183] R. Ramesh, N.A. Spaldin, *Nature Materials* **6**, 2007, 21

[184] D. Mukherjee, *Growth and Characterization of Epitaxial Tin Films and Multiferroic Heterostructures of Ferromagnetic and Ferroelectric Materials*, PhD thesis, University of South Florida, 2010, at: http://digital.lib.usf.edu/SFS0028034/00001/citation.

[185] S. Ryu, J.H. Park, H.M. Jang, *Appl. Phys. Lett*. **91**, 2007, 142910

[186] G. Srinivasan, E.T. Rasmussen, J. Gallegos, R. Srinivasan, *Phys. Rev. B* **64**, 2001, 214408

[187] J. Ryu, A.V. Carazo, K. Uchino H. Kim, *J. Electroceram.* **7**, 2001, 17

[188] G. Srinivasan, E.T. Rasmussen, B.J. Levin, R. Hayes *Phys. Rev. B* **65**, 2002, 134402

[189] T. Wu, M.A. Zurbuchen, S. Saha, R.V. Wang, S.K. Streiffer, J.F. Mitchell, *Phys. Rev. B* **73**, 2006, 134416

[190] M.I. Bichurin, V.M. Petrov, G. Srinivasan, *Phys. Rev. B* **68**, 2003, 054402

[191] H. Zheng, J. Wang, S.E. Lofland, Z. Ma, L. Mohaddes-Ardabili1, T. Zhao, L. Salamanca-Riba1, S.R. Shinde, S.B. Ogale, F. Bai, D. Viehland, Y. Jia, D.G. Schlom, M. Wuttig, A. Roytburd, R. Ramesh, *Science* **303**, 2004, 661

[192] R. A. Islam, S. Priya, *Advances in Condensed Matter Physics* **vol. 2012**, 2012, Article ID 320612

[193] J. Li, I. Levin, J. Slutsker, V. Provenzano, P.K. Schenck, R. Ramesh, J. Ouyang, A.L. Roytburd, *Appl. Phys. Lett*. **87**, 2005, 072909

[194] J.G. Wan, X.W. Wang, Y.J. Wu, J.M. Liu, *Appl. Phys. Lett*. **86**, 2005, 122501

[195] S. Ren, M. Wuttig, *Appl. Phys. Lett.* **91**,2007, 083501

[196] M. Murakami, S. Fujino, S.H. Lim, L.G. Salamanca-Riba, M. Wuttig, I. Takeuchi, B. Varughese, H. Sugaya, T. Hasegawa, S.E. Lofland, *Appl. Phys. Lett*. **88**, 2006, 112505

[197] F. Zavaliche, H. Zheng, L. Mohaddes-Ardabili, S.Y. Yang, Q. Zhan, P. Shafer, E. Reilly, R. Chopdekar, Y. Jia, P. Wright, D.G. Schlom, Y. Suzuki, R. Ramesh, *Nano Lett.* **5**, 2005, 1793

[198] X.L. Zhong, J.B. Wang, M. Liao, G.H. Huang, S.H. Xie, Y.C. Zhou, Y. Qiao, J.P. He, *Appl. Phys. Lett*. **90**, 2007, 152903

[199] H. Ryu, P. Murugavel, J.H. Lee, S.C. Chae, T.W. Noha, *Appl. Phys. Lett*. **89**, 2006, 102907

[200] J. Zhai, N. Cai, Z. Shi, Y. Lin, C.W. Nan, *J. Phys. D* **37**, 2004, 823

[201] T. Zhao, A. Scholl, F. Zavaliche, K. Lee, M. Barry, A. Doran, M.P. Cruz, Y.H. Chu, C. Ederer, N.A. Spaldin, R.R. Das, D.M. Kim, S. H. Baek, C.B. Eom, R. Ramesh, *Nat. Mater*. **5**, 2006, 823

[202] I. Sosnowska, T. Peterlin-Neumaier, E. Steichele, *J. Phys. C* **15**, 1982, 4835

[203] R. Przenioslo, M. Regulski, I. Sosnowska, *J. Phys. Soc. Jpn*. **75**, 2006, 084718

[204] D. Lebeugle, D. Colson, A. Forget, M. Viret, A.M. Bataille, A. Gukasov, *Phys. Rev. Lett*. **100**, 2008, 227602

[205] G. Catalan and J.F. Scott, *Adv. Mater*. **21**, 2009, 2463

[206] V.V. Shvartsman,, W. Kleemann, R. Haumont, J. Kreisel, *Appl. Phys. Lett*. **90**, 2007, 172115

[207] C. Ederer, N.A. Spaldin, *Phys. Rev. B* **71**, 2005, 060401(R)

[208] H. Bea, M. Bibes, S. Fusil, K. Bouzehouane, E. Jacquet, K. Rode, P. Bencok, A. Barthelemy, *Phys. Rev. B: Condens. Matter Mater. Phys.* **74**, 2006, 02010

[209] D. Lebeugle, D. Colson, A. Forget, M. Viret, P. Bonville, J.F. Marucco, S. Fusil, *Phys. Rev. B* **76**, 2007, 024116

[210] M. Lorenz, G. Wagner, V. Lazenka, P. Schwinkendorf, H. Modarresi, M.J. Van Bael, A. Vantomme, K. Temst, O. Oeckler, M. Grundmann, *Appl. Phys. Lett.* **106**, 2015, 012905.

[211] A.F. Popkov, M.D. Davydova, K.A. Zvezdin, S.V. Solovyov, A.K. Zvezdin, *Phys. Rev. B* **93**, 2016, 094435

[212] F. Bai, J. Wang, M. Wuttig, J. Li, N. Wang, A.P. Pyatakov, A.K. Zvezdin, L.E. Cross, D. Viehland, *Appl. Phys. Lett.* **86**, 2005, 032511

[213] S. Prosandeev, I.A. Kornev, L. Bellaiche, *Phys. Rev. B* **83**, 2011, 020102(R)

[214] M. Lorenz, V. Lazenka, P. Schwinkendorf, F. Bern, M. Ziese, H. Modarresi, A. Volodin, M.J.V. Bael, K. Temst, A. Vantomme, M. Grundmann, *J. Phys. D: Appl. Phys*. **47**, 2014, 135303

[215] A. Kumar, J.F. Scott, R.S. Katiyar, *Appl. Phys. Lett.* **99**, 2011, 062504

[216] J.C. Yang, Y.L. Huang, Q. He, Y.H. Chu, *J. Appl. Phys*. **116**, 2014, 066801

[217] F. Zavaliche, S.Y. Yang, T. Zhao, Y.H. Chu, M.P. Cruz, C.B. Eom, R. Ramesh, *Phase Transitions* **79**, 2006, 991

[218] J. Seidel, L.W. Martin, Q. He, Q. Zhan, Y.H. Chu, A. Rother, M.E. Hawkridge, P. Maksymovych, P. Yu, M. Gajek, N. Balke, S.V. Kalinin, S. Gemming, F. Wang, G. Catalan, J.F. Scott, N.A. Spaldin, J. Orenstein, R. Ramesh, *Nature Materials* **8**, 2009, 229

[219] S.M. Wu, S.A. Cybart, P. Yu, M.D. Rossell, J.X. Zhang, R. Ramesh, R.C. Dynes, *Nature Materials* **9**, 2010, 756

[220] S.M. Wu, S.A. Cybart, D. Yi, J.M. Parker, R. Ramesh, R.C. Dynes, *Phys. Rev. Lett*. **110**, 067202

[221] S.H. Lim, M. Murakami, J.H. Yang, S.Y. Young, *Appl. Phys. Lett.* **92**, 2008, 012918

[222] A. Lahmar, K. Zhao, S. Habouti, M. Dietze, C.H. Solterbeck, M. Es-Souni, *Solid State Ionics* **202**, 2011, 1

[223] G.W. Pabst, L.W. Martin, Y.H. Chu, R. Ramesh, *Appl. Phys. Lett.* **90**, 2007, 072902

[224] Y. Shuai, S. Zhou, D. Bürger, H. Reuther, I. Skorupa, V. John, M. Helm, H. Schmidt, *J. Appl. Phys.* **109**, 2011, 084105

[225] H. Bea, M. Bibes, A. Barthélémy, K. Bouzehouane, E. Jacquet, A. Khodan, J.P. Contour, *Appl. Phys. Lett*. **87**, 2005, 072508

[226] Y.H. Chu, Q. Zhan, C.H. Yang, M.P. Cruz, L.W. Martin, T. Zhao, P. Yu, R. Ramesh, P.T. Joseph, I.N. Lin, W. Tian, D.G. Schlom, *Appl. Phys. Lett*. **92**, 2008, 102909

[227] G. L. Yuan, S.W. Or, *J. Appl. Phys*. **100**, 2006, 04109

[228] H. Uchida, R. Ueno, H. Funakubo, S. Koda, *J. Appl. Phys*. **100**, 2006, 014106

[229] J. Wu, Z. Fan, D. Xiao, J. Zhu, J. Wang, *Prog. Mater. Sci*. **84**, 2016, 335

[230] Y. Shuai, S. Zhou, S Streit, H. Reuther, D. Bürger, S. Slesazeck, T. Mikolajick, M. Helm, H. Schmidt., *Appl. Phys. Lett*. **98**, 2011, 232901

[231] G.D. Hu, X. Cheng, W.B. Wu, C.H. Yang, *Appl. Phys. Lett.* 91, 2007, 232909

[232] G.D. Hu, S.H. Fan, C.H. Yang, W.B. Wu, *Appl. Phys. Lett*. 92, 2008, 192905

[233] S.T. Zhang, Y. Zhang, M.H. Lu, C.L. Du, Y.F. Chen, Z.G. Liu, Y.Y. Zhu, N.B. Ming, *Appl. Phys. Lett.* **88**, 2006, 162901

[234] S.R. Das, R.N.P. Choudhary, P. Bhattacharya, R.S. Katiyar, *J. Appl. Phys*. **101**, 2007, 034104

[235] S. Fujino, M. Murakami, V. Anbusathaiah, S.H. Lim, V. Nagarajan, C.J. Fennie, M. Wuttig, L. Salamanca-Riba, I. Takeuchi, *Appl. Phys. Lett.* **92**, 2008, 202904

[236] A. Ablat, R. Wu, M. Mamat, J. Li, E. Muhemmed, C. Si, R. Wu, J. Wang, H. Qian, K. Ibrahim, *Ceramics International* **40**, 2014, 14083

[237] J. Liu, M. Li, L. Pei, J. Wang, B. Yu, X. Wang, X. Zhao, *J. Alloys Compd* **493**, 2010, 544

[238] G.S. Lotey, N.K. Verma, *AIP Conference Proceedings* **55**, 2013, 1536

[239] B. Bhushan, A. Basumallick, S.K. Bandopadhyay, N.Y. Vasanthacharya, D. Das, *J. Phys. D: Appl. Phys*. **42**, 2009, 065004

[240] A. Lebon, P. Adler, C. Bernhard, A.V. Boris, A.V. Pimenov, A. Maljuk, C.T. Lin, C. Ulrich, B. Keimer, *Phys. Rev. Lett*. **92**, 2004, 037202

[241] H.W. Chang, F.T. Yuan, K.T. Tu, Y.C. Lo, S.Y. Tu, C.R. Wang, A.B. Yang, C.S. Tu, S.U. Jen, W.C. Chang, *J. Appl. Phys.* **117**, 2015, 17C734

[242] R. Das, K. Mandal, *J. Magn. Magn. Mater.* **324**, 2012, 1913

[243] C.H. Yang, J. Seidel, S.Y. Kim, P.B. Rossen, P. Yu, M. Gajek, Y.H. Chu, L.W. Martin, M.B. Holcomb, Q. He, P. Maksymovych, N. Balke, S.V. Kalinin, A.P. Baddorf, S.R. Basu, M.L. Scullin, R. Ramesh, *Nature Materials* **8**, 2009, 485

[244] N. Wang, J. Cheng, A. Pyatakov, A.K. Zvezdin, J.F. Li, L.E. Cross, D. Viehland, *Phys. Rev. B* **72**, 2005, 104434

[245] F. Azough, R. Freer, M. Thrall, R. Cernik, F. Tuna, D. Collison, *J. Eur. Ceram. Soc.* **30**, 2010, 727

[246] S.O. Leontsev, R.E. Eitel, *J. Am. Ceram. Soc.* **92**, 2009, 2957

[247] L. Chen, W. Ren, W. Zhu, Z.G. Ye, P. Shi, X. Chen, X. Wu, X. Yao, *Thin Solid Films* **518**, 2010, 1637

[248] S. Gupta, A. Garg, D.C. Agrawal, S. Bhattacharjee, D. Pandey, *J. Appl. Phys.* **105**, 2009, 014101

[249] J. Wu, J. Wang, *J. Phys. D: Appl. Phys*. **42**, 2009, 195405

[250] N. Kumar, B. Narayan, S. Kumar, K.C. Verma, R. Ranjan, J. Shah, R.K. Kotnala, *Mater. Res. Express* **4**, 2017, 095701

[251] C.M. Fernandez-Posada, A. Castro, J.M. Kiat, F. Porcher, O. Pena, M. Alguero, H. Amorın, *Nature Communications* **7**, 2016, 12772

[252] P. Mandal, A. Manjón-Sanz, A.J. Corkett, T.P. Comyn, K. Dawson, T. Stevenson, J. Bennett, L.F. Henrichs, A.J. Bell, E. Nishibori, M. Takata, M. Zanella, M.R. Dolgos, U. Adem, X. Wan, M.J. Pitcher, S. Romani, T.T. Tran, P.S. Halasyamani, J.B. Claridge, M.J. Rosseinsky, *Adv. Mater*. **27**, 2015, 2883

[253] C.A. Bridges, M. Allix, M.R. Suchomel, X. Kuang, I. Sterianou, D.C. Sinclair, M.J. Rosseinsky, *Angew. Chem. Int. Ed.* **46**, 2007, 8785

[254] S.Y. Chong, R.J. Szczecinski, C.A. Bridges, M.G. Tucker, J.B. Claridge, M.J. Rosseinsky, *J. Am. Chem. Soc*. **134**, 2012, 5836

[255] P. Mandal, M.J. Pitcher, J. Alaria, H. Niu, M. Zanella, J.B. Claridge, M.J. Rosseinsky, *Adv. Funct. Mater*. **26**, 2016, 2523

[256] J. Zhang, W. Sun, J. Zhao, L. Sun, L. Li, X.J Yan, K. Wang, Z.B. Gu, Z.L. Luo, Y. Chen, G.L. Yuan, M.H. Lu, S.T. Zhang, *Appl. Mater. Interfaces* **9**, 2017, 25397

Chapter 3: Experimental methods

3.1 Solid state synthesis

The solid-state method was used for the preparation of bulk $SrZn_{1-x}Li_xO_2$ and $Bi_y[Bi_{0.85}Ca_{0.15}][Ti_{0.235}Fe_{0.69}Mg_{0.085}]O_3$ (y= 0, 0.21) samples. The solid-state route is a widely used methods for the preparation of polycrystalline solids starting from a mixture of solid reactants[257]. The synthesis of new solid phase materials relies on the formation of thermodynamic products at high temperatures and usually requires several grinding steps followed by subsequent firings under different atmospheres. Repeated grinding steps reduce the particle size of reacting solids and facilitates the ion diffusion and mixing of precursors in high annealing temperatures[258].

Unless stated otherwise, all the used starting materials were kept overnight at 200 °C inside an oven before mixed to ensure their dryness when weighted. The exploratory synthesis of the examined compounds was carried in milligram-scale quantities (below 500 mg) and all the samples were hand-ground in a mortar and pestle. When the synthesis of BTFM-CTO samples was scaled up (5 g), ball milling of the starting materials was held in a Fritsch pulverisette planetary mill for 24 hours at 350 rpm using yttrium stabilised zirconia pots and ceramic balls (of 5 mm diameter). The ball milling slurry was prepared using 4 ml of isopropanol solvent for every 1 g of sample. Before firing, all the samples were pelletized using a uniaxial press and cold isostatic pressure apparatus. Pt foiled lined Al_2O_3 crucibles were used during the sintering process to ensure no reactions of the examined samples with the Al_2O_3 crucibles will take place.

In a variation of the solid-state route, reactive Li and K precursors were used when investigating doping of $SrZnO_2$. Stoichiometric quantities of SrO, ZnO and Li_2O_2 were mixed, hand-ground and pressed into pellets inside a helium dry box (LabMaster 130, MBraun) before sealed under vacuum in quartz tubes at a pressure of ca. 10^{-6} Torr and fired at different temperatures.

3.2 Pulsed laser deposition

The developments on thin-film deposition techniques during the last century have enabled a great progress towards the engineering and application of new and miniaturized materials in a variety of fields, spanning from hard coatings on metallic surfaces to electronic and semiconductor devices, optoelectronic (LEDs, detectors), magnetic recording media, multifunctional "smart" materials (multiferroic), energy storage and generation materials (solar cells and batteries) etc.

The different methods of thin film depositions can be categorized in two ways, depending on the process in which the growing films are obtained: chemical or physical. In the chemical method, a fluid precursor (typically liquid or gas-phase) undergoes a chemical transformation over a substrate depositing a solid thin film layer. Some characteristic examples of chemical deposition methods are the chemical solution deposition, the spin coating, the chemical vapour deposition (CVD) and the atomic layer deposition (ALD).

The physical deposition, in all the different forms in which it can be encountered, is a vacuum process where the as-grown film is deposited to the substrate in the form of condensed vapour particles of a solid or gas-phase material source without chemical reactions taking place in the process. Over the years, different methods of physical deposition have been developed such as evaporation, sputtering (including high-power impulse magnetron sputtering, HiPIMS), cathodic arc deposition, molecular beam epitaxy and pulsed laser deposition.

Among them, the pulsed laser deposition (PLD) is a widely used deposition technique for growing a great variety of materials, including functional metal oxides as well other advanced ceramic materials such as chalcogenide, nitride, silicon carbide, silicon dioxide and III-IV semiconductors, but also metals, intermetallic alloys and even polymers and polymer-metal compounds.

The process of PLD can be summarized in a sequence of three steps: (i) the irradiation and vaporization of a target by a fixed laser beam, (ii) the formation and propagation of a plasma plume to the substrate and (iii) the nucleation of the ablated material and the film growth on the substrate surface.

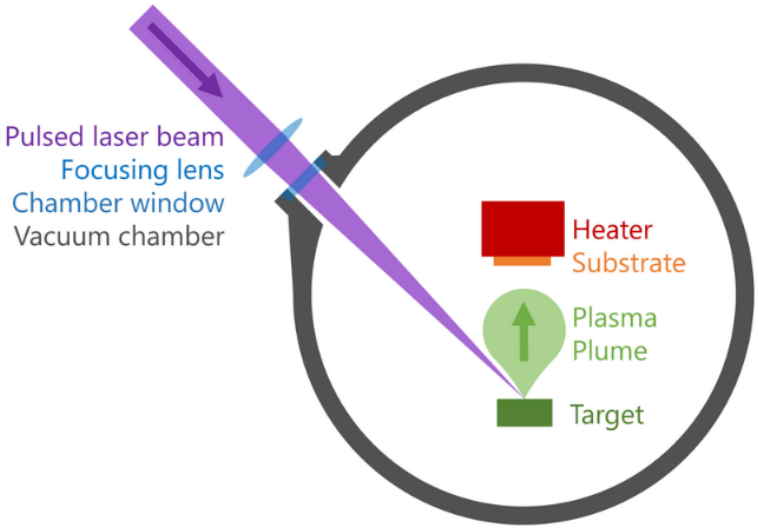

Figure 3. 1: Schematic diagram of the pulsed laser deposition system. Taken from[259].

In the first place, a pulsed laser beam, produced by an excited dimer molecule gas (examples: KrF, ArF), is focused by a system of mirrors and lens inside a vacuum chamber onto a rotating target and the ablation process is begun. Due to the short wavelength of the used UV light, the absorption of the high-energy laser radiation tends to be relative high and the target ablation is only confined to in its near-surface area without heating large volumes of the target. As the laser fluence increased, the absorbed energy by the target increases higher than the evaporation energy of the constituent cations and thus an instant process of vaporization and ionization is taking place, producing a high-energy plasma.

With the background pressure inside the deposition chamber kept at high-vacuum conditions, the produced plasma adopts a directional plume-shape and expands perpendicular to the target surface whilst its kinetic energy is reduced (observed in the emission of Bremsstrahlung photons). The interaction of the plume with the background chamber atmosphere will also increase further the ionization of ablated species assisting the stabilization of intermediate molecular species which facilitate the formation of multi-cation phases[260].

As the plume travels a certain distance inside the chamber, it will arrive on the substrate which is kept rotating to ensure the thickness uniformity of the deposited film. At the same time, the substrate is also kept heated to facilitate the diffusion and nucleation of the approaching ablated species towards a continuous thin film layer[261]. A uniform and macroscopically highly ordered film growth will be obtained when the arriving species (typically referred in the literature as

adatoms) are compatible with the substrate and can attach directly on it favouring a two-dimensional layer by layer growth (also referred as Frank-Van der Merwe growth)[262].

The thin film crystal growth can be approached thermodynamically as a phase transformation of supersaturated gas adatoms to islands of solid nuclei which subsequently are growing and crystallised. Depending on the "wettability" of the film/substrate system, defined as a balance of the free energy of the system, and the lattice mismatch of film to substrate, different film growth modes can be observed as illustrated in **Figure 3. 2**.

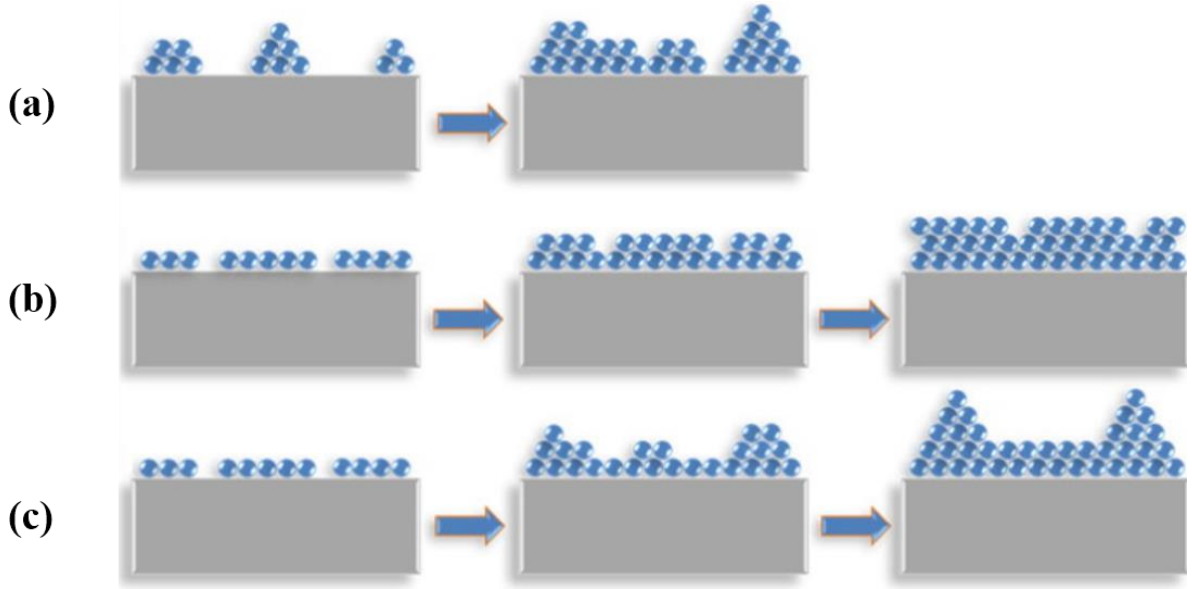

Figure 3. 2: Different modes of film growth: (a) 3D island growth (Volmer-Weber mode) of a film/substrate system with poor wettability, (b) layer-by-layer growth (Frank-Van der Merwe mode) and (c) mixed growth (Stranski - Krastanov mode) of a film/substrate system with a large lattice mismatch despite its good wettability. Taken from[263].

The attraction of PLD as a method of choice for exploring the synthesis of new materials and the properties of film heterostructures is lying on its ability to grow high quality complex layer structures while maintaining the target stoichiometry.

One of the biggest advantages of PLD is its ability to ensure the stoichiometric material transfer from the bulk target to film. More specifically, the non-equilibrium process of the plasma plume formation enables the evaporation of target particles with energies higher than the vapour pressure limit of the constituent cations and allows the stoichiometric deposition of films even in the case of complex multi-cation compounds.

The ability to control several degrees of freedom during the film growth process (temperature, pressure, energy) and the rapid crystallization of the ablated material arriving on the substrate are offering the potential of obtaining metastable, non-equilibrium phases[264,265]. In addition, the freedom to adjust growth parameters such as the substrate temperature, background oxygen pressure (especially for metal oxide films) as well as substrate-induced lattice strains are offering additional tools to engineer the properties of deposited films.

The "pulsed" character of film growth in PLD, with a pulse duration typically less than 40 microseconds, is also allowing, in comparison to other deposition techniques, a large supersaturation of arriving adatoms on the substrate surface and as a result a very large nucleation density even at slow growth rates[259]. Under those conditions, a smooth and highly-ordered "layer-by-layer" film growth can be obtained by adjusting the flux of arriving adatoms to the number of a monolayer[261].

With the particles produced in the laser-induced plasma process reaching temperatures up to 3000 K[265] it allows processing some of most refractory materials, such as carbides and borides. The vacuum-isolated chamber of growth also provides the capability of handling toxic materials, such as lead and cadmium, under safe conditions. Overall, the conceptually simple and versatile operation mode of PLD offers remarkable material deposition capabilities for growing complex, multi-cation structures on a variety of gas atmospheres and pressures.

During this thesis, pulsed laser depositions were carried out in a PLD system (Nano PLD of PVD Products Inc.) equipped with a KrF excimer laser source (Lambda Physik) emitting light pulses of 34 ns at 248 nm wavelength. The laser beam was focused on the target with an incident angle of 45º. The base pressure of the deposition chamber was kept below 5×10^{-7} Torr with the use of a mechanical (rough) and a turbomolecular vacuum pump. Finally, the vacuum chamber was equipped with a gas management system enabling the insertion of O_2 into the system.

3.3 Structural characterization

3.3.1 X-ray Diffraction

3.3.1.1 Basics of X-ray diffraction

X-ray diffraction is a powerful and non-destructive tool for obtaining crystallographic information about the structure and composition of crystalline solids. The extensive use of x-rays in crystallography is based on their similar wavelength to the inter-planar spacing of the crystalline materials (in the range of 1.5 - 3.5 Å) which allows the x-rays to penetrate deep into the structure of the examined samples and reveal valuable information on their crystallographic morphology.

When an incident monochromatic X-ray beam is irradiated to a crystalline material, a characteristic pattern of diffracted x-rays is produced as a result of its constructive interference with the crystalline structure of the material. As known from Bragg's law, the observed pattern of diffraction peaks appears at specific angles where incident and scattered beams are in-phase, according to:

$$n\,\lambda = 2\,d\,sin\theta_B \qquad \textbf{(Eq. 3. 1)}$$

where n is an integer number, λ is the wavelength of the incident beam, θ_B is the Bragg angle of the incident beam and d is the interplanar distance between parallel lattice planes of the diffracted crystalline material, as denoted in **Figure 3. 3**. At angles different than the Bragg angle, the scattered beam is found to be in an out-of-phase condition resulting on a destructive interference with the incident bean occurs.

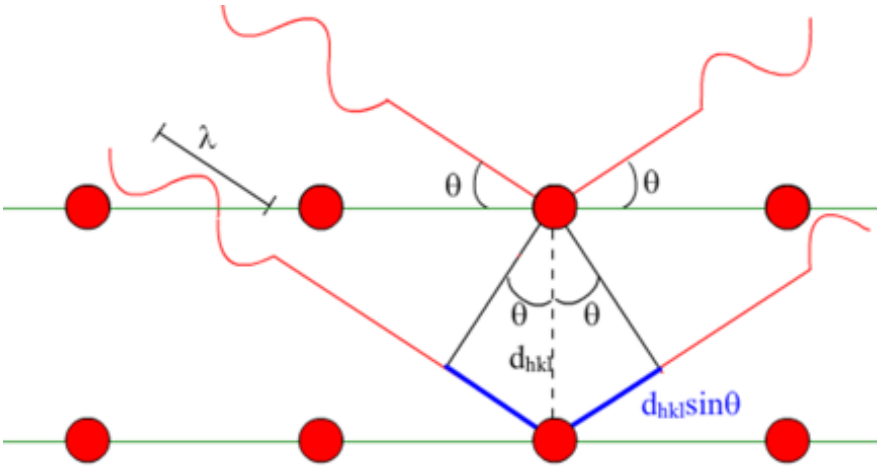

Figure 3. 3: Schematic representation of Bragg reflection on a crystalline structure. Taken from[266].

Since each crystalline material has its own characteristic lattice structure, it will also produce a unique diffraction pattern associated with the specific unit cell geometry of the examined sample: its lattice parameters (a, b, c) and lattice angles (α, β, γ). Families of primary and higher order reflections of parallel planes are revealed when the diffraction pattern of a polycrystalline sample is plotted in a θ/2θ scan over a range of θ angles and can be indexed according to the miller indices (h, k, l), while the interplanar d-spacing of the various crystallographic planes is associated, based on crystallographic considerations, with the specific unit cell geometry of the examined material.

In the case of thin films, the as-grown films might be amorphous, polycrystalline or fully oriented and studying their crystalline structure necessitate the use of more advanced x-ray techniques.

During this work, powder X-ray diffraction data as well as the out-of-plane thin film X-ray diffraction data were collected in a two circle Panalytical X'Pert PRO diffractometer with a Co-source (Co-K_{a1}). Other thin film X-ray diffraction data such as rocking curve, X-ray reflectivity measurements and in-house reciprocal space maps were collected in a four circle Panalytical X'Pert PRO diffractometer or a SmartLab diffractometer of Rigaku Corp., both having a Cu-source (Cu- K_{a1}).

3.3.1.2 Pawley refinements

The measured powder X-ray diffraction (PXRD) patterns can be analysed using different refinement strategies allowing to extract valuable information on the crystallinity of the studied materials. Among other methods, Pawley refinements is an intensity extraction method that can be used to evaluate the phase purity and the lattice parameters of the examined samples when a full structural model is not required. The input parameters of a Pawley refinement are the space group symmetry and an approximate set of cell parameter values while the observed peaks of the powder patterns are treated as free fitting parameters.

Finally, the quality of the obtained refinements can be assessed with the use of fitting factors such as the weighted profile factor, R_{wp}:

$$\boldsymbol{R_{wp}} = \sqrt{\frac{\sum \boldsymbol{w_i}(\boldsymbol{y_{i,obs}} - \boldsymbol{y_{i,calc}})^2}{\sum \boldsymbol{w_i} \boldsymbol{y_{i,obs}^2}}} \times \mathbf{100} \qquad \textbf{(Eq. 3. 2)}$$

where $y_{i,obs}$ and $y_{i,calc}$ and the observed and calculated intensities and w_i is the weighting given to a data point *i*.

3.3.1.3 Rocking curve (ω-scans)

Although the growth of highly ordered films is expected to give rise on a unique diffraction pattern of X-ray reflection peaks, a peak position distribution is, in practice, detected as a result of a certain degree of long-range misorientation.

To assess the crystallinity of the as-grown films, the in-plane orientation of different film domains can be probed by rocking curve measurements. Under this configuration, symmetric scans are performed on the out-of-plane film direction with the detector set to the selected 2θ Bragg reflection and the sample tilted (rocked) in the vicinity of omega angle as shown in **Figure 3. 4**.

The distribution of orientations around the examined reflection can be analysed after the deconvolution of their reflection peaks to a sum of Gaussian and Lorentzian components (Voigt profile) and, accordingly, the mosaic spread of the film can be quantified by the obtained full width at half maximum (FWHM) of the studied reflection[264]. This value is indicative of the long-range disorder and mosaicity of the as-grown films with a narrow peak demonstrating a higher degree of in-plane orientation and a smaller mosaic spread (< 1˚).

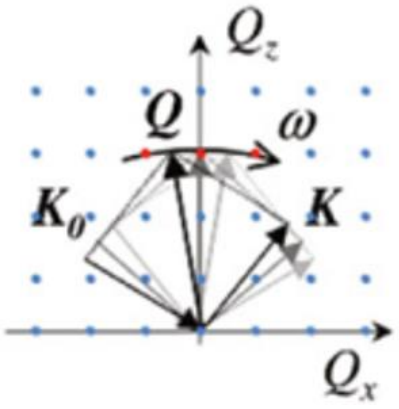

Figure 3. 4: Schematic representation of Rocking curve measurement**.** Taken from[267].

3.3.1.4 X-ray reflectivity (xrr)

The technique of X-ray reflectivity is a non-destructive method for measuring the thickness of films, thinner than 200 nm, which utilizes the total reflection of X-rays incident onto a flat sample surface under a grazing angle smaller than a certain critical angle (θ_o) value.

Given the electromagnetic nature of X-rays, a combination of reflection and refraction effects is expected to occur at the interface of different media irradiated by X-rays. As can be seen in **Figure 3. 5**, the incident X-ray beam can be totally reflected, propagated and/or partially penetrated onto the irradiated media according to the relationship between the incident grazing angle and the total reflection critical angle of the examined media, with the later depending on the electronic density of the media and being typically below 0.5°.

During the XRR measurement, a coupled θ/2θ scan of the film at low incident angles (2θ < 5°) is performed. As the grazing angle is exceeding the critical angle of the film specimen, a part of the incident beam is penetrated the film and reflected at the film-substrate interface due to different density of the two media.

The different optical paths of the reflected beams from the air-film and film-substrate interfaces are giving rise to constructive and destructive interactions with the interference condition being calculated by trigonometry from[268]:

$$2d\sqrt{sin^2\theta_m - sin^2\theta_c} = m\lambda \qquad \textbf{(Eq. 3. 3)}$$

where d is the film thickness, θ_c the critical angle, θ_m the incident angle at points of constructive interference and m the order of the constructive interference.

In addition, the reflected X-ray beam is also carrying information on the surface roughness and density of the examined film sample.

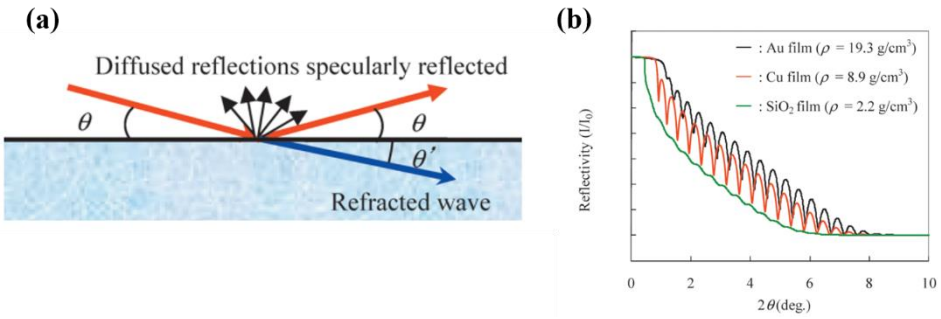

Figure 3. 5: (a) Reflection and refraction of X-rays on material surface, (b) X-ray reflectivity curves of different materials on Si substrates. Taken from[269].

3.3.1.5 Asymmetric scans (phi and pole figures scans)

The use of more advanced crystallographic techniques, such as pole figure scans, is needed to complete a comprehensive study of the crystal structure of highly oriented films.

Valuable information on the crystal symmetry of textured films and their epitaxial relationship to the underlying substrate can be obtained when two-dimensional x-ray maps are generated around high-intensity, asymmetrical, in-plane reflections of the film.

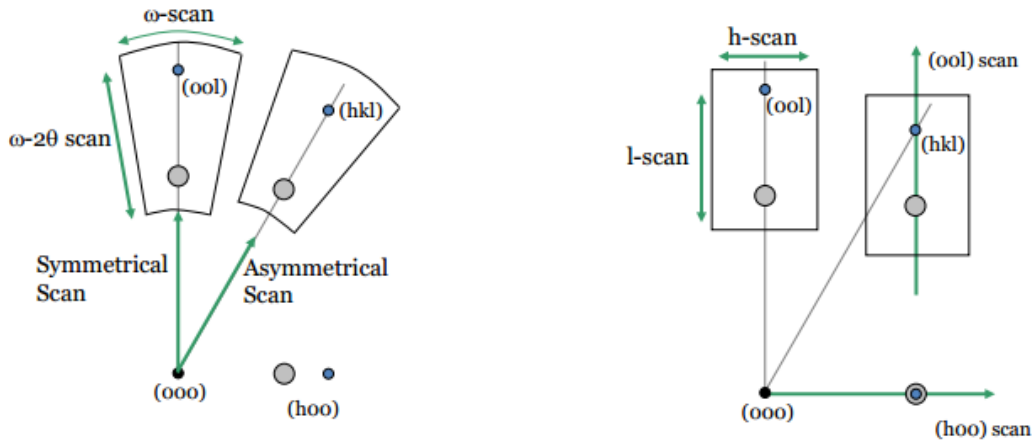

Figure 3. 6: Symmetric and asymmetric scans. Taken from[270].

A phi-scan around the selected asymmetrical reflection is typically collected as a first step in order to access information on the in-plane texture of the as-grown films. To perform this type of scans, the selected asymmetrical plane has to be placed parallel to the incident x-ray beam by tilting the sample stage at a certain Ψ angle (angle between surface normal and selected in-plane reflection) while keeping the $\omega=\theta$ condition. Under this set up, illustrated in **Figure 3. 7**, a phi-scan is collected by rotating the sample around its normal direction (ϕ angle) by 360º degrees.

In a subsequent step, several ϕ-scans are performed at different Ψ angles by tilting the film normal vector with respect to the scattering vector (Ψ angle) as well as the azimuth (ϕ angle) of the film resulting to a 2-dimensional pole figure map of selected set of crystal plane normals with respect to the sample frame[271].

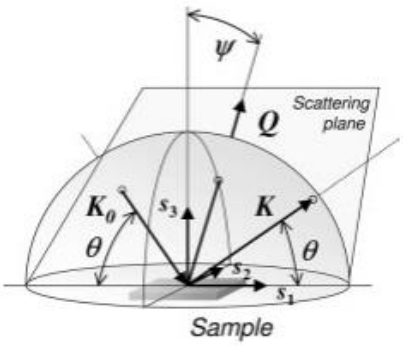

Figure 3. 7: Phi scan and pole figure configuration. Taken from[267].

3.3.1.6 Reciprocal space map

The Ewald sphere is a useful crystallographic concept correlating the 3D real space diffraction parameters of a film to reciprocal lattice parameters (RLP), as illustrated in **Figure 3. 8**. More specifically, using the Ewald sphere representation, it is possible to convert the real space parameters of incident angle (θ), incident (k_o) and diffracted (k_1) wavevectors into a reduced reciprocal vector Q of two orthonormal components: Q_x and Q_z, as shown in **Figure 3. 9**.

The relationship between the reciprocal parameters of the reciprocal space maps and the real space parameters is described by the equations[267]:

$$Q_x = K[\cos(\theta - \omega) - \cos(\theta + \omega)] \quad \textbf{(Eq. 3. 4)}$$

$$Q_z = K[\sin(\theta - \omega) - \sin(\theta + \omega)] \quad \textbf{(Eq. 3. 5)}$$

where K=2π/λ is defined as the magnitude of the x-ray wave vector and coincides with the radius of the Ewald sphere.

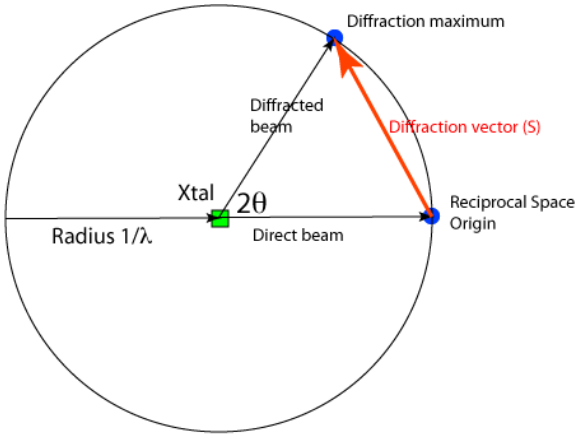

Figure 3. 8: Bragg scattering conditions in the Ewald sphere construction. Only reflections lying on the Ewald sphere are diffracting. Taken from[272].

For the reciprocal space maps, an asymmetric $\omega - 2\theta$ scan is obtained after a series of θ/2θ scans are conducted while the normal direction of the film is being rotated by $\omega \pm \Delta\omega$. The resulted scans are dimensional scannings of $(2\theta, \omega)$ in a parallelogram area of the Ewald sphere around the targeting reciprocal lattice point.

Under the reciprocal Q-representation, several film properties, not accessible with other crystallographic techniques, can be studied such as the thickness and the chemical composition of sub-layers, their lattice parameters and their epitaxial relationship to the substrate.

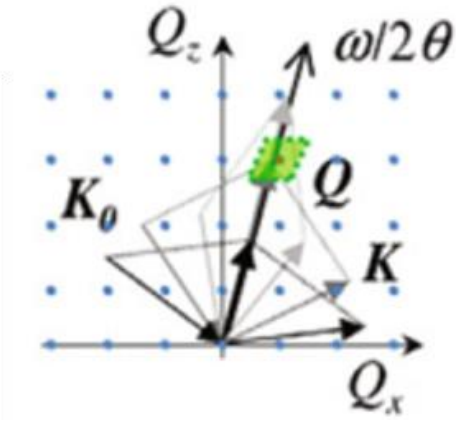

Figure 3. 9: Configurations of reciprocal space map. Taken from[267].

In the reciprocal space map plot each set of peaks correspond to a set of planes with in the crystal, describing completely the set of planes and more importantly orientation and spacing of the given planes.

3.3.1.7 Synchrotron sources of x-rays

Monochromatic x-rays of synchrotron radiation of a low beam divergence and a higher collimation can be used to characterise in detail the crystal structure of samples. In our work, high-resolution synchrotron diffraction data of BTFM-CTO films were collected at the beamline station I11 of the Diamond Light source at the Harwell Science and Innovation Campus in Oxfordshire, UK.

In general, the production of synchrotron radiation is based on high energy electrons accelerated in a series of particle accelerators. At first, electrons generated by an electron gun

are accelerated by a linear accelerator (linac) and will be brought up to their final energy as they are circulated in a closed orbit with the use of a series of bending magnets into a following accelerator section (booster ring). Finally, an array of dipole magnets of alternating polarity will bend and directed the electron path towards the end of the beam line where a variety of insertion devices can further tailor the spectral characteristics of the synchrotron radiation.

The I11 beam line uses radiation produced from an undulator insertion device generating radiation with energies in the range of 5-30 KeV. Two Si(111) monochromators converted the diverging light of the source to a collimated light with wavelength of 0.6 Å.

3.3.2 Atomic Force Microscopy (AFM)

AFM is a high-resolution surface imaging technique in the range of nanometers. It is a scanning probe microscopy technique which is based on the atomic interactions (attractive or repulsive in their nature) between the instrument cantilever and the examined sample.

In the AC (tapping) mode, which was the scanning mode used in this work, a sharp tip at the end of the cantilever is brought in close proximity to the sample while it is oscillating at a constant amplitude by a piezoelectric modulator. As the oscillating tip lightly touches (tap) and scans the surface of the sample in a raster pattern, its oscillation amplitude is changed according to the sample surface morphology. The motion of the tip along the samples surface is monitored by a photodetector which detects changes on the deflection angle of a reflected laser beam into image, as seen in **Figure 3. 10**.

The AFM instrument used in the work related to this thesis was a Keysight 5600LS Atomic Force Microscope (AFM).

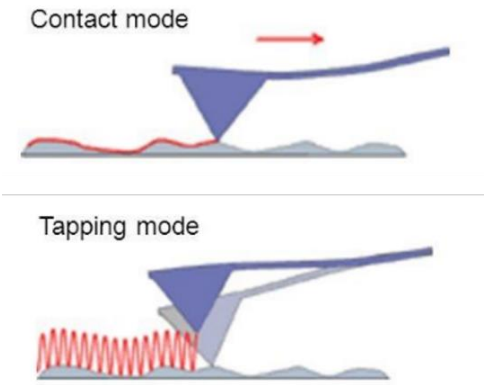

Figure 3. 10: Common AFM modes. Taken from[273].

3.3.3 Electron microscopy techniques

The use of electron microscopy is a widely used technique to obtain high-resolution images of samples surface morphology. It uses a short-wavelength beam of electrons (in the order of 10^{-12} m) that can produce magnified and higher resolution images of objects than that of an optical microscope that is operating in the visible light ($4x10^{-7}$ to $7x10^{-7}$ m).

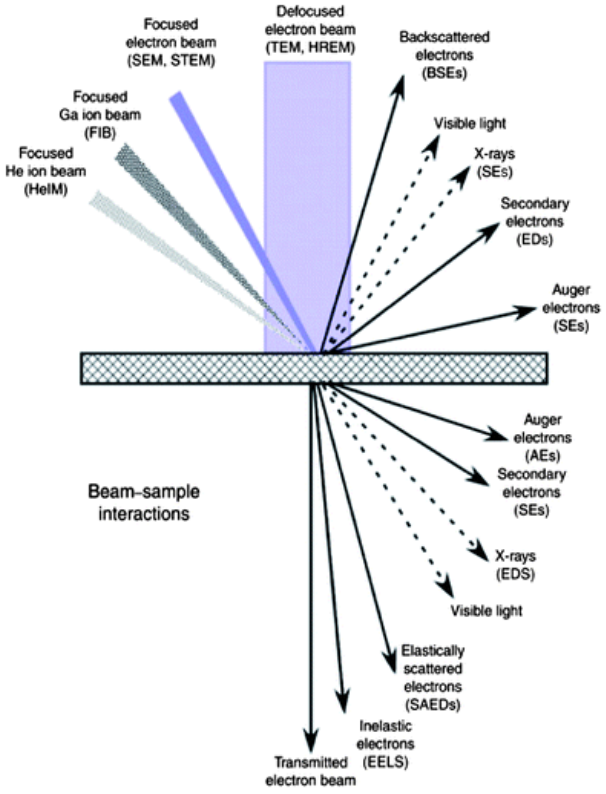

Figure 3. 11: Schematic representation of the interactions of an electron beam with a sample. Taken from[274].

When the surface of a sample is irradiated by a high energy electron beam, several types of signals are produced such as backscattered electrons, secondary electrons, Auger electrons, X-rays, elastically and inelastically scattered electrons, as illustrated in **Figure 3. 11**. Electrons emitted by the examined sample are detected, amplified and their signal is accordingly used to produce digital micrographs[275].

There are different types of electron microscopes used to image and characterise materials. In this thesis, scanning (SEM) and transmission (TEM) electron microscopy were utilised in conjunction with energy dispersive x-ray spectroscopy (EDX). In both techniques, SEM and TEM, electrons are emitted by an electron gun and accelerated through a high potential

difference of about 20 kV under high vacuum. To focus the produced electron beam onto the samples a system of condenser and objective lenses, sets of electromagnetic coils and apertures is used, located inside the electron gun column. Typically, the resolution of conventional SEMs is relatively limited, in the order of about 5 to 10 nm, while the TEM resolution can reach a higher precision of 0.1 nm where individual atoms can be distinguished.

3.3.3.1 Transmission electron microscopy (TEM)

In TEM the electron beam is focused and partially transmitted through a thin specimen. Those electrons that are elastically scattered by the sample will be accordingly focalized, magnified by other lenses and detected by a sensor (fluorescent screen, camera sensors etc).

Two basic operations are available on TEM: imaging and diffraction mode. In imaging mode, the microscopist inserts an objective aperture in the focal plane of objective lens allowing only the detection of electrons passing through the sample without being scattered. This way, the characteristic bright field (BF) image of TEM is obtained.

In diffraction mode, a selected-area aperture is inserted into the focal plane of the objective lens and the direct (unscattered) electron beam is blocked allowing only passing the diffracted beams. The use of intermediate lens is allowing to focus on the diffraction patterns formed in the focal plane of the objective lens and magnifying the initial image as the dark field (DF) image of TEM is formed.

In this thesis, Transmission Electron Microscopy (TEM) and Energy Dispersive X-ray spectroscopy (EDX) were used to measure the elemental composition of BTFM-CTO bulk samples. TEM investigations were performed by Dr. Marco Zanella with an aberration corrected JEOL 2100 equipped with a windowless EDAX detector.

3.3.3.2 Scanning electron microscopy (SEM)

In contrast to TEM where electrons of the primary beam are detected as they are passing through the specimen, SEM is detecting x-rays and secondary electrons that are emitted from samples surface due to excitations caused by the primary electron beam.

SEM can provide large area images of the samples when the beam is scanned across the specimen surface and emitted secondary electrons are detected with the use of special detectors.

Prior to the SEM measurement the samples are coated (typically with gold or carbon) to avoid charging artefacts.

In addition, the detection of x-rays emitted from the examined specimen, characteristic for each element present in the sample, can be used in qualitative and quantitative analysis of sample composition in conjunction with energy dispersive x-ray spectroscopy. SEM investigations were performed by Dr. Marco Zanella.

3.3.3.3 Energy dispersive x-rays

Energy dispersive x-ray spectroscopy is an analytical technique that can be used in conjunction with TEM or SEM. EDX is based on the characteristic x-ray excitation of elements present on the sample when an electron beam is irradiated onto the specimen. The unique atomic structure (atomic number) of each chemical element is producing a characteristic electromagnetic emission spectrum allowing this way the identification of sample elements.

In addition to the qualitative analysis, the elemental composition of the samples can also be provided by EDX. Since the intensity of the emitted x-rays is related to the volume of the elements, a quantitative assessment of sample composition can be obtained after measuring the line intensities of each element. The accurate measurement of samples composition is also requiring the calibration of the technique with the use of standards of known composition.

3.3.3.4 Raman spectroscopy

Raman spectroscopy is a common spectroscopic technique for studying the structural fingerprint of compounds by observing the vibrational, rotational, and other low-frequency modes of them.

The Raman effect arises from the inelastic interactions of a monochromatic light with molecular vibrations, phonons or other excitations of a system. These interactions can be monitored spectroscopically by shifts in the energy of the monochromatic light and information about the vibrational modes and the chemical bonding of the system can be obtained.

The Raman spectra were recorded using 514.5 nm radiation illuminating a 500 μm diameter using collection times of 20 x 10 s on a JY LabRam-HR spectrometer which was operated in a backscattered geometry by Dr. Marco Zanella.

3.4 Optical properties

The band gap of $SrZnO_2$ and the effect of lithium incorporation on the optical properties of the parent material were investigated by UV-visible absorption spectroscopy based on the theoretical considerations presented earlier in **section 1.3.2**.

UV-visible spectroscopy measurements of $SrZn_{1-x}Li_xO_2$ bulk samples were performed over a 200-800 nm range on a Shimadzu UV-2550 spectrometer with a data point distance of 0.5 nm and an integration time of 2 s. Data were collected in reflectance mode with a scan speed of 0.2 points/nm and slit width of 5 nm.

The optical gaps of $SrZn_{1-x}Li_xO_2$ samples were determined by the linear extrapolation of $(\alpha h\nu)^2$ plots against the energy for a direct transition (Tauc plots). The absorption coefficient was derived by the collected diffuse reflectance spectra of the samples using the Kubelka-Munk $F(R_a)$ function according to the relation:

$$F(R_a) = \frac{\alpha}{s} = \frac{(1-R_a)^2}{2R_a} \quad \textbf{(Eq. 3. 6)}$$

where α is the absorption coefficient, s is the scattering coefficient, and R_a is the energy dependent diffuse reflectance.

3.5 Electrochemical characterization

The temperature and oxygen partial pressure dependence of resistivity of bulk $SrZn_{1-x}Li_xO_2$ samples was studied by two methods: (a) alternative current two-probe impedance spectroscopy and (b) direct current four-probe conductivity measurements and (c) Seebeck coefficient measurements.

3.5.1 Four probe DC conductivity

The resistance, R, of a material is describing its ability to oppose the flow of electric current and, according to Ohm's law, is defined as the voltage across it divided by the current passing through the sample:

$$R = \frac{V}{I} \quad \textbf{(Eq. 3. 7)}$$

where V is the voltage across the studied material and I the current passing through it.

The electrical resistivity is a fundamental property of the material that is independent of its size or geometry. It is defined by:

$$\rho = R \times \frac{A}{l} \quad \textbf{(Eq. 3. 8)}$$

where R (Ω) is the measured resistance, A (m^2) is the area and l (m) the length of the sample.

In addition, the electrical conductivity (σ) of a material is defined as the inverse of the electrical resistivity (ρ):

$$\sigma = \frac{1}{\rho} \quad \textbf{(Eq. 3. 9)}$$

The change in the DC resistivity of a rectangular-shaped specimen can be measured by the four-probe method. Under this configuration, a dc pulse is applied on the two outer probes of the specimen while the voltage drops across the specimen is measured with voltmeter on the two inner probes.

3.5.2 AC impedance spectroscopy

A more precise and accurate way of measuring the resistivity of a material can be obtained through AC impedance measurements.

In contrast to the DC conductivity, the electrochemical impedance is a frequency dependent measurement of resistance on a sample subjected to a sinusoidal waveform excitation (applied voltage):

$$V(t) = Vo\ \sin(\omega t) \quad \textbf{(Eq. 3. 10)}$$

$$I(t) = Io\ \sin(\omega t + \theta) \quad \textbf{(Eq. 3. 11)}$$

Where $V(t)$ and $I(t)$ are respectively the voltage and current at time t and Vo, Io are the amplitude of the waves and θ the phase difference between them.

According to Ohm's Law, the impedance can once again be defined as the ratio of voltage over current passing through the examined specimen:

$$Z(\omega) = \frac{V(t)}{I(t)} = \frac{V_o \sin(\omega t)}{I_o \sin(\omega t+\theta)} = Z_o \frac{\sin(\omega t)}{\sin(\omega t+\theta)} \quad \textbf{(Eq. 3. 12)}$$

where, Z(ω) impedance amplitude and θ the phase angle.

Therefore, the impedance can be expressed as a complex number with a real and imaginary part:

$$Z(\omega) = |Z_m|e^{(-j\theta)} = |Z_m|\cos(\theta) + j|Z_m|\sin(\theta) = Z' + jZ'' \quad \textbf{(Eq. 3. 13)}$$

where $|Z_m| = \sqrt{(Z')^2 + (Z'')^2}$ is the impedance magnitude and $\theta = tan^{-1}(\frac{Z''}{Z'})$ is the phase angle of the complex number.

The advantage of the AC impedance spectroscopy is the precise and accurate measurement of material resistivity under very small voltage excitation amplitudes (typically bellow 10 mV), where DC measurements are more likely to subject potential control distortions.

Moreover, the AC impedance spectroscopy is capable of distinguishing different contributions of material resistivity (bulk, grain boundaries and electrode contributions) upon different regions of frequencies and characteristic relaxation times.

Based on the electrochemical impedance theory, a number of simple electrical circuits can be described by expressions of impedance such as:

Ohmic resistor: $Z(\omega) = R + \text{j}0$ **(Eq. 3. 14)**

Capacitor: $Z(\omega) = 0 + \frac{1}{\text{j}\omega C}$ **(Eq. 3. 15)**

Inductor: $Z(\omega) = 0 + \text{j}\,\omega\, L$ **(Eq. 3. 16)**

More complicated electrochemical processes which deviate from an ideal electrical element, can be described by a constant phase element (CPE):

$$Z(\omega) = 0 + \frac{A}{(\text{j}\omega)^n} \quad \textbf{(Eq. 3. 17)}$$

where A and n are constants.

The **(Eq. 3.17)** can be reduced to any of the basic electrical elements such as an ohmic resistor when *n*=0 and *A*=R, a capacitor when *n*=1 and *A*=1/C, and an inductor when *n*=-1 and *A*=L.

According to those considerations, the frequency-dependent impedance spectrum of an electrochemical system can be expressed as the sum of basic electrical elements in parallel or series connections. The assignment of these model elements to real physical processes allows the analysis of the conductivity mechanism of these electrochemical systems.

This way, the impedance response of a ceramic sample can be assigned to different R and C contributions of a given time constant ($\tau = RC$) related to the distinct relaxation time (relaxation frequencies) of various physical phenomena[276, 277]:

$$R_{total} = R_{bulk} + R_{grain\ boundary} + R_{electrode} \quad \textbf{(Eq. 3. 18)}$$

and can be depicted on a Nyquist plot as illustrated in **Figure 3. 12**.

Table 3.1: Capacitance values and their physical interpretation.

Capacitance (F)	Phenomenon Responsible
10^{-12}	Bulk
10^{-11} – 10^{-8}	Grain Boundary
10^{-7} – 10^{-5}	Sample – electrode interface
10^{-4}	Electrochemical reactions

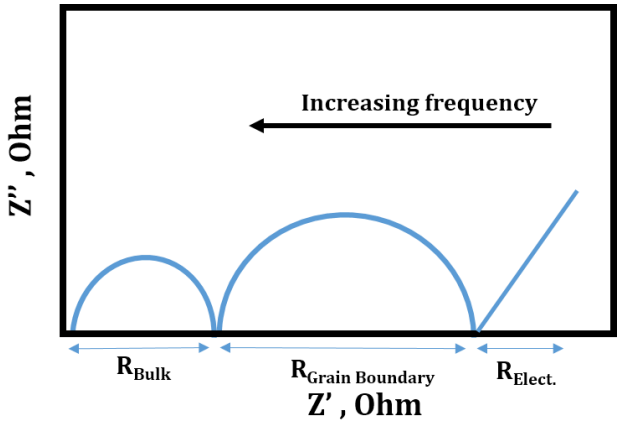

Figure 3. 12: Nyquist diagram for the impedance measurements of a bulk sample.

3.5.3 Seebeck coefficient measurements

The measurement of the Seebeck coefficient is a direct way of identifying the carrier type (electrons or holes) of a semiconductor. The principle of the measurement is based on the Thomson effect according to which, when a current is passed through a heated conductor, an electromotive force (EMF) will induced to the conductor.

In line with these observations, T.J. Seebeck discovered in 1821 that when two different conductors are placed in contact and under a temperature gradient, an electromotive force (EMF) will appear as a consequence of an accumulation of excess carriers at the colder end[278]. With the carriers (electrons or holes) on the hotter end of the junction possessing a higher thermal energy compared with that of colder carriers, a higher proportion of excess carriers will be diffused from the hotter to the colder end, resulting to the generation of a potential difference across the junction.

The Seebeck coefficient (S) is accordingly defined as:

$$S = -\Delta V / \Delta T \qquad \textbf{(Eq. 3. 19)}$$

where ΔV is the change in voltage across the sample resulting from a temperature difference of ΔT. Therefore, a p-type material will demonstrate a positive Seebeck coefficient, while an n-type material exhibits a negative Seebeck coefficient.

During this thesis, impedance measurements were performed using a high-temperature measurement cell (NorECs AS ProbostatTM, Oslo, Norway) as illustrated in **Figure 3. 13**. Measurements were conducted from 550 to 600 °C under a pure oxygen atmosphere, using Pt paste electrodes. A temperature gradient was applied across the sample and the change in voltage was measured.

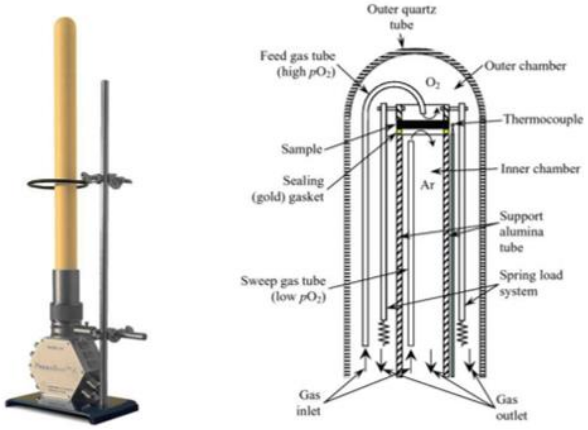

Figure 3. 13: ProboStat^{TM} cell and schematic diagram of the device geometry. Taken from www.norecs.com.

3.6 Dielectric measurements

The dielectric constant and dielectric losses of the examined BTFM-CTO films were studied with the use of an Agilent E4980 Precision LCR meter connected to a PC through a GPIB plug and controlled by LabView software.

The dielectric measurements were performed in an out-of-plane capacitor geometry using a buffer $SrRuO_3$ (SRO) layer as bottom film electrode while Pt electrodes of 240 μm diameter were sputtered on the surface of the films through a shadow metal mask to form the metal-insulator-metal (MIM) capacitor structure of **Figure 3. 14**.

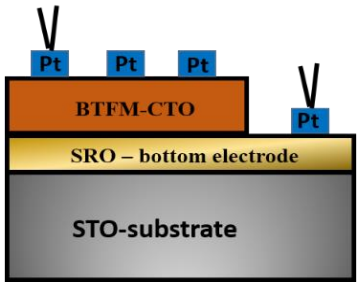

Figure 3. 14: Capacitor cell geometries used for the dielectric measurements.

Under this configuration, an AC bias of 200 mV was applied in the frequency range of 20 Hz to 2 MHz and the dielectric constant was evaluated from the formula:

$$\varepsilon_r' = \frac{C_p\, d}{\varepsilon_o\, S} \qquad \textbf{(Eq. 3. 20)}$$

where *Cp* is the capacitance (F) values recorded during the measurement, ε_o is the free space permittivity value (8.859×10^{-12} Fm^{-1}), *S* is the point electrode area (m^2), and *d* is the thickness (m) of the films.

The complex dielectric permittivity of a material under an AC electric field is being defined, in the most general case, by the form:

$$\varepsilon_r^{\,*} = \varepsilon_r' - j\,\varepsilon_r'' \qquad \textbf{(Eq. 3. 21)}$$

where the real ε_r' and imaginary ε_r'' parts of the dielectric permittivity represent, respectively, the reversibly stored and the loss energy of the field in the material.

While at low frequencies the polarisation within the dielectric medium oscillates in phase with the alternating field, at high frequencies the rate of dielectric relaxation is becoming much

slower and, as a consequence, the induced by the polarization current lags behind the applied voltage by a phase angle δ and the dissipated energy (heat) of the dielectric medium is known as dielectric loss and is defined as the relative magnitude of $\varepsilon_r{}''$ with respect to $\varepsilon_r{}'$:

$$tan\delta = \frac{\varepsilon_r{}''}{\varepsilon_r{}'} \quad \textbf{(Eq. 3. 22)}$$

The quantity tanδ is directly calculated by LabVIEW software.

3.7 Ferroelectric measurements

The ferroelectric properties of the BTFM-CTO films were examined with the use of an experimental set-up consisted of a commercial aixPES workstation (aixACCT Systems GmbH, Germany), a probe station equipped with an optical microscope, pole pieces and micro-manipulators.

To measure the ferroelectric properties of BTFM-CTO films, a Sawyer-Tower circuit is utilized which is consisted of a signal generator (E), a reference capacitor (C_o) connected in series with the capacitor (C_x) of the measured ferroelectric sample and an oscilloscope controlled by a LabVIEW equipped PC, as can be seen in **Figure 3. 15**.

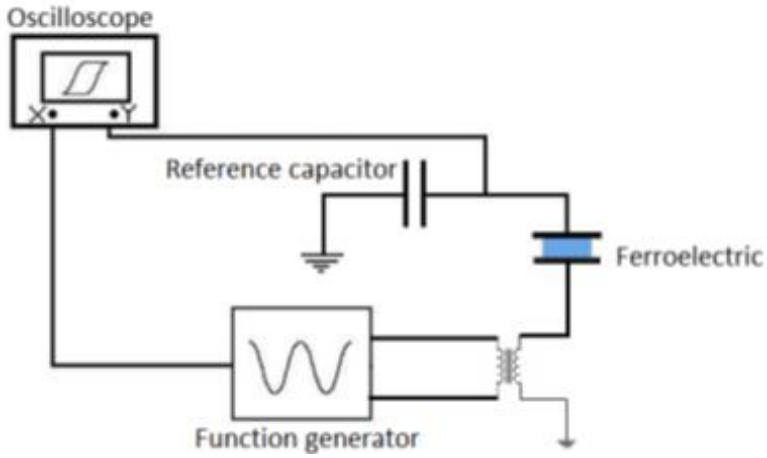

Figure 3. 15: (a) Block diagram of the Sawyer-Tower circuit used for ferroelectric measurements of the BTFM-CTO films. Taken from[279].

The signal generator E supplies an alternating electrical current in the circuit and charging the connected electronic devices. Since the reference (C_o) and sample (C_x) capacitors are connected in series they will, in effect, contain the same amount of charge:

$$Q_o = Q_x \qquad \textbf{(Eq. 3. 23)}$$

With the capacitance of the reference capacitor (C_o) being substantial bigger than that of the measured ferroelectric film (C_x), the voltage across the film sample (U_x) will be by far larger than that of reference capacitor (U_o) and approximately equal to the voltage of the signal generator E.

At the same time, the polarization signal P of the ferroelectric film is found to be proportional to its charge and, given the charge balance of the two capacitors in the Sawyer-Tower circuit, proportional to the voltage of the reference capacitor (U_x), according to:

$$P = Q_x / A = Q_o / A = C_o U_o / A \quad \textbf{(Eq. 3. 24)}$$

where Q_x and Q_o are the charges across the film sample and reference capacitor and A the area of sample electrodes.

Under this configuration, the ferroelectric hysteresis loop of BTFM-CTO films were monitored on the oscilloscope with the voltage of the sample capacitor (U_o) served as the x-channel and the voltage of the reference capacitor (U_x) as the y-channel.

3.8 Magnetic measurements

Using the Josephson junction in superconductive circuits, a superconducting quantum interference device (SQUID) can even measure the very weak magnetic signals of small samples -laying in the order of one thousandth of a flux quantum (flux quantum is 2.07×10^{-7} Gcm^2)[280].

A schematic illustration of the basic principles of a SQUID magnetometer and the Josephson junction is presented in **Figure 3. 16**. The Josephson junction is built out of two superconductors arranged in a tunnel configuration that are separated by a thin barrier layer as depicted in **Figure 3. 16a**. Once the junction is connected to a superconducting circuit, its output voltage will become sensitive to the motion of a magnetic sample placed inside the superconducting coil according to the electromagnetic induction principle. A small displacement in the position of the measured magnetic sample inside the superconducting coil will change the magnetic flux passing through the coil and it will generate a voltage and an induced current across the superconducting coil.

With the Josephson junction being connected to the superconducting coil, this change of current density will ultimately be detected as an amplitude fluctuation of voltage across the junction proportional to the detected magnetic signal, as shown in **Figure 3. 16b**.

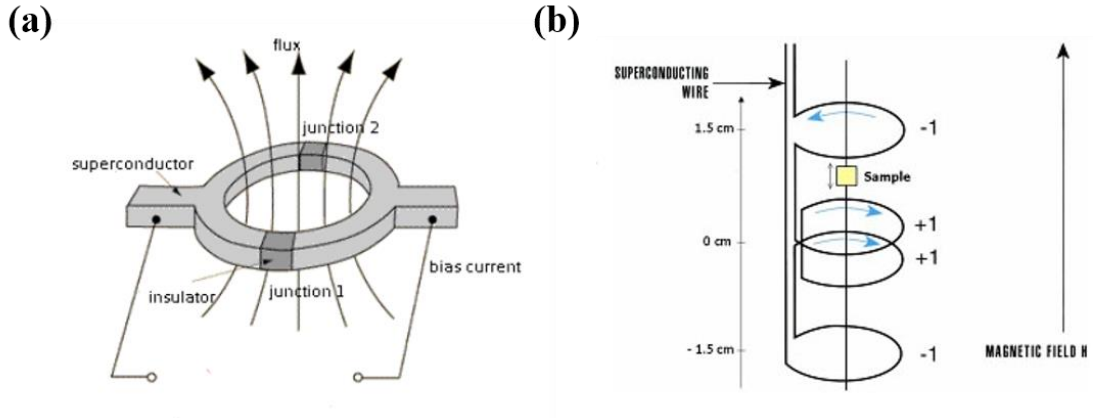

Figure 3. 16: Schematic illustration of: (a) Josephson junction (taken from[281]) and (b) and the basic principle of SQUID magnetometer (taken from[282]).

In addition, when a magnetic property measurement system (MPMS) is integrated into a SQUID a variety of other magnetic properties, such as the Curie temperature, saturated magnetization and susceptibility can also be measured under variable temperatures and magnetic fields. In order to control the temperature of the measurements the MPMS is also equipped with a heater and a liquid helium cooling system while a superconducting shield is placed inside the magnet to protect the SQUID detector and stabilize the ambient laboratory magnetic field[280].

In this thesis, the magnetic properties of BTFM-CTO films deposited on STO substrates were measured with the use of commercial superconducting quantum interference devices (SQUID, MPMS XL-7 and MPMS3 of Quantum Design, USA) at a temperature range of 2–800 K and a magnetic field range of -7.0 to 7.0 T. The measurements were performed by Dr. Hongjun Niu.

References

[257] R. Tilley, *Understanding Solids: The Science of Materials*, John Wiley & Sons, 2005

[258] A.R. West, *Basic solid-state chemistry*, Wiley, 1999

[259] R. Eason, *Pulsed Laser Deposition of Thin Films*, Wiley, 2006

[260] R. Eason, *Pulsed Laser Deposition of Thin Films*, John Wiley & Sons, 2007

[261] J. Schou, *Appl. Surf. Sci*. **255**, 2009, 5191

[262] A. P. Singulani, *Advanced Methods for Mechanical Analysis and Simulation of Through Silicon Vias*, PhD thesis, TU Wien, at: http://www.iue.tuwien.ac.at/phd/singulani/

[263] L.W. Martin, Y. Chu, R. Ramesh, *Mater. Sci. Eng*. **R68**, 2010, 89

[264] E. Coy, *Growth and characterization of new multiferroic materials*, PhD thesis, Universität de Barcelona, 2015, at: https://dialnet.unirioja.es/servlet/tesis?codigo=128136

[265] P.R. Willmott, J.R Huber, *Rev. Mod. Phys*. **72**, 2000, 315

[266] University of Cambridge, *X-ray Diffraction Techniques*, 2004, at: https://www.doitpoms.ac.uk/tlplib/xray-diffraction/printall.php

[267] M. Birkholz, *Thin Film Analysis by X-Ray Scattering*, Wiley-VCH, 2006

[268] J. Als-Nielsen, D. McMorrow, *Elements of Modern X-Ray Physics*, John Wiley & Sons, 2011

[269] M. Yasaka, *The Rigaku Journal* **26**, 2010, 1

[270] A. Vailionis, *Thin Film Scattering: Epitaxial Layers*, *5th Annual SSRL Workshop*, 2010, at: http://www-ssrl.slac.stanford.edu/conferences/workshops/sxst2014/documents/

[271] A.D. Rolle, *Intro to X-ray Pole Figures*, 2016, at: http://pajarito.materials.cmu.edu/rollett/27750/L4-Xray_PFs-26Jan16.pdf

[272] P. Jeffrey, *X-ray Data Collection Course*, 2006, at: http://xray0.princeton.edu/~phil/Facility/Guides/XrayDataCollection.html

[273] M. Manning. *Atomic Force Microscopy Lecture 7*, at: http://slideplayer.com/slide/9702681

[274] J. Wu, C. Shaw, D.C. Martin, *Polym. Sci.* 2, 509, 2012

[275] J. Kuo (ed.), *Electron Microscopy: Methods and Protocols*, Springer, 2014

[276] J.R. MacDonald (ed.), *Impedance Spectroscopy: Emphasising solid materials and systems*, John Wiley & Sons, 1987

[277] K. Huang, J.B. Goodenough, *Solid oxide fuel cell technology - principles, performance and operation*, Woodhead Publishing Limited, 2009

[278] A. R. West, *Solid State Chemistry and its Applications*, Wiley, 2007

[279] NSF Nanosystems Engineering Research Center for Translational Applications of Nanoscale Multiferroic Systems (TANMS), *Piezoelectric Characterization*, at: http://mentors.tanms-erc.org/mentor-responsibilities/piezoelectric-characterization

[280] M. Mcelfresh, *Fundamentals of Magnetism and Magnetic Measurements*, Purdue University, Quantum Design, USA, 1994

[281] C. Beck, *Physica C* **473**, 2012, 21

[282] Walther-Meißner-Institute, *SQUID Magnetometry*, 2012, at: https://www.wmi.badw.de/methods/squid.htm

Chapter 4: *P*-type doping of $SrZnO_2$

The synthesis and the chemical stability of $SrZnO_2$ is examined in **section 4.1**. Different dopants were explored by (i) the conventional solid-state route and (ii) strictly anaerobic conditions in **section 4.2**. Our motivation was to identify suitable *p*-type doping candidates while retaining the transparency of the parent material.

The incorporation of Li into $SrZnO_2$ was obtained through the conventional solid-state route only when the volatility of lithium was suppressed with the use of sacrificial powder of the same composition, in **section 4.2.1.3**. PXRD and ICP studies have been employed to investigate the structural properties of an exploratory and a following measurement series of doped $SrZn_{1-x}Li_xO_2$ samples confirming the reproducibility of highly crystalline $SrZn_{1-x}Li_xO_2$ materials.

The *p*-type doping of $SrZn_{1-x}Li_xO_2$ was initially examined under variable-pO_2 conditions by means of AC impedance and DC conductivity measurements on samples of different geometries (disc- and rectangular-shaped) and lithium content, in **sections 4.3.1** and **4.3.2**. Conductivity measurements over a period of 40 days confirmed the long-term stability of *p*-type doping in $SrZn_{1-x}Li_xO_2$. Furthermore, thermopower measurements, in **section 4.3.3**, validated the hole type charge carriers of $SrZn_{1-x}Li_xO_2$. Optical measurements made on the examined samples are presented in **section 4.4**. Attempts finally to grow $SrZnO_2$ films by PLD are summarized in **section 4.5.**

4.1 Synthesis of $SrZnO_2$

4.1.1 Synthesis of $SrZnO_2$ by conventional solid-state route

For the synthesis of $SrZnO_2$, stoichiometric quantities of $SrCO_3$ (99.99%) and ZnO (99.99%) were mixed, hand-ground dry with a mortar and pestle and isostatically pressed into 10 mm diameter pellets for 15 minutes at 2,000 bar and heated in an Pt-lined alumina boat at 1090 °C for 6 hours under an oxygen flow of 10 ml/min. The heating and cooling rate during the sintering process was 5 °C/min, and the whole procedure of grinding, pelletizing and firing was repeated a total of two times.

$$SrCO_3 + ZnO \rightarrow SrZnO_2 \qquad \textbf{(Eq. 4. 1)}$$

Figure 4. 1 shows the Pawley refinements of PXRD data from a single-phase $SrZnO_2$ sample collected on a two circle Panalytical X'Pert Pro diffractometer with a monochromated Co $K_{\alpha 1}$ source (λ = 1.78896 Å).

Although the synthesis temperature was close to the melting point of $SrZnO_2$ (1250 °C), the density of the as-received pellets through this route was relatively low, in the range of 70 ~ 75% of the theoretical value.

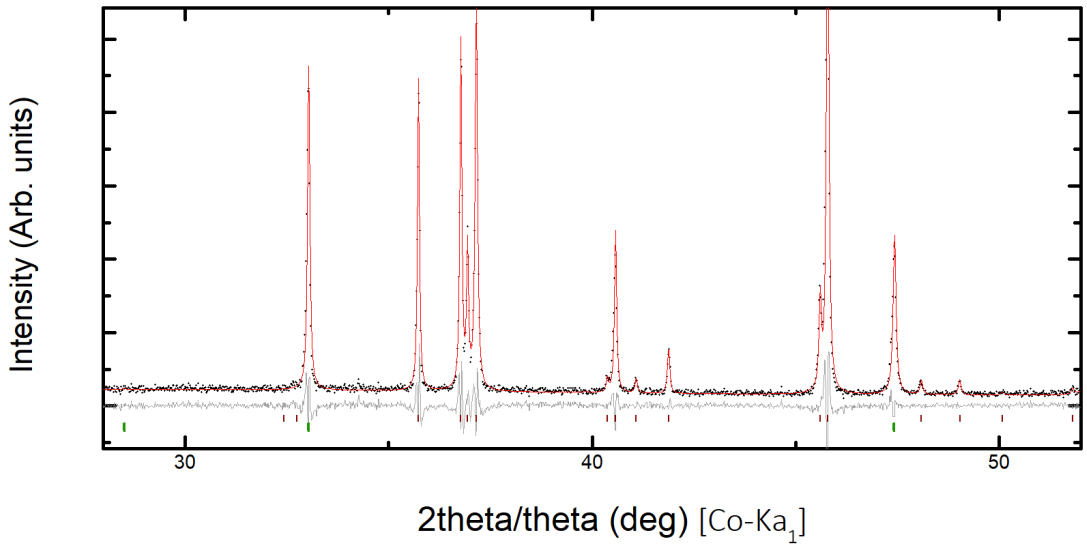

Figure 4. 1: Pawley refinements, in space group *Pnma*, to PXRD data of $SrZnO_2$ synthesised by conventional solid state route after three subsequent firings.

4.1.2 Chemical instability of $SrZnO_2$ in ambient atmosphere

The chemical stability of $SrZnO_2$ was in the first place investigated when extra $SrCO_3$ and ZnO reflections were observed on an originally single-phase powder sample that was exposed to ambient atmosphere for 48 hours (scans -a and -b, respectively, in **Figure 4. 2)**. In contrast, when the synthesised single-phase $SrZnO_2$ was stored in a dry air at room temperature did not show any sign of decomposition over a period of three months (scan -c in **Figure 4. 2**).

Lastly, extra ZnO reflections were also detected when an originally single-phase $SrZnO_2$ sample was re-fired (for a fourth time) in static ambient atmosphere (scan -d in **Figure 4. 2**) an indication of the slow $SrZnO_2$ decomposition to ZnO and (amorphous) $SrCO_3$ during the cooling step under ambient conditions.

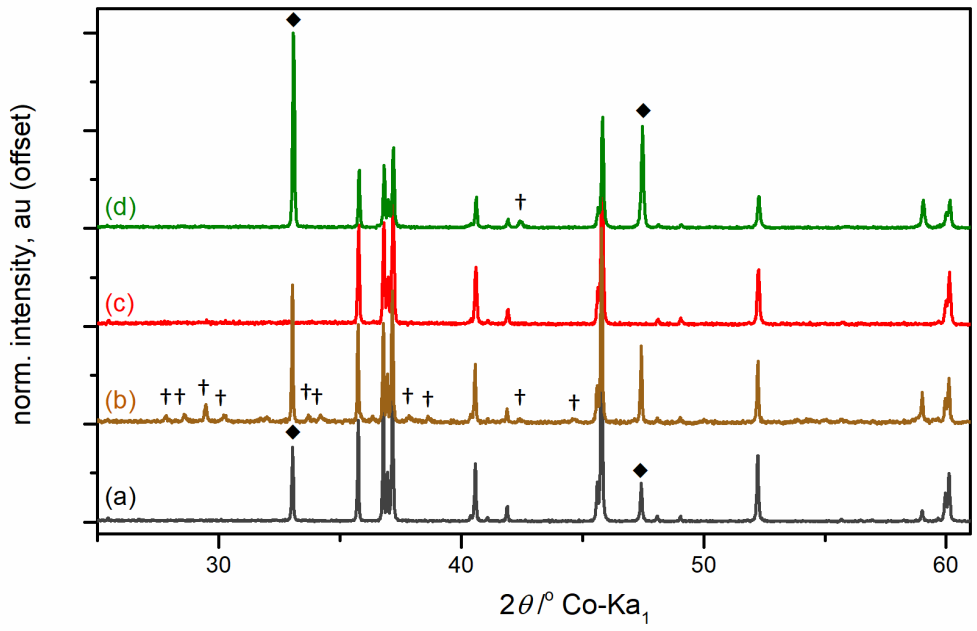

Figure 4. 2: Chemical instability of $SrZnO_2$ under different conditions. (a) PXRD of an as-received single-phase $SrZnO_2$ powder sample (scan-a) sintered under a 10 ml/min flow of oxygen followed by repeated PXRD scans (of the originally single-phase sample) after being: (b) exposed in ambient atmosphere for 48 hours, (c) stored in in dry conditions under ambient atmosphere for three months and (d) re-fired under static atmosphere. Reflections denoted with the symbol (◆) correspond to KCl, used as internal standard, and (†) to the reagents ($SrCO_3$, ZnO).

4.1.3 Ball milling $SrZnO_2$ reagents

With the obtained density of hand-grinding $SrZnO_2$ pellets approaching only the 70 ~ 75% of the theoretical value, we also tried the synthesis of denser pellets by mechanically grinding the precursors in a planetary ball mill (Pulverisette, Fritch).

To study the effect of ball milling, a single-phase $SrZnO_2$ powder sample (batch-a of **Figure 4. 3**) was initially synthesised following the sintering protocol of **section 4.1.1** and accordingly was *separated* into four *samples which were subjected to different grinding treatments* before a final sintering step:

- Sample-b was ball-milled in ethanol for 24 hours in ZrO_2 pots using 10 mm ZrO_2 balls at 350 rpm. Once the wet ball milling was completed the samples were left to dry in air under stirring at 70 °C and then were placed overnight in the oven at 140 ºC.
- Sample-c was ball-milled in isopropanol under the same grinding protocol as sample-b.
- Sample-d was subjected to dry ball milling (as before: for 24 hours using 10 mm ZrO_2 balls) and
- Sample-e was only hand-ground dry.

After grinding, all the samples were separately ground, uniaxially pressed into pellets and placed closely together in a Pt-lined alumina boat before being fired, for a fourth time, at 1090 °C for 6 hours in a 10 ml/min flow of oxygen and a heating/cooling rate of 5 °C/min.

As it can be seen in **Figure 4. 3**, the PXRD pattern of the samples subjected to dry or wet ball milling (samples -b, -c, -d) were not found to be single-phase while volume deformities (air voids and notches) deteriorate the density of the ceramics. Among the examined samples, only the dry hand-ground $SrZnO_2$ sample was found to remain single-phase after the last (forth) firing step.

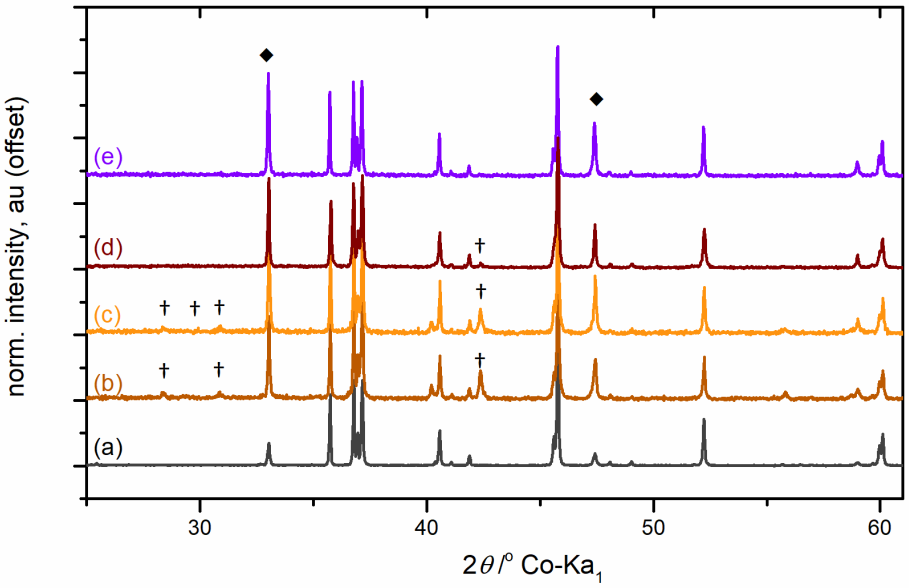

Figure 4. 3: Effect of ball milling on synthesis of a single-phase $SrZnO_2$: (a) PXRD of an as-synthesised single-phase $SrZnO_2$ powder sample after 3 subsequent firings with intermediate, solvent-free, hand grinding steps under oxygen flow. (b-e) Resulting PXRD of $SrZnO_2$ samples subjected to different grinding treatment before a last (4^{th}) firing step: (b) wet ball-milled in ethanol; (c) wet ball-milled in isopropanol; (d) in dry ball-milled; (e) solvent-free, hand grinding step. Symbol (◆) corresponds to reflections of the used internal standard KCl and (†) to reflections of reagents ($SrCO_3$, ZnO).

Finally, a similar experiment was addressed, in **Figure 4. 4**, to examine the effect of solvents as grinding agents. A single-phase $SrZnO_2$ powder batch was originally synthesised after 3 firings according to the protocol of **section 4.1.1** and then separated into two samples. The first sample was hand-ground dry and ethanol was used as a grinding agent for the second sample before the samples fired together for a fourth time under oxygen flow. Once more, the emergence of ZnO impurities in the collected PXRD data of the solvent-ground samples demonstrated the detrimental role of the resulting liquid phases towards a single phase SrZnO2, possibly due to the formation of hydroxides.

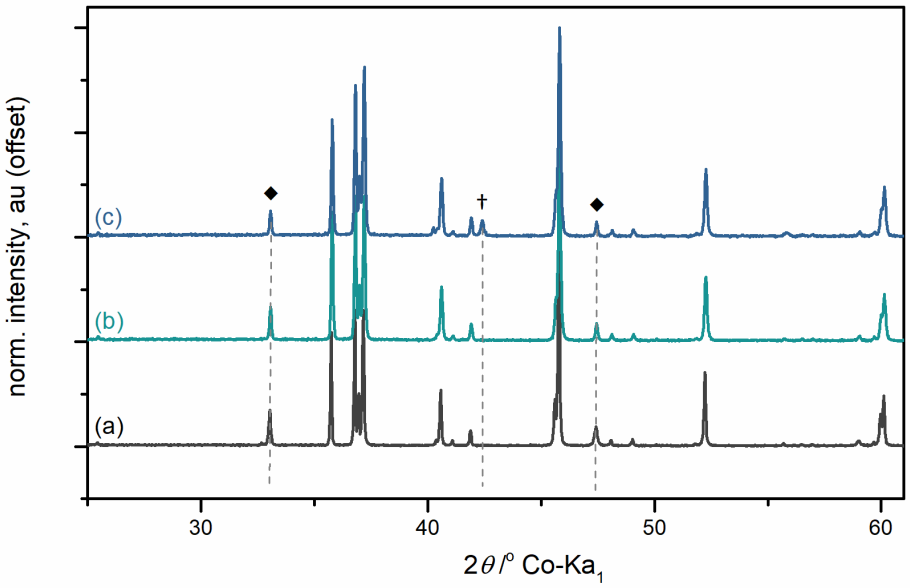

Figure 4. 4: The role of grinding agents on obtaining a single-phase $SrZnO_2$ sample. (a) PXRD of a synthesised single-phase $SrZnO_2$ batch after 3 subsequent firings of intermediate hand grinding steps under oxygen flow. Resulting samples PXRD after a last firing with: (b) an intermediate, solvent-free, hand grinding step and (c) ethanol used as hand grinding agent. Symbol (◆) corresponds to reflections of the used internal standard KCl and (†) to reflections of reagents (ZnO).

In conclusion, our work in this section have shown that a single-phase $SrZnO_2$ was synthesised following a conventional, hand-ground, solid-state route. Attempts to synthesise denser, single-phase ceramic $SrZnO_2$ samples when the reacting agents were milled (wet- or dry-milling) did not result in denser or single-phase materials. We should, however, note that the as-synthesised $SrZn_{1-x}Li_xO_2$ pellets -obtained under the same solvent free, hand-grinding treatment protocol (in **section 4.2.1.3**)- were much denser (above 90% of the theoretical value) and therefore suitable for electrical measurements.

4.2 Doping of $SrZnO_2$

4.2.1 Exploratory investigation of dopants: Ag, Na, K, Li

4.2.1.1 By conventional solid-state route without sacrificial pellets: Ag, Na

Initial attempts to synthesize $SrZn_{1-x}Ag_xO_2$ and $Sr_{1-x}Na_xZnO_2$ samples following the conventional solid-state protocol of **section 4.1.1** were not successful.

As before, samples of $SrZn_{1-x}Ag_xO_2$, ($0 < x < 0.2$, nominal molar ratio) and $Sr_{1-x}Na_xZnO_2$, ($0 < x < 0.15$, nominal molar ratio) from stoichiometric quantities of $SrCO_3$ (99.99 %), ZnO (99.99 %), $AgNO_3$ (99.99 %) and Na_2CO_3 (99.99 %), was attempted to be prepared by solid state reactions under oxygen flow, according to the reactions:

$$SrCO_3 + (1-x)\ ZnO + x\ AgNO_3 \rightarrow SrZn_{1-x}Ag_xO_2 \quad \textbf{(Eq. 4. 2)}$$

$$(1-x)\ SrCO_3 + x/2\ Na_2CO_3 + ZnO \rightarrow Sr_{1-x}Na_xZnO_2 \quad \textbf{(Eq. 4. 3)}$$

The reagents were dried overnight at 200 °C, weighed, hand-ground and heated in an Pt-lined alumina boat at 1090 °C for 6 hours under an oxygen flow of 10 ml/min. Similarly to the synthesis of $SrZnO_2$, these steps were repeated 2 times with intermediate, solvent-free, hand grinding steps.

However, the PXRD patterns of **Figure 4. 5** have shown that a single phase doped material was not accessible for either of the two systems. More specifically, in the case of $SrZn_{1-x}Ag_xO_2$, no change on the refined unit cell of the obtained samples was observed as dopant content was increased (**Figure 4. 5a**) while an extra reflection of metallic silver at 44.5° revealed the difficulty of incorporating Ag into $SrZnO_2$ (**Figure 4. 5b**). Similarly to $SrZn_{1-x}Ag_xO_2$,, no trend of a unit cell volume change was obtained for the $Sr_{1-x}Na_xZnO_2$ samples with the exception of the most Na-rich sample (**Figure 4. 5d**), while additionally their PXRD patterns (including the Na-rich sample of x=0.15) were found to contain ZnO (**Figure 4. 5c**).

In the following section (**section 4.2.1.3**), the use of Na as a potential dopant will be re-examined while attempting to suppress its volatility with the use of sacrificial pellets.

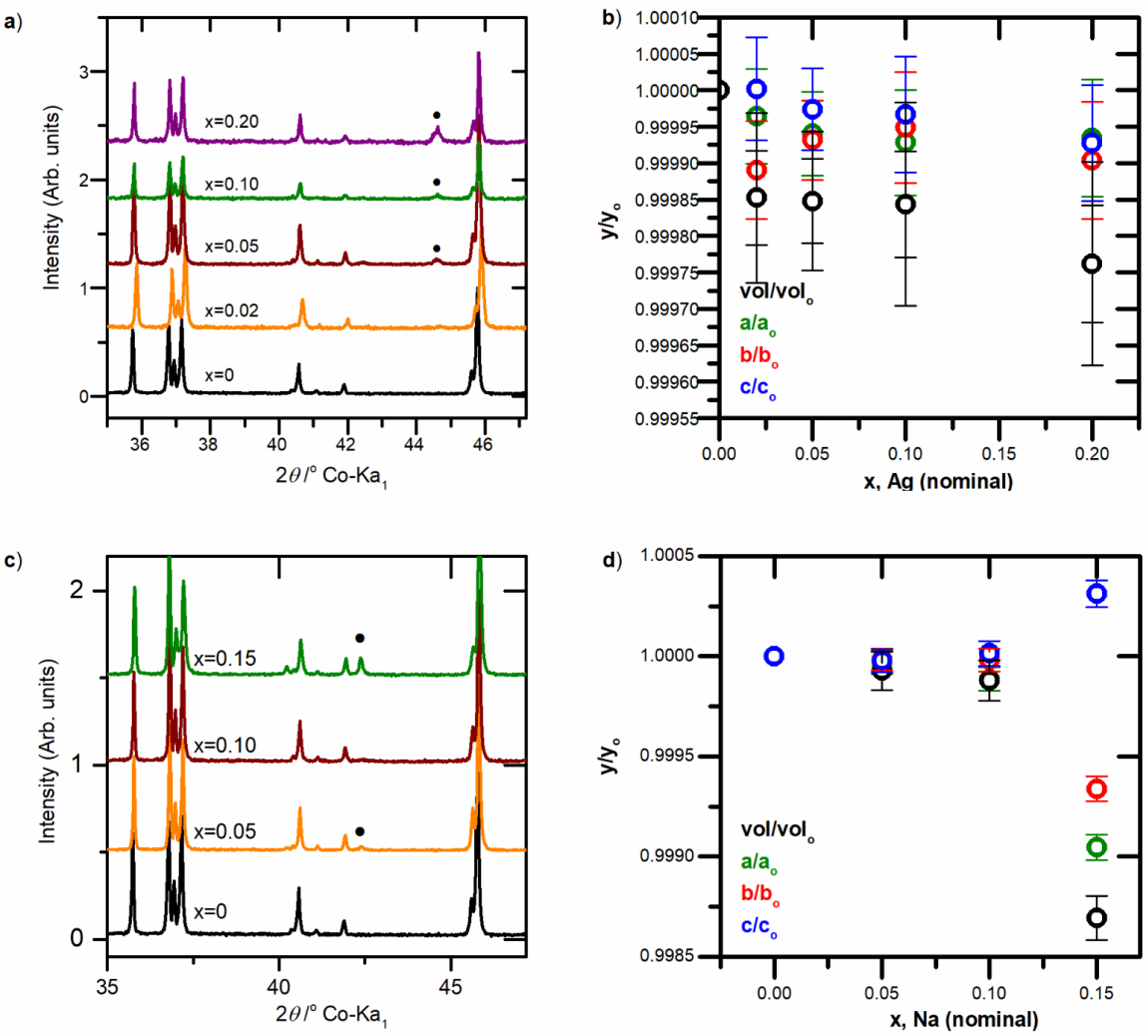

Figure 4. 5: PXRD patterns and normalized lattice parameter trends of (a, b) $SrZn_{1-x}Ag_xO_2$ and (c, d) $Sr_{1-x}Na_xZnO_2$, synthesised via conventional solid-state reactions for different nominal dopant content, *x*. The refined lattice parameters were obtained by Pawley fitting of PXRD data in space group *Pnma*, for: (b) $SrZn_{1-x}Ag_xO_2$ and (d) $Sr_{1-x}Na_xZnO_2$. KCl (space group: $Fm\bar{3}m$, a = 6.2916 Å) was used as an internal standard to determine the lattice parameters of the examined samples. Symbol (•) indicates the presence of ZnO reagent.

4.2.1.2 By anaerobic conditions of reactive reagents: K, Li

The use of highly reactive reagents (SrO, KO_2, Li_2O_2) was also investigated as an alternative route of doping $SrZnO_2$. As a first step, the synthesis of $SrZnO_2$ starting from SrO and ZnO was carried under anaerobic conditions in sealed quartz tubes according to the reaction:

$$SrO + ZnO \rightarrow SrZnO_2 \qquad \textbf{(Eq. 4. 4)}$$

Stoichiometric quantities of SrO and ZnO were mixed, hand-ground and pressed into pellets inside a helium dry box (LabMaster 130, MBraun, Garching, Germany) before being sealed under vacuum in quartz tubes at a pressure of ca. 10^{-6} Torr. Several of these quartz tubes were fired over a wide range of temperatures (500 - 850 ºC) to identify the sintering temperature of $SrZnO_2$.

Using this route, a single-phase $SrZnO_2$ was obtained at temperatures as low as 850 °C as seen in **Figure 4. 6**.

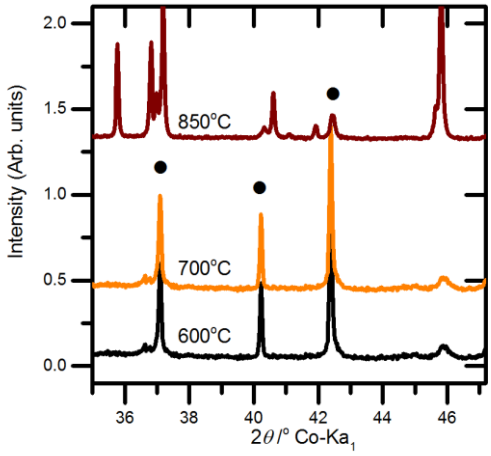

Figure 4. 6: Reaction products for the stoichiometric reaction, under strictly anaerobic conditions, of SrO and ZnO in different sintering temperatures. Symbol (●) indicates the presence of reagent ZnO.

In a following step, we attempted to synthesize $Sr_{1-x}K_xZnO_2$ and $SrZn_{1-x}Li_xO_2$ under anaerobic conditions. A number of samples made out of the same batch (nominal compositions: $Sr_{0.97}K_{0.03}ZnO_2$ and $SrZn_{0.96}Li_{0.04}O_2$), fired in a range of temperatures between 500-900 °C, in order to identify the sintering temperature of single phase doped samples. To do so, stoichiometric quantities of the starting reagents, SrO, ZnO, KO_2 and Li_2O_2 were weighted and hand-ground inside a helium filled dry box (LabMaster 130, MBraun). In each case, a number of pellet-samples were made out of these two batches ($Sr_{0.97}K_{0.03}ZnO_2$ and $SrZn_{0.96}Li_{0.04}O_2$), sealed in quartz tubes at pressure of ca. 10^{-6} Torr and fired over a range of temperatures from 500-900 °C to assess the sintering temperature of doped $SrZnO_2$, according to the reactions:

$$(1\text{-}x)\ SrO + ZnO + x\ KO_2 \rightarrow Sr_{1-x}K_xZnO_2 \qquad \textbf{(Eq. 4. 5)}$$

$$SrO + (1\text{-}x)\ ZnO + x/2\ Li_2O_2 \rightarrow SrZn_{1-x}Li_xO_2 \qquad \textbf{(Eq. 4. 6)}$$

Our results have shown that doping $SrZnO_2$ was not finally accessible by this method, neither for K nor Li. In both cases, the PXRD of the as-synthesised samples were found to contain extra impurities phases while no change was detected on the obtained cell volume of the samples, as summarised in **Figure 4. 7a,b** and **Table 4. 1**. In agreement with these findings, ICP-OES measurements on the as-synthesised samples, in **Figure 4. 8a,b**, have also revealed an increased amount of dopant losses as the firing temperature was increased.

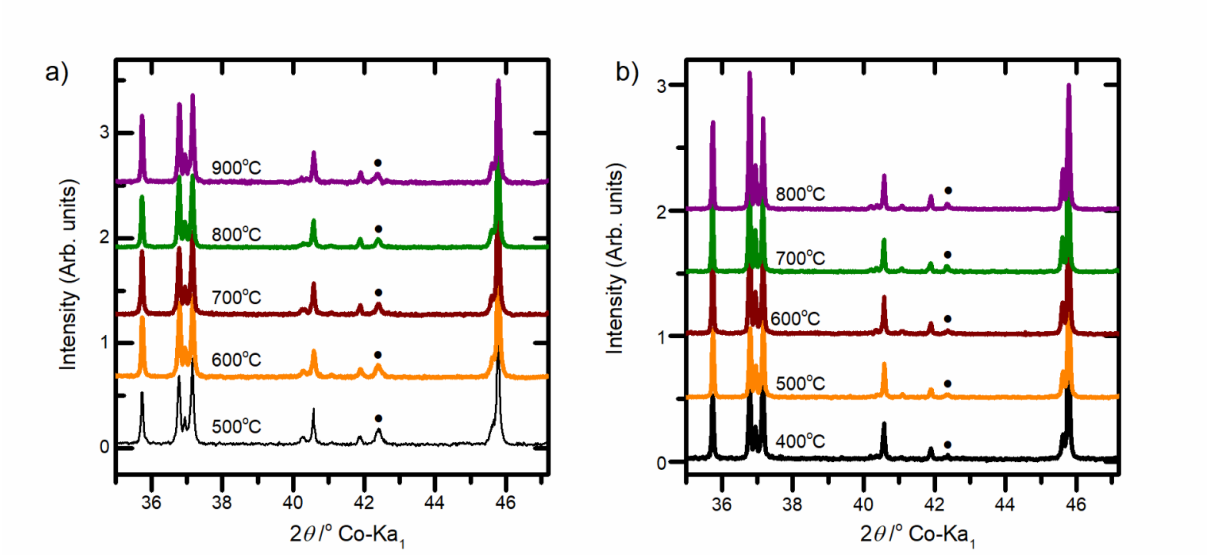

Figure 4. 7: XRD of samples obtained in attempted synthesis of (a) K:$SrZnO_2$ and (b) Li:$SrZnO_2$ under anaerobic conditions in sealed quartz tubes. Symbol (●) indicates the presence of ZnO reagent.

Table 4. 1: ICP-OES elemental analysis of as-synthesised $Sr_{1-x}K_xZnO_2$ and $SrZn_{1-x}Li_xO_2$ samples, at different temperatures, in sealed quartz tubes under anaerobic conditions.

$Sr_{1-x}K_xZnO_2$			
Sintering Temperature (°C)	**Nominal Formula**	**Experimental Formula**	**Volume Unit Cell (Å^3)**
500	$Sr_{0.97}K_{0.03}ZnO_2$	$Sr_{0.92(4)}K_{0.031(1)}ZnO_2$	220.85(3)
600	$Sr_{0.97}K_{0.03}ZnO_2$	$Sr_{0.97(2)}K_{0.025(3)}ZnO_2$	220.78(3)
700	$Sr_{0.97}K_{0.03}ZnO_2$	$Sr_{0.97(2)}K_{0.017(2)}ZnO_2$	220.81(2)
800	$Sr_{0.97}K_{0.03}ZnO_2$	$Sr_{0.97(2)}K_{0.004(3)}ZnO_2$	220.80(2)
900	$Sr_{0.97}K_{0.03}ZnO_2$	$Sr_{0.98(2)}K_{0.003(3)}ZnO_2$	220.75(2)

Table 4. 2 -Continued

$SrZn_{1-x}Li_xO_2$			
Sintering Temperature (°C)	**Nominal Formula**	**Experimental Formula**	**Volume Unit Cell (Å^3)**
400	$Sr\ Zn_{0.96}\ Li_{0.04}O_2$	$Sr\ Zn_{0.97(2)}\ Li_{0.040(1)}\ O_2$	220.78(2)
500	$Sr\ Zn_{0.96}\ Li_{0.04}O_2$	$Sr\ Zn_{0.97(2)}\ Li_{0.037(4)}\ O_2$	220.74(1)
600	$Sr\ Zn_{0.96}\ Li_{0.04}O_2$	$Sr\ Zn_{0.96(1)}\ Li_{0.032(1)}\ O_2$	220.77(2)
700	$Sr\ Zn_{0.96}\ Li_{0.04}O_2$	$Sr\ Zn_{0.98(2)}\ Li_{0.026(2)}\ O_2$	220.77(1)
800	$Sr\ Zn_{0.96}\ Li_{0.04}O_2$	$Sr\ Zn_{1.01(5)}\ Li_{0.0006(1)}\ O_2$	220.76(2)

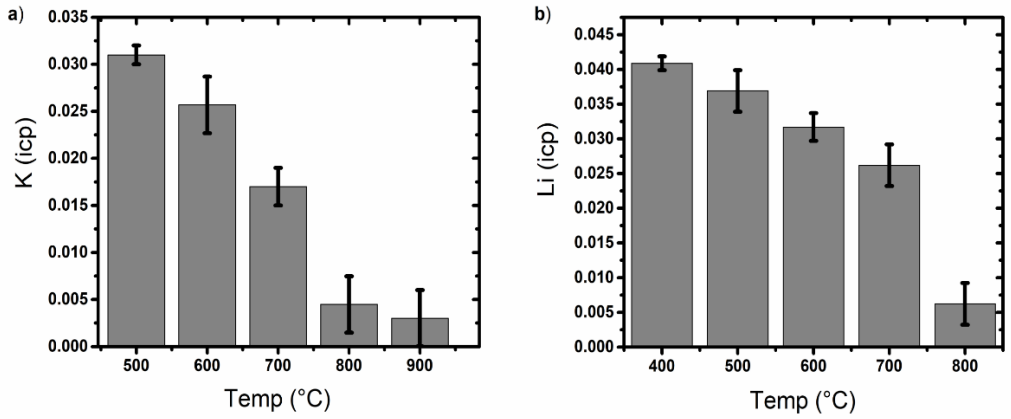

Figure 4. 8: Dopant losses (measured by ICP-OES) on a number of: (a) $Sr_{1-x}K_xZnO_2$ and (b) $SrZn_{1-x}Li_xO_2$ samples synthesised under anaerobic conditions at different temperatures with the use of KO_2 and Li_2O_2 precursors. Samples nominal compositions were: (a) $Sr_{0.97}K_{0.03}ZnO_2$ and (b) $SrZn_{0.96}Li_{0.04}O_2$).

4.2.1.3 By conventional solid-state route and use of sacrificial pellets: Na and Li

Since our attempts to dope $SrZnO_2$ with the use of more reactive peroxide reagents have failed, we returned to the conventional solid-state route and attempted to suppress the dopants volatility with the use of sacrificial pellets. We focused our attention to Na and Li for which earlier experimental (Na) or theoretical (Li) data has shown evidence of possible incorporation.

For this series of exploratory syntheses, we adhered to the sintering protocol of **section 4.2.1.1** with the adjunction of burying the sample pellets among sacrificial pellets (bottom – top) of the same composition. The used sacrificial material (pellets and loose powder) was always made from fresh batches.

Starting with $Sr_{1-x}Na_xZnO_2$, stoichiometric quantities of $SrCO_3$ (99.99 %), ZnO (99.99 %), and Na_2CO_3 (99.99 %) of 0.2 g total mass product and x = 0.015, 0.03 and 0.05 (x, nominal molar ratio) were mixed and examined, according to:

$$(1-x)\ SrCO_3 + x/2\ Na_2CO_3 + ZnO \rightarrow Sr_{1-x}Na_xZnO_2 \qquad \textbf{(Eq. 4. 7)}$$

Although the as-prepared $Sr_{1-x}Na_xZnO_2$ samples were found to be single-phase materials, in **Figure 4. 9a**, the absence of any change on their refined lattice parameters, in **Figure 4. 9b**, has shown that incorporating Na into the $SrZnO_2$ crystalline structure was not possible.

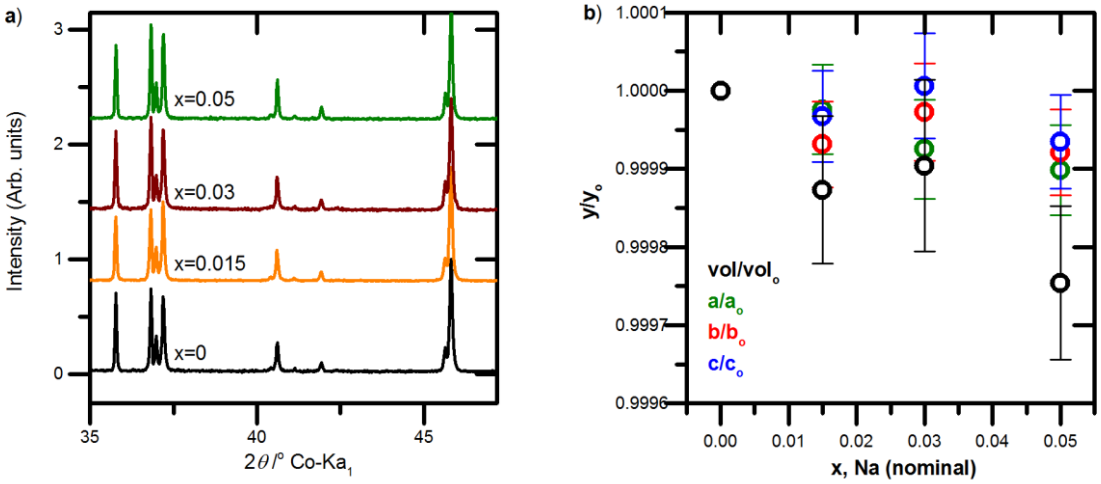

Figure 4. 9: (a) PXRD and (b) refined lattice parameters (in the form of: a/a_o, b/b_o, c/c_o) data of $Sr_{1-x}Na_xZnO_2$ samples, synthesised through conventional solid-state reactions under oxygen atmosphere and the use of sacrificial pellets.

Doping $SrZnO_2$ was eventually proven accessible for $SrZn_{1-x}Li_xO_2$ over the composition range $0 \leq x \leq 0.15$ (x, nominal content) when the samples were sintered in sacrificial powders and the volatility of lithium was suppressed. The formation of single-phase $SrZn_{1-x}Li_xO_2$ pellets were carried out according to the reaction:

$$SrCO_3 + (1-x)\ ZnO + x/2\ Li_2CO_3 \rightarrow SrZn_{1-x}Li_xO_2 \qquad \textbf{(Eq. 4. 8)}$$

As before, 0.2 g of total mass product were synthesised using stoichiometric quantities of $SrCO_3$ (99.99 %), ZnO (99.99 %) and Li_2CO_3 (99.99 %) and where subsequently sandwiched among sacrificial pellets (bottom – top) and finally buried in sacrificial powder of the same composition. The samples were subjected to three subsequent firings at 1090 °C under oxygen flow (10 ml/min) with intermediate hand-grinding steps. As can be seen in **Figure 4. 10a**, the PXRD patterns of the as-synthesised $SrZn_{1-x}Li_xO_2$ samples were found to be single phase and consistent with the orthorhombic $SrZnO_2$ structure for analysed-Li content $x_{ICP} < 0.06$ (by ICP-OES). The unit cell volume of these samples, in **Figure 4. 10b** and **Table 4. 3**, obtained by Pawley refinements (presented analytically in **Figure 4. 11**), was found to decrease approximately linearly up to 0.04 – 0.055 % of analysed Li content indicating the successful doping of the parent material. ICP-OES studies have shown that a systematic loss of dopant was also found on the as-synthesised samples compared with their starting, nominal, composition, in **Figure 4. 12**.

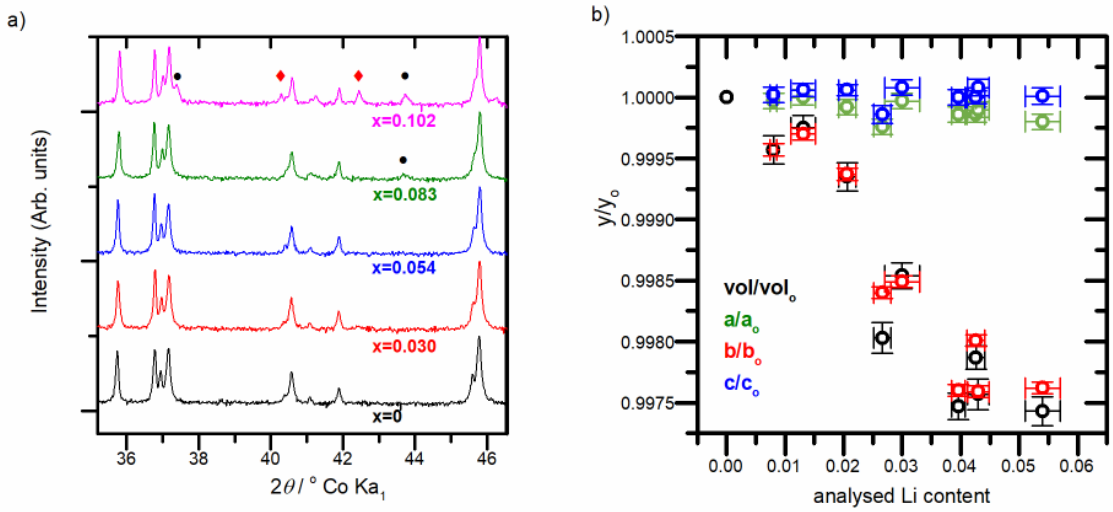

Figure 4. 10: (a) PXRD patterns stacked in order of increasing analysed Li content (x_{ICP}) for the 0.2g series of $SrZn_{1-x}Li_xO_2$ samples, plotted with *square root intensity scaling* to emphasise weak features. Symbol (◆) indicates the presence of ZnO peaks and unindexed peaks are marked by symbol (●). (b) Lattice parameter trends as function of analysed Li content (x_{ICP}), obtained from Pawley refinements of $SrZn_{1-x}Li_xO_2$ PXRD data for 0.2 g $SrZn_{1-x}Li_xO_2$ samples (exploratory series of small scale of samples). KCl was used as an internal standard for the determination of lattice parameters.

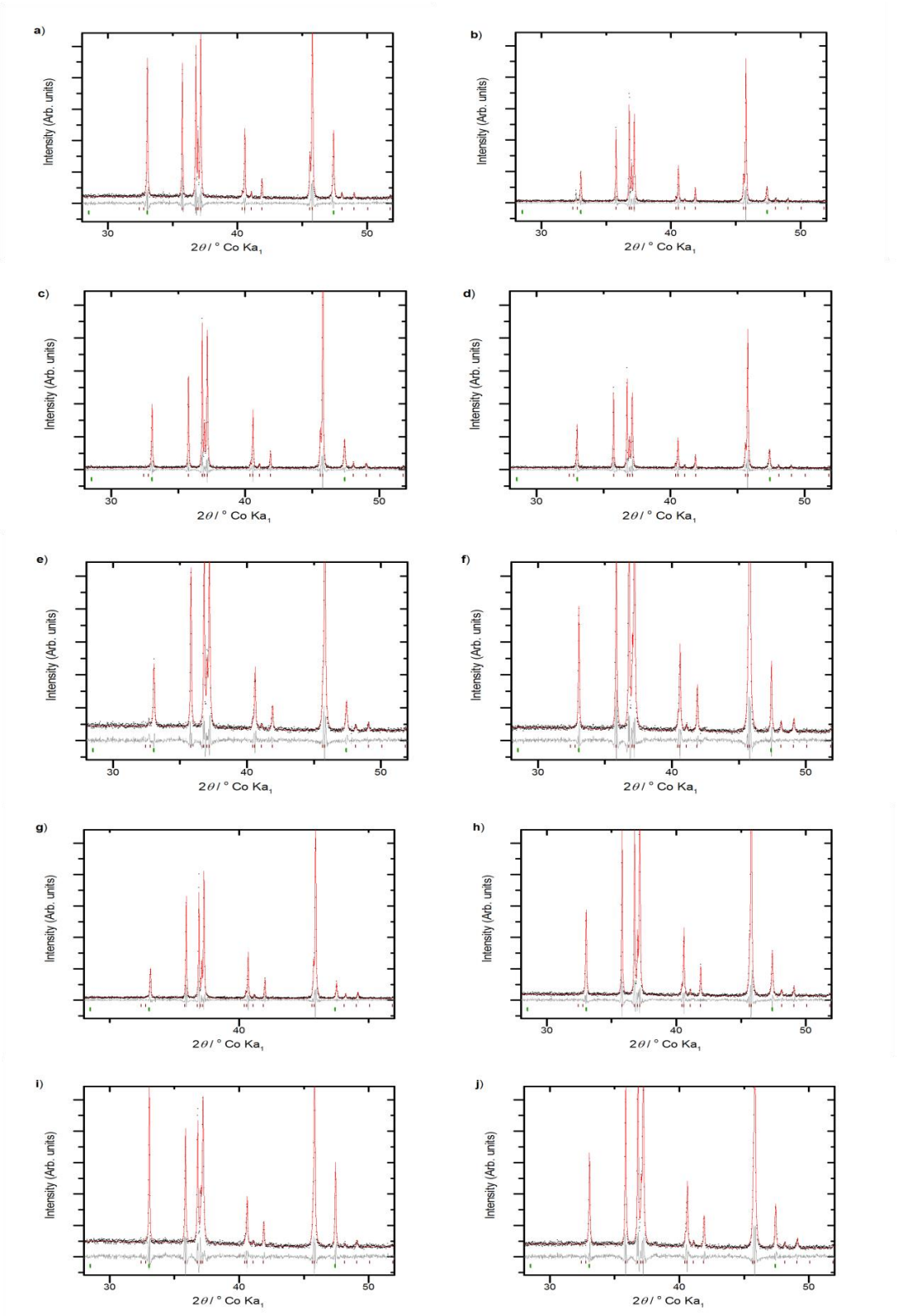

Figure 4. 11: Pawley refinements, in space group *Pnma*, to PXRD of the 0.2 g series $SrZn_{1-x}Li_xO_2$ samples for: (a) x=0, (b) x=0.008, (c) x=0.013, (d) x=0.021, (e) x=0.027, (f) x=0.030, (g) x=0.039, (h) x=0.0425, (i) x=0.043 and (j) x=0.054 analysed Li content in the synthesised samples. Black circles, y_{obs}; red line, y_{calc}; grey line, ($y_{obs} - yc_{alc}$); wine markers, hkl (*Pnma*) reflections of $SrZn_{1-x}Li_xO_2$ samples; green markers, hkl (Fm-3m) reflections of the used internal standard KCl (a_o= 6.2916 Å).

Table 4. 3: Refined lattice parameters (*a*, *b*, *c*) and the corresponding unit cell volumes (by Pawley refinements) of the 0.2 g exploratory series $SrZn_{1-x}Li_xO_2$ samples. The stoichiometric composition of the as-synthesised samples was determined from ICP-OES measurements. The detailed Pawley fits of the PXRD are shown in **Figure 4. 11.**

As-analysed Li content, x_{ICP}	**Refined Lattice Parameters (space group *Pnma*)**			
	a (Å)	*b* (Å)	*c* (Å)	*Volume* (Å^3)
0	3.3388(2)	5.8295(2)	11.3406(4)	220.73(1)
0.008(2)	3.3387(2)	5.8270(6)	11.3409(6)	220.63(2)
0.013(2)	3.3388(2)	5.8277(5)	11.3412(5)	220.67(2)
0.021(1)	3.3385(2)	5.8258(3)	11.3413(3)	220.58(2)
0.027(1)	3.3380(2)	5.8202(7)	11.3390(7)	220.29(2)
0.030(3)	3.3387(2)	5.8207(6)	11.3415(6)	220.40(2)
0.040(1)	3.3383(2)	5.8155(6)	11.3406(6)	220.17(2)
0.043(1)	3.3383(2)	5.8179(4)	11.3406(4)	220.26(1)
0.043(2)	3.3385(2)	5.8154(7)	11.3415(7)	220.19(2)
0.054(1)	3.3381(2)	5.8156(6)	11.3407(6)	220.16(2)

Moving to higher content of analysed-Li content for $x_{ICP} = 0.083$ and $x_{ICP} = 0.102$ in **Figure 4. 10a**, minor ZnO impurities peaks emerged at 40.28^o and 42.45^o together with the non-indexed peaks at 37.39^o and 43.72^o whose intensity was found to increase as Li content increases. Raman measurements of single-phase (for $x_{ICP} = 0$ and $x_{ICP} = 0.030$, analysed Li) and impurity containing ($x_{ICP} = 0.102$, analysed) $SrZn_{1-x}Li_xO_2$ samples did not reveal any difference between them or any association of their absorption peaks with Li-based compounds of Li_2CO_3, LiOH and Li_2O, in **Figure 4. 13**.

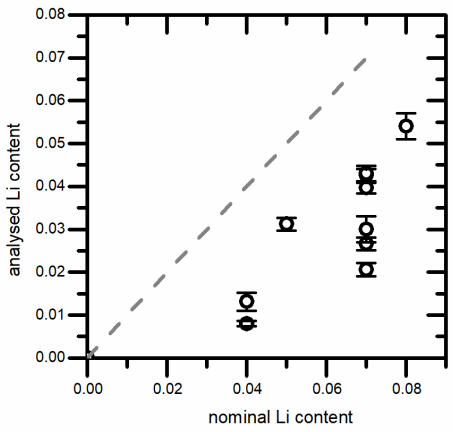

Figure 4. 12: Analysed lithium content against nominal composition of the as-synthesised $SrZn_{1-x}Li_xO_2$ samples of 0.2g series, with the dashed grey line highlighting the 1:1 nominal to analysed Li content ratio.

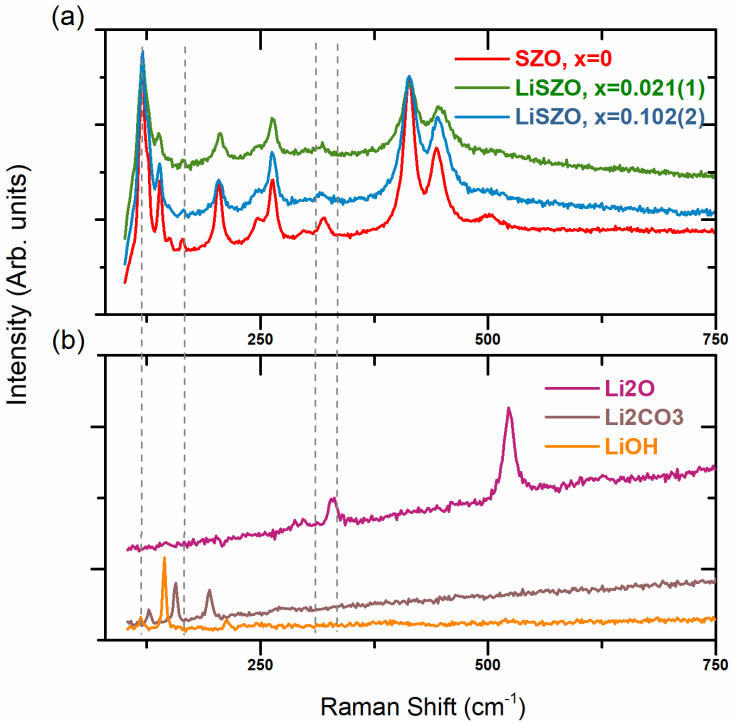

Figure 4. 13: (a) Raman spectra of 0.2 g $SrZn_{1-x}Li_xO_2$ samples (exploratory series of small scale, 0.2 g, of samples) with: (i) x=0, (ii) x=0.030 (both phase pure by PXRD) and (iii) x=0.102 (containing unindexed PXRD peaks related to a high lithium dopant concentration). (b) For comparison are also presented the Raman spectra of: (iv) Li_2O, (v) Li_2CO_3 and (vi) LiOH. As can be seen, no correction was observed on the Raman peak position between $SrZn_{1-x}Li_xO_2$ and the Li-related compounds. Neighbouring but not identical peaks are shown in grey dot lines.

4.2.2 Synthesis of electrical measurement $SrZn_{1-x}Li_xO_2$ samples

Following the successful synthesis of small-scale $SrZn_{1-x}Li_xO_2$ samples, a second series of larger scale (2.0 g) samples, suitable for electrical measurements, was synthesised for $0 \leq x_{ICP} \leq 0.053$ (x_{ICP}, analysed Li content). The synthetic protocol of this series of samples was slightly changed by increasing the number of sintering cycles (to a maximum of seven) until a stable unit cell volume was obtained for at least two subsequent firings. Apart from that, samples were mixed, hand-ground, sandwiched among sacrificial pellets (bottom – top) and buried under same composition sacrificial powder as in **section 4.2.1.3** before subsequent firings at 1090 °C under 10 ml/min of oxygen flow.

The PXRD patterns of this large-scale (2.0 g) series of $SrZn_{1-x}Li_xO_2$ samples were all found to be single-phase, in **Figure 4. 14a**, while the resulting unit cell volume of these samples,

obtained by Pawley refinements of the PXRD data in **Figure 4. 15**, was also found to decrease linearly as analysed Li content was increased, driven by a contraction of the unit cell along the crystallographic *b* axis as shown in **Figure 4. 14b**.

A good match between the unit cell volume changes of small (0.2 g) and large (2.0 g) scale $SrZn_{1-x}Li_xO_2$ samples was found in **Figure 4. 16**, confirming the reproducibility of the synthesised $SrZn_{1-x}Li_xO_2$ materials.

In the following sections, the values given for *x* refer to the analysed composition obtained using ICP-OES analysis and will be denoted as x_{ICP}.

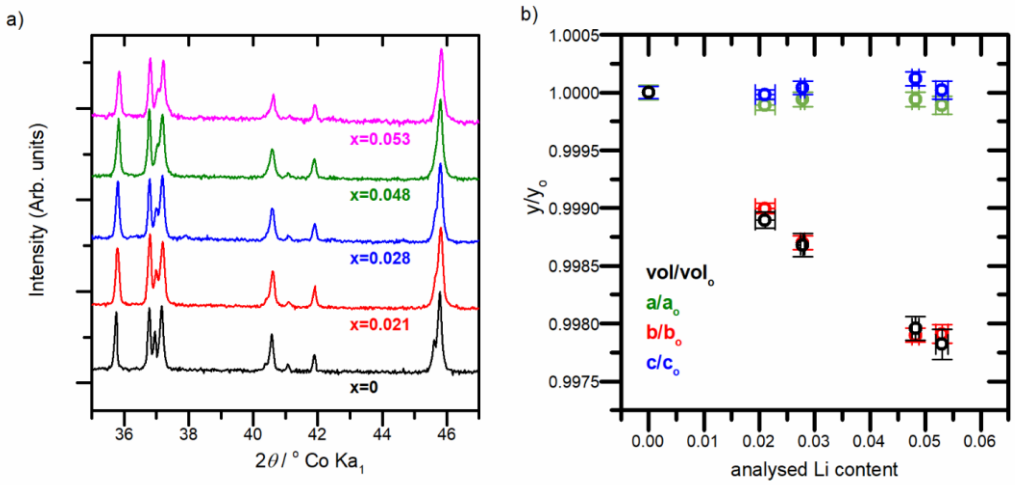

Figure 4. 14: (a) PXRD patterns stacked in order of increasing analysed Li content for the 2.0 g series of $SrZn_{1-x}Li_xO_2$ samples, plotted with square root intensity scaling to emphasise weak features. (b) Lattice parameter trends as function of analysed Li content, obtained from Pawley refinements of PXRD data of 2.0 g $SrZn_{1-x}Li_xO_2$ samples (electrical measurement samples). KCl was used as an internal standard for the determination of lattice parameters.

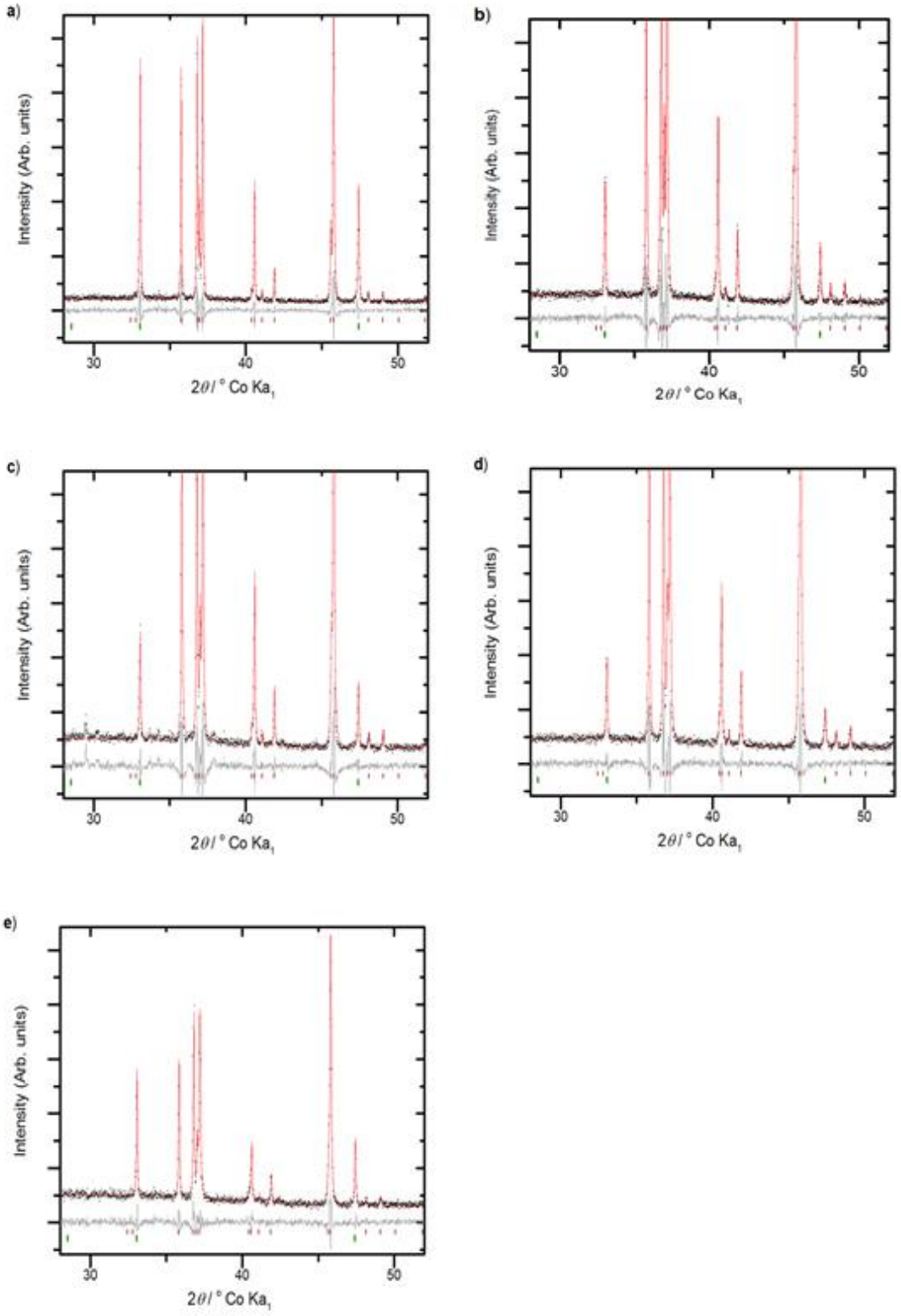

Figure 4. 15: Pawley fits, in space group *Pnma*, to PXRD of the 2.0 g series $SrZn_{1-x}Li_xO_2$ samples for: (a) x=0, (b) x=0.021, (c) x=0.028, (d) x=0.048 and (e) x=0.053 analysed Li content in the synthesised samples. Black circles, y_{obs}; red line, y_{cal}; grey line, ($y_{obs} - y_{calc}$) wine markers, hkl (*Pnma*) reflections of $SrZn_{1-x}Li_xO_2$ samples; green markers, hkl (Fm-3m) reflections of the used internal standard KCl (a_o= 6.2916 Å).

Table 4. 4: Refined lattice parameters (*a*, *b*, *c*) and corresponding unit cell volumes, obtained by Pawley refinements to PXRD data, of the as-synthesised 2.0 g series $SrZn_{1-x}Li_xO_2$ samples (samples for DC-conductivity measurements). The stoichiometric composition of samples was determined by ICP-OES. The detailed Pawley fits of the PXRD are shown in **Figure 4. 15.**

$SrZn_{1-x}Li_xO_2$ samples *Lithium is given in 3 decimal places*	**Li content (x_{ICP})** *ICP-OES values*	**Refined Lattice Parameters (space group *Pnma*)**			
		a (Å)	*b* (Å)	*c* (Å)	*Volume* (Å^3)
$SrZnO_2$	0	3.3387(2)	5.8291(2)	11.3400(3)	220.69(2)
$SrZn_{0.93(2)}Li_{0.028(1)}O_2$	0.0278(4)	3.3386(2)	5.8219(3)	11.3410(5)	220.44(2)
$SrZn_{0.94(2)}Li_{0.048(1)}O_2$	0.0482(6)	3.3386(2)	5.8172(3)	11.3420(5)	220.28(2)
$SrZn_{0.93(3)}Li_{0.053(1)}O_2$	0.053(1)	3.3384(2)	5.8173(4)	11.3408(8)	220.24(2)

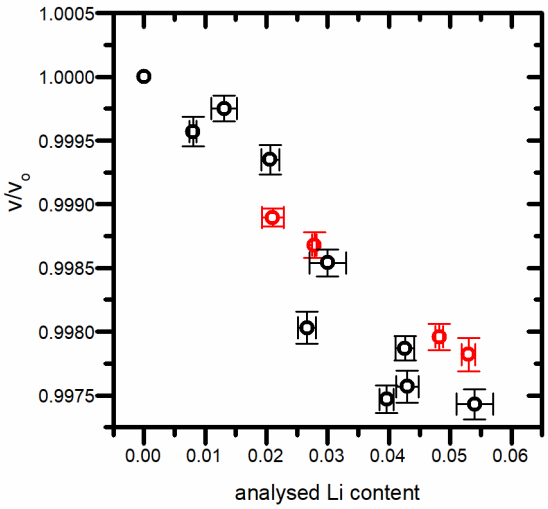

Figure 4. 16: Change of unit cell volume as a function of analysed Li content for both series of $SrZn_{1-x}Li_xO_2$ samples: small (0.2 g) and large (2.0 g) scale samples are presented in black and red circles, respectively.

4.3 Electrical measurements of $SrZn_{1-x}Li_xO_2$

In summary, in this section the *p*-type behaviour of $SrZn_{1-x}Li_xO_2$ was validated by thermopower and variable-pO_2 resistivity measurements and was found to be maintained for 40 days after storage in dry air, confirming the long-term stability of our *p*-type compounds.

Preliminary AC impedance measurements on a small scale (0.2 g) sample with $x_{ICP} = 0.027$ have shown the dominant bulk contribution to the total conductivity of $SrZn_{1-x}Li_xO_2$ as well as its *p*-type character under oxidising conditions. Given the dominant bulk conductivity contribution of $SrZn_{1-x}Li_xO_2$, AC and DC measurements were found to be in good agreement and regardless of the geometry of the examined specimens. The *p*-type character of $SrZn_{1-x}Li_xO_2$ was also verified by variable-pO_2 conductivity (DC) measurements of samples with different lithium content. The structural stability of the examined $SrZn_{1-x}Li_xO_2$ samples was assessed by PXRD and ICP (analysed Li content) studies with the completion of the electrical measurements.

4.3.1 Preliminary AC impedance measurements

Preliminary AC impedance measurement were performed on a small scale (0.2 g) $SrZn_{1-x}Li_xO_2$ sample to evaluate its conductivity response over variable-pO_2 measurements and evaluate its bulk and grain boundaries contributions.

For these measurements, a circular disc-shaped pellet of 10 mm diameter and 1-2 mm thickness of a $SrZn_{1-x}Li_xO_2$ sample with $x_{ICP} = 0.027$ was polished and coated with conductive gold paste. To ensure the good bonding of the gold paste, the pellet was dried at 150 ^oC for 1 hour and subsequently fired at 550 °C for 2 hours.

4.3.1.1 Temperature depended AC impedance measurements

The AC impedance measurements were performed over the frequency range of 1 Hz to 1 MHz and a modulation potential of 10 mV on a Solartron 1255B Frequency Response Analyser (Solartron Analytical, Farnborough, U.K.) coupled to a Solartron 1296 Dielectric Interface under the setup shown in **Figure 4. 17**. The measurements were initially recorded for

temperatures between 400 °C and 700 °C (starting from 700 °C) under 1 atm of O_2 and were repeated under 0.01 atm of O_2. The sample was held at each temperature point for 90 minutes to allow thermal equilibration and measurements were made using ZPlot v.2.9b (Scribner Associates).

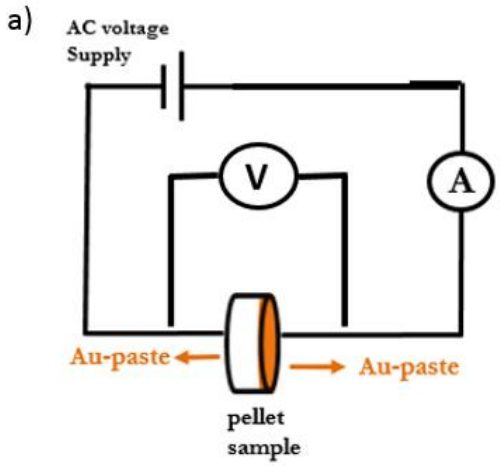

Figure 4. 17: Two probe AC impedance measuring setup.

Typical AC impedance spectra of the sample under investigation (x_{ICP} = 0.027) at 500 ºC and 600 ºC under 1 atm of O_2 are presented in **Figure 4. 18a**,**b.** It can be seen there that for both temperatures one large semicircle is observed at high and intermediate frequencies related to the bulk conductivity of the sample given their high capacitance value ($C_b > 10^{-11}$ F). A second smaller semicircle, emerging at low frequencies in the spectra of both temperatures, has been assigned to the electrode response ($C_{el} \sim 10^{-5}$ F). Overall, the impedance spectra did not display any evidence of grain boundary contribution (typically seen in the capacitance range of 10^{-8} to 10^{-11} F) to the total conductivity of $SrZn_{1-x}Li_xO_2$ samples.

The two spectra were fitted to the conventional equivalent circuit of two parallel (RQ) elements in series, where R and Q are respectively for resistance and constant phase elements, in **Appendix C**. One extra capacitance, C_p, was added parallel to the bulk (R_bQ_b) element, representing the limiting, frequency-independent bulk permittivity of the sample ε_∞, to improve fittings at high-frequencies in agreement with previous literature reports[283,284].

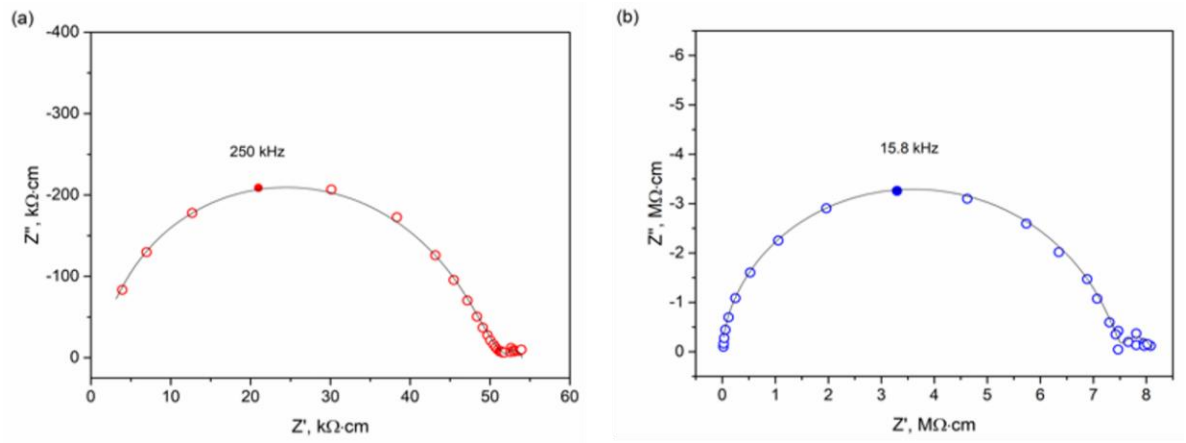

Figure 4. 18: AC impedance spectra of the x_{ICP} = 0.027, $SrZn_{1-x}Li_xO_2$, sample at (a) 500 ºC and (b) 600 ºC, under 1 atm O_2 atmosphere. Black line represents the results of the nonlinear least square fit.

The temperature dependence of sample conductivity under oxygen partial pressures (pO_2) of 1 and 0.01 atm are summarized in **Figure 4. 19**. The activation energies (Ea) of the sample at the studied oxygen partial pressures was calculated from the corresponding Arrhenius equations of **Figure 4. 19** and were found to be comparable at 1.44(7) eV and 1.28(8) eV, respectively, given the standard deviation of the measurements. However, the high values of activation energy indicate the possible ionic contribution to the total material conductivity which can only be confirmed by further measurements of the independent electronic and ionic conductivity components.

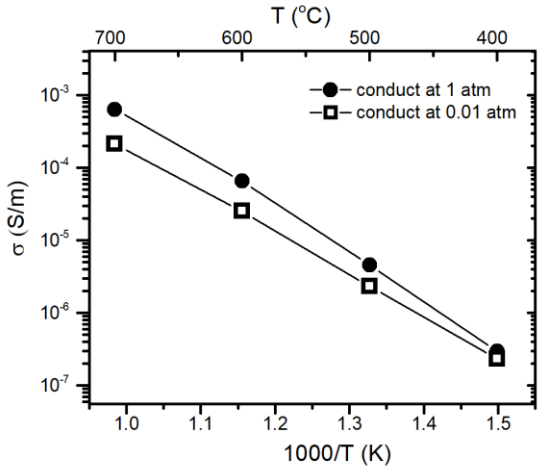

Figure 4. 19: Arrhenius plots of AC impedance measurements for temperatures between 400 to 700 ºC for the x_{ICP} = 0.027 $SrZn_{1-x}Li_xO_2$, sample under oxygen partial pressure (pO_2) of 1 and 0.01 atm.

4.3.1.2 Variable-pO_2 AC impedance measurements

In a following step, the conductivity of the x_{ICP} = 0.027 sample was also measured at 700 ^oC over a wider range of oxygen partial pressures, in **Figure 4. 20**. Starting at the end of the previous measurement (shown in **Figure 4. 19**), the temperature of the sample was returned to 700 ^oC and conductivity measurements were carried out between oxygen partial pressures of 1 and 10^{-12} atm by mixing different gasses (O_2, 1%O_2/Ar, Ar) with the use of a central control unit (Brooks Instruments, mod. 5850) and a zirconia-based pO_2-sensor (Rapidox 2100, Cambridge Sensotec Ltd.). The total gas flow rate was 30 mL/min and data were recorded after an equilibration period of 2 hours at each pO_2 point of measurement to ensure a stable conductivity.

The sample's pO_2-response of conductivity was found to be similar with the conductivity of many other electroceramic oxides with its electrical response displaying three domains: (a) an electron hole dominant region, (b) an intermediate independent to pO_2 conductivity area and (c) an electron dominant region, as pO_2 was reduced.

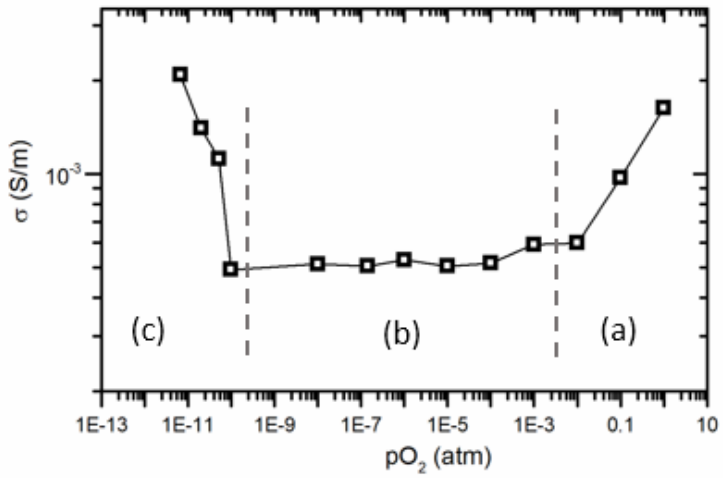

Figure 4. 20: Conductivity measurements as a function of pO_2, measured from high- to low-pO_2, at 700 °C for the x_{ICP} = 0.027, $SrZn_{1-x}Li_xO_2$, sample at 700 ^oC.

It is worth noting that in a set of exploratory conductivity measurements of $SrZn_{1-x}Li_xO_2$ samples (not shown here) over a range of temperatures and oxygen partial pressures we obtained a stable (over time) resistance only at $pO_2 > 0.2$ atm and temperatures $T \leq 600$ °C.

These results are consistent with the oxygen-rich environment in which the synthesis of single-phase materials was obtained (see **section 4.1.1**), suggesting the gradual decomposition of the material after its prolonged low-pO_2 exposure.

Given these findings, the electrical measurements of $SrZn_{1-x}Li_xO_2$ samples with different lithium of the following section were conducted at oxygen partial pressures between $0.3 \leq pO_2 \leq 1.0$ atm and temperature of 600 °C to eliminate possible signs of samples decomposition. In these cases, the stability of the samples was evaluated after completion of the measurements, by PXRD and Li content (ICP) analyses to identify possible changes in their unit cell volume or dopant concentration.

4.3.2 Variable-pO_2 conductivity (DC) measurements

4.3.2.1 Agreement of DC and AC measurements

The AC impedance measurements in **section 4.3.1** showed that the high resistance of the $SrZn_{1-x}Li_xO_2$ samples was lying close to the detection limit (10^8 Ohm) of the impedance analyser (Solartron 1255B Frequency Response Analyser). Measuring the conductivity of $SrZn_{1-x}Li_xO_2$ samples under reducing pO_2 conditions is expected to further increase the resistance of the samples, beyond the detection limit of the impedance analyser.

Given the wider measurement range (up to 10^{10} Ohm) of the available in-lab DC supply system (Keithley 220 programmable current source), we processed the rest of variable-pO_2 conductivity measurements of $SrZn_{1-x}Li_xO_2$ (of different Li content) using a four-probe DC technique.

To do so, firstly we evaluate the agreement between alternative (AC) and direct (DC) current measurements by comparing the obtained activation energy of $SrZn_{1-x}Li_xO_2$ (2.0 g) samples of different Li content ($x_{ICP} = 0$ and $x_{ICP} = 0.028$) under those two configurations (AC and DC). For these measurements, rectangular-shaped specimens of the samples were cut at 1.5 × 2 × 11.5 mm, polished and wrapped with four Au electrodes before being painted on the electrodes with Au paste and left to dry at 150 °C for 1 hour and 550 °C for 2 hours to ensure good bonding.

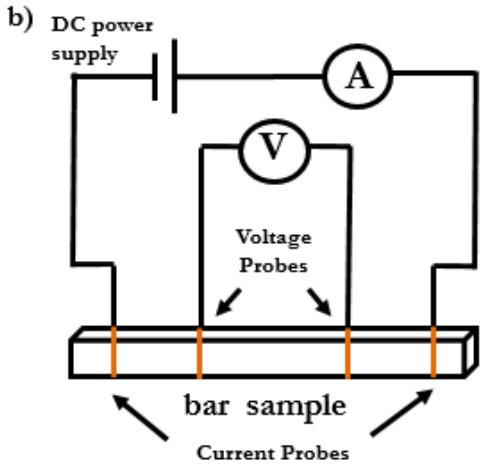

Figure 4. 21: Geometry of a four-probe DC conductivity measurement setup.

For the DC measurements, electrical current was applied on the two outer probes of the specimens, in the range of 0.05-0.5 mA, using a constant-current supply (Keithley 220 programmable current source) and voltage drops were measured with a Keithley 2182 Nanovoltmeter on the two inner probes, as depicted in **Figure 4. 21**. The measurements were performed at variable temperatures between 500 – 600 °C under an oxygen partial pressure of 1 atm.

Apart from the DC measurements, AC electrical measurements were also performed at the ends of the measurement pO_2 range. For the AC impedance measurements, the two inner electrodes of the examined samples have been attached to a Solartron 1255B Frequency Response Analyser (Solartron Analytical, Farnborough, U.K.) coupled to a Solartron 1296 Dielectric Interface, and the conductivity of the samples was evaluated from their low frequency impedance, i.e. intersection of the bulk semicircle with the real axis on the complex plane.

In **Figure 4. 22a**, the results of DC conductivity measurements of the two samples ($x_{ICP} = 0$ and $x_{ICP} = 0.028$) have been plotted in the form of Arrhenius plots as a function of temperature (with blue and black open-circles, respectively). In addition, the AC impedance measurements are also plotted in **Figure 4. 22a** in the form of open-square points for both samples (light blue and grey open-squares for $x_{ICP} = 0.028$ and $x_{ICP} = 0$, respectively). From the comparison of the obtained results, it is concluded the good agreement between the conducted DC and AC measurements confirming once more the dominant bulk conductivity contribution of the samples (see also **section 4.3.1**).

Given the higher conductivity of the doped sample (x_{ICP} = 0.028), the AC and DC measurements of this sample were extended to lower temperatures (up to 350 °C) without however detecting any change in the activation energy as presented in the extended data of **Figure 4. 22b**.

Finally, the effect of sample geometry (rectangular and circular disc shape specimens) on the performed AC measurements has been also evaluated by comparing the obtained AC impedance data of the rectangular-shaped x_{ICP} = 0.028 sample examined in this section with the AC impedance data of the disc-shaped x_{ICP} = 0.027 sample in **section 4.3.1**. Once more, as can be seen from the extended data of **Figure 4. 22b**, the AC impedance values of the two samples were found to coincide well, confirming the agreement of AC measurements regardless of the samples geometry (rectangular and disc-shaped specimens).

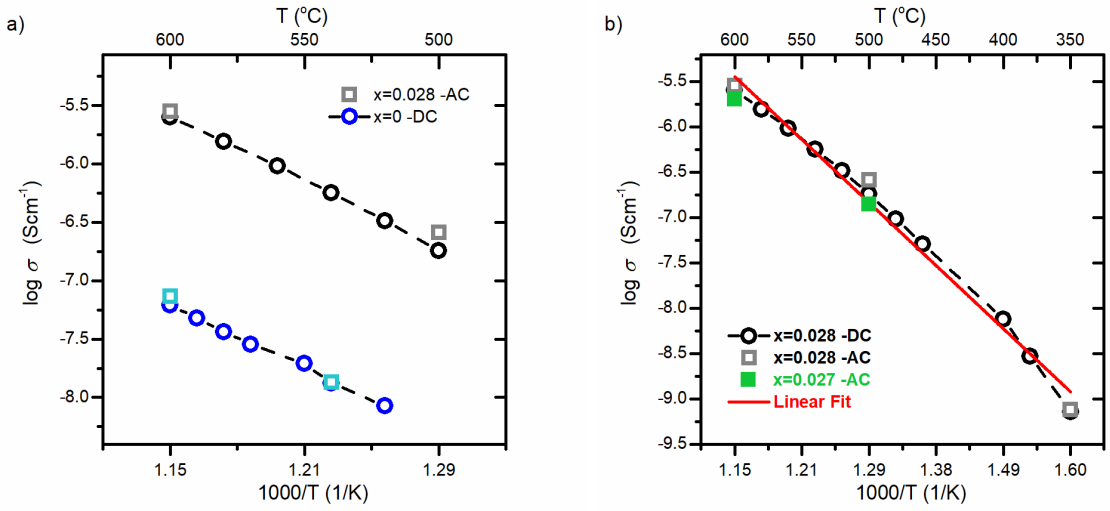

Figure 4. 22: (a) DC conductivity measurements, in the form of Arrhenius plots, for two rectangular shaped $SrZn_{1-x}Li_xO_2$ (2.0 g) samples of: x=0 (blue points) and x=0.028 (black points) under 1 atm of pO_2 and temperatures between 600°C and 500°C. With blue and grey open-square points, are superimposed the AC impedance measurements that were collected parallel to the DC measurements for the x=0 and x=0.028 samples, respectively. (b) Extended DC conductivity data of the doped rectangular shaped sample (x=0.0278) for temperature up to 350 °C. The AC impedance measurements of a circular disk-shaped $SrZn_{1-x}Li_xO_2$ sample with x=0.027 (small scale sample of 0.2 g) was also plotted with filled green square points for comparison reasons.

In summary, AC and DC conductivity measurements conducted on different geometry specimens have shown a good agreement between the two methods. Given the wider

measurement range (up to 10^{10} Ohm) of the available in-lab DC supply system (Keithley 220 programmable current source), variable-pO_2 conductivity measurements of $SrZn_{1-x}Li_xO_2$ samples with different Li content will be performed in the following section under the four probes DC measurement protocol of rectangular-shape specimens.

4.3.2.2 Variable-pO_2 conductivity measurements

To examine the effect of Li doping into $SrZnO_2$, four large scale (2.0 g) samples of variable Li content (x_{ICP} = 0, 0.028, 0.048 and 0.053) were synthesised following the established protocol of **section 4.2.2**, cut in rectangular-shape specimens, gold wrapped and connected with four probes to a Keithley 220 programmable current source.

The DC measurements were performed at 600 °C and over a range of pO_2 from 1 to 0.3 atm. As before, the oxygen partial pressure was in-situ monitored with a zirconia-based pO_2 sensor (Rapidox 2100, Cambridge Sensotec Ltd.) and the total gas flow rate was set to 30 mL/min with the use of mass flow controllers and a control unit (Brooks Instruments, mod. 5850 and mod. 0154, respectively). Conductivity measurements were performed on samples under equilibrium conditions (typically equilibrating for 3 hours at each pO_2 point of measurement).

The variable-pO_2 conductivity measurements of the four $SrZn_{1-x}Li_xO_2$ samples are presented in **Figure 4. 23a**. An increase of at least one order of magnitude was observed in the conductivity of the doped samples compared to the undoped. The conductivity of the doped samples has also shown a more acute response to pO_2 variations. In **Figure 4. 23b**, the conductivities of $SrZn_{1-x}Li_xO_2$ samples are plotted as a function of Li content at pO_2 = 0.3 and 1.0 atm, showing a common trend as the insertion of dopant initially increases the conductivity of the parent compound while further increase of doping content results in a degradation of conductivity with dopant ions starting to act as scattering centres.

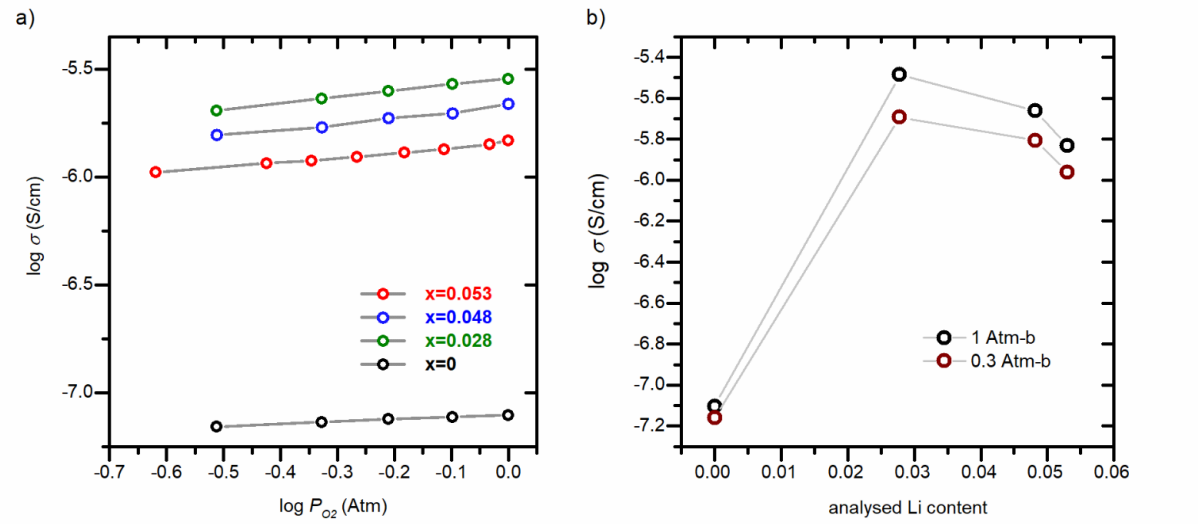

Figure 4. 23: DC conductivity measurements of 2.0 g $SrZn_{1-x}Li_xO_2$ samples. (a) Conductivity measurements as a function of pO_2, measured from high- to low-pO_2, at 600 °C for $SrZn_{1-x}Li_xO_2$ samples, with x = 0, 0.028, 0.048 and 0.053. (b) Conductivity as a function of analyzed Li content in high- and low-pO_2 conditions.

When the obtained conductivities were fitted to a power law dependence, according to $\sigma \propto pO_2^{1/n}$, the exponent ($1/n$) was found to increase from 0.11(1) for x_{ICP} = 0 to values around 0.25, as seen in **Figure 4. 24** and

Table 4. 5. which is consistent with holes being the dominant charge carriers under oxidizing conditions[285,286] and in agreement with Gupta's calculations[287] on substituting Zn by Li in the prototype $SrZnO_2$.

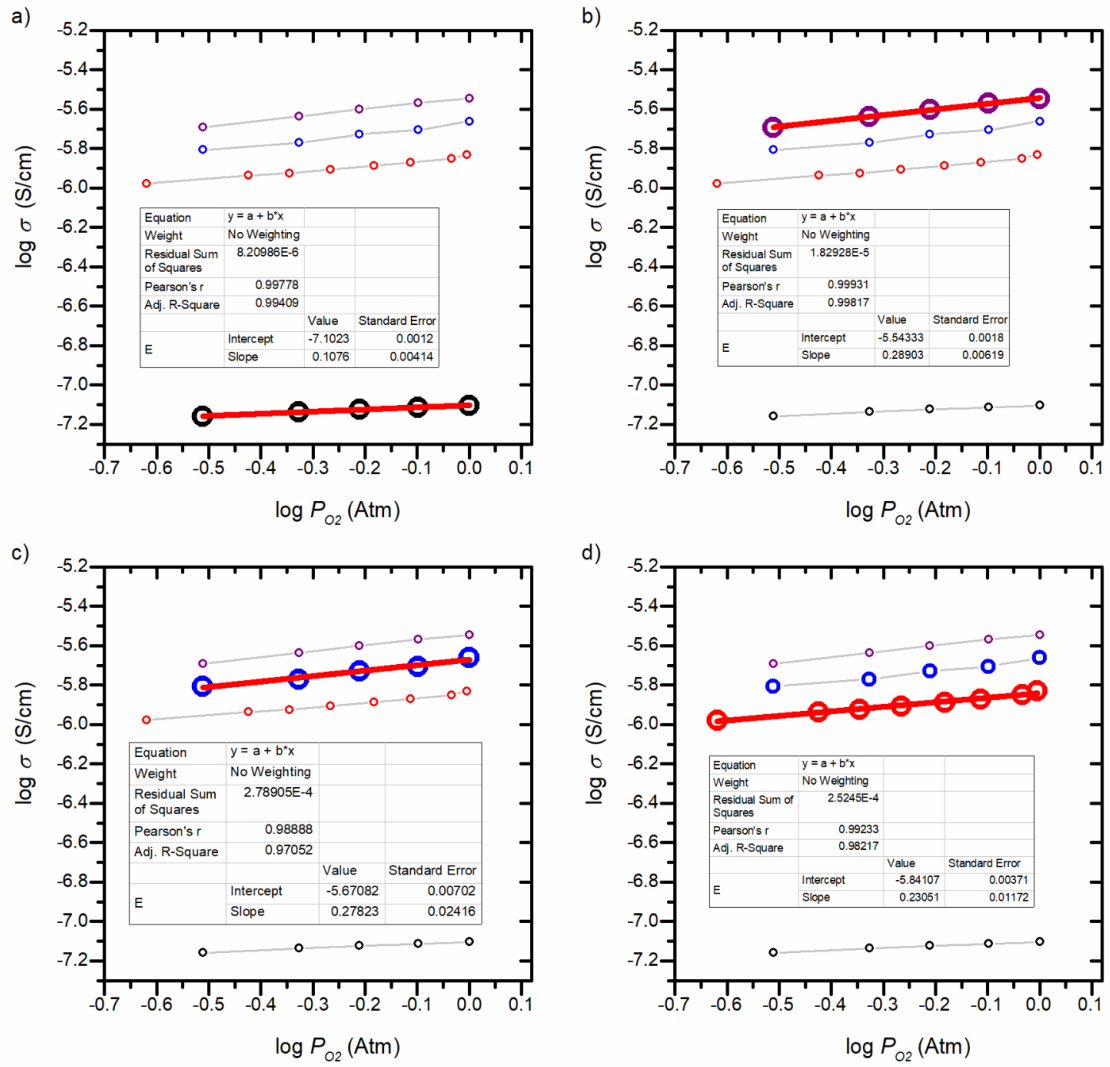

Figure 4. 24: Fittings of pO_2 variable DC conductivity data of $SrZn_{1-x}Li_xO_2$ samples for: (a) $x_{ICP} = 0$, (b) $x_{ICP} = 0.028$, (c) $x_{ICP} = 0.048$ and (d) $x_{ICP} = 0.053$.

Table 4. 5: The power law dependence of measured samples' DC conductivity to oxygen partial pressure.

$SrZn_{1-x}Li_xO_2$ samples *Lithium is given in 3 decimal places*	**Li content** *(ICP-OES values)*	**Power dependence,** *1/n*
$SrZnO_2$	0	0.11(1)
$SrZn_{0.93(2)}Li_{0.028(1)}O_2$	0.0278(4)	0.29(1)
$SrZn_{0.94(2)}Li_{0.048(1)}O_2$	0.0482(6)	0.28(2)
$SrZn_{0.93(3)}Li_{0.053(1)}O_2$	0.053(1)	0.23(1)

The overall defect equilibrium taking place upon doping with Li can be summed up as follows:

$$\frac{1}{2}O_2 + Li_2O \xrightarrow[2SrZnO_2]{} 2Li'_{Zn} + 2O_O^{\times} + 2h^{\cdot} \quad \textbf{(Eq. 4. 9)}$$

where Li'_{Zn} acceptors are being compensated by holes.

The equilibrium of **(Eq. 4.9)** can be considered as the result of two successive reactions:

(a) the incorporation of Li_2O into $SrZnO_2$

$$Li_2O \xrightarrow[2SrZnO_2]{} 2Li'_{Zn} + O_O^{\times} + \ddot{V}_O \quad \textbf{(Eq. 4. 10)}$$

where, according to electroneutrality considerations: $\left[Li'_{Zn}\right] \approx 1/2\left[\ddot{V}_O\right]$,

(b) the oxidation reaction:

$$\frac{1}{2}O_2 + \ddot{V}_O \leftrightarrow 2O_O^{\times} + 2h \quad \textbf{(Eq. 4. 11)}$$

Combining the charge neutrality conditions of **(Eq. 4.10)** with the oxidation reaction **(Eq. 4.11)** we are obtaining:

$$K_{ox} = \frac{h^2}{[\ddot{V}_O]p_{O_2}^{\frac{1}{2}}} \quad \textbf{(Eq. 4. 12)}$$

the power law dependence of the hole concentration on the oxygen partial pressure is expressed according to:

$$h \approx \left(\frac{K_{ox}\left[Li'_{Zn}\right]}{2}\right)^{\frac{1}{2}} p_{O_2}^{\frac{1}{4}} \quad \textbf{(Eq. 4. 13)}$$

which agrees with the observed dependence of conductivity of Li doped $SrZnO_2$ on the oxygen activity above 0.2 atm.

4.3.2.3 Electrical conductivity and stability

The electrical stability of $SrZn_{1-x}Li_xO_2$ was examined for two of the four samples (x_{ICP} = 0.053 and x_{ICP} = 0.048) by repeated variable-pO_2 conductivity (DC) measurements.

At first, the conductivity of the x_{ICP} = 0.053 sample was assessed over a reversed pO_2 sweep of oxidizing conditions. For this reason, after the initial measurement of the sample under reducing conditions (initially in **Figure 4. 23a**), its conductivity was re-measured as the sample was returned to fully oxidizing atmosphere. All these measurements are summarized in **Figure 4. 25**, from points 1 to 2 (reducing conditions) and points 2 to 3 (oxidizing conditions). Overall,

the sample was found to maintain its *p*-type response although the exponent (1/*n*) in the power law pO_2-dependence of conductivity was reduced from 0.23(1) to 0.17(1) due to Li losses during the conductivity measurements (see also next section on the structural stability of the examined samples, **section 4.3.2.4**).

The long-term stability of *p*-type conduction in $SrZn_{1-x}Li_xO_2$ was assessed by re-measuring the x_{ICP} = 0.048 sample after a 40 day period during which the sample was kept in dry conditions under ambient atmosphere. Following the first measurement (presented initially in **Figure 4. 23a**), the measurement was repeated under the same protocol of reducing pO_2 conditions (from 1 to 0.3 atm) at 600 °C. The two subsequent measurements are summarized in **Figure 4. 25**, where it is clear that the *p*-type response of the sample was retained over the examined period.

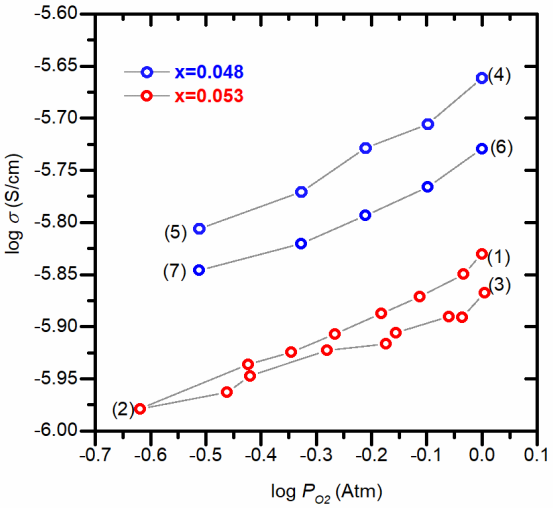

Figure 4. 25: Electrical stability of $SrZn_{1-x}Li_xO_2$. The stability of $SrZn_{1-x}Li_xO_2$ over a reversed pO_2 sweep was assessed on a sequence of measurements over reducing/oxidizing conditions: from point 1 to 2 and back to point 3 for the x= 0.053 sample. Long-term stability of *p*-type conduction in $SrZn_{1-x}Li_xO_2$ (x= 0.048 sample) was evaluated by re-measuring the sample conductivity after storage in dry air for 40 days: first measurement from points 4 to 5 and repeated measurement on points 6 to 7.

In summary, our results have shown that $SrZn_{1-x}Li_xO_2$ ($0 < x \leq 0.053$) is sufficiently robust for measurement of properties on a single pO_2 sweep although it will degrade by Li loss after repeated cycling or extended heating even in the limited pO_2 range selected here.

4.3.2.4 Structural Stability of $SrZn_{1-x}Li_xO_2$

The structural and compositional stability of the $SrZn_{1-x}Li_xO_2$ samples was assessed by PXRD and Li content measurements (ICP analysis) when the conductivity measurements were completed.

The collected PXRD data of the samples, displayed in square root intensity scale to emphasise weak features in **Figure 4. 26**, have shown little to no change compared to those before the measurements. No change was also observed in the lattice parameters and unit cell volumes of the samples, obtained by Pawley refinements, in **Table 4. 6**. However, losses of Li were detected by ICP-OES during the pO_2 conductivity measurements, also in **Table 4. 6**, in consistency with the observed degradation of material electrical properties over extended heating or low pO_2 atmospheres, in **Figure 4. 25**. In addition, the Li losses also resulted in minor ZnO impurities in the PXRD data of the samples after the DC measurements, in **Figure 4. 26**.

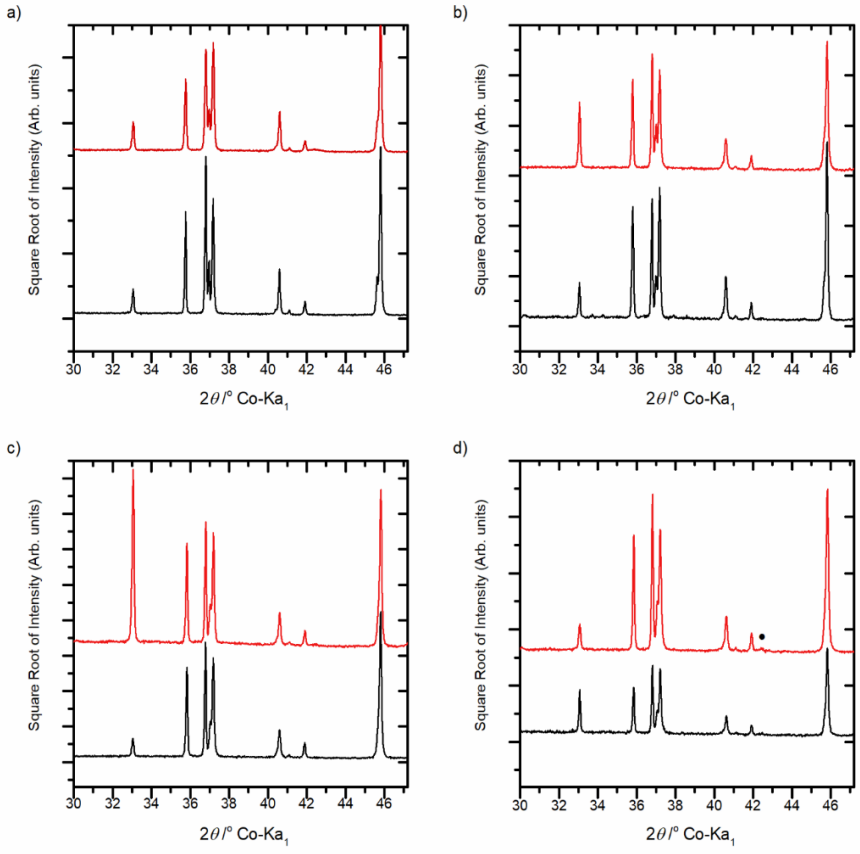

Figure 4. 26: PXRD data, in square root intensity scale, of $SrZn_{1-x}Li_xO_2$ samples before (in black) and after (in red) the four-probe DC measurements for: (a) x=0, (b) x=0.028, (c) x=0.048 and (d) x=0.053. Symbol (●) indicates the presence of decomposition products (ZnO impurities) at the end of the measurements.

Table 4. 6: Refined lattice parameters (*a*, *b*, *c*) and the corresponding unit cell volumes of the 2.0 g series $SrZn_{1-x}Li_xO_2$ samples after the DC conductivity measurements. The data were obtained by Pawley refinement of PXRD data. The stoichiometric composition of the examined samples was determined by ICP-OES.

$SrZn_{1-x}Li_xO_2$ samples, *Lithium is given in 3 decimal places*	**x, Li content**		**Refined Lattice Parameters (S.G. *Pnma*)**				
			a (Å)	*b (Å)*	*c (Å)*	*Volume (Å³)*	*Volume (Å³)*
	Before	*After*	*After DC – measurement*				*Before DC-meas*
$SrZnO_2$	0	0	3.3387(2)	5.8290(2)	11.3397(4)	220.68(2)	220.69(2)
$SrZn_{0.93(2)}Li_{0.028(1)}O_2$	0.0278(4)	0.0164(2)	3.3382(2)	5.8238(3)	11.3405(6)	220.47(2)	220.44(2)
$SrZn_{0.94(2)}Li_{0.048(1)}O_2$	0.0482(6)	0.0301(9)	3.3382(2)	5.8187(2)	11.3405(5)	220.28(2)	220.28(2)
$SrZn_{0.93(3)}Li_{0.053(1)}O_2$	0.053(1)	0.042(1)	3.3382(2)	5.8163(3)	11.3393(7)	220.18(2)	220.24(2)

4.3.3 Seebeck measurements

The dominant hole-carrier type of these compositions was directly confirmed by three consecutive measurements of the Seebeck coefficient of a $SrZn_{1-x}Li_xO_2$ rectangular-shaped sample (x_{ICP} = 0.021) in the temperature range 550 - 600 °C and under 1 atm of pO_2.

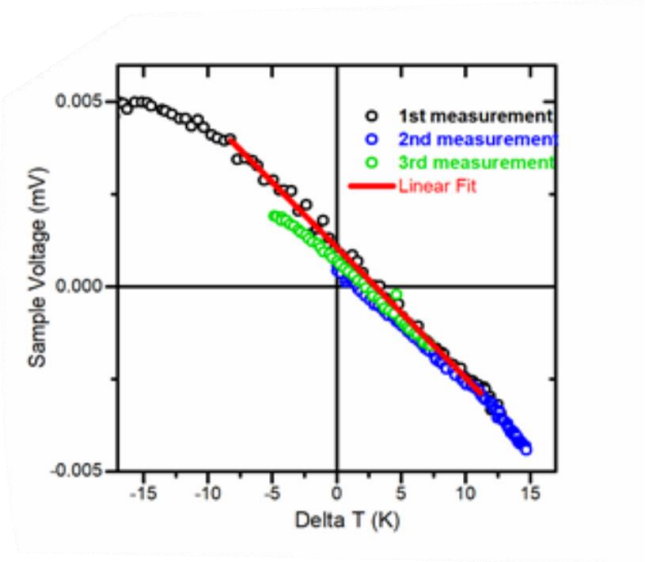

Figure 4. 27: Seebeck voltage as function of temperature difference across the $SrZn_{1-x}Li_xO_2$ (x = 0.021) sample, measured in the temperature range of 550 to 600 °C under 1 atm of pO_2. The Seebeck coefficient is determined from the slope. Three consequent measurements were performed in black, blue and green points, respectively.

The Seebeck coefficient of the examined sample, derived from the slope of the thermopower measurements in **Figure 4. 27**, was found positive at: 353(4) μV/K, 317(3) and 307(5) μV/K for the three subsequent measurements, verifying the *p*-type conduction in $SrZn_{1-x}Li_xO_2$.
The slight decrease in the Seebeck coefficient over consecutive measurement was found in agreement with the gradual degradation of the compound by Li loss, as discussed before (**sections 4.3.2.2** and **4.3.2.3**).

4.4 Optical measurements of $SrZn_{1-x}Li_xO_2$

The optical properties of $SrZn_{1-x}Li_xO_2$ and the effect of Li doping into $SrZnO_2$ on the optical band gap of the parent compound were studied by ultraviolet-visible (UV-Vis) spectroscopy.

For these measurements, we focused on the large scale (2.0 g) $SrZn_{1-x}Li_xO_2$ samples. Their UV-Vis spectra were obtained from powder collected while the pellet samples were cut to electrical specimens. Their UV-Vis spectra were recorded on a Perkin-Elmer Lambda 900 UV spectrometer in the range of 200–800 nm, a data point distance of 0.5 nm and an integration time of 2 s. Data were collected with a scan speed of 0.2 points/nm and slit width of 5 nm.

The optical band gap of $SrZnO_2$ and $SrZn_{1-x}Li_xO_2$ were estimated by utilizing the Tauc plots and extrapolating the linear region of $(\alpha h\nu)^2$ against the $(h\nu)$ axis for a direct transition, in **Figure 4. 28a**, where the Kubelka-Munk function was used for α.

$$F(R_a) = \frac{\alpha}{s} = \frac{(1-R_a)^2}{2R_a} \qquad \textbf{(Eq. 4. 14)}$$

A characteristic absorption was observed in the optical data of $SrZnO_2$ at around 4.3 eV, significantly higher than the literature reported band gap of 3.41 eV[288] and much closer to the HSE06 computed band gap 3.80 eV[287].

Absorption data, in **Figure 4. 28b**, revealed the appearance of two absorption edges: the first one attributed to $SrZnO_2$ (around 4.06 - 4.42 eV) and the second due to minor ZnO impurities (around 3.18 - 3.35 eV), identified only with synchrotron PXRD, in **Figure 4. 29**. The high Kubelka-Munk absorption coefficient of ZnO suggesting that even small amounts of ZnO can produce strong absorption features in the optical spectrum. For instance, the measured Kubelka-Munk absorption coefficient of ZnO ($K\text{-}M_{ZnO} = 4.4$) at 3.3 eV was turned to be 5,000 higher than that of $SrZn_{1-x}Li_xO_2$ ($K\text{-}M_{SZO} = 8.3 \times 10^{-4}$).

The optical band gap of $SrZn_{1-x}Li_xO_2$ samples was found to be unchanged within error from the parent $SrZnO_2$ (inset table in **Figure 4. 28a**), in agreement with the computed electronic structure of the doped material which do not show any acceptor bands above the valence band.

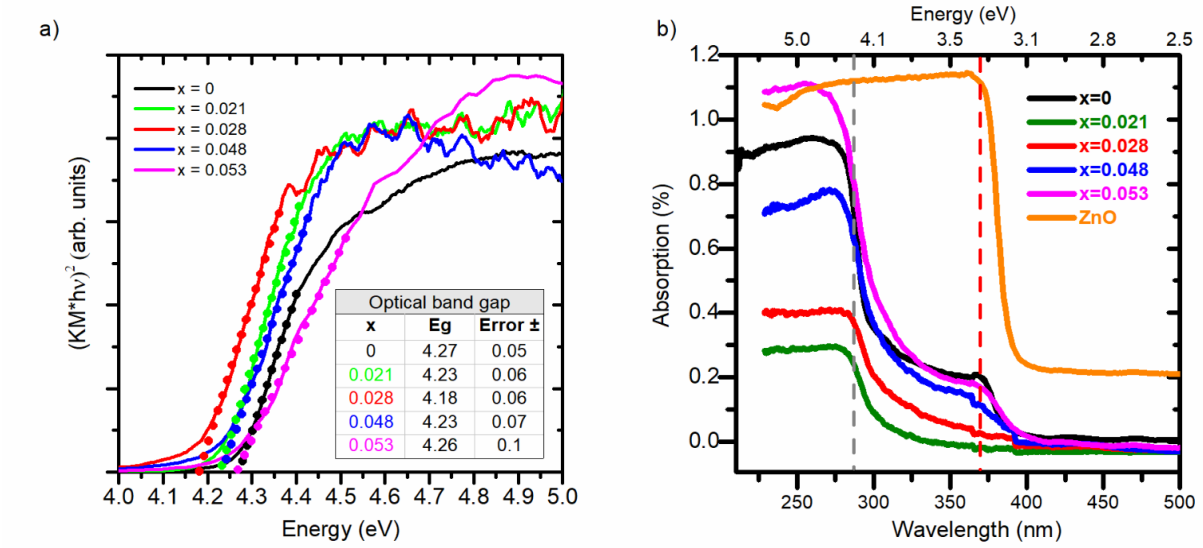

Figure 4. 28: (a) Tauc plots and (b) Absorption data of $SrZn_{1-x}Li_xO_2$ samples. The dashed lines represent the measured optical band gaps for $SrZnO_2$ (in grey) and ZnO (in red) at 4.27 eV and 3.37 eV respectively.

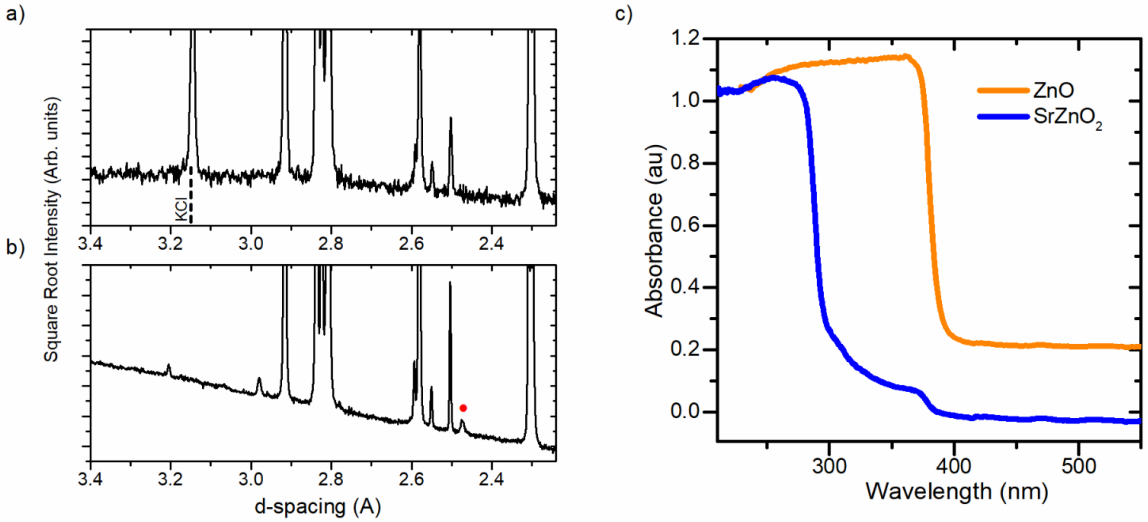

Figure 4. 29: Lab (a) and synchrotron (b) PXRD data, in square root intensity scaling, for $SrZnO_2$ sample. Symbol (●) indicates ZnO-indexed reflection peak not previously detected in laboratory PXRD data. (c) Absorption data of this sample, where the minor absorption edge around 370-390 nm corresponds to the absorption of ZnO (c.f. orange curve).

4.5 Thin film deposition of $SrZnO_2$

4.5.1 Exploratory depositions

To investigate the growth of $SrZnO_2$ films by PLD, a 20-mm diameter target was prepared by scaling up the synthetic protocol of **section 4.1.1**. The crystalline structure of the target showed to be single-phase and its unit cell lattices were found to be in agreement with our earlier findings, in **Figure 4. 30**.

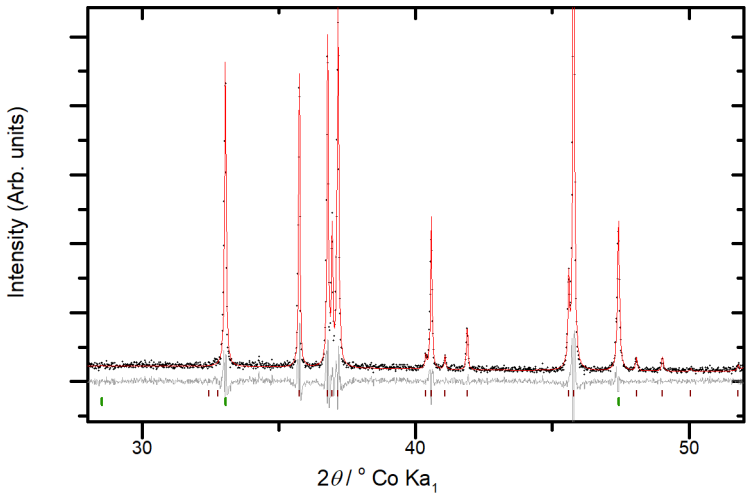

Figure 4. 30: PXRD pattern of the as-synthesised $SrZnO_2$ PLD-target.

Once the PLD target was made, a set of exploratory film growths on (0001)-Al_2O_3 (sapphire) substrates were performed over a wide range of oxygen pressures (1 to 500 mTorr) and substrate temperature (500 to 900 °C), as summarized in **Figure 4. 31**. In these depositions, the substrate-target distance was held at 100 mm, the laser fluence at 0.96 Jcm^{-2} with a repetition of 2 Hz and the films thickness was set to 60,000 pulse laser shots.

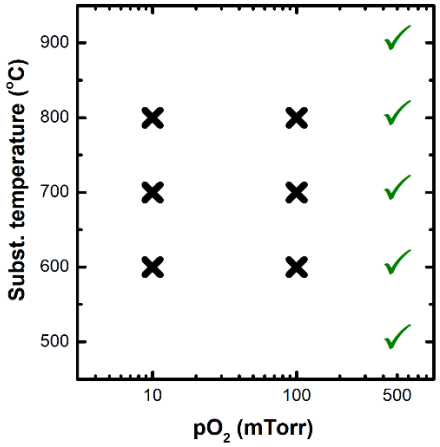

Figure 4. 31: Summary of examined $SrZnO_2$ film growth conditions. With green tick are marked the growth conditions where a single-oriented film was obtained.

At first sight, our results seem to confirm the only available reference on $SrZnO_2$ growth by pulsed laser deposition (PLD) where, according to Jung et al.[289], a (112)-oriented $SrZnO_2$ film was reported to have been grown on (0001)-Al_2O_3 at 500 °C and a partial pressure of oxygen of 300 mTorr. In **Figure 4. 32**, our findings have shown that single-oriented films were only possible to grow at 500 mTorr. The crystallinity of the as-grown films was found to be improved as the substrate temperature reached 800 °C. Further increase of temperature (to 900 °C) gave rise to secondary reflections while depositions at lower oxygen pressures (5, 10 and 100 mTorr -not shown) resulted in amorphous films. The coincidence, however, of diffraction peaks of $SrZnO_2$ and ZnO at the vicinity of the as-grown film peaks (see also **Appendix B**) requires further study of their crystal structure. In the following section, more conclusive results on the crystal structure of the as-grown films will be obtained by pole figure measurements.

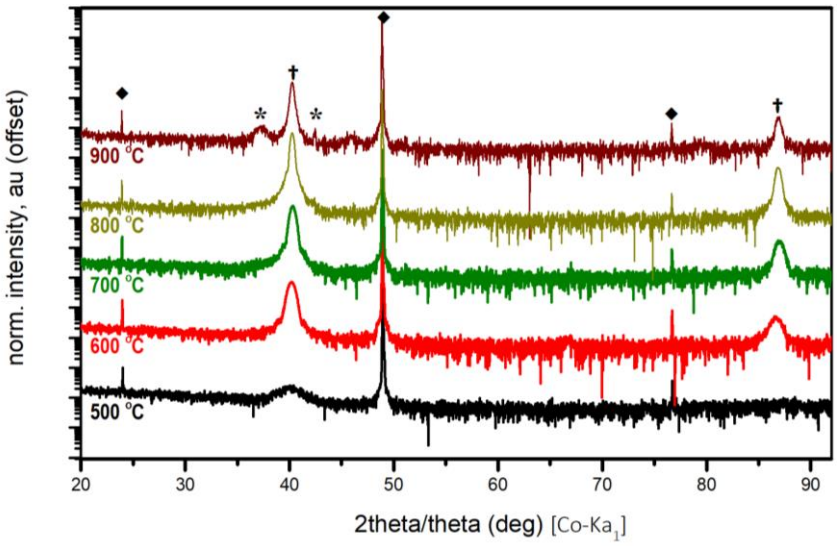

Figure 4. 32: Out-of-plane θ/2θ scans of films grown on (0001) Al_2O_3 substrates at different substrate temperatures. The rest of the deposition parameters were as follows, chamber pO_2 pressure: 500 mTorr; pulsed laser shots: 60,000; target to substrate distance: 100 mm and laser fluence of 0.96 J.cm^2. Peaks denoted with (✝) indicate main reflections of the as-grown films (ZnO) and with the symbol (*) are marked secondary impurity phases. With (◆) are highlighted the Al_2O_3 substrate peaks.

4.5.2 Pole Figure characterization

To determine the in-plane symmetry of the as-grown films of **Figure 4. 32**, pole figure measurements have been performed on the film obtained at 800 °C, with a four circle Panalytical X'Pert PRO diffractometer (Cu-K_{a1}). Assuming the films had grown along the (012)-$SrZnO_2$ direction, pole figures measurements were initially performed focusing on the high intensity in-plane (111)-$SrZnO_2$ reflection.

The three sharp pole figures at ψ = 38° and φ spacing of 120°, in **Figure 4. 33**, are coming from the (111) planes of the underneath Al_2O_3 substrate. Moving to higher ψ angles, a set of six poles at ψ = 56° and φ-offset of 60° reveals the six-fold symmetry of the as-grown film contrary to the expected four-fold orthorhombic symmetry of $SrZnO_2$.

To complete the characterization of the film, we also confirmed the (00*l*)-growth of ZnO films on (0001)-Al_2O_3 by pole figure measurements performed in the high intensity in-plane (011)-ZnO reflection. In agreement with our previous results, the collected data in **Figure 4. 34** confirmed a six-fold symmetry on the pole figure of the film, at ψ = 38° and φ-spacing of 120°, corresponded to the hexagonal ZnO.

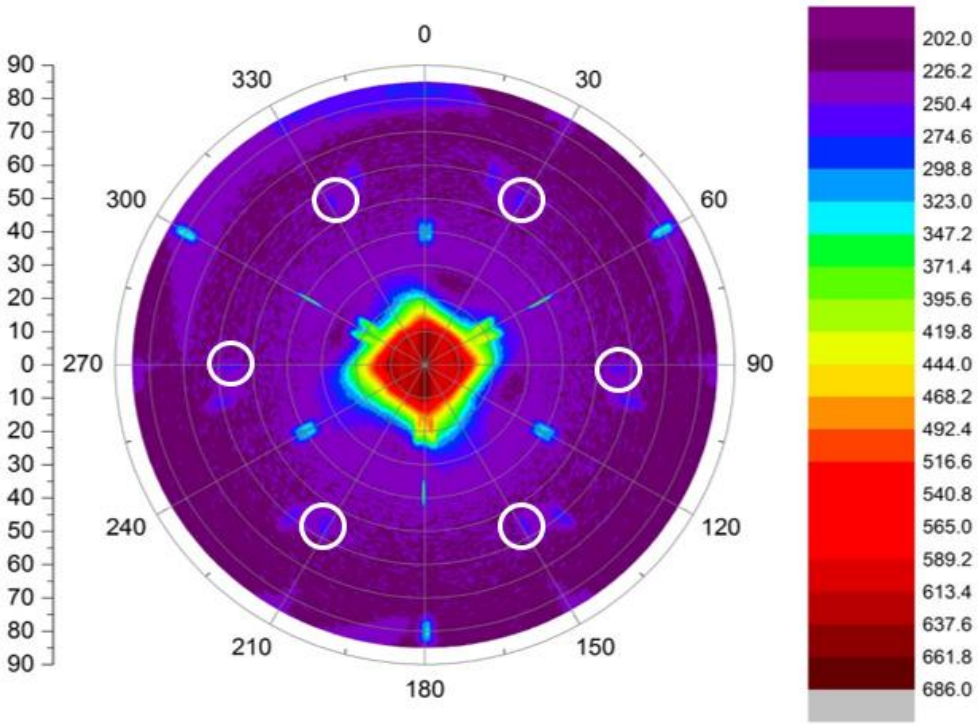

Figure 4. 33: Pole figure on the film grown at 800 °C of **Figure 4. 32**. Scan for peaks at 2θ = 37.05° corresponding to $SrZnO_2$ (111). With open white cycles are marked the poles of the examined film.

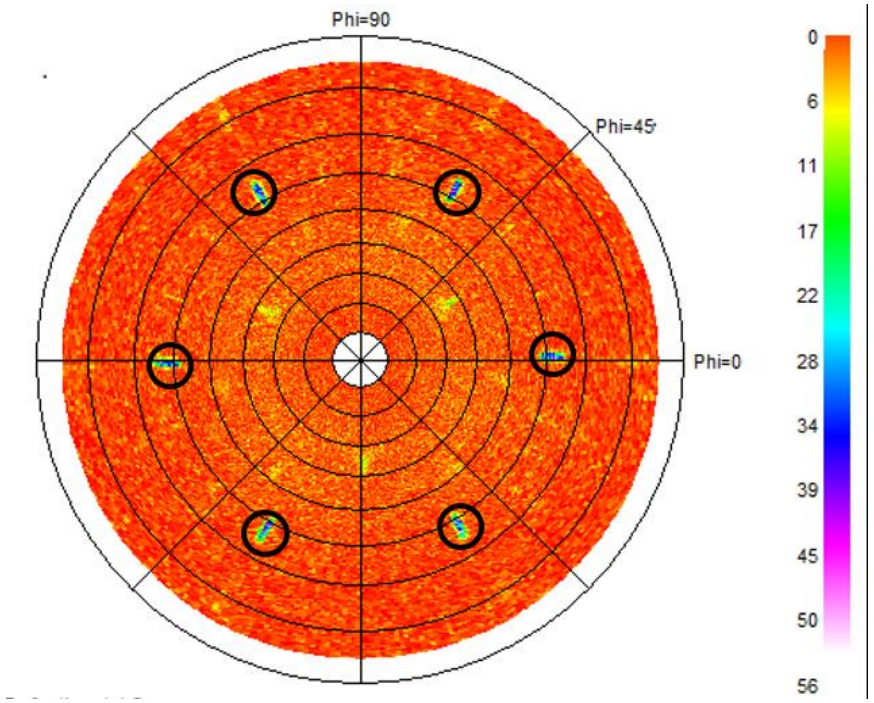

Figure 4. 34: Repeat of pole figure scan on the film grown at 800 °C of **Figure 4. 32**. Scan for peaks at 2θ = 42.30° corresponding to ZnO (011). With open black cycles are marked the poles of the examined film.

4.5.3 EDX/SEM characterization of SZO films

To further elaborate our understanding on the as-grown films of **Figure 4. 32** in **section 4.5.1**, the temperature dependence of their Sr/Zn composition ratio was studied by energy dispersive X-ray analysis.

The elemental composition of the studied films, in atomic percentage (at %), is summarized in **Table 4. 7** along with the growth conditions of the studied films. There, it can be seen that the predominant deposition of Zn was confirmed in all the examined films, in agreement with our previous pole figure measurements.

Table 4. 7: Elemental composition of films grown under different substrate temperatures at 500 mTorr.

Film sample	Temp	pO_2	Laser Fluence	Distance Target-subsrt.	Thickness	Zn – Sr ratio
	(°C)	(mTorr)	(J/cm^2)	(mm)	(laser shots)	(atomic. %)
1	700	500	0.96	100	60,000	100 – 0
2	800	500	0.96	100	60,000	100 – 0
3	900	500	0.96	100	60,000	100 – 0

In a following step, we investigated the role of laser energy on the crystallinity and composition of the as-grown films. To do so, a next set of depositions was carried out at laser fluences of 0.90, 1.00 and 1.12 J/cm^2 with a substrate temperature of 800 °C and a chamber pO_2 of 500 mTorr, in **Figure 4. 36**. The substrate-to-target distance was initially kept at 100 mm for the films grown at 0.90 J/cm^2 and 1.00 J/cm^2 and reduced to 65 mm for the film grown at 1.12 J/cm^2.

EDX measurements have shown that the films grown at 0.90 J/cm^2 and 1.00 J/cm^2 were found to be dominantly Zn-based, as can be seen in **Table 4. 8**. On the contrary, the elemental composition of the film grew at 1.12 J/cm^2 revealed the stoichiometric deposition of Sr and Zn cations (1:1). However, the obtained XRD scan of this film was found to be similar to these of the Zn-based films, in **Figure 4. 36,** indicating the amorphous deposition of a Sr-rich phase together with the single-oriented ZnO film.

Characteristic EDX spectra of ZnO and $SrZnO_2$ films are presented in **Figure 4. 35**.

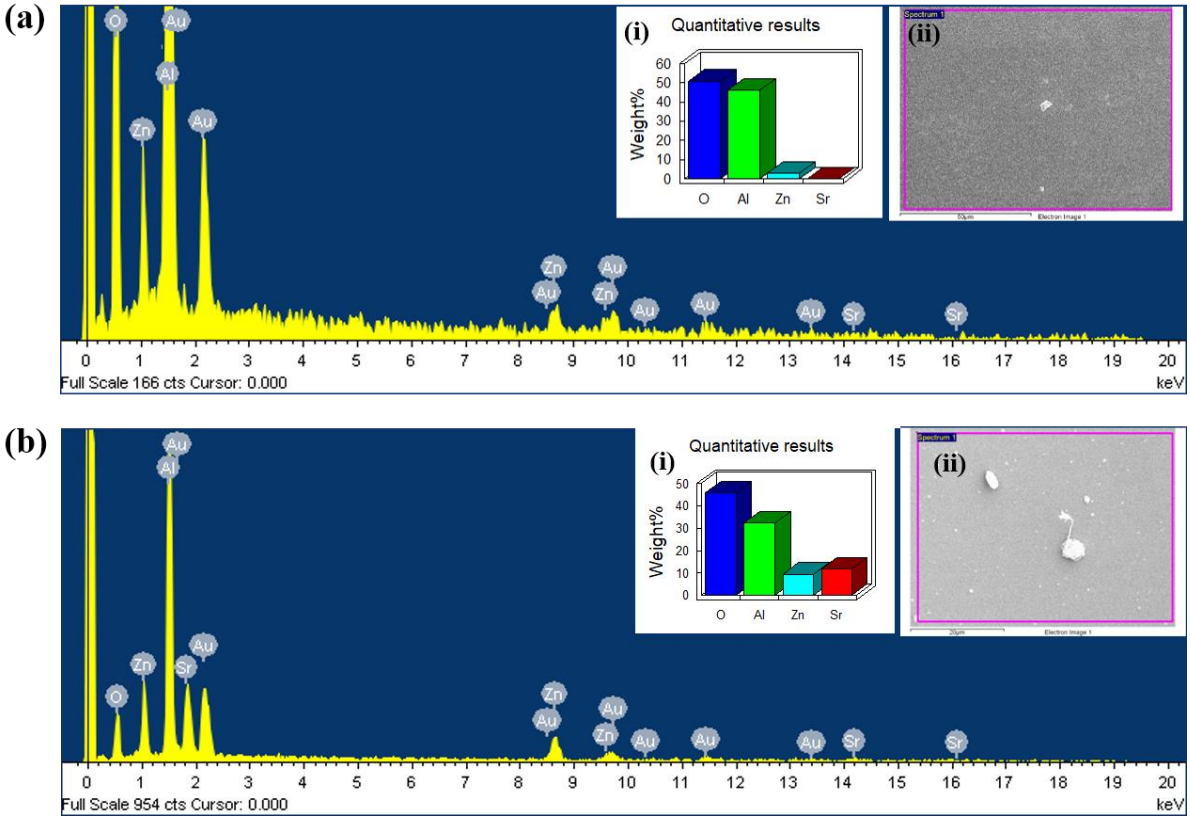

Figure 4. 35: EDX spectra by scanning electron microscopy of (a) ZnO and (b) $SrZnO_2$ films. In insets (i) and (ii) are shown the received by the software semi-quantitative reports of elemental composition and the SEM micrographs of the measurements, respectively. The high intensity Al peak, in both spectra, is originating from the Al_2O_3 substrate. Au signal is coming from the used Au coating.

Lastly, one more film was deposited under vacuum (base pressure of $2x10^{-7}$ Torr) and at room temperature (RT) with a substrate-to-target distance of 65 mm and a laser fluence of 1.12 J/cm^2, in **Figure 4. 37**. Although X-rays revealed the amorphous nature of the as-grown film, EDX measurements unveiled the predominant deposition of Sr, in **Table 4. 8**.

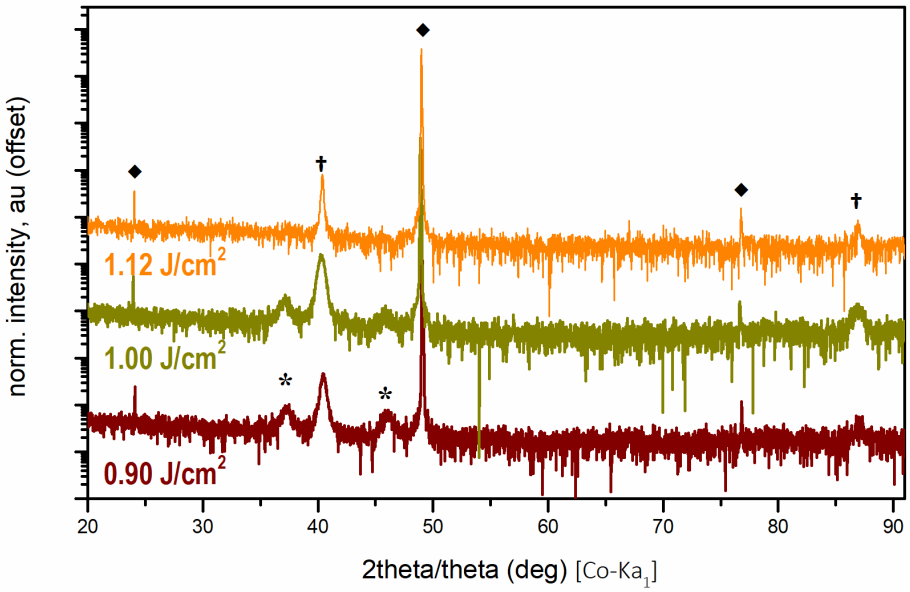

Figure 4. 36: Out-of-plane θ/2θ scans of films grown on (0001) Al_2O_3 substrates at different laser fluences, pO_2 and substrate-to-target distance. Films deposited at: 0.90, 1.00 and 1.12 J/cm^2 with substrate temperature: 800 °C; chamber pO_2: 500 mTorr; pulsed laser shots: 60,000. The substrate-to-target distance was initially set to 100 mm for the films grown at 0.90 and 1.00 J/cm^2 and reduced to 65 mm for the film of 1.12 J/cm^2. As before, peaks denoted with (✝) indicate main reflections of the as-grown films (ZnO) and with the symbol (*) are marked secondary impurity phases. Al_2O_3 substrate peaks are highlighted with (◆).

Table 4. 8: Elemental composition of film grown under different substrate temperatures at 500 mTorr (**Figure 4. 36**) and under vacuum at room temperature (**Figure 4. 37**).

Film sample	Temp	pO_2	Laser Fluence	Distance Target-subsrt.	Thickness	Zn – Sr ratio
	(ºC)	(mTorr)	(J/cm^2)	(mm)	(laser shots)	(atomic. %)
1	800	500	0.90	100	60,000	100 – 0
2	800	500	1.00	100	60,000	100 – 0
3	800	500	1.12	65	60,000	50 – 50
4	RT	Vacuum (2x10^{-4})	1.12	65	60,000	33 – 67

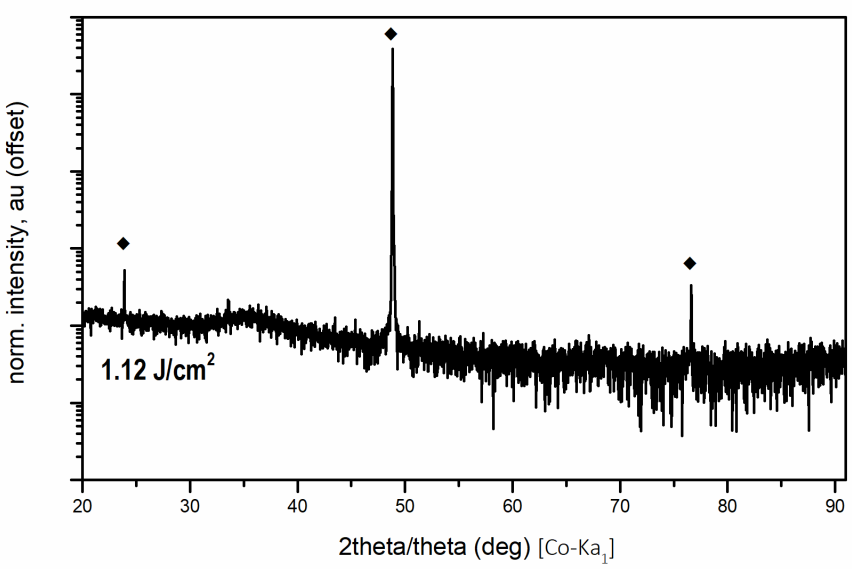

Figure 4. 37: Amorphous film grown at room temperature under vacuum (base pressure of $2x10^{-7}$ Torr) with laser fluence of 1.12 J/cm^2 and a 65 mm distance of target to substrate. Al_2O_3 substrate peaks are highlighted with (◆).

4.5.4 Polycrystalline $SrZnO_2$

4.5.4.1 Polycrystalline $SrZnO_2$ at higher laser fluences

Having seen in the previous section that an increased laser fluence of 1.12 J/cm^2 led to the stoichiometric deposition of Sr and Zn, we will focus our attention on depositions of even higher laser fluences.

Films of 60,000 laser shots were grown at laser fluences of 1.12, 1.25 and 1.41 J/cm^2 while keeping the substrate temperature and oxygen pressure at 800 °C and 500 mTorr, respectively. The substrate-to-target distance was kept on this set of depositions at 65 mm.

With the completion of the depositions, the XRD scans of the films were immediately collected on a two circle Panalytical X'Pert PRO diffractometer (Co K_{a1}) revealing the growth of polycrystalline $SrZnO_2$ and ZnO films *at* all the used laser fluences, as seen in **Figure 4. 38a** and **Figure 4. 39a**.

However, the polycrystalline $SrZnO_2$ was found to be chemically stable in dry conditions (over an examined period of one month) only when the films were deposited at a laser fluence higher

than 1.25 J/cm^2. On the contrary, films grown at lower fluences (of 1.12 J/cm^2) were found to decompose to ZnO and (amorphous) $SrCO_3$, as seen in **Figure 4. 38b** and **Figure 4. 39b**.

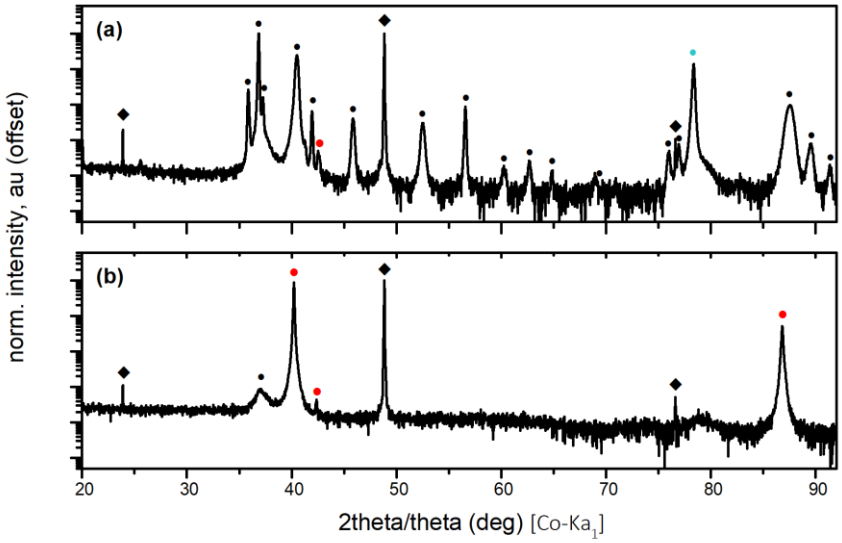

Figure 4. 38: Out-of-plane θ/2θ scans. Chemical stability of polycrystalline $SrZnO_2$ grown on (0001) Al_2O_3 substrates at 800 °C, pO_2 of 500 mTorr and laser fluence of 1.12 J.cm^2. (a) XRD scan collected immediately after the film deposition, (b) Repeated XRD scan of the previous film after stored in dry conditions over a period of two weeks. Peaks denoted with (•) indicate film reflections of $SrZnO_2$ and with (•) of ZnO film. With (◆) are highlighted the Al_2O_3 substrate peaks.

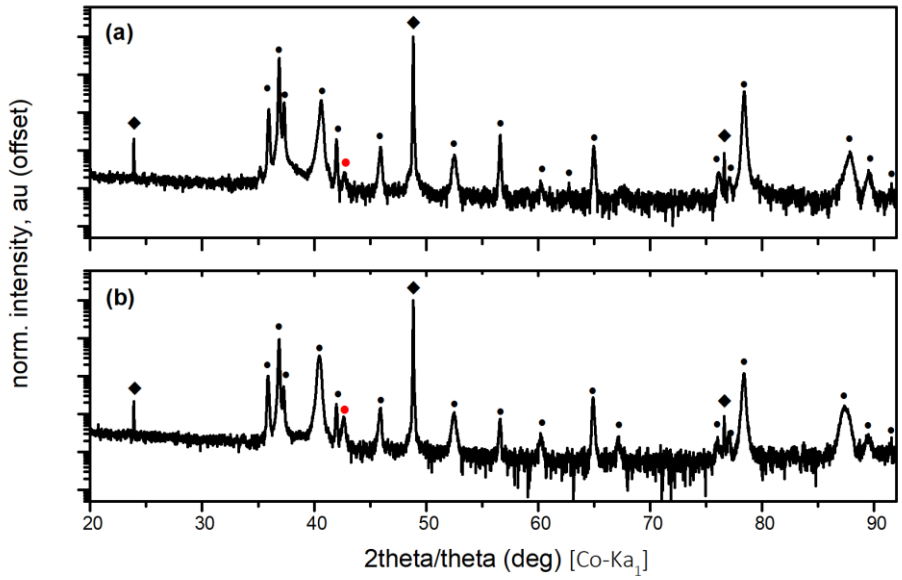

Figure 4. 39: Out-of-plane θ/2θ scans. Chemical stability of polycrystalline $SrZnO_2$ films deposited on (0001) Al_2O_3 at 800 °C, pO_2 of 500 mTorr and laser fluences of: (a) 1.25 J.cm^2 and (b) 1.41 J.cm^2. The $SrZnO_2$ films retained their polycrystalline nature while stored in dry conditions over one month period. As before, peaks denoted with (•) indicate film reflections of $SrZnO_2$ and with (•) of ZnO. With (◆) are highlighted the Al_2O_3 substrate peaks

The texture of the as-grown polycrystalline $SrZnO_2$ films was studied with the Williamson-Hall (W-H) method. To do so, we focused on the film deposited at the highest laser fluence (1.25 J/cm^2) of **Figure 4. 39a** and we calculated the size (β_L) and strain (β_e) broadening of non-overlapping to ZnO peak reflections according to the relations:

$$\beta_e = Ce\ tan\theta \quad \textbf{(Eq. 4. 15)}$$

$$\beta_L = \frac{K\lambda}{L\ cos\theta} \quad \textbf{(Eq. 4. 16)}$$

Assuming that their convolution is a simple sum we can write:

$$\beta_{tot} = \beta_e + \beta_L \quad \textbf{(Eq. 4. 17)}$$

and so:

$$\beta_{tot}\ cos\theta = C\varepsilon sin\theta + \frac{K\lambda}{L} \quad \textbf{(Eq. 4. 18)}$$

Finally, when plotting the $\beta_{tot}\cos\theta$ as a function of $\sin\theta$, in **Figure 4. 40**, the anisotropic growth of $SrZnO_2$ films towards the (00*l*) direction was possible to be observed.

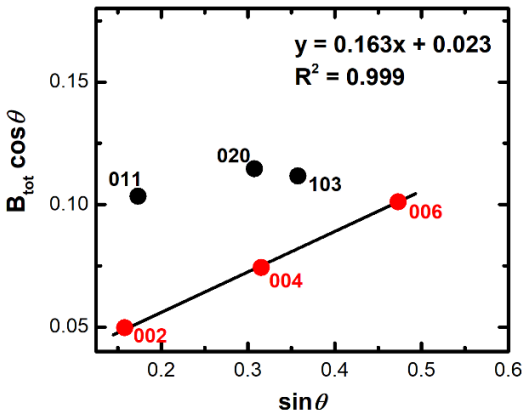

Figure 4. 40: Williamson-Hall (W-H) plot of the polycrystalline $SrZnO_2$ film grown at 800 ºC, pO_2 of 500 mTorr and laser fluence of 1.25 J/cm^2 (film on **Figure 4. 39a**).

4.5.4.2 Film growths at low pO_2 conditions

With the film deposited at room temperature in **Table 4. 8** of **section 4.5.3** found to be Sr-rich, we have also examined the room temperature growth of films under different oxygen pressures.

Three films were deposited at room temperature under oxygen pressures of: (a) 1, (b) 10 and (c) 100 mTorr. The rest of the growth conditions were accordingly set as follows: laser fluence,

1.25 J/cm^2; target-to-substrate distance, 65 mm and laser shots, 60,000. Once the films were deposited, they were annealed at 800 °C inside the deposition chamber for 4 hours under 500 mTorr and their XRD patterns were collected as soon as the films were cooled down, in **Figure 4. 41a**.

In all the cases, films of a mixture of ZnO, $SrCO_3$ and $SrZnO_2$ were obtained, with the $SrZnO_2$ phase being however less crystalline than the polycrystalline $SrZnO_2$ film of **section 4.5.4.1**. Among them, the film deposited at 1 mTorr demonstrated the more pronounced growth of $SrZnO_2$, although not chemically stable inside in dry air over one week period, in **Figure 4. 41b**. In all the cases, EDX/SEM measurements verified the Sr-rich composition of the films, in **Table 4. 9**.

With the deposition of Sr being favoured at low pO_2, we also attempted at last the grow of $SrZnO_2$ at 1 mTorr and 800 °C followed by a post-deposition anneal step at 800 °C and 500 mTorr for 4h to facilitate the recrystallization of the film. Again, however, far from obtaining a polycrystalline $SrZnO_2$ film, the resulting deposition was an amorphous film not free of the parasitic $SrCO_3$ and ZnO phases, as seen in **Figure 4. 41c**.

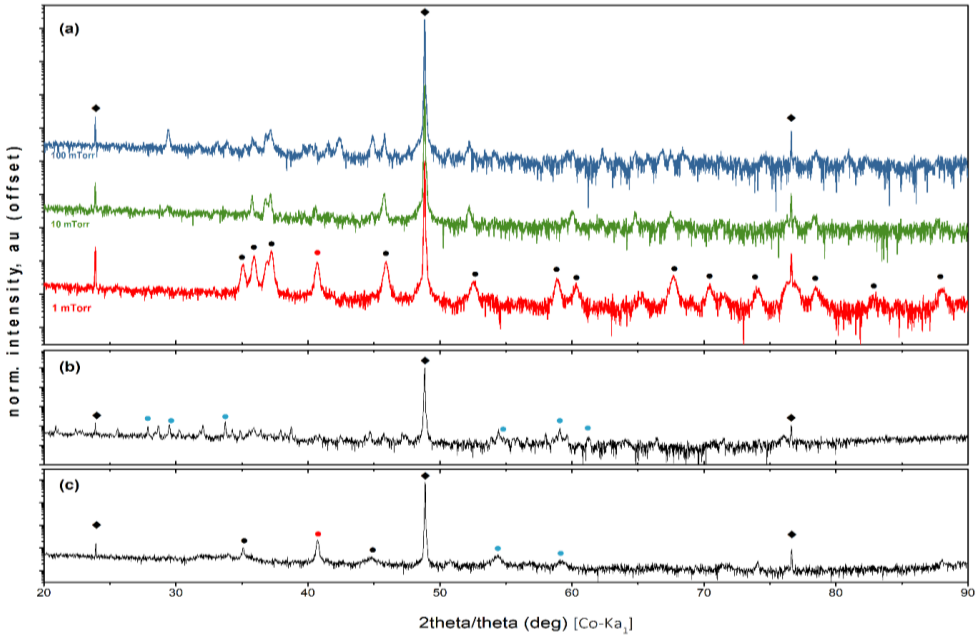

Figure 4. 41: (a) Out-of-plane 2θ/θ scans of films grown on (0001) Al_2O_3 substrates at room temperature and different pO_2 and subsequently subjected to an in-situ post-deposition treatment for 4h at 800 °C under 500 mTorr. (b) Chemical stability of an as-grown polycrystalline SZO film at RT under 1 mTorr, over a period of one week. The sample was kept during this period in dry conditions under ambient atmosphere. (c) out-of-plane 2θ/θ for a film grown at 800 °C under 1 mTorr and subject in post-deposition anneal for 4h at 800 °C under 500 mTorr. In all the figures, peaks denoted with (•) indicate film reflections of SZO, with (•) of ZnO and (•) of $SrcO_3$. The Al_2O_3 substrate peaks are highlighted with (◆).

Table 4. 9: Elemental composition of films grown under different oxygen pressures at RT.

Film sample	Temp	pO_2	Laser Fluence	Distance Target-subsrt.	Thickness	Zn – Sr ratio
	(°C)	(mTorr)	(J/cm^2)	(mm)	(laser shots)	(atomic. %)
1	RT	1	1.25	65	60,000	30 – 70
2	RT	10	1.25	65	60,000	23.2 – 76.8
3	RT	100	1.25	65	60,000	26.3 – 73.7

4.6 Summary and conclusions

Despite the great interest in *p*-type doping of ZnO, the synthesis of a stable and low resistance *p*-type zinc oxides is still in search. In this route, computational chemistry provides a pathway to the theoretical understanding of existing experimental limits, offering a screening approach to identify candidate compounds and designing new systems. Towards this direction, computational studies by Gupta et al. have been successfully utilized to screen *p*-type dopants in $SrZnO_2$. Calculations of substitution energetics and finite temperature doping effect of $SrZnO_2$ have suggested Li^{1+} as the most favourable, among other group-I candidates, *p*-type dopant.

During the work of this thesis, we experimentally investigated the solid-state synthesis of Li, Na, K and Ag doped $SrZnO_2$ through the routes of (i) the conventional solid-state synthesis and (ii) the anaerobic conditions of peroxide precursors. At the end, the successful incorporation of Li into $SrZnO_2$ was possible through the conventional solid-state route when lithium volatility was suppressed with the use of sacrificial powders. Highly crystalline $SrZn_{1-x}Li_xO_2$ ceramics have been synthesized first in an exploratory and accordingly in a following measurement series of confirming the reproducibility of the $SrZn_{1-x}Li_xO_2$ materials by PXRD and ICP studies.

Preliminary AC impedance measurements on $SrZn_{1-x}Li_xO_2$ samples of different geometries (disc- and rectangular-shaped) were found to be in agreement with DC conductivity measurements, confirming the dominant bulk conductivity contribution of the system.

The $SrZn_{1-x}Li_xO_2$ samples showed an increase of more than an order of magnitude in their conductivity compared to the parent $SrZnO_2$. The conductivity of $SrZn_{1-x}Li_xO_2$ was seen to increase with the partial pressure of oxygen suggesting a *p*-type conduction, which was later confirmed by thermopower measurements and the observation of a positive Seebeck coefficient. However, the conductivities of $SrZn_{1-x}Li_xO_2$, ranging from 1×10^{-6} to 3.5×10^{-6} S/cm at 600°C, where found to be significantly lower than the reported values of other thin-film *p*-type conducting materials. In addition, the high values of measured activation energies for $SrZnO_2$ and $SrZn_{1-x}Li_xO_2$ indicate the possible contribution of ionic components (lithium or oxygen diffusion) to the total material conductivity which could be investigated in future work by independent electronic and ionic conductivity measurements.

The low conductivity of $SrZn_{1-x}Li_xO_2$ could possibly be attributed to donor compensation mechanisms such as the formation of oxygen vacancies and interstitial lithium atoms and

neutralizing the acceptors Li'_{Zn} dopants, as previously has been seen on *p*-type ZnO doping, and could be studied computationally in more detail.

Since K was being suggested by the computational study of Gupta et al.[287] as the second most favorable energetically candidate of $SrZnO_2$, $Sr_{1-x}K_xZnO_2$ doping under the same synthetic protocol of sacrificial powders used for $SrZn_{1-x}Li_xO_2$ is worth to be experimentally re-examined in the future.

The optical gap of $SrZnO_2$ was found at 4.27 eV and unchanged within error with the incorporation of Li into the structure. This value is higher than that previously reported at 3.41 eV on the literature, confirming the optical transparency of $SrZn_{1-x}Li_xO_2$ samples as their conductivity was increased.

Additional experimental work was carried out to identify the growth conditions towards a single-oriented $SrZnO_2$ film on Al_2O_3 (000l) substrate by PLD. Preliminary depositions of single-oriented films deposited on (0001)-Al_2O_3 substrates, according to literature references, have been identified by pole figure measurements as ZnO.

A stoichiometric deposition of Sr:Zn was only obtained for films grown in higher laser energies, confirmed by EDX/SEM measurements, although the resulted polycrystalline $SrZnO_2$ films were not found to be free of extra ZnO reflections. The deposited $SrZnO_2$ films showed a decomposition behaviour towards ZnO and (amorphous) $SrCO_3$ over time unless stored under dry conditions, limiting the range of applications that can be implemented.

Overall, this work demonstrated a viable workflow for the identification of *p*-type transparent materials that combines experimental and computational approaches. Guided by computational studies of the relative energetics of competing phases, we experimentally confirm the successful synthesis of $SrZn_{1-x}Li_xO_2$ as a new *p*-type transparent material. Although the low conductivity of $SrZn_{1-x}Li_xO_2$ is limiting its practical applications, its successful synthesis has also marked a doping strategy that could be applied in the future to other zinc containing *p*-type oxides.

References

[283] M.A. Hernández, N. Masó, A.R. West, *Appl. Phys. Lett.***108**, 2016, 152901

[284] N. Maso, A.R. West, *Chem. Mater.* **27**, 2015, 1552

[285] H. Rickert, *Electrochemistry of Solids - An Introduction*, Springer-Verlag, Berlin, 1982

[286] P. Ren, N. Masó and A.R. West, *Phys. Chem. Chem. Phys.***15**, 2013, 20943

[287] C.A Tzitzeklis, J.K. Gupta, M.S. Dyer, T.D. Manning, M.J. Pitcher, H.J. Niu, S. Savvin, J. Alaria, G.R. Darling, J.B. Claridge, M.J. Rosseinsky, *Inorg. Chem*., 2018, 57 (19), 11874

[288] A. Manavbasi, J.C. LaCombe, M. Batzill, U. Diebold, *J. Lumin.* **79**, 2005, 129

[289] Y.R. Jung, H.K. Yang, B.K. Moon, B.C. Choi, J.H. Jeong, H. Choi, J.H. Kim, K.H. Kim, *J. Nanosci. Nanotechnol*. **11**, 2011, 871

Chapter 5: Ferroelectric and magnetic properties of BTFM-CTO films

The epitaxial growth of morphotropic $0.85BiTi_{0.1}Fe_{0.80}Mg_{0.1}$ - $0.15CaTiO_3$ (BTFM-CTO) films and their ferroelectric and magnetic properties were studied in this chapter.

Stoichiometric and Bi-rich BTFM-CTO targets were obtained after scaling up the synthetic protocol which was originally developed by Mandal et al.[290] and their structural and elemental characterization was carried out by PXRD and SEM/EDX studies in **section 5.1**.

Exploratory depositions in LAO and STO substrates identified a narrow window of growth conditions in which stoichiometric BTFM-CTO films were obtained, in **section 5.2.2**. The reproducible growth of morphotropic BTFM-CTO films was examined in films of different thicknesses in STO substrates, in **section 5.2.3**. The epitaxial growth of high quality morphotropic (orthorhombic/rhombohedral) BTFM-CTO films in STO and tetragonal-like films in LAO substrates was confirmed by in-house and synchrotron XRD studies in **sections 5.2.4** and **5.2.5**, respectively.

The electrical properties of morphotropic BTFM-CTO films were examined in **section 5.3**. To do so, the growth and characterization of morphotropic BTFM-CTO films had initially to be repeated on a $SrRuO_3$ buffer layer acting as a bottom electrode, in **section 5.3.1**. The ferroelectric properties of BTFM-CTO were accordingly studied on relatively thick films (13,000 laser shots) where the morphotropic growth of BTFM-CTO was better controlled. The magnetic properties of the as-grown BTFM-CTO films are presented in **section 5.4**.

5.1 Synthesis of BTFM-CTO targets

5.1.1 Synthetic protocol of BTFM-CTO targets

There is a substantial amount of work in PLD growth reviewing the stoichiometric deposition of volatile elements such as bismuth[291]. The use of a Bi-rich target, typically of 10-25% excess, is one of the most common approaches to compensate the bismuth losses during the deposition. In this work, the deposition of $0.85BiTi_{0.1}Fe_{0.80}Mg_{0.1}$ - $0.15CaTiO_3$ (BTFM-CTO) films was investigated using two different targets: (a) target-A of the nominal, stoichiometric composition: $[Bi_{0.85}Ca_{0.15}][Ti_{0.235}Fe_{0.69}Mg_{0.085}]O_3$ and (b) target-B of a Bi-rich composition with the formula: $Bi_{0.21}[Bi_{0.85}Ca_{0.15}][Ti_{0.235}Fe_{0.69}Mg_{0.085}]O_3$.

The sintering protocol used to prepare phase-pure BTFM-CTO targets has been originally developed by Mandal et al.[290]. High purity starting materials of $CaCO_3$ (99.997% Alfa Aesar), Fe_2O_3 (99.998% Alfa Aesar), TiO_2 (99.995% Alfa Aesar) and ultra-pure Bi_2O_3 (99.9995% Alfa Aesar) were dried overnight at 473 K before weighing. As-received hydrated magnesium carbonate hydroxide, $(MgCO_3)_4 \cdot Mg(OH)_2 \cdot 5H_2O$ (99.99% Alfa Aesar), was used as Mg source.

The detailed steps of the protocol for large scale targets were as follows:

(1) The starting materials were stoichiometrically weighed in 4 separated batches that were ball-mixed for 22 hours in ethanol to improve the homogeneity of the synthesized targets.

(2) Next, the four batches were dried and hand-ground one by one before mixed all together, re-ground and subjected to a first calcination step for 12 hours at 750 ºC into an open lid alumina crucible.

(3) The resultant mixture was then re-ground and separated in 4 pellets of 20 mm diameter and 1-2 mm thick, placed the one over the other inside a closed lid (lined with Pt foil) crucible, before calcined for a second time at 920 ºC for 12 hours.

(4) The received pellets were once more ground separately and ball milled in ethanol for 22 hours with the addition of 2 wt. % polyvinyl butyral (organic binder). Each batch was dried and ground separately before mixed and reground all together.

(5) For the last sintering step, the mixture was pelletized, pressed isostatically under 2000 bar, placed in a close lid, Pt-foiled alumina crucible and fired at 930 ºC for 12 hours. All the firings were conducted in ambient atmosphere.

The crystalline phases and the chemical composition of the resulting targets were characterized with the use of PXRD and EDX studies.

5.1.2 Characterization of BTFM-CTO targets

The PXRD patterns of the as-synthesized targets were collected after detailed scans (0.01°/min step size) on finely ground small scale (0.3 g) pellets of the exact same sintering history. The obtained PXRD data were thereafter compared to the PXRD pattern of a phase-pure $0.85BiTi_{0.1}Fe_{0.80}Mg_{0.1}$ - $0.15CaTiO_3$ bulk sample, synthesised by Dr. Mandal.

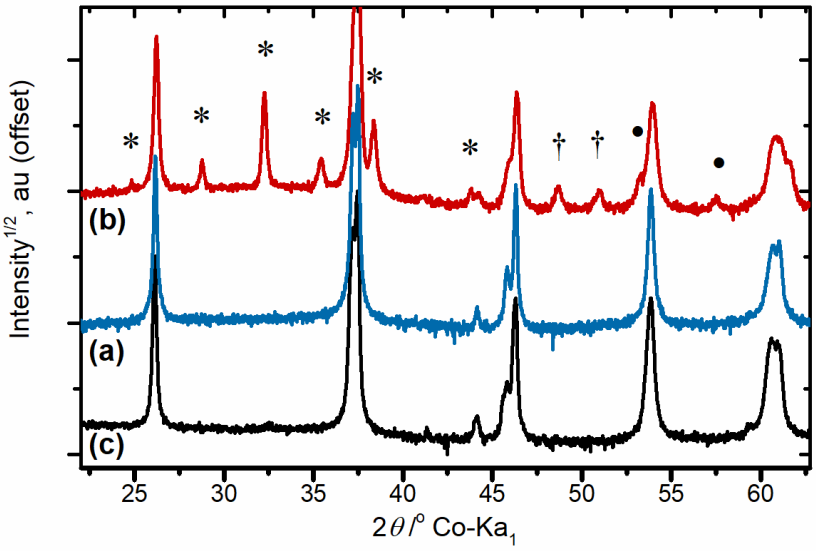

Figure 5. 1: PXRD patterns of (a) stoichiometric and (b) Bi-rich BTFM-CTO targets. For comparison reasons, the PXRD pattern of (c) a phase-pure BTFM-CTO bulk sample (synthesised by Dr. Mandal) is also presented. Impurity peaks of $Bi_5FeTi_3O_{15}$ (*), $MgFe_2O_4$ (†) and $Bi_{25}FeO_{40}$ (•) are denoted in the case of the Bi-rich target. All the patterns were collected at the same scanning conditions of 0.01°/min step size.

As seen in **Figure 5. 1**, the collected PXRD pattern of the stoichiometric target was found to coincide well with the phase-pure bulk $0.85BiTi_{0.1}Fe_{0.80}Mg_{0.1}$-$0.15CaTiO_3$ sample, synthesized by Dr. Pranab Mandal. In the case of the Bi-rich target, $0.85Bi_{0.21}Ti_{0.1}Fe_{0.80}Mg_{0.1}$ - $0.15CaTiO_3$, the excess of Bi has given rise to secondary impurity phases of $Bi_5FeTi_3O_{15}$ (*), $MgFe_2O_4$ (†) and $Bi_{25}FeO_{40}$ (•).

Elemental composition analysis of the stoichiometric (target-A) and Bi-rich (target-B) targets was performed by EDX/TEM spectroscopy in a JEOL 2000FX instrument equipped with an EDAX spectrometer. Several particles of powder from each sample were chosen at random and analysed to determine the powder composition. The powders of each sample were dispersed in small amount of ethanol and deposited on a copper TEM grid. Correction factors, obtained from suitable reference compounds, were also applied to the collected raw data.

To inspect the elemental composition of the targets, their EDX/TEM data were plotted according to the cation positions in the perovskite unit cell on: (i) ternary diagrams of the Fe/Ti/Mg (B-site) cations and (ii) column charts of the Bi/Ca (A-site) cations. Lastly, to assess the ratio of the ferroelectric bismuth (in A-site) to the magnetic iron (in B-site), the (iii) Bi/Fe content of the targets was also plotted in column charts.

As can be seen in **Figure 5. 2** and **Figure 5. 3**, the analysed EDX/TEM data of the stoichiometric target have shown an elemental composition coinciding well with the expected nominal composition. Altogether, the TEM results and the free of impurities PXRD pattern of the examined sample confirmed the synthesis of a phase-pure, stoichiometric $0.85BiTi_{0.1}Fe_{0.80}Mg_{0.1}$ - $0.15CaTiO_3$ target.

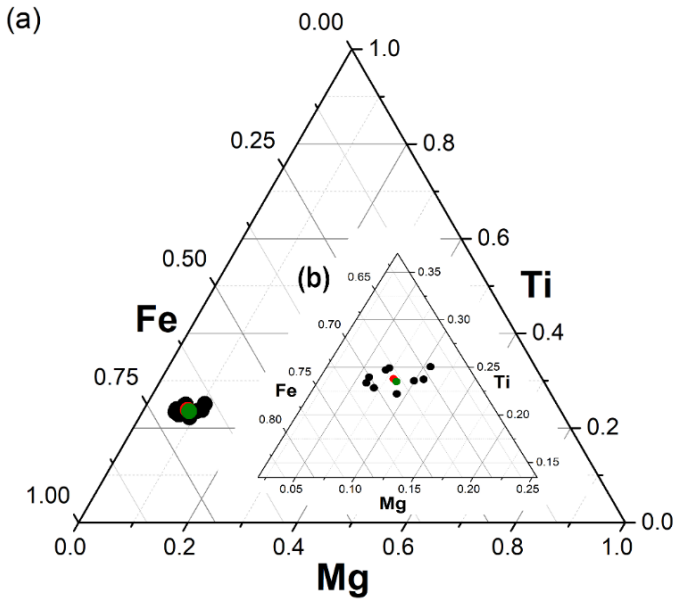

Figure 5. 2: (a) Ternary diagram of Fe-Ti-Mg (B-site cations) elemental chemical composition (EDX/TEM), in atoms %, for the stoichiometric BTFM-CTO target. Nine particles of powder were randomly measured. The average composition of all the measurements is given in red filled circle and the nominal composition in green filled circle, respectively. Inset (b) shows a magnified area of the collected data.

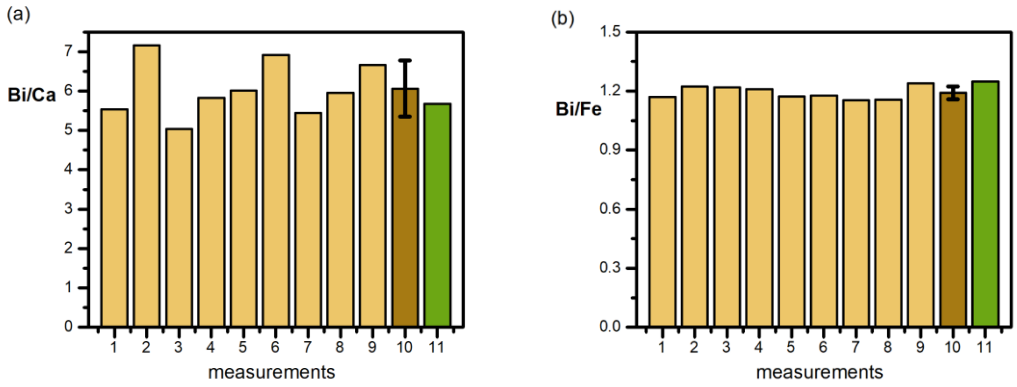

Figure 5. 3: Column charts of (a) Bi/Ca (a) and (b) Bi/Fe ratios obtained from EDX/TEM data on nine randomly chosen particles of the stoichiometric BTFM-CTO target. The mean value of the measured distribution of Bi/Ca = 6.1(7), and Bi/Fe = 1.19(3), is given in column n.10 (dark yellow) with the uncertainty shown (black error bars) as ±1σ. The nominal composition of the ratios (5.67 for Bi/Ca and 1.25 for Bi/Fe) is also presented in column n. 11 (green) of both charts, respectively.

In the case of the Bi-rich target (target-B), the EDX/TEM measurement indicated a Bi content close to the expected Bi-rich nominal composition (in **Figure 5. 4** and **Figure 5. 5**). However, the presence of Bi-related impurities (observed in **Figure 5. 1c**) has also led to notable inhomogeneities in its composition, as can be seen in **Figure 5. 5a**. and **Figure 5. 5b**.

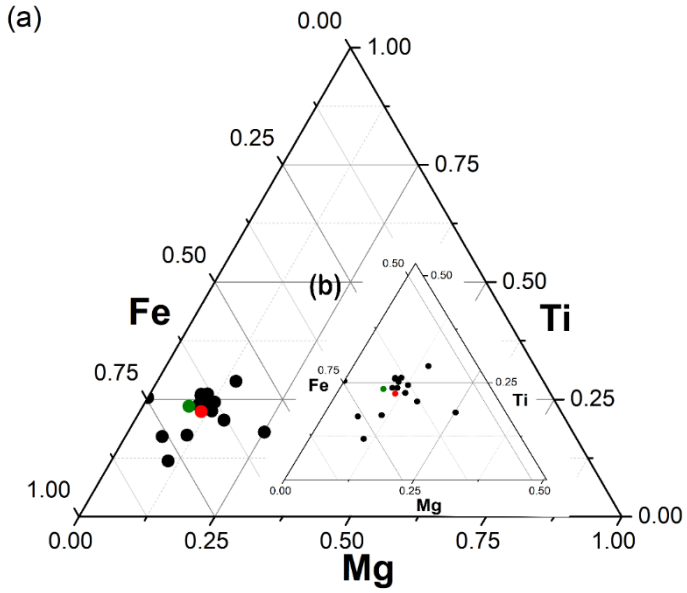

Figure 5. 4: (a) Ternary diagram of Fe-Ti-Mg (B-site cations) elemental chemical composition (EDX/TEM), in atoms %, for the Bi-rich BTFM-CTO target. Fifteen particles of powder were randomly measured. The average composition of all the measurements is given in red filled circle and the nominal composition in green filled circle, respectively. Inset (b) shows a magnified area of the collected data.

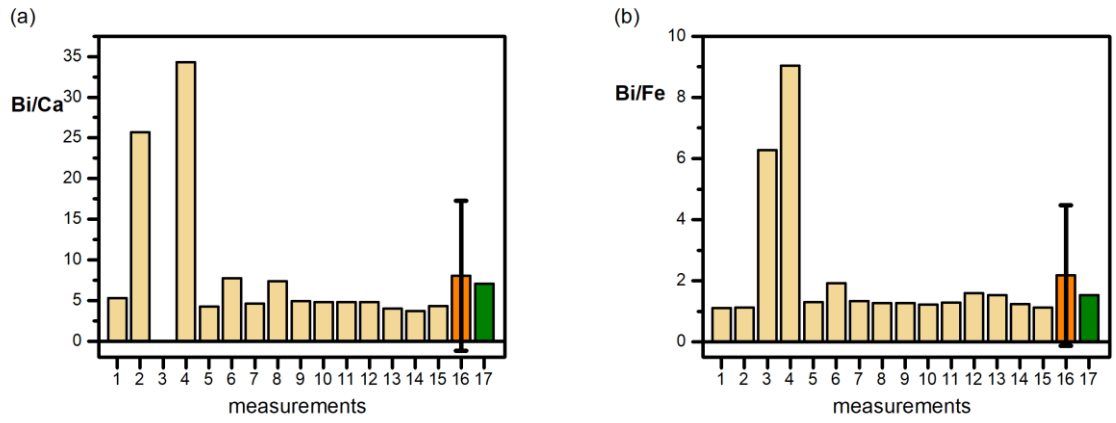

Figure 5. 5: Column charts of (a) Bi/Ca (a) and (b) Bi/Fe ratios obtained from EDX/TEM data on fifteen randomly chosen particles of the Bi-rich BTFM-CTO target. The mean value of the measured distribution of Bi/Ca (= 8.0) and Bi/Fe (= 2.2) is given in column n. 16 (orange) with the uncertainty shown (black error bars) as $\pm 1\sigma$. The nominal value of these ratios (7.07 for Bi/Ca and 1.48 for Bi/Fe) is also presented in column n. 17 (green) of both charts.

Finally, the molar concentrations of the as-synthesised targets, obtained by EDX/TEM analysis, are presented in **Table 5. 1** (nominal and measured compositions) after normalizing their metal content to a total number of two cations (of the ABO_3 chemical formula). As can be seen in the table, the measured molar concentrations of the two targets were found in good agreement with the nominal composition, in agreement with the composition diagrams of **Figure 5. 2** - **Figure 5. 5**.

Table 5. 1: Compositional analysis of BTFM-CTO targets from EDX/TEM data. Metal content was normalised to Fe.

Target	nominal composition	measured composition
stoichiometric	$[Bi_{0.85}Ca_{0.15}]\,[Ti_{0.235}Fe_{0.68}Mg_{0.085}]\,O_3$	$[Bi_{0.80(2)}Ca_{0.14(2)}]\,[Ti_{0.24(2)}Fe_{0.69(7)}Mg_{0.08(2)}]\,O_3$
Bi-rich	$[Bi_{1.06}Ca_{0.15}]\,[Ti_{0.235}Fe_{0.68}Mg_{0.085}]\,O_3$	$[Bi_{1.04(4)}Ca_{0.20(2)}]\,[Ti_{0.27(2)}Fe_{0.69(4)}Mg_{0.18(4)}]\,O_3$

In the following sections, the morphotropic growth of phase-pure BTFM-CTO films by means of pulsed laser deposition will be examined for these two targets. The effect of growth conditions on the composition and crystallinity of the as-grown BTFM-CTO films will be investigated on LAO and STO substrates.

5.2 Exploratory Growth of BTFM-CTO films

5.2.1 Exploratory depositions on LAO

Exploratory depositions on one-side polished (001)-oriented $LaAlO_3$ (LAO) substrates were initially undertaken to investigate the growth of BTFM-CTO films. On this set of depositions, the oxygen partial pressure was set at 0.5 mTorr and the laser fluency at 1.5 J/cm^2 for film thickness of 60,000 pulsed laser shots. The substrate-to-target distance was set to 65 mm and the depositions were carried out with the stoichiometric BTFM-CTO target.

At first, the effect of substrate temperature was examined in a series of film growths at temperatures between 550 and 750 ºC. As can be seen in **Figure 5. 6** a free of impurities film was obtained at temperatures lower than 750 ºC where two set of BTFM-CTO reflections are noticed: a more crystalline set (for the tetragonal-like phase) at: 22.3º, 45.7º and 71.2º and the set of the pseudocubic (00*l*) reflections at: 25.8º, 53.6º and 83.5º lying closer to the substrate (00*l*) peaks. The presence of the first set of reflections (tetragonal-like phase) was seen to be narrowed down in the film deposited at 750 ºC where also Fe-related impurities have also been detected.

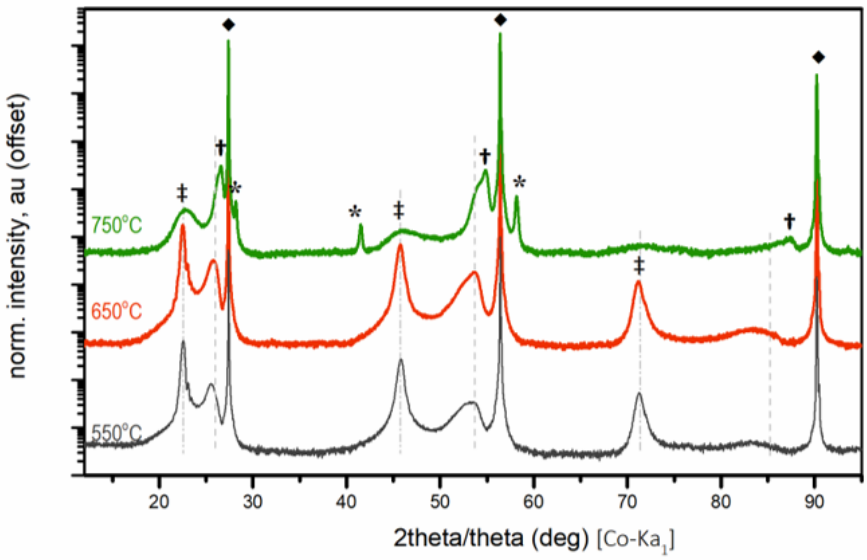

Figure 5. 6: Out-of-plane θ/2θ scans of BTFM-CTO films deposited at different temperatures on (001) LAO substrates. Deposition parameters were as follows, chamber pO_2: 0.5 mTorr; laser fluence: 1 J/cm^2; film thickness: 60,000 laser shots, target: stoichiometric BTFM-CTO. Reflections denoted with (†) indicate the $(00l)_{PC}$ film peaks and with (‡) the extra set of tetragonal-like reflections. Symbol (◆) highlights the LAO substrate peaks and (*****) Fe_2O_3 impurities.

As we will discuss in detail on the following sections, the set of reflections in lower 2θ angles (at 22.3º, 45.7º and 71.2º) is assigned to a strain-induced tetragonal-like BTFM-CTO phase, stabilized only in films of a larger substrate lattice mismatch, in LAO. These findings are in line with similar observations in the literature of strain-induced $BiFeO_3$ films on LAO substrates[292,293].

5.2.1.1 In-situ post-deposition heat-treatment of BTFM-CTO films

In a following set of experiments, we repeated the growth of BTFM-CTO films on LAO substrates at 650 ºC whereas the as-grown films were subjected immediately after the end of the deposition to a post-deposition annealing treatment under high-oxygen pressure (150 Torr). Interestingly, the (unexpected and uncontrollable) power surge of the chamber heater, resulting in a temperature increase of 200 ºC inside the chamber as illustrated in **Figure 5. 7**, has led to the stabilization of the pseudocubic film phase against the tetragonal-like phase (of lower 2θ positions), in **Figure 5. 8**.

The most important, however, remark on the obtained XRD patterns of **Figure 5. 8** was the observed deconvolution of the pseudocubic BTFM-CTO reflections, in film A of **Figure 5. 8**, which becomes more evident on reflections at higher 2θ angles. Given the closeness of the d_{space} parameters for the pseudocubic (00*l*) reflections of the rhombohedral (c_{002-pc}^{Rhomb} =1.976 Å) and orthorhombic (c_{002-pc}^{Orth} =1.81 Å) BTFM-CTO phases, the observed splitting of the $(00l)_{PC}$ peaks is indicating the stabilization of the as-grown BTFM-CTO film in the vicinity of the morphotropic composition.

However, as can be seen in films B and C of **Figure 5. 8**, the emergence of the morphotropic phases was not found to be reproducible or free of extra (Bi- and Fe-related) impurities.

The acute heat treatment of as-grown BTFM-CTO films subjected to the high-oxygen pressure post-deposition anneal (as illustrated in **Figure 5. 7**) was also attempted to be repeated outside of the PLD chamber by means of a rapid thermal annealing (RTA) vacuum furnace where interesting findings on the film thickness and temperature dependence of the morphotropic phase transition were obtained, in **Appendix D**.

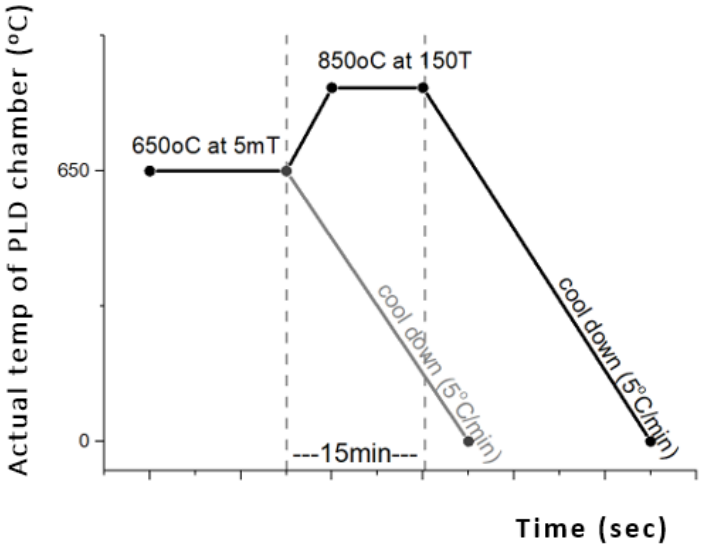

Figure 5. 7: Diagram of the in-situ post-deposition heat treatment of BTFM-CTO films due to the uncontrollable power surge of chamber heater. The insertion of oxygen (150 Torr) at the end of the deposition gave rise to a power surge which resulted in a temperature increase of 200 °C as the heat controller of the chamber is trying to maintain stable the temperature of the chamber.

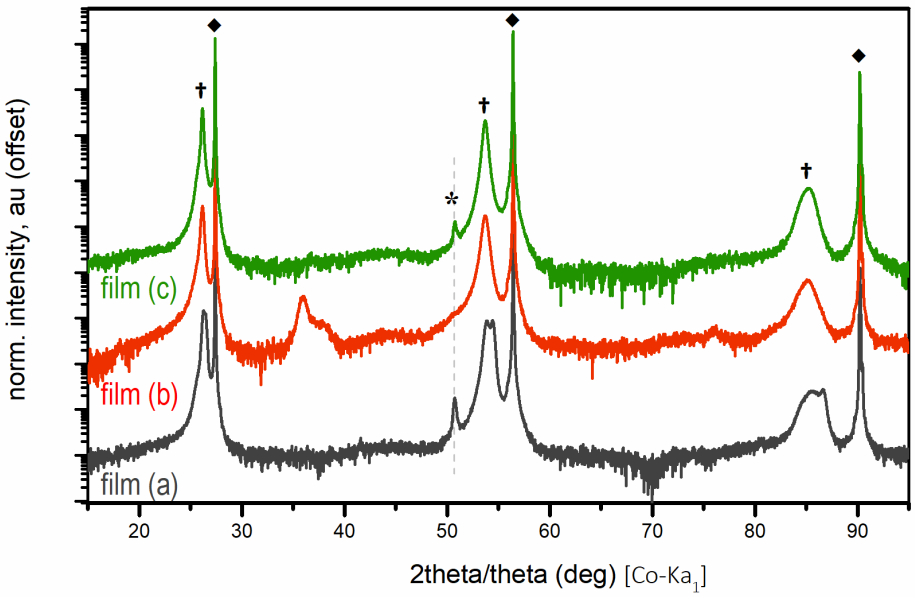

Figure 5. 8: Out-of-plane θ/2θ scans. Reproducibility of BTFM-CTO films deposited on (001) LAO and subjected to an in-situ post-deposition heat-treatment. The films were initially deposited under the same conditions (described in **section 5.2.1**) and subjected afterwards to the in-situ post-deposition heat-treatment of **Figure 5. 7**. Reflections denoted with (†) indicate the $(00l)_{PC}$ film peaks. LAO substrate peaks are marked with (◆) and Fe_2O_3 impurities with (*).

5.2.2 EDX/SEM characterization of BTFM-CTO films

The use of energy dispersive x-ray analysis (EDX/SEM) in conjunction with x-ray diffraction has been utilized to determine the role of growth conditions on the crystallinity and the chemical composition of the as-received films. We focused our attention on BTFM-CTO thin films grown on STO substrates where a smaller substrate-film lattice mismatch is expected to accommodate the epitaxial growth of a morphotropic BTFM-CTO film.

Three films at laser fluences of: (a) 0.5, (b) 0.66 and (c) 1.15 J/cm^2 were grown on STO substrates at 650 ºC under 0.5 mTorr of oxygen pressure using the stoichiometric BTFM-CTO target. To eliminate the substrate interference on the EDX measurements, the films thickness was set in the range of μm (> 120,000 laser shots).

The collected XRD patterns of the deposited films, in **Figure 5. 9**, revealed their preferentially $(00l)_{PC}$-oriented growth, given the smaller lattice mismatch between film and STO substrate. However, the films were not free of impurities and an Fe-related impurity emerged at around 51º.

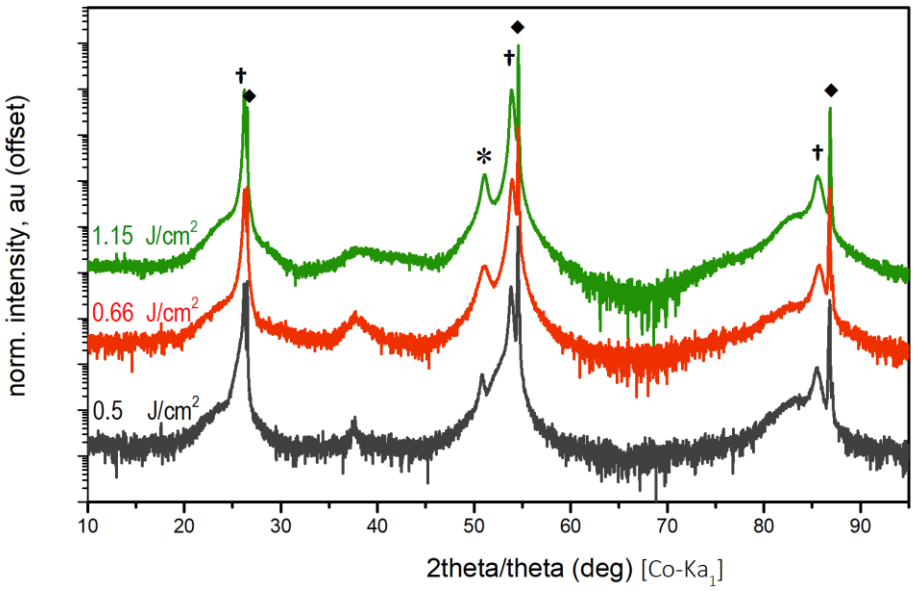

Figure 5. 9: Out-of-plane θ/2θ scans of BTFM-CTO films at different laser fluence values on (001)-STO substrates: (a) 0.5 J/cm^2 (grey), (b) 0.66 J/cm^2 (red), and (c) 1.15 J/cm^2 (green). The rest of the deposition parameters were as follows, temperature: 650 ºC; pO_2: 0.5 mTorr; pulsed laser shots: 180,000; target: stoichiometric BTFM-CTO. Reflections denoted with (†) indicate the $(00l)_{PC}$ film peaks and with (‡) the extra set of reflections of the tetragonal BTFM-CTO. Symbol (◆) highlights the STO substrate peaks and (*) Fe_2O_3 impurities.

For the EDX/SEM measurements, EDX spectra were acquired at different points of the film surface and the received by the software semi-quantitative view of samples elemental composition was later refined by a correction factor accounting for interference effects. The elemental (atomic) composition of the films was normalised to a total metal content of two (of ABO_3) and presented in **Table 5. 2**. A characteristic spectrum of the EDX measurement is shown in **Figure 5. 10**.

As can be seen in **Table 5. 2**, the EDX analysis suggested a deficiency of Bi for all the films of **Figure 5. 9** regardless of the used laser fluence. It is worth noting here, however, the small distribution of the collected EDX/SEM data, presented analytically in **Appendix E.1**, which indicates the compositional uniformity of the studied films.

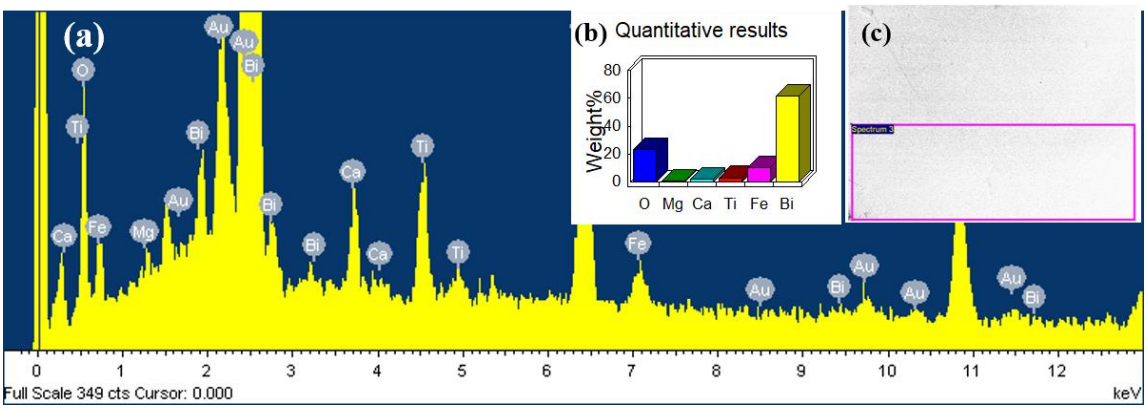

Figure 5. 10: (a) The resulting spectrum of energy dispersive x-ray microanalysis (EDX) by scanning electron microscopy (SEM) and (b) the tabulated results of the elemental composition of the BTFM-CTO films with the (c) inset image showing a characteristic film area selected for EDX measurements.

Table 5. 2: EDX-SEM compositional analysis of BTFM-CTO films deposited at different laser fluences with the use of stoichiometric target. Metal content has normalised to Ca.

Film sample	Deposition conditions			Composition	Bi/Fe ratio
	Temp (°C)	pO_2 (mTorr)	Laser fluence (J/cm^2)	nominal: $[Bi_{0.85}Ca_{0.15}]\,[Ti_{0.235}Fe_{0.69}Mg_{0.085}]\,O_3$	nominal: 1.23
1	650	0.5	0.50	$[Bi_{0.41(4)}Ca_{0.15(3)}]\,[Ti_{0.23(2)}Fe_{0.48(3)}Mg_{0.05(1)}]\,O_3$	0.85(6)
2	650	0.5	0.66	$[Bi_{0.56(6)}Ca_{0.15(1)}]\,[Ti_{0.22(1)}Fe_{0.51(4)}Mg_{0.08(2)}]\,O_3$	1.1(1)
3	650	0.5	1.15	$[Bi_{0.55(1)}Ca_{0.15(1)}]\,[Ti_{0.31(3)}Fe_{0.56(1)}Mg_{0.05(1)}]\,O_3$	0.98(2)

In a following step, we turned to the Bi-rich target and examined the obtained composition of BTFM-CTO films deposited over a range of oxygen partial pressures at a laser fluence of 1.5 J/cm^2.

Since the films were grown this time on LAO substrates, the extra set of the tetragonal-like phase reflections was again emerged -together with additional impurity peaks- in **Figure 5. 11**. More importantly however, the collected XRD patterns revealed a correlation between the growth oxygen pressure and the nature of the emerged impurities: higher oxygen pressures were found to supress the Bi volatility and thus favouring the growth of Bi-related impurities (detected in the region of 35-40º) while a Fe-related impurity appears on the broad shoulder of the (002)-$_{PC}$ film peak (around 51º) at lower oxygen pressures.

These observations were also confirmed by EDX analysis where a higher that the nominal Bi/Fe ratio was detected on films grown at 70 and 100 mTorr, in **Table 5. 3**. On the contrary, the film grown at 5 mTorr, although not free of Fe impurities, has shown a Bi/Fe ratio much closer to the nominal composition. The full EDX data are presented in **Appendix E.2.**

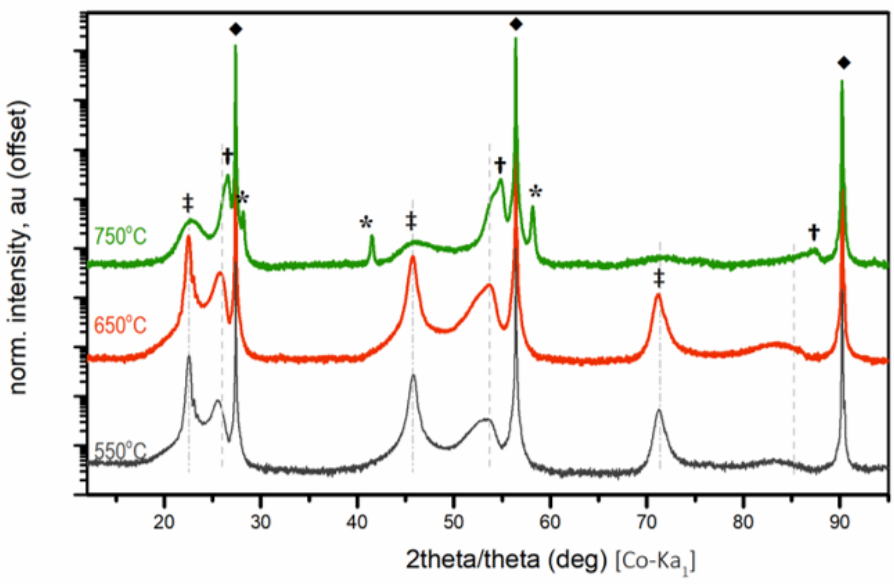

Figure 5. 11: (a) Out-of-plane θ/2θ scans and (b) magnified view around the (002)$_{PC}$ peak position of BTFM-CTO films deposited with a Bi-rich target on LAO substrates at different pO_2 for: 5 mT (grey), 70 mT (red) and 100 mT (green). The rest of the deposition parameters, were as follows: temperature: 650 ºC; laser fluence: 1.5 J/cm^2; pulsed laser shots: 180,000. Reflections denoted with (†) indicate the (00*l*)$_{PC}$ film peaks and with (‡) the tetragonal-like BTFM-CTO phase. Symbol (◆) highlights the STO substrate peaks and (*****) Fe_2O_3 impurities.

Table 5. 3: EDX-SEM compositional analysis of BTFM-CTO films deposited on LAO substrates at different oxygen pressures with the use of Bi-rich target. Metal content has normalised to Ca**.**

Film No.	Deposition conditions			Composition	Bi/Fe ratio
	Temp (ºC)	pO_2 (mTorr)	Laser fluence (J/cm^2)	nominal: $[Bi_{0.85}Ca_{0.15}]$ $[Ti_{0.235}Fe_{0.69}Mg_{0.085}]$ O_3	Nominal: 1.23
1	650	5	1.50	$[Bi_{0.71(3)}Ca_{0.15(2)}]$ $[Ti_{0.23(1)}Fe_{0.56(3)}Mg_{0.06(1)}]$ O_3	1.27(8)
2	650	70	1.50	$[Bi_{0.84(3)}Ca_{0.15(1)}]$ $[Ti_{0.19(2)}Fe_{0.63(4)}Mg_{0.05(2)}]$ O_3	1.33(8)
3	650	100	1.50	$[Bi_{0.79(4)}Ca_{0.15(1)}]$ $[Ti_{0.22(2)}Fe_{0.59(3)}Mg_{0.05(1)}]$ O_3	1.3(1)

5.2.3 Optimization of film growth on STO

5.2.3.1 Growth of $(001)_{PC}$-oriented BTFM-CTO films on STO

The effect of small pO_2 changes on the obtained crystalline structure of BTFM-CTO films was studied by a combination of XRD and EDX analyses.

At first, thick BTFM-CTO films of 180,000 laser shots (to cancel the substrate interference in the EDX measurements) were grown in a range of oxygen pressures (5 to 50mTorr) while the substrate temperature and the laser fluence were respectively held at 650 ºC and 1.5 J/cm^2. These depositions were carried out using the Bi-rich target.

The deposited films on STO substrates, in **Figure 5. 12**, have shown a preferentially $(00l)_{PC}$ growth orientation but also confirmed our earlier findings on the pO_2-dependence of impurities. As previously seen in **section 5.2.2,** a Fe-related impurity peak (at 51º) was found to emerge for films grown at pO_2 as low as 5 mTorr while at higher pO_2 (above 15 mTorr) the suppression of Bi volatility was seen to result in films with Bi impurities (at 38º).

EDX measurements on the films grown at 10 and 50 mTorr verified these findings. As can be seen in **Table 5. 4** (and more extensively in **Appendix E.3**), the film deposited at 50 mTorr was found to be Bi-rich with a Bi/Fe ratio of 1.56(8), while the film grown at 10 mTorr had a Bi/Fe ratio of 1.31(6) -and much closer to the nominal ratio of 1.23.

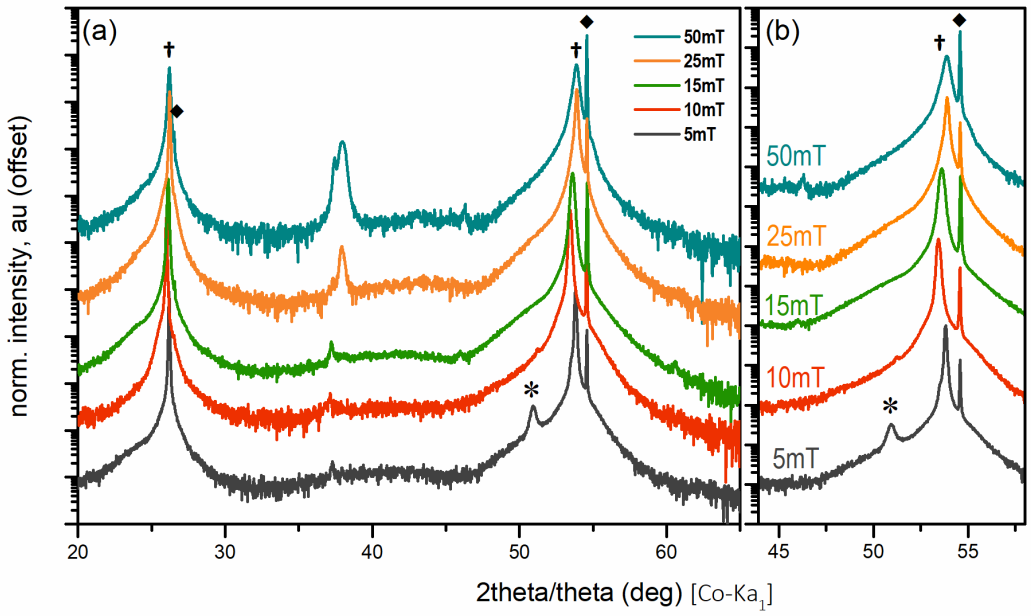

Figure 5. 12: (a) Out-of-plane θ/2θ scans and (b) magnified view around the $(002)_{PC}$ peak position of BTFM-CTO films on STO substrates at different pO_2 for: 5 mTorr (grey), 10 mTorr (red), 15 mTorr (green), 25 mTorr (orange), 50 mT (cyan). The growth conditions were as follows, temperature: 650 ºC; laser fluence: 1.5 J/cm^2 pulsed laser shots: 180,000; target: Bi-rich BTFM-CTO. Reflections denoted with (✝) indicate the $(001)_{PC}$ film peaks. Symbol (◆) highlights the STO substrate peaks and (*) Fe_2O_3 impurities.

Table 5. 4: EDX-SEM compositional analysis of BTFM-CTO films deposited on STO substrates at 10 and 50 mTorr (of **Figure 5. 12**) using the Bi-rich target. Metal content has normalised to Ca.

Film No.	Deposition conditions			Composition	Bi/Fe ratio
	Temp (ºC)	pO_2 (mTorr)	Laser fluence (J/cm^2)	nominal: $[Bi_{0.85}Ca_{0.15}]$ $[Ti_{0.235}Fe_{0.69}Mg_{0.085}]$ O_3	Nominal: 1.23
1	650	10	1.50	$[Bi_{0.76(2)}Ca_{0.15(2)}]$ $[Ti_{0.24(2)}Fe_{0.58(3)}Mg_{0.04(3)}]$ O_3	1.31(6)
2	650	50	1.50	$[Bi_{0.94(2)}Ca_{0.15(2)}]$ $[Ti_{0.23(1)}Fe_{0.60(2)}Mg_{0.04(2)}]$ O_3	1.56(8)

Up to now, the complementary use of EDX and XRD analysis has shown that the growth of a single-phase, free of impurities, BTFM-CTO film should be lying close to the region of 10 mTorr and 650 ºC.

The thickness of the films studied up to now was in the range of μm scale in order to cancel the interference of substrates in the EDX measurements. To further optimize the growth of BTFM-CTO films, we will focus our attention in the following discussion on much thinner films, of tens of nm thickness, suitable for the electrical and magnetic measurements. A number of depositions were carried out under small variations in growth conditions, between 650 – 710 ºC and 10 – 15 mTorr, as summarized in **Table 5. 5** and **Figure 5. 13**.

Table 5. 5: Growth conditions for the films of **Figure 5. 13.**

Film	Deposition. Temper (oC)	pO_2 (mTorr)	Thickness (in pulsed laser shots)	Fluence (J/cm^2)	Target
(1)	650	15	6,500	1.5	Bi-rich
(2)	650	15	6,500	1.5	Bi-rich
(3)	650	10	4,000	1.5	Bi-rich
(4)	680	15	6,500	1.5	Bi-rich
(5)	710	15	6,500	1.5	Bi-rich

The most striking outcome of this set of depositions was the successfully reproducible growth of perovskite BTFM-CTO on the morphotropic composition, as characteristically demonstrated in the deconvolution of the $(00l)_{PC}$ peak. In agreement with the diffraction data of the bulk material, we can accordingly assign the high and low d_{space} $(00l)_{PC}$ peak components of **Figure 5. 13**, denoted as (**†-1**) and as (**†-2**), to the orthorhombic and rhombohedral phases.

In addition, we can also observe the morphological evolution of the as-grown samples towards a single-phase BTFM-CTO film. Although a single-phase BTFM-CTO film was possible to be obtained at 650 ºC and 15 mTorr (film 1 in **Figure 5. 13**), it has been proven that the reproducibility of this growth could easier be accomplished as the growth temperature was increased to 710 ºC (film 5 in **Figure 5. 13**).

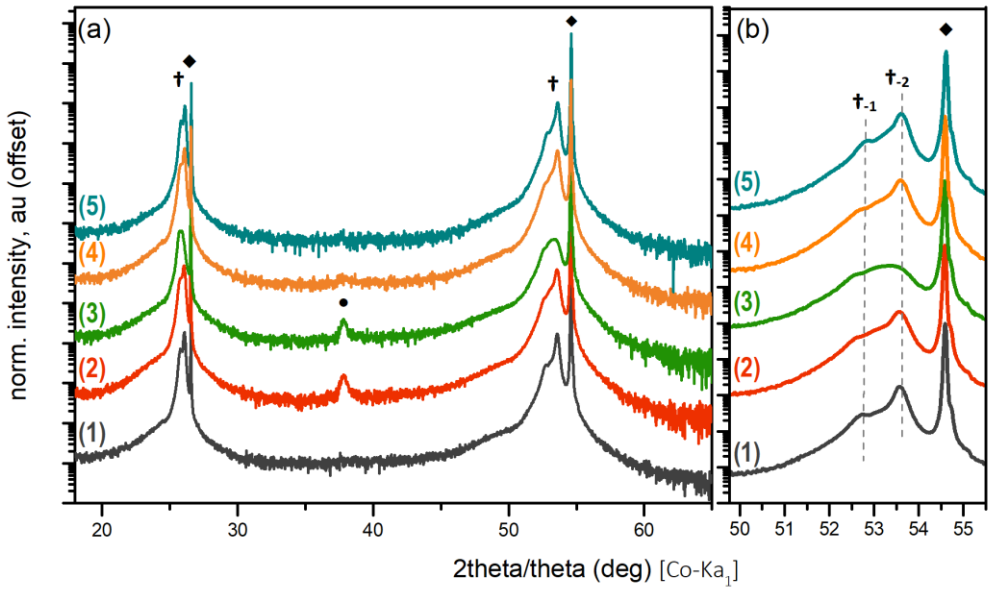

Figure 5. 13: (a) Out-of-plane θ/2θ scans and (b) magnified view around the $(002)_{PC}$ peak position of BTFM-CTO thin-films on STO substrates at different temperatures & pO_2. The exact conditions for each of the samples are summarized in **Table 5. 5**. Reflections denoted with (†-1) and (†-2) indicate the orthorhombic and rhombohedral components of the $(002)_{PC}$ peak splitting at high and low d_{space} values, respectively. Symbol (◆) highlights the STO substrate peaks and (•) a reflection of another BTFM-CTO orientation.

5.2.3.2 The crystalline structure of morphotropic BTFM-CTO films

A better insight on the crystal structure of the $(00l)_{PC}$-oriented morphotropic BTFM-CTO films of **Figure 5. 13** could be gained by x-ray diffraction rocking curves measurements and atomic force microscopy (AFM). To do so, we focused on the two samples where a single-oriented BTFM-CTO film growth was achieved without extra reflections:

- film -1, at: 650 ºC; 15 mTorr; 6500 shots; 1.5 J/cm^2
- film -5, at: 710 ºC; 15 mTorr; 6500 shots; 1.5 J/cm^2

The crystallinity of these two films was assessed by rocking curves measurements recorded at the splitting of their $(002)_{PC}$ reflection peak, in **Figure 5. 14**. For both films, detailed omega scans around the $(002)_{PC}$ peak splitting revealed the presence of two distinct components, attributed to the mixture of the rhombohedral (R) and orthorhombic (O) phases. In agreement with the diffraction data of the bulk material, the ω-peak component at higher angles (lower

d_{space}) was found to be the majority rhombohedral phase, while the ω-peak component at low angles (higher d_{space}) confirmed the minority character of the orthorhombic phase.

A substantial difference was observed in the mosaicity of the two peak components with the minority orthorhombic phase being more crystalline. While the rhombohedral phase, located at higher ω angles, was found to present a full width half maximum (FWHM) of 0.37-0.42°, the orthorhombic phase was seen to adapt better to the substrate by demonstrating a much higher degree of crystallinity at 0.030 - 0.044°.

When comparing the mosaic spreads of the films deposited at 710 °C and 650 °C, an overall improvement in the obtained crystallinity of the film deposited at higher temperatures was also obtained. The rocking curves measurements of these samples are shown in **Figure 5. 14** with their fitting parameters presented in **Table 5. 6**.

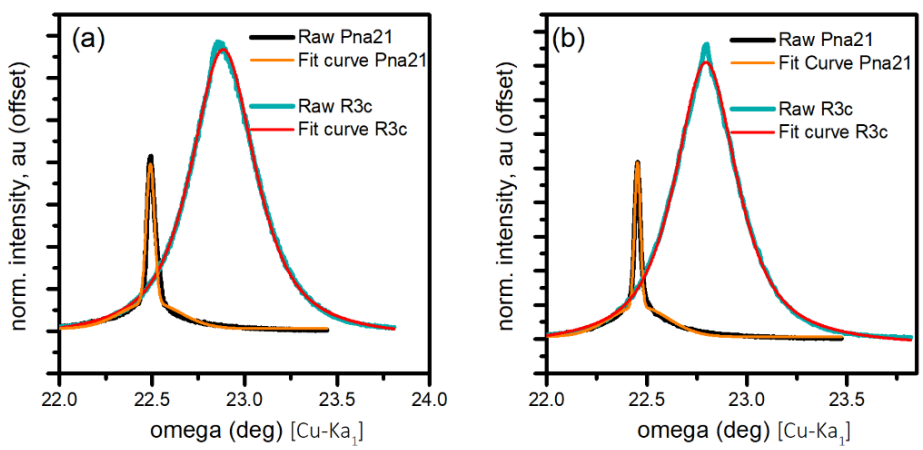

Figure 5. 14: X-ray diffraction rocking curves (raw data and fit curve) around the $(002)_{PC}$ reflection peak of as-grown BTFM-CTO films on STO substrates for: (a) 650 ºC and (b) 710 ºC in **Figure 5. 13**.

Table 5. 6: Mosaicity and surface roughness of BTFM-CTO films deposited at different temperatures on STO substrates.

Film	Roughness		Mosaicity							
			Peak -1 (Pna21)				Peak -2 (R3c)			
	RSM (nm)	Peak-to-Valley (nm)	FHWM (deg.)	Adj. R-Square	Model	c-axis	FHWM (deg.)	Adj. R-Square	Model	c-axis
650 ºC (n1)	1.38	11.27	0.044(1)	0.977	Gauss	3.953	0.421(1)	0.999	PsdVoigt1	3.886
710 ºC (n5)	2.32	24.75	0.029(1)	0.993	Gauss	3.960	0.339(4)	0.990	Gaussian	3.901

The surface topology of the examined samples was also evaluated by AFM studies on 2x2 μm area scans. Both samples were found to present a smooth morphology with a root-mean-square roughness (R_{rms}) smaller than 3.5 nm, as seen in **Figure 5. 15**, **Figure 5. 16** and **Table 5. 5**. The most interesting however observation concerning the topology of the two examined samples was the strongly textured, square-like, outgrowth of the film grown at 710 °C, as can be seen in **Figure 5. 16**.

Contrary to the island growth of the film at 650 °C, the deposited at 710 °C film exhibited a textured, criss-cross, surface topology in good agreement with literature references of epitaxially grown $BiFeO_3$ thin films in (001)-oriented STO substrates. For instance, Zhou et al.[294] on their extensive topological study of epitaxially grown $BiFeO_3$ films on (001) STO substrates of various miscut angles by PLD have reported a strong correlation between substrate miscut and obtained $BiFeO_3$ film surface morphology with epitaxial films deposited on low miscut STO substrates displaying a similar criss-cross surface feature. The reader should also note here that the used STO substrates in our work had a nominally zero miscut.

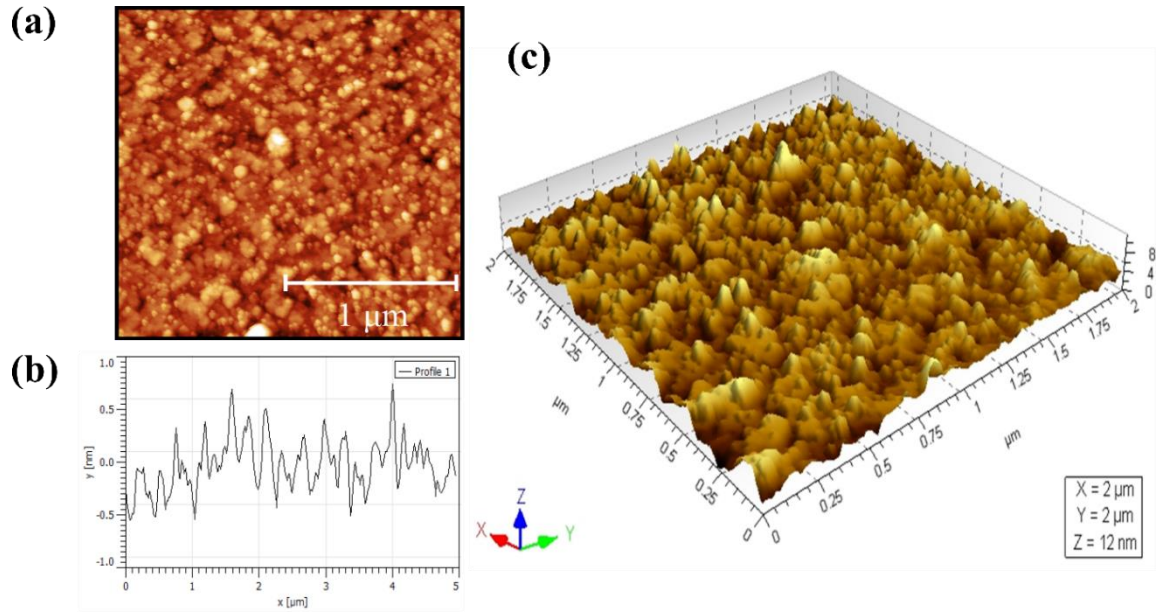

Figure 5. 15: Island film growth for BTFM-CTO film on (001)-STO deposited at 650 °C under 15 mTorr (film-1 in **Figure 5. 13**): (a) AFM plain-view image, (b) line profile and (c) 3D projection of a 2 x 2 μm area of the as-deposited film.

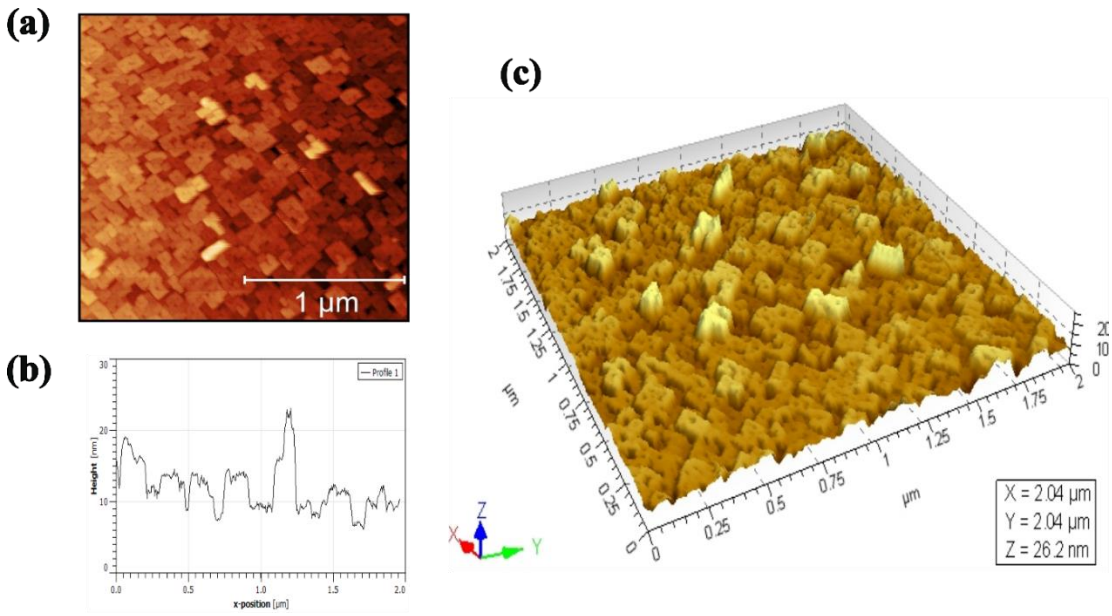

Figure 5. 16: Textured, rectangular criss-cross film growth of BTFM-CTO film on (001)-STO deposited at 710 °C under 15 mTorr (film-5 in **Figure 5. 13**): (a) AFM plain-view image (2 x 2 µm), (b) line profile and (c) 3D projection of a 2 x 2 µm area of the as-deposited film.

Altogether, our findings have clearly highlighted the improved crystal quality and superior morphology of the samples deposited at 710 °C, suggesting a higher crystal quality of films grown at elevated temperatures. Given the observed formation of Fe impurities on films grown at 750 °C (already seen in **section 5.2.1**), our work until now has successfully identified the presence of an optimum narrow growth window of highly crystalline and single-phase BTFM-CTO films for temperatures between 650 and 750 °C and pO_2 between 5 and 15 mTorr.

5.2.3.3 Reproducibility of the morphotropic BTFM-CTO film growth

It is well known in the PLD literature, that experimental difficulties regarding the reproducibility of the growing conditions are an obstacle in repeatable results. While a number of deposition parameters such as the oxygen pressure, substrate temperature and annealing conditions can be easily measured and therefore are considered well-controlled, other parameters can be inspected more difficult and small changes are not subjected to the same level of control[295]. Parameters of this sort are the accurate control of laser energy density, the spot area calibration as well as the state of the ablated target before every deposition.

During the course of this thesis, and given the complexity of the cation structure of our material, we had carefully worked on controlling these parameters with precision. The nominal growth conditions of our depositions was routinely checked according to a protocol entailing:

- polishing target's surface before every single deposition to secure the compositional homogeneity of used target, given the different ablation threshold of target's cations
- the measurement of the laser energy inside the chamber, using a single-channel laser power meter (3sigma, Coherent Inc) and
- the track and evaluation of the laser beam imprint (using a thermal paper) at the target position inside the chamber.

However, the repeatable growth of BTFM-CTO films in the MPB was sometimes difficult leading occasionally to a less well-defined peak splitting.To understand the influence of less well-defined deposition parameters on stabilizing the film growth in the MPB regime we studied the effect of substrate position towards the plasma plume.

Figure 5. 17 depicts the XRD diffraction patterns of two films (-1 and -2) deposited simultaneously under the optimum deposition conditions of **section 5.2.3.1** (for 710 ºC; 15 mTorr; 1.5 J/cm^2, 13,000 laser shots and the Bi-rich target).

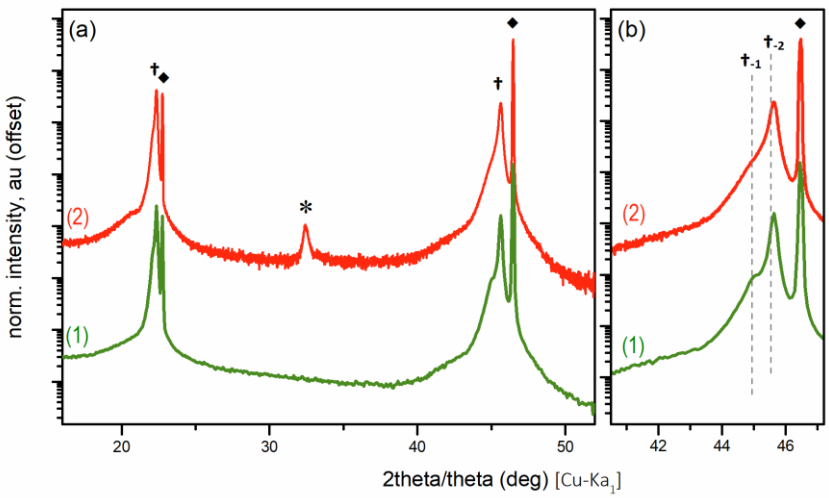

Figure 5. 17: (a) Out-of-plane θ/2θ scans and (b) magnified view around the $(002)_{PC}$ peak position of BTFM-CTO films of **Figure 5. 18**. Films-1 and -2 were grown simultaneously under the same (nominal) conditions. The orthorhombic and rhombohedral component of the BTFM-CTO films in the MPB region are marked, respectively, with the symbols (✝-1) and (✝-2) and with the symbol (∗) a secondary reflection of BTFM-CTO. With (◆) are highlighted the substrate peaks.

The only variable parameter on these two depositions was the relative position of the substrates (STO) towards the plasma plume of the target with film-1 being placed in the centre of target's surface normal direction and film -2 placed slightly off-centred as illustrated in **Figure 5. 18**.

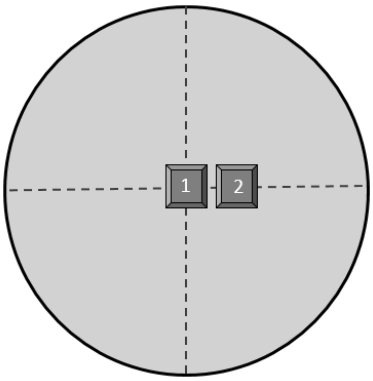

Figure 5. 18: Schematic representation of films -1 and -2 position in the substrate holder. Film-1 has placed in the centre of target's surface normal direction while film-2 was standing slightly off-centre.

As seen in **Figure 5. 17**, the morphotropic growth of BTFM-CTO films was found to depend on the substrate position towards the plasma plume, with film-1 exhibiting a more distinct and well-separated $(002)_{PC}$ peak splitting than film-2. The emergence of an additional peak, at around 32º, was also noticed in film-2, possibly attributed to a secondary BTFM-CTO reflection or a Bi-related impurity.

These findings were further confirmed by rocking curve measurements around the $(002)_{PC}$ peak of the two films, in **Figure 5. 19**. There, while the presence of two distinct mosaic populations was clearly observed on film-1, exhibiting a well-separated $(002)_{PC}$ peak splitting, the low-angle ω peak component (attributed to the orthorhombic phase) was not possible to be observed for film-2.

When finally comparing the mosaicity of the rhombohedral phase of the two films (high-angle ω peak component) in **Table 5. 7**, an improved crystallinity for the film placed along the target-surface normal direction (film-1) was observed.

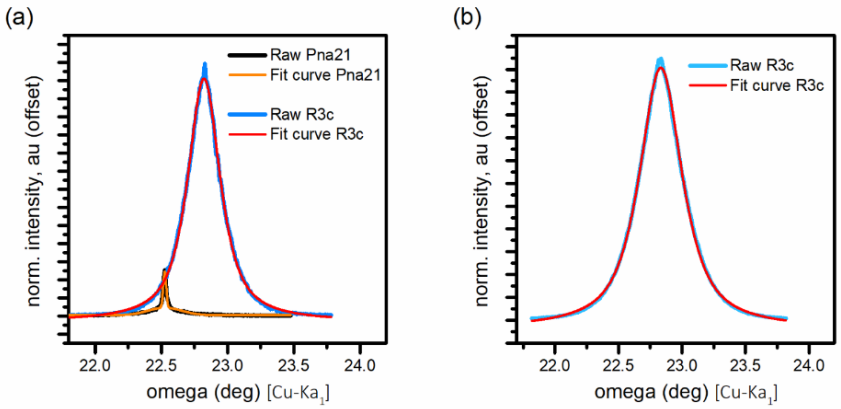

Figure 5. 19: X-ray diffraction rocking curve (in linear scale) around the (002)-$_{PC}$ peak splitting of the as-grown BTFM-CTO films of **Figure 5. 17** and **Figure 5. 18**: (a) film-1 and (b) film-2.

Table 5. 7: Mosaicities of films deposited while investigating the epitaxial MPB growth of BTFM-CTO in reference with their relative position towards the plasma plume in **Figure 5. 17 / Figure 5. 18**.

Film No	Mosaicity							
	Peak -1 (Pna21)				Peak -2 (R3c)			
	FHWM (deg.)	Adj. R-Square	Model	c-axis	FHWM (deg.)	Adj. R-Square	Model	c-axis
(1)	0.022(1)	0.984	Gauss	3.947	0.294(1)	0.999	PsdVoigt1	3.896
(2)		—			0.404(1)	0.999	PsdVoigt1	3.895

In summary, the deposition protocol established in this section (**section 5.2.3**) confirmed the reproducible growth of BTFM-CTO films at the morphotropic boundary of the rhombohedral and orthorhombic phases. However, the stabilization of the two-phase in the coexistence region was also found to be a challenging task and even small changes in the growth conditions (such as the exact target-to-substrate position) could result in the distortion of the MPB.

5.2.4 Epitaxial growth on STO

5.2.4.1 Epitaxial morphotropic growth of BTFM-CTO over different thicknesses

Our results so far on the chemical composition, the structural properties and the morphological characteristics of the studied films have indicated a narrow window of optimum conditions for the growth of highly crystalline morphotropic BTFM-CTO films. In summary, these conditions were found to be as follows: substrate temperature, 710 ºC; oxygen pressure: 15 mTorr and laser fluence: 1.5 J/cm^2.

In this section, the morphotropic growth of BTFM-CTO films will be examined as a function of film thickness. Three films of 3,000, 4,500 and 13,000 pulsed laser shots were deposited according to the conditions descripted in **section 5.2.3.1** and their XRD patterns confirmed the reproducible growth of single-oriented BTFM-CTO films in the MPB composition, in **Figure 5. 20**.

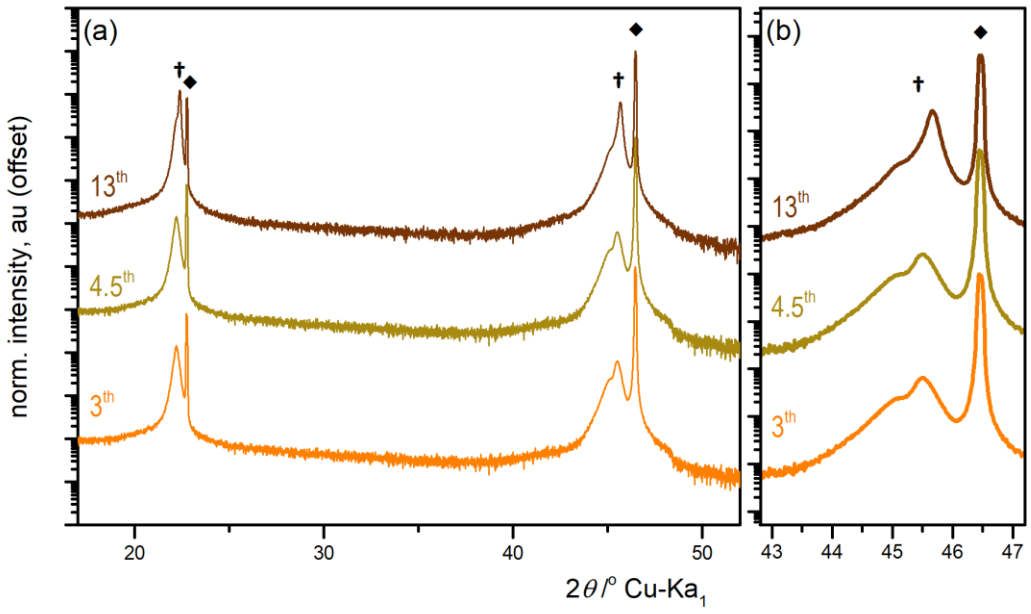

Figure 5. 20: (a) Out-of-plane θ/2θ scans and (b) magnified view around the $(002)_{PC}$ peak position of BTFM-CTO films deposited on STO substrates at different thicknesses of 3,000, 4,500 and 13,000 pulsed laser shots. Growth parameters as follows, deposition temperature: 710 ºC; oxygen pressure: 15 mTorr and laser fluence: 1.5 J/cm^2 using the Bi-rich target.

X-ray reflectivity (XRR) measurements were performed on the examined films to determine their thickness, in **Figure 5. 21**. By fitting the XRR data of the 3,000 and 4,500 laser shots films we received corresponding film thickness of 64 and 82 nm, respectively, and a linear rate of film growth. Based on this growth rate, the thickness of the 13,000 laser shots film is expected to be approximately 240 nm. As was expected for the thickness of the 13,000 shots film (expected to exceed 150-200 nm), its XRR frequency oscillations are greatly decreased and eventually disappeared with the increase of its thickness[296], in **Figure 5. 21c**.

The RC measurements of the examined films, performed in the vicinity of the $(002)_{PC}$ reflection, demonstrated two distinct mosaic spreads of: (i) a broader rhombohedral peak component at higher ω-values and (ii) a more crystalline orthorhombic peak at lower angles, in agreement with our previous findings in **section 5.2.3.2**.

Interestingly, while the mosaicity of the orthorhombic phase at lower ω-values remained stable over different thicknesses films, the crystallinity of the rhombohedral component, at higher angles, was seen to deteriorate from 0.126° to 0.389° as the film thickness increased from 64 to 240 nm. The fitting parameters of the RC measurements in **Figure 5. 21** are summarized in **Table 5. 8**.

Another characteristic feature of the XRR scans in **Figure 5. 21** is the progressive decrease of intensity for the orthorhombic fraction of the morphotropic phase with the increase of film thickness suggesting the relaxation of the as-grown films towards the majority rhombohedral phase.

Table 5. 8: Thickness and mosaicities of BTFM-CTO films for different number of laser shots.

	Thickness (nm)	Mosaicity							
		Peak -1 (Pna21)				Peak -2 (R3c)			
	(nm)	FHWM (deg.)	Adj. R-Square	Model	c-axis	FHWM (deg.)	Adj. R-Square	Model	c-axis
3.000	64	0.039(1)	0.993	Gauss	3.946	0.126(2)	0.990	PsdVoigt1	3.904
4.500	82	0.032(1)	0.991	Gauss	3.954	0.178(1)	0.993	PsdVoigt1	3.911
13.000	(237)	0.038(1)	0.989	Gauss	3.947	0.389(1)	0.999	PsdVoigt1	3.893

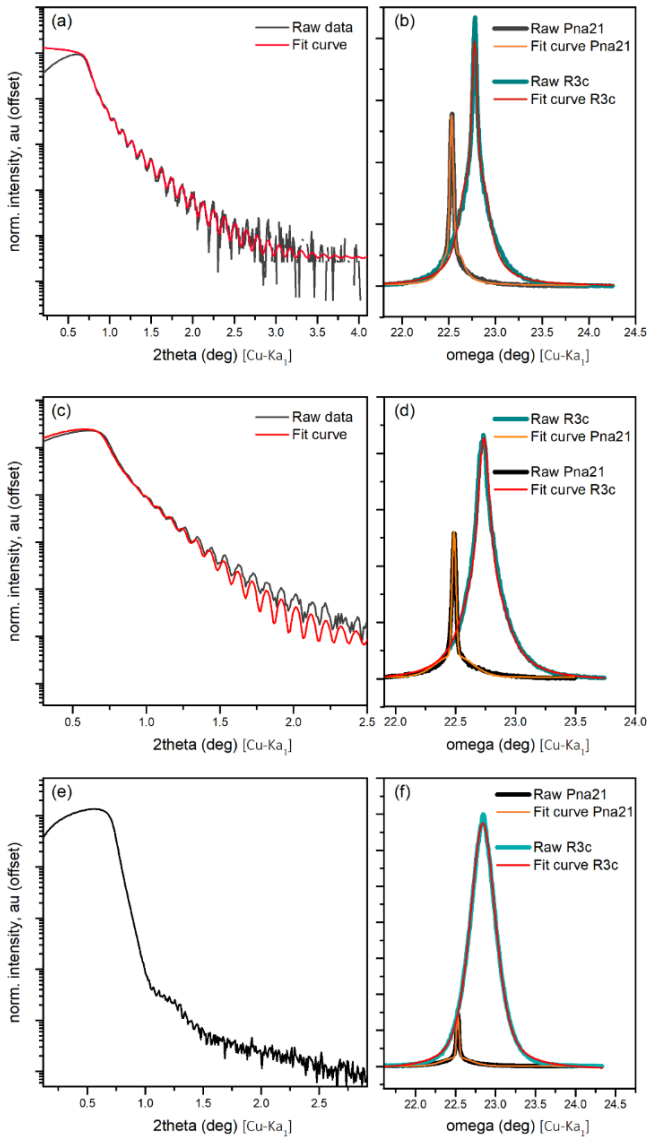

Figure 5. 21: X-ray reflectivity (XRR) patterns (in log. scale) and x-ray diffraction rocking curves (in linear scale) around the (002)-$_{PC}$ peak splitting of as-grown BTFM-CTO films on STO substrate at varying thicknesses of: 3,000 (a-b), 4,500 (c-d) and 13,000 (e-f) laser shots. The films were grown at 710 ^{o}C, under chamber pO_2 of 15 mTorr and laser fluence of 1.5 J/cm^2 using the Bi-rich target.

5.2.4.1 Reciprocal space maps and lattice parameters

The coexistence of the rhombohedral and orthorhombic phases in BTFM-CTO films grown on STO substrates was investigated with in-house reciprocal space maps (RSM) performed with the SmartLab diffractometer of Rigaku Corp.

Allowed and sufficiently intense diffraction peaks of the rhombohedral and orthorhombic BTFM-CTO film phases were identified (in the reciprocal space) using simulation data from the SmartLab software[297], as illustrated in **Figure 5. 22**. Wide RSM scans were accordingly performed around the symmetric $(002)_{PC}$ and the asymmetric $(103)_{PC}$ and $(113)_{PC}$ reflections of a thick film (13,000 pulses of **Figure 5. 20**).

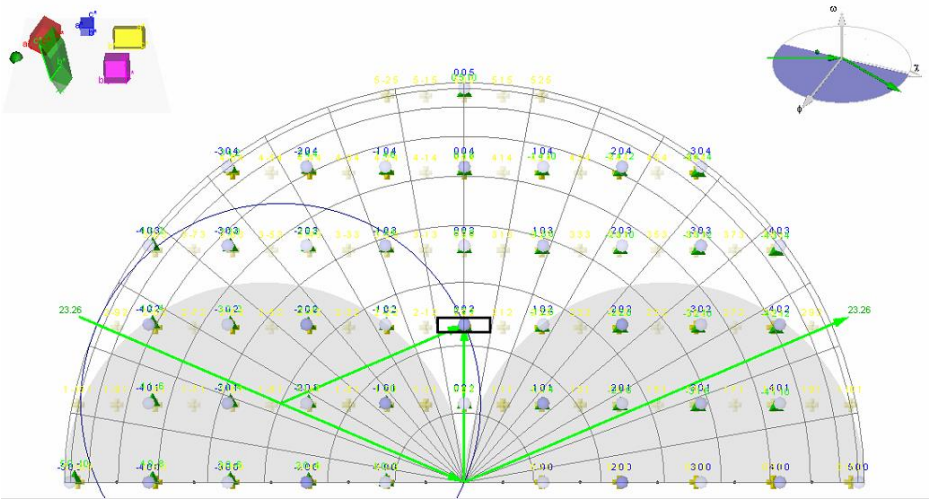

Figure 5. 22: Visualization of diffraction space (simulated data) in the reciprocal space for the rhombohedral and orthorhombic phases of BTFM-CTO film using [100] and [001] vectors as the in-plane and out-of plane directions, respectively. The diffraction space model was obtained using the SmartLab software.

As can be seen in **Figure 5. 23** - **Figure 5. 25**, the observed film reflections were decomposed into two separate phases (orthorhombic and rhombohedral components) confirming the coherent BTFM-CTO film growth in the MPB region. More specifically, the deconvolution of the film reflections into two components is clearly seen in the (b) "TOPO" sub-figures of **Figure 5. 23** - **Figure 5. 25** and marked with white arrows. The combination of a low intensity reflection for the minority phase component (orthorhombic phase) and the limitations of the available in-lab instrument resolution do not allow us to distinguish directly the two film components in the "FLAT" sub-figures of these Figures (a sub-figures). However, the

skewness of the observed film peaks (marked with the curved white arrows in the "FLAT" sub-figures) is an indirect demonstration of the morphotropic BTFM-CTO film.

In all the RSMs, the $q_{parallel}$ (q_x) values of the two film phases were found to coincide well with these of the substrate confirming the strained epitaxial growth of the film on the used substrate.

As was expected, the $q_{perped.}$ (q_z) values of the film phases were found to lie at lower values than that of the substrate reflections given that the out-of-plane film lattice parameters were bigger than that of the substrate.

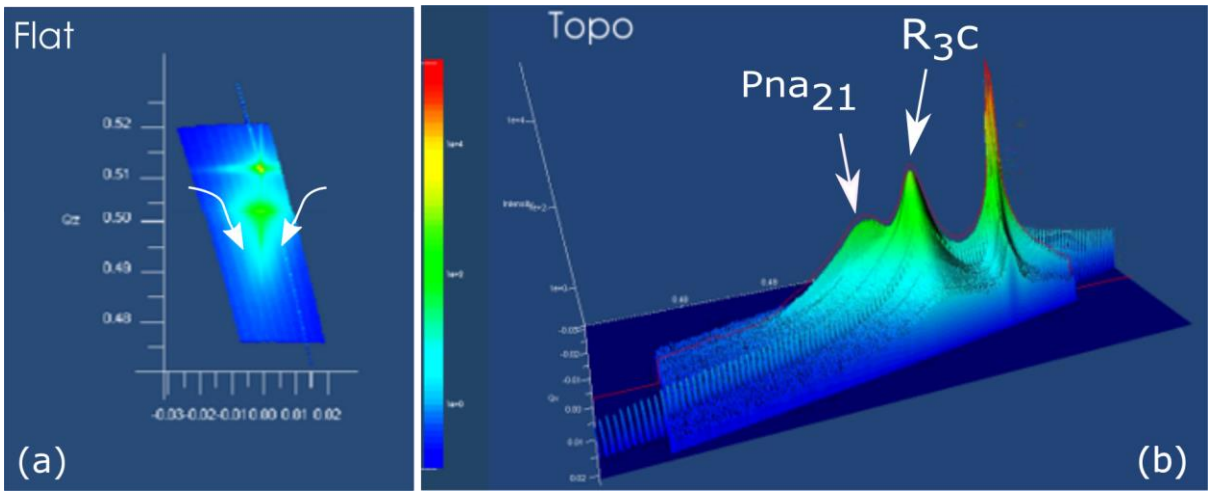

Figure 5. 23: (a) "Flat" and (b) "Topo" view of the reciprocal space map around the $(002)_{PC}$ XRD reflexion of BTFM-CTO film grown on STO. In (a) "Flat" sub-figure, with white curved arrows is marked the skewness of the two convoluted film peaks. With white straight arrows, in (b) "Topo" sub-figure, are denoted the two deconvoluted film component (orthorhombic and rhombohedral phases). The film was grown at 710 ^{o}C, 15 mTorr, with 1.5 J/cm^2 for 13,000 pulsed laser shots using the Bi-rich target. The observed monochromator streaks in (b) "Topo" sub-figure are caused by strong air-scattering (10e^8 counts) of the diffracted beam at certain diffraction angles where the Bragg condition is fulfilled for the substrate.

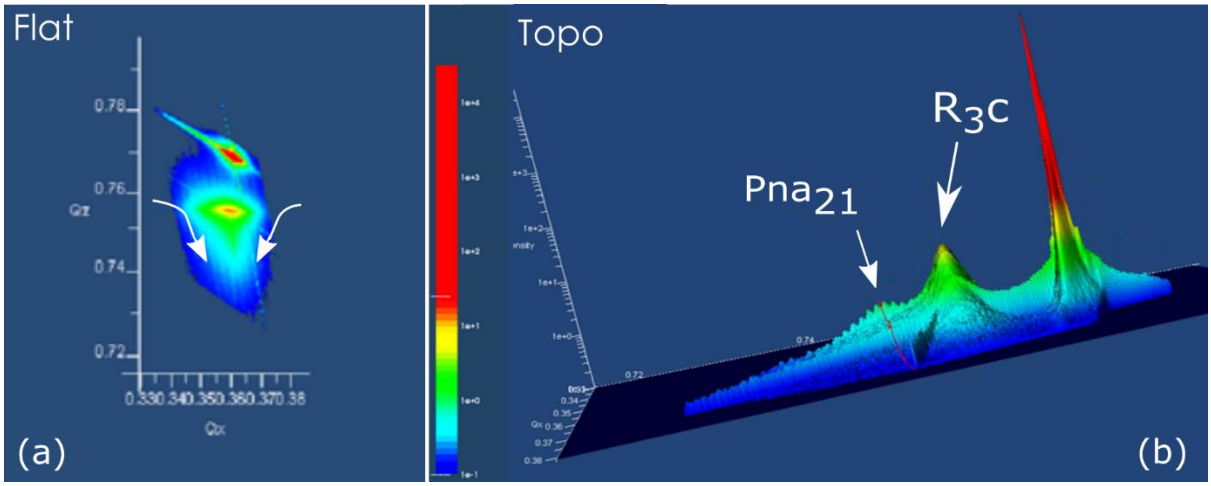

Figure 5. 24: (a) "Flat" and (b) "Topo" view of the reciprocal space map around the $(103)_{PC}$ XRD reflexion of BTFM-CTO film grown on STO. In (a) sub-figure, white curved arrows marked the skewness of the two convoluted film peaks. In (b) "Topo" sub-figure, with white straight arrows are denoted the two deconvoluted film component (orthorhombic and rhombohedral phases). The film was grown at 710 ^{o}C, 15 mTorr, with 1.5 J/cm^2 for 13,000 pulsed laser shots using the Bi-rich target. The observed streaks (in "Topo" -view image) are caused by strong air-scattering (10e^8 counts) of the diffracted beam.

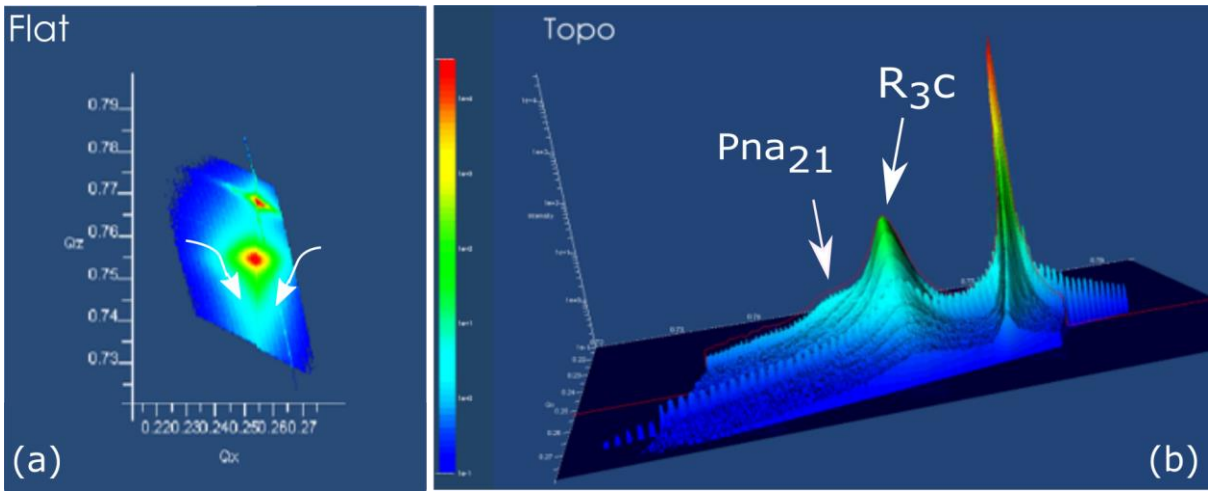

Figure 5. 25: (a) "Flat" and (b) "Topo" view of the reciprocal space map around the $(113)_{PC}$ XRD reflexion of BTFM-CTO film grown on STO. As before: in (a) sub-figure, white curved arrows marked the two convoluted film peaks while in (b) "Topo" sub-figure the two deconvoluted film component (orthorhombic and rhombohedral phases) are denoted with white straight arrows. The film was grown at 710 ^{o}C, 15 mTorr, with 1.5 J/cm^2 for 13,000 pulsed laser shots using the Bi-rich target. The observed streaks in (b) "Topo" sub-figure are caused by strong air-scattering (10e^8 counts) of the diffracted beam.

5.2.5 Epitaxial growth on LAO

Having explored the epitaxial growth of BTFM-CTO films in STO, we focused again on films grown on LAO substrate. We remind here to the reader our previous findings on the strain-induced stabilization of a mixture of a pseudocubic and tetragonal-like BTFM-CTO film phases and their thickness-dependent post-deposition relaxation to the pseudocubic phase following an in-situ heat-treatment., in **section 5.2.1.**

To explore this thickness-dependent phase transition of BTFM-CTO, a number of films were deposited on LAO substrates with thicknesses of 250, 1,000 and 40,000 laser shots under the growth conditions of **section 5.2.3.1**.

Out-of-plane XRD measurements, in **Figure 5. 26**, have shown the stabilization of a single-phase film for thicknesses up to 1,000 laser shots, while thicker films (of 40,000 laser shots) resulted in a multiphase sample, in agreement with our previous findings (in **section 5.2.1**). The high crystal quality of the as-grown BTFM-CTO films (for 250 and 1,000 laser shots) was verified by the observed Laue oscillations around the main film reflection peaks and the absence of impurity phases.

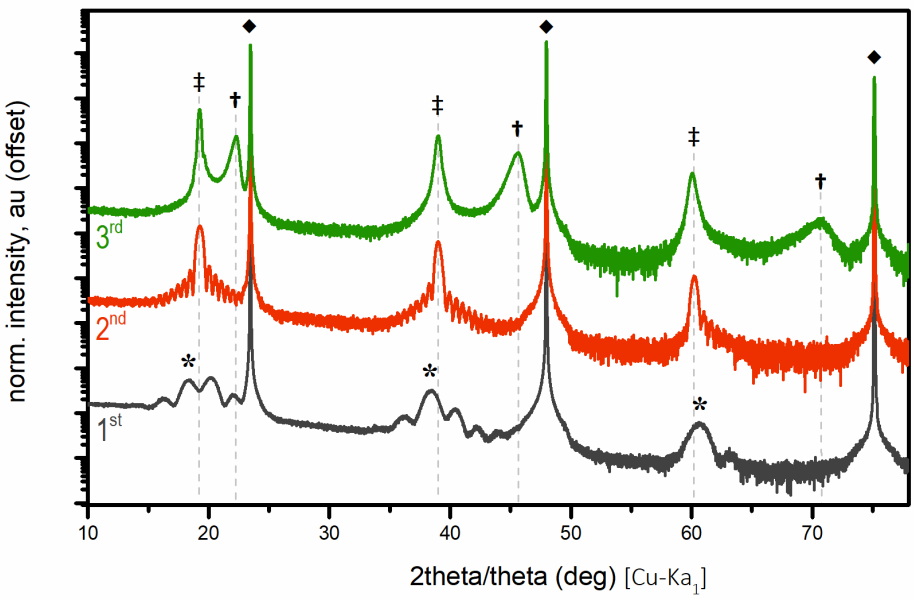

Figure 5. 26: Out-of-plane θ/2θ scans of BTFM-CTO films on LAO substrates at different thicknesses, for: (1) 250, (2) 1,000 and (3) 40,000 pulsed laser shots. Growth conditions were as those in **section 5.2.3.1**. Reflections denoted with (†) indicate the tetragonal-like phase and with (‡) the reflections of $(00l)_{PC}$ MPB phase emerging on relaxed films. Symbol (◆) highlights the LAO substrate peaks. The main reflection of the 5 nm ultra-thin BTFMO-CTO film is denoted with the symbol (∗).

The growth rate of these BTFM-CTO films was assessed by fitting the XRR spectra as well as the out-of-plane X-ray Laue oscillations of the 1,000 laser shots film in **Figure 5. 26**. As seen in **Figure 5. 27** and **Table 5. 9**, in both cases the thickness of the examined film was found to be approximately 19 nm, in agreement with the previously calculated growth rate of BTFM-CTO films on STO substrates (**section 5.2.3.2**). Rocking curve measurements around the second-order reflection revealed the high crystalline quality of the film with a mosaicity of about 0.034, in **Table 5. 9**.

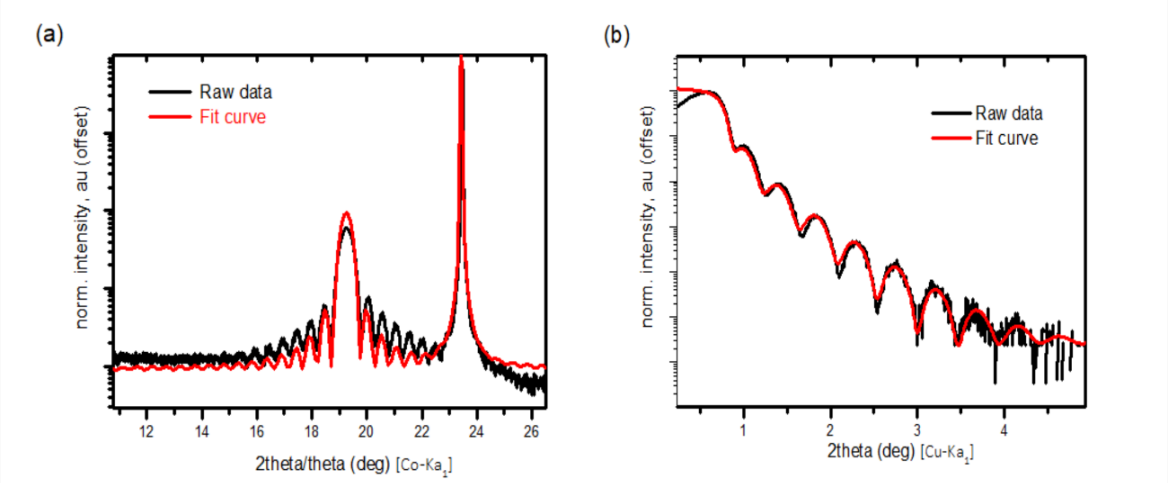

Figure 5. 27: Fits of: (a) the Laue oscillations around the tetragonal-like $(002)_{PC}$ reflection (at $2\theta = 38.5^{o}$) and (b) X-ray reflectivity (XRR) pattern of the 1,000 laser shots BTFM-CTO film.

Table 5. 9: Thickness and mosaicity of BTFM-CTO film on LAO substrate.

	Thickness (nm)		Mosaicity			
	XRR-data	XRD -data (Laue Oscillations)	FHWM (deg.)	Adj. R-Square	Model	c-axis
1.000	18.5	19.24	0.034(1)	0.996	PsdVoigt1	4.134

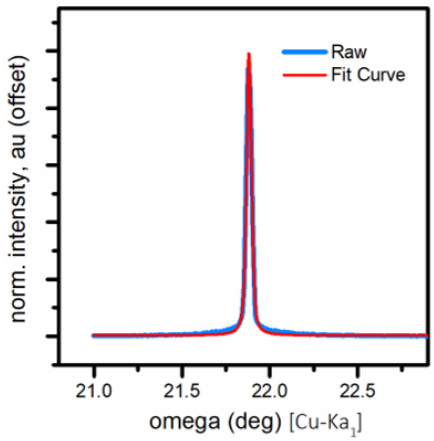

Figure 5. 28: X-ray diffraction rocking curves (in linear scale) around the tetragonal-like $(002)_{PC}$ reflection (at $2\theta=38.5^{o}$) of the 1,000 laser shots BTFM-CTO film of **Figure 5. 26**.

The crystal structure of the BTFM-CTO films grew on LAO was investigated by synchrotron X-ray reciprocal-space maps on the 1,000 laser shots BTFM-CTO film (in **Figure 5. 26**) at the Diamond Light source, UK (I07 beamline).

To assess the epitaxial growth of BTFM-CTO on LAO substrate, we firstly investigated the in-plane alignment of the film to the substrate by asymmetric, two-dimensional *HL* and *KL* cross section scans along the *L* direction (for $0 < L < 3.5$) while targeting the (10) and (11) *HK*-reflections of the LAO substrate, as illustrated in **Figure 5. 29**. In both cases, as can be seen in **Figure 5. 30a** and **Figure 5. 30b**, the film was found to be fully strained to the substrate along the in-plane directions. The *L* units of the film peak reflections were found to lie in lower values than the LAO substrate, in agreement with our in-house out-of-plane measurements

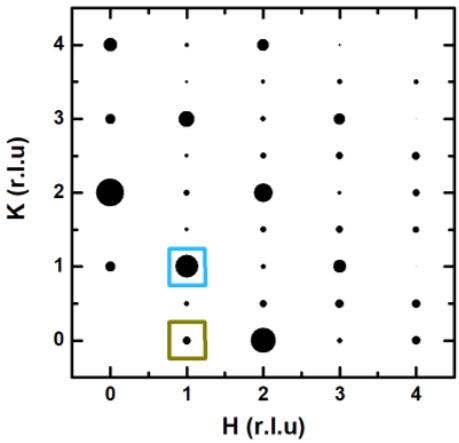

Figure 5. 29: Allowed XRD reflexions along the HK crystallographic plane (with L=0) of LAO. Axis are given in reciprocal lattice units. The green and blue squares are denoting the (10) and (11) -(*HK*) points.

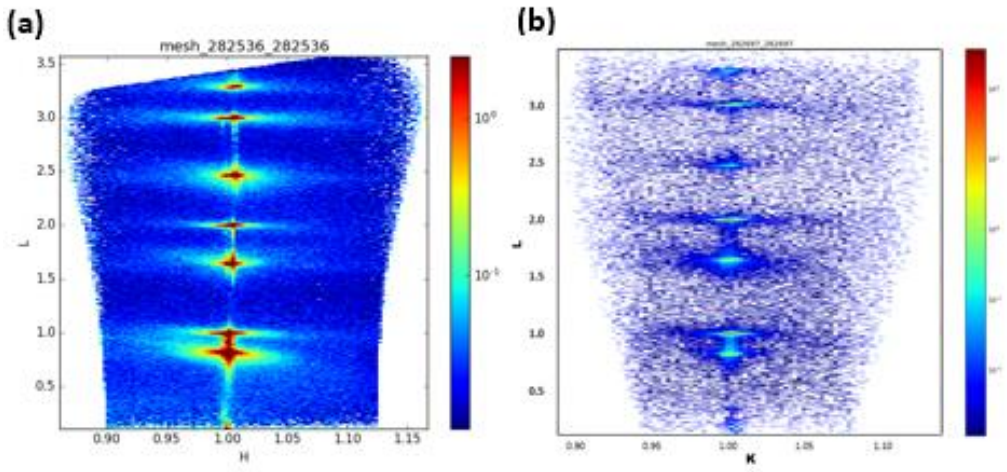

Figure 5. 30: Two-dimensional *HL* and *KL* cross sections scans along the (*10L*) and (*11L*) directions, respectively, for the 1,000 laser shots thick BTFM-CTO film in **Figure 5. 26**. The RSM scans were collected on the I07 beamline at the Diamond Light source-UK.

Given the characteristically distinct symmetry of half-order peaks in the rhombohedral and orthorhombic structures, as illustrated in reciprocal space units in **Figure 5. 31**, we further investigated the crystal phase of the BTFM-CTO film by cross section scans around half-order reflection peaks of the LAO substrate.

To do so, we initially focused, respectively, on the (0.5, 1.5) *HK*- orthorhombic reflection and (1.5, 0.5) *HK*- rhombohedral reflection points of the two symmetries where half-order peaks are expected and we performed the corresponding two-dimensional *HL* and *KL* cross sections scans along the *L* direction (with $0 < L < 3.5$), as shown in **Figure 5. 32**. In order to exclude the possibility of an orthorhombic film growth where the long c-axis is lying along the in-plane direction of LAO, illustrated in **Figure 5. 33b**, we also focused on the (1.5, 0.5) *HK*-reflection point of the "permutated" orthorhombic symmetry where we repeated two-dimensional *HL* and *KL* cross sections scans along the *L* direction, in **Figure 5. 34**.

In both cases, the absence of film reflections indicates a film symmetry higher than the rhombohedral or orthorhombic symmetries and thus the tetragonal-like growth of BTFM-CTO films. These findings are in line with similar observations in the literature for strain-induced $BiFeO_3$ films in LAO substrates[292,293].

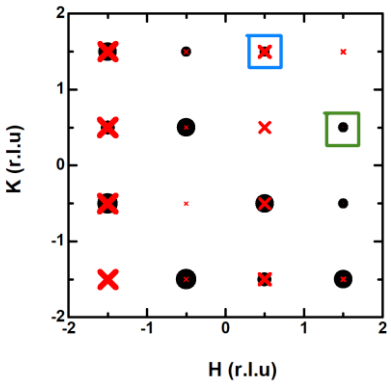

Figure 5. 31: Allowed half-order XRD reflexions along the HK crystallographic plane (with L=0) of the rhombohedral (black cycles) and orthorhombic (red crosses) symmetry. Axis are given in reciprocal lattice units. The blue and green squares are denoting the (0.5, 1.5) and (1.5, 0.5) -(*HK*) points. Note here that at the (0.5, 1.5) -(*HK*) crystallographic point of the figure reflections of both the rhombohedral and orthorhombic symmetries are expected.

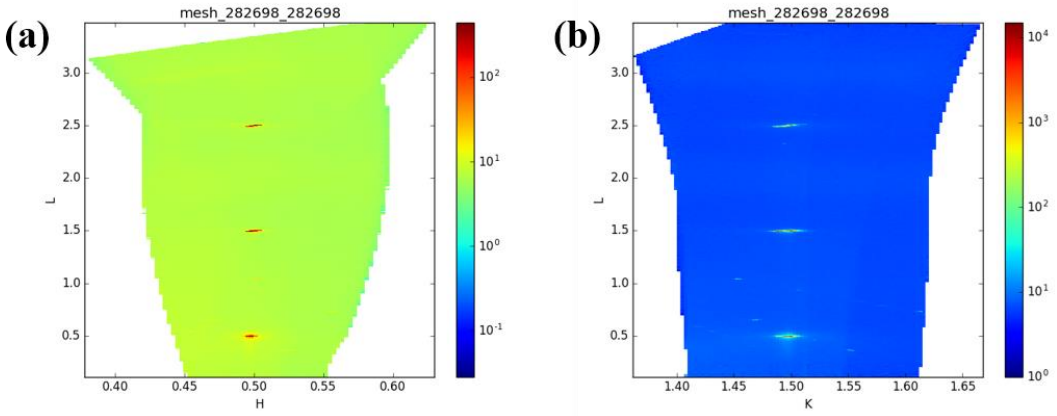

Figure 5. 32: Two-dimensional *HL* and *KL* cross sections scans along *L* direction for the 1,000 laser shots thick BTFM-CTO film, in **Figure 5. 26**, targeting: (a) the (0.5, 1.5) -(*HK*) reflection point of the orthorhombic symmetry and (b) the (1.5, 0.5) -(*HK*) reflection point of the rhombohedral symmetry. The RSM scans were collected on the I07 beamline at the Diamond Light source-UK.

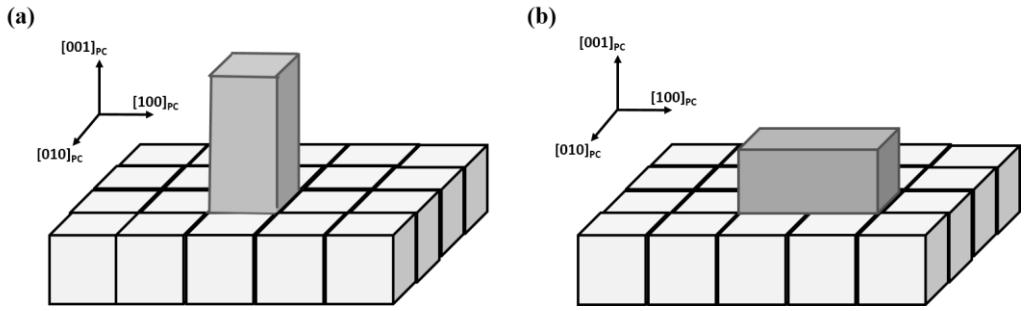

Figure 5. 33: Schematic representation of the possible arrangements of an orthorhombic BTFM-CTO film on top of the rhombohedral LAO substrates resulted from the permutation of its axes.

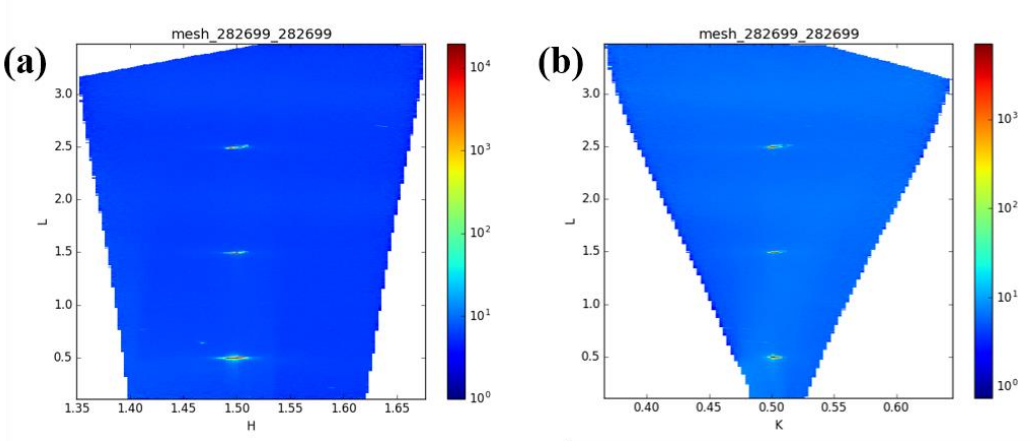

Figure 5. 34: Two-dimensional *HL* and *KL* cross sections scans along the: (a) the (*HL*) and (b) (*HL*) direction of the (1.5, 0.5) -(*HK*) point of the "permutated" orthorhombic symmetry for the 1,000 laser shots thick BTFM-CTO film, in **Figure 5. 26**. The RSM scans were collected on the I07 beamline at the Diamond Light source-UK.

5.3 Electrical properties of BTFM-CTO films

5.3.1 Optimization of BTFM-CTO/ SRO heterostructures

5.3.1.1 Growth of SRO buffer layer

Dielectric measurements of BTFM-CTO films grew on conductive 10% Nb-doped STO (Nb:STO) substrates, according to the geometry of **Figure 5. 35a**, revealed a non-Ohmic behaviour and large leakage currents as has been also previously reported in the literature[298]. To overcome these difficulties, a different capacitor geometry has employed using a buffer $SrRuO_3$ (SRO) layer as bottom film electrode, as seen in **Figure 5. 35b**.

SRO has been extensively used in oxide thin film systems as a conductive (in the range of 10^5 to 10^6 S/m), highly chemically stable and compatible with the perovskite films. The growth of SRO films by pulsed laser deposition has been well studied[299,300]. According to Gan et al.[301], it has an orthorhombic structure at room temperature with lattice parameters: a_0 = 5.5670 Å, b_0 = 5.5304 Å and c_0 = 7.8446 Å.

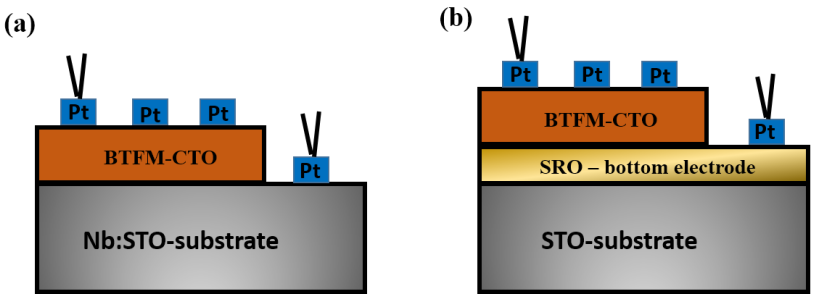

Figure 5. 35: Different capacitor cell geometries that were used. The used circular top Pt electrodes of the capacitor cell, of 50 nm thickness and 0.05 cm^2 point electrode area, were sputtered with a shadow mask.

Following literature reports[302], SRO films were grown on (001) STO substrates by PLD at 620 ºC under 95 mTorr of oxygen pressure and a laser fluency of 1 J/cm^2. The initial thickness of the as-grown SRO films was set to 9,000 laser shots.

Single-oriented SRO films on STO were obtained with the observation of Laue oscillations around the (00*l*) out-of-plane film peaks confirming the growth of high quality film, in **Figure**

5. 36. These results were further supported by mosaicity studies on the $(002)_{PC}$ peak of the as-grown films showing a low crystalline spread (FHWM of 0.03°), in **Figure 5. 37b**. The growth rate of SRO film was evaluated by XRR measurements and found to be 3.3 nm/1000 laser shot, corresponding to a 30 nm thick film, in **Figure 5. 37a**.

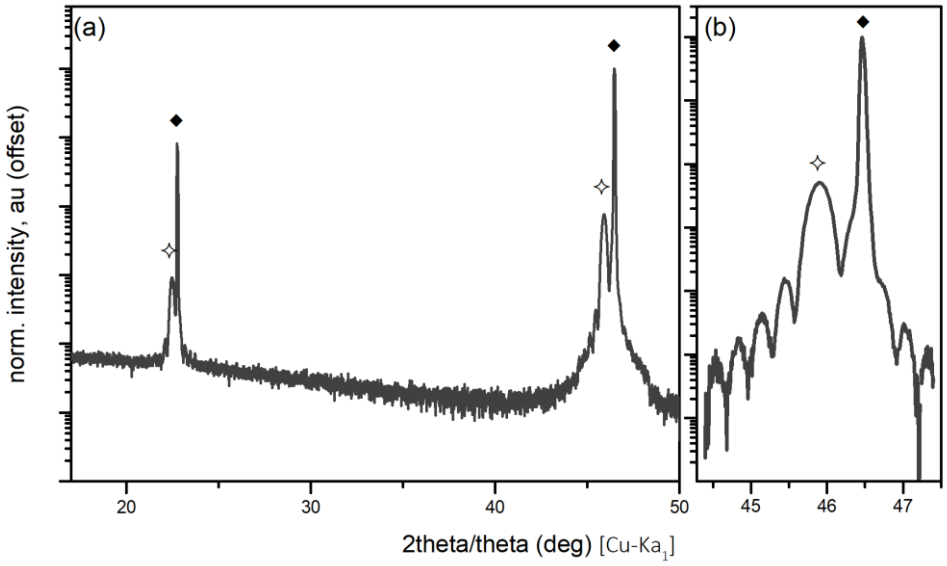

Figure 5. 36: (a) Out-of-plane θ/2θ scans and (b) magnified view around the (002) peak position of SRO films on STO substrate. Deposition parameters as follows, deposition temperature: 620 °C; chamber pO_2: 95 mTorr; laser fluence: 1 J/cm^2; pulsed laser shots: 9,000. Reflections denoted with (◊) indicate the $(00l)_{PC}$ SRO film peaks. The symbol (◆) corresponds to STO substrate peaks.

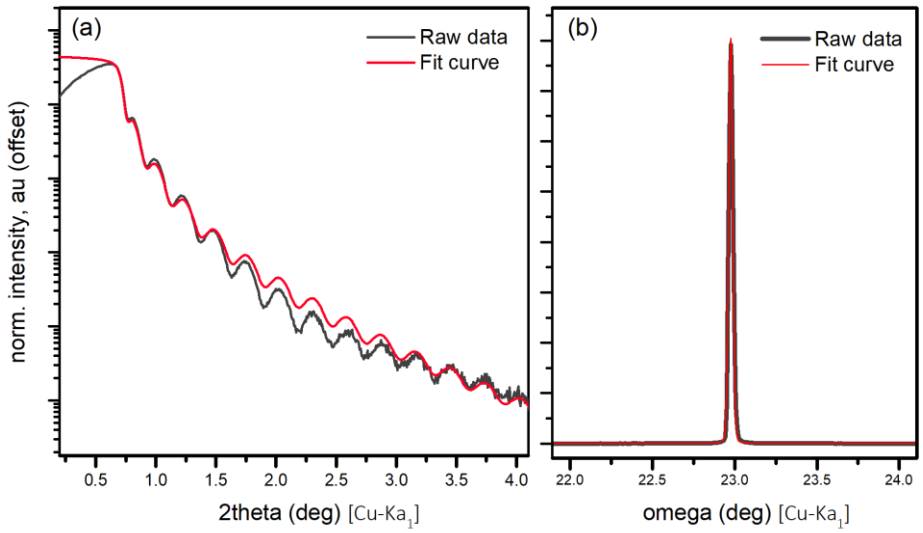

Figure 5. 37: (a) X-ray reflectivity (XRR) pattern (black line) and the best fit (red line) to a 9,000 laser shots thick SRO film and (b) x-ray diffraction rocking curve (raw data and fit curve) around $(002)_{PC}$ of as grown SRO film. Film grown at 620 °C, under 95 mTorr of chamber pO_2 and laser fluence of 1 J/cm^2 for 9000 laser shots.

Finally, the surface topology of the as-grown SRO film, studied by AFM in **Figure 5. 38**, revealing a smooth terrace surface with a root-mean-square value surface roughness (R_{rsm}) of 1 nm.

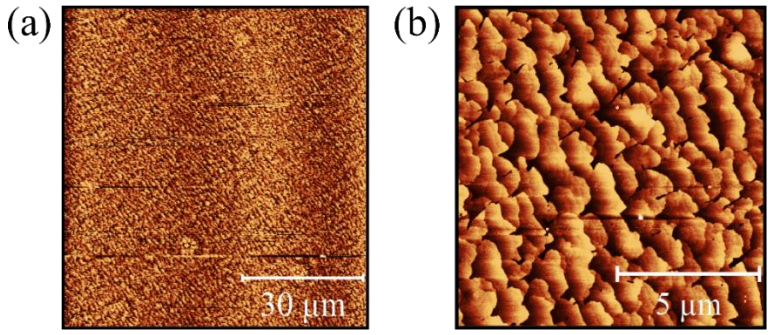

Figure 5. 38: (a) Plain-view AFM images (of 70 x 70 um) of as-grown SRO film on (001) STO. (b) Zoom-in topography (10 x 10 um) of the previous image.

5.3.1.2 Growth of BTFM-CTO/SRO heterostructures

Having grown high-crystalline, single-oriented SRO thin film bottom electrodes, we investigated the deposition of epitaxial BTFM-CTO films on SRO-buffered STO substrate.

The protocol of the BTFM-CTO/SRO heterostructure depositions involved the following steps:

a. The deposition of SRO bottom film electrode on STO (at 620 ºC, 95 mTorr) and the evaluation of its crystallinity by out-of-plain θ/2θ and rocking curve measurements prior to its use as buffer layer,
b. The SRO-buffered STO substrate was positioned under a shadow mask and placed back to the chamber where it was pumped overnight to a low base pressure, below $6x10^{-7}$ Torr,
c. For the growth of the BTFM-CTO thin films, the deposition chamber was heated up to 710 ºC under an oxygen pressure of 95 mTorr to prevent the degradation of SRO as the substrate was annealed at temperatures higher than SRO deposition temperature (620 ºC),
d. When the temperature reached 710 ºC the substrate was kept at 95 mTorr of oxygen pressure for 20 min to anneal and relax the SRO film,
e. Finally, the oxygen pressure was reduced to 15 mTorr and the deposition of BTFM-CTO was started as soon as the temperature of the substrate stabilized at 710 ºC (in

approx. 3 min). When the deposition finished, the BTFM-CTO films were cooled down at room temperature at a rate of 20 ºC/min, under 15 mTorr.

f. The BTFM-CTO films were grown using the Bi-rich target.

Following these conditions, BTFM-CTO films of different thicknesses (3,000, 7,500 and 13,000 laser shots) were grown on a 30 nm (9,000 laser shots) SRO buffer film. At first sight, the resulting out-of-plane XRD scans of the films, in **Figure 5. 39**, revealed the deposition of a single-oriented heterostructure of BTFM-CTO/SRO on STO with the presence of the SRO buffer layer being seen as a distinct peak reflection between the $(00l)_{PC}$ BTFM-CTO and STO peaks.

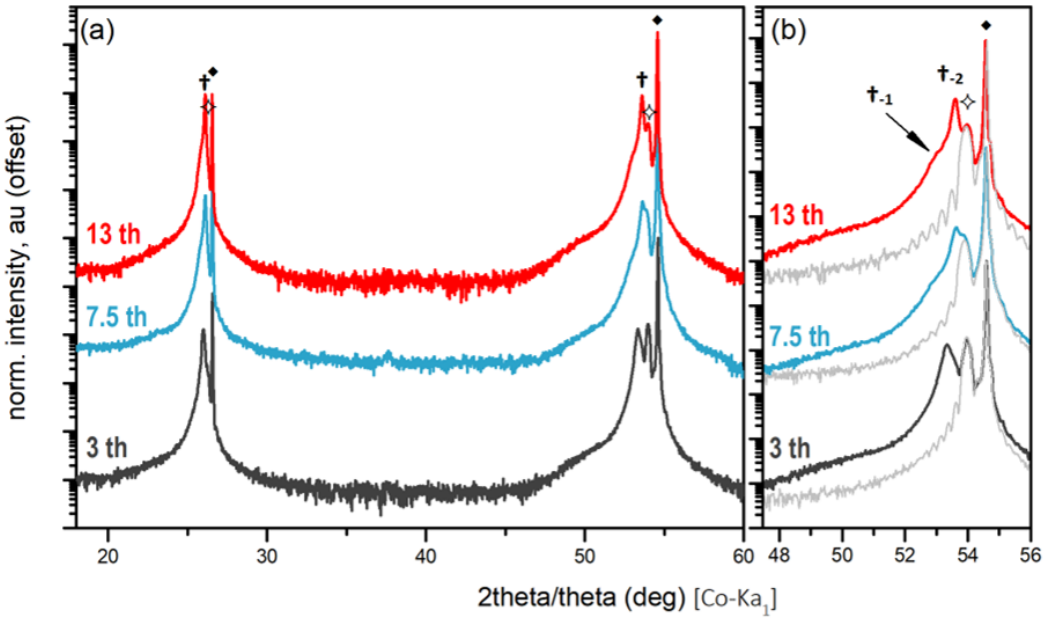

Figure 5. 39: (a) Out-of-plane θ/2θ scans and (b) magnified view around the $(002)_{PC}$ peak position of BTFM-CTO films of varying thicknesses: 3,000, 7,500 and 13,000 pulses on SRO/STO substrates. Growth conditions as described in **section 5.3.1.2**. Symbols (**†-1**) and (**†-2**) mark, respectively, the orthorhombic and rhombohedral components of the $(002)_{PC}$ BTFM-CTO peak splitting. Reflections from the SRO buffer layer are highlighted with (◊) and those from the STO substrate with (◆).

However, the morphotropic growth of the BTFM-CTO films proved challenging and a careful examination of the out-of-plane scans reveals the absence (or very weak presence) of splitting for the $(00l)_{PC}$ peaks of the 3,000 and 7,500 laser shots films. These findings were also confirmed by rocking curve measurements. Detailed omega scans around the $(002)_{PC}$ film peak

of the 13,000 laser shots film verified the co-existence of two well-distinct crystalline phases, as illustrated in **Figure 5. 40c**. In addition, the mosaic spread of both phases was found to be improved when compared to the spreads of the same thickness BTFM-CTO films in STO (in **section 5.2.4.1** and **Table 5.8)** due to the smaller lattice mismatch between BTFM-CTO and SRO.

In the case of the 3,000 and 7,500 laser shots BTFM-CTO films, only a single crystal phase was detected, evidenced by the absence of splitting on their out-of-plane $(00l)_{PC}$ reflection peaks. The mosaic spread of this phase was seen to increase from 0.027 to 0.41 as the film thickness increased from 3,000 to 7,500 laser shots due to relaxation effects.

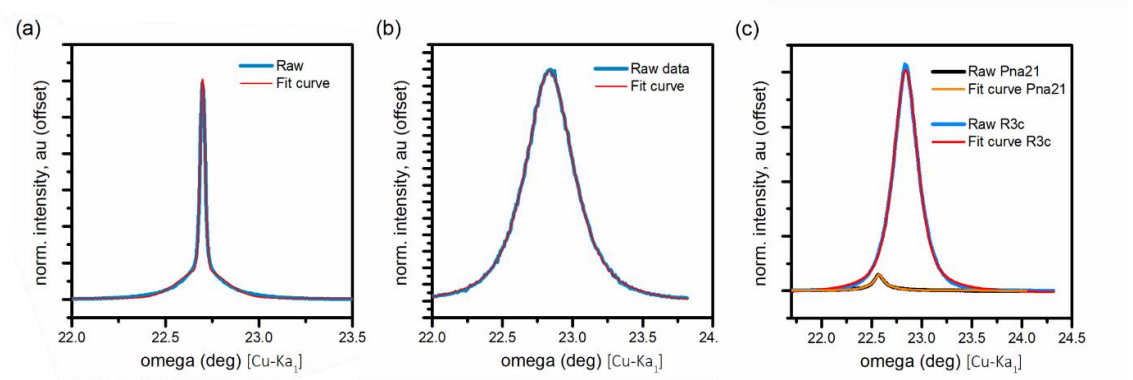

Figure 5. 40: X-ray diffraction rocking curve (raw data and fit curve) around the $(002)_{PC}$ peak of $SrRuO_3$-buffered BTFM-CTO for different thicknesses of: (a) 3,000, (b) 7,500 and (c) 13,000 laser shots. Growth conditions as described in **section 5.3.1.2.**

AFM studies of the BTFM-CTO/SRO films confirmed the observed structural differences between the 13,000 laser shots film and the other two films (for 3,000 and 7,500 laser shots). In the case of the 13,000 laser shots film, a well-ordered and textured growth was revealed by the AFM images shown in **Figure 5. 43**. On the contrary, the other two films were found to demonstrate a less-ordered morphology favouring island growths in **Figure 5. 41** and **Figure**

5. 42. A smooth surface topology was nevertheless observed for all the films with a root-mean-square roughness (R_{rms}) not exceeding the 3 nm, in **Table 5. 10**.

In summary, our work on the epitaxial deposition of BTFM-CTO films on SRO-buffered STO substrates showed the difficulties of a reproducible morphotropic growth of BTFM-CTO films at different thicknesses. Combined crystallographic and topological studies revealed the absence of a morphotropic growth and a less well-ordered surface morphology for the thinner BTFM-CTO of 3,000 and 7,500 pulses.

Table 5. 10: Surface roughness and mosaicities of $SrRuO_3$-buffered BTFM-CTO films of different thicknesses

Film	Roughness		Mosaicity			
			Peak			
	RSM (nm)	Peak-to-Valley (nm)	FHWM (deg.)	Adj. R-Square	Model	c-axis
3000	2.23	27.7	0.027(1)	0.997	Gauss	3.917
7500	1.38	12	0.413(1)	0.999	PsdVoigt1	3.894

Film	Roughness		Mosaicity							
			Peak -1 (Pna21)				Peak -2 (R3c)			
	RSM (nm)	Peak-to Valley (nm)	FHWM (deg.)	Adj. R-Square	Model	c-axis	FHWM (deg.)	Adj. R-Square	Model	c-axis
13000	2.50	30.3	0.130(1)	0.996	Gauss	4.016	0.291(1)	0.999	PsdVoigt1	3.972

However, as we have already seen in **sections 5.2.3.2** and **5.2.3.3**, these difficulties in stabilizing the morphotropic growth of BTFM-CTO films should not be intrinsically related to the thickness of the as-grown films but rather ascribed to small changes on the ablation/growth conditions beyond the better controlled nominal conditions of temperature, oxygen pressure and laser energy.

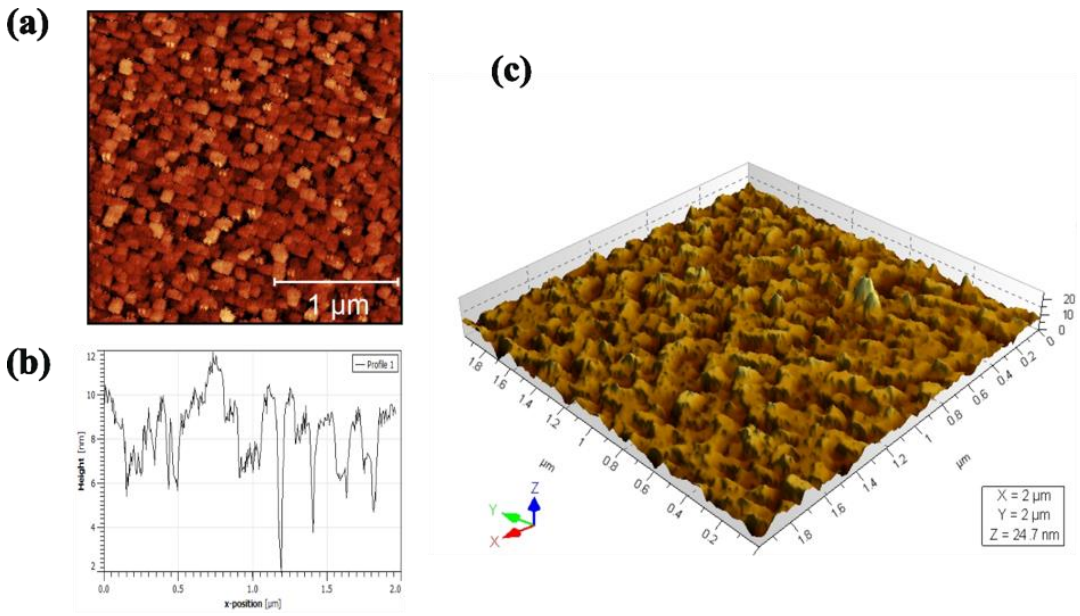

Figure 5. 41: (a) AFM plain-view image, (b) line profile and (c) 3D projection of a 2x2 µm area of the 3,000 pulses thick BTFM-CTO/SRO in **Figure 5. 39**.

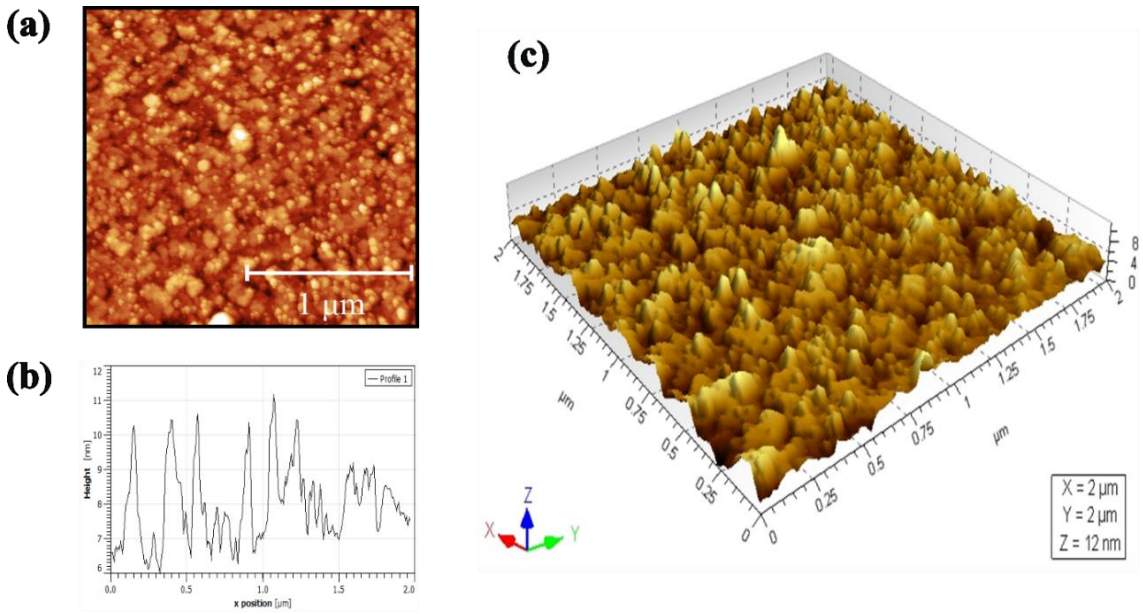

Figure 5. 42: (a) AFM plain-view image, (b) line profile and (c) 3D projection of a 2x2 µm area of the 7,500 pulses thick BTFM-CTO/SRO in **Figure 5. 39**.

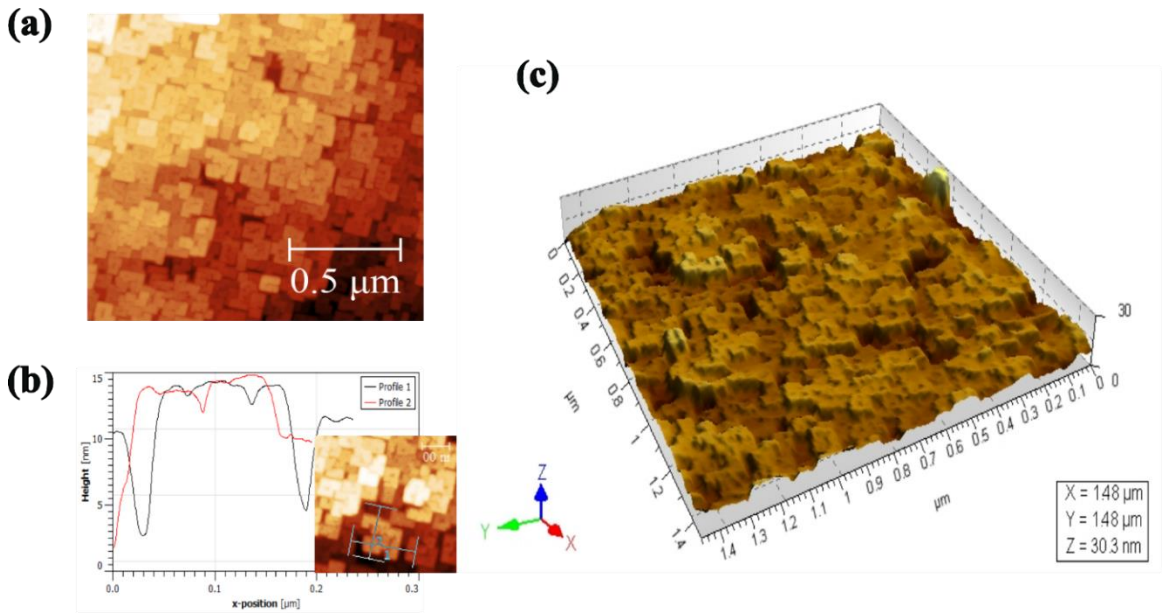

Figure 5. 43: (a) AFM plain-view image of a 1.5x1.5 µm area, (b) magnified line profile around textured surface features (c) 3D projection of a 1.5x1.5 µm area of the 13,000 pulses thick BTFM-CTO/SRO in **Figure 5. 39**.

5.3.2 Dielectric measurements of BTFM-CTO films

The dielectric behaviour of SRO-buffered BTFM-CTO films in **section 5.3.1.2** was evaluated by measurements of their dielectric constant and losses. Prior to these measurements, the ohmic character of the employed electrodes in our capacitor cell, illustrated in **Figure 5. 35b**, was assessed in forward and reverse voltages (-0.03 < V > 0.03) with the use of an Agilent E4980 Precision LCR meter.

As seen in **Figure 5. 44**, all the examined films shown an ohmic behaviour regardless of their thickness. However, only the thicker film (of 13,000 laser shots) was found to be sufficiently insulating with a resistance as high as 1.6 GΩ whereas the thinner films demonstrated a rather conductive behaviour (with a resistance below 1 KΩ).

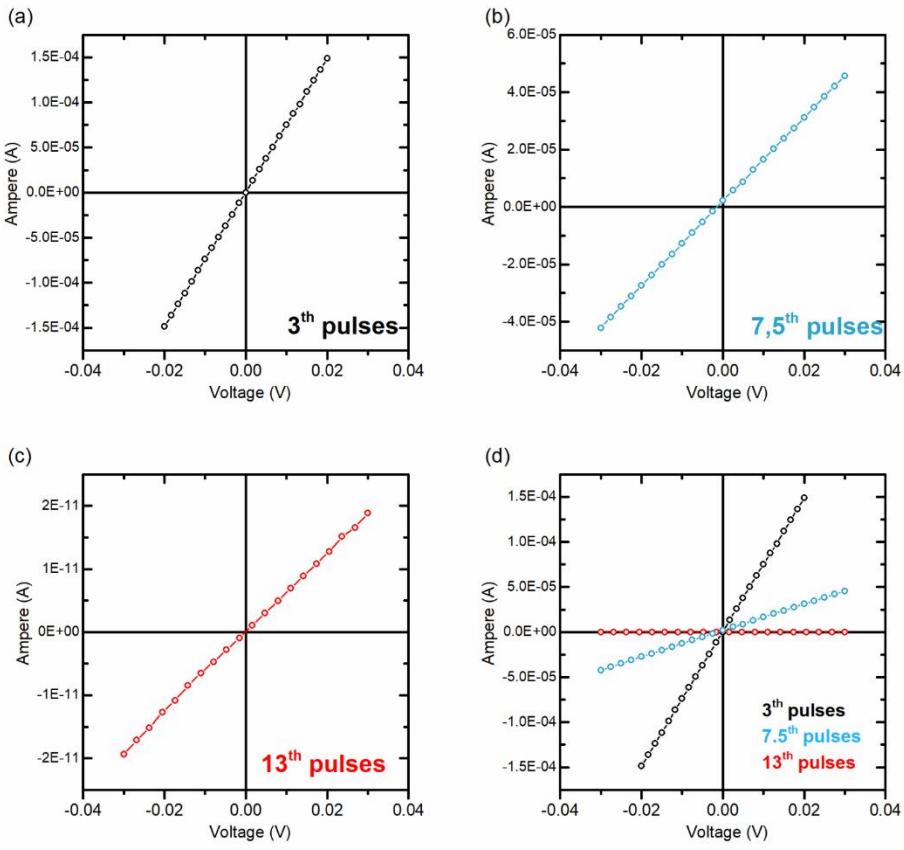

Figure 5. 44: Current-voltage measurements in the range of ±0.03 V for BTFM-CTO of variable thicknesses: (a) 3,000, (b) 7,500, (c) 13,000 pulsed laser shots and (d) plotting all the films together. The obtained resistances of the films, calculated from the slope of the graphs, were accordingly found: 134(2), 683(1) and 1.589(3) MOhm. The capacitor structure used is shown in **Figure 5. 35b**.

The dielectric constant ε, and dielectric loss tanδ, of the as-grown films were measured on an Agilent E4980 Precision LCR meter by applying an AC voltage of 0.2 V in the frequency range of 20 Hz to 2 MHz. More specifically, the dielectric constant of the films ε_r was calculated from the capacitance readings according to:

$$\varepsilon_r = \frac{C_p\, d}{\varepsilon_o\, S}$$

where C_p is the capacitance (F), ε_o is the free space permittivity value (8.859x10^{-12} F/m), S is the point electrode area (m^2), and d is the thickness (m) of the films[303].

The measured dielectric constants of the films were found to decrease at higher frequencies, in agreement with literature reports describing the effect of higher frequencies on the polarization of a medium[304]. As seen in **Figure 5. 45**, only the 13,000 shots film, among the examined samples, demonstrated a considerably stable and relative high dielectric constant along the whole range of measured frequencies while the two other films (3,000 and 7,500 pulses) showed very high losses.

More specifically, when measured at 1 kHz, the 13,000 shots film was found to display a high dielectric constant, ε_r = 270, and losses of the same order (tanδ_{FILM} = 0.02) as that of bulk BTFM-CTO (tanδ_{BULK} = 0.03).

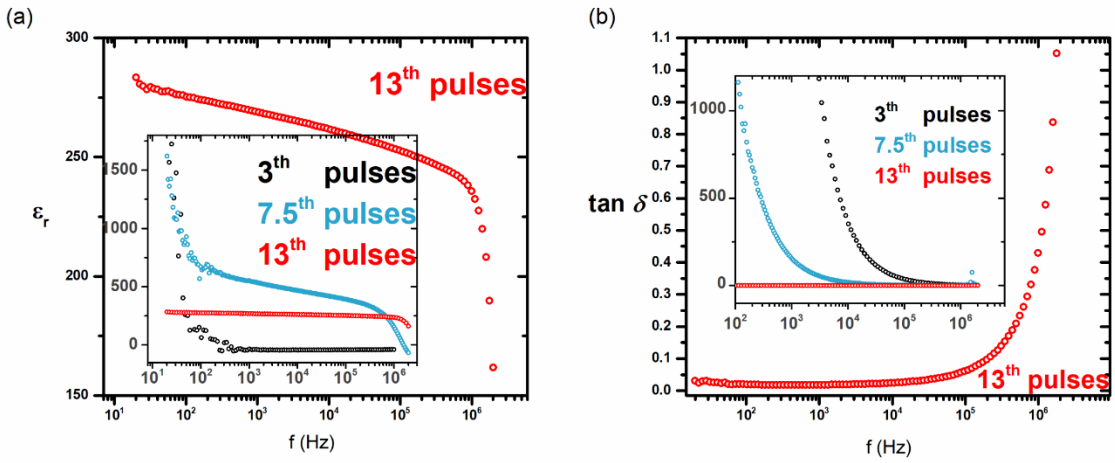

Figure 5. 45: Frequency dependent (in log scale) of (a) real part of dielectric constant (ε_r) and (b) dielectric loss (tan δ) for Pt/BTFM-CTO/SRO/STO samples of different BTFM-CTO thicknesses (in pulses).

The poor dielectric performance of the thinner BTFM-CTO films was found in agreement with the current-voltage measurements of the films (in **Figure 5. 44**) and indicates the leakage current behaviour of films that failed to stabilise in the MPB composition (in **section 5.3.1.2**). The reader, however, should note here that the lossy behaviour of BTFM-CTO films crystallized away from the MPB phase should not be inherently correlated to their thickness, as was already seen in **section 5.2.4.1**. It should however be noted that a systematic investigation of the thickness-dependent ferroelectric properties of morphotropic BTFM-CTO films is missing from this work and needs to be addressed in the future.

5.3.3 Ferroelectric measurements

5.3.3.1 Reproducibility of BTFM-CTO films in the MPB

With the thinner films (< 13,000 pulses) showing a poor dielectric behaviour, we focused our attention on the ferroelectric properties of thicker (13,000 laser shots) BTFM-CTO films.

To examine the reproducibility of the ferroelectric properties of BTFM-CTO, three SRO-buffered BTFM-CTO films of the same thickness were grown under the same nominal conditions as in **section 5.3.1.1**.

The XRD data of these samples (out-of-plane θ-2θ and rocking curve scans) are summarized in **Figure 5. 46** and **Figure 5. 47** as it follows:

- the initial SRO-buffered BTFM-CTO film, already seen in **section 5.3.1.1**, labelled as film-1, and
- repetitions of the same thickness films, labelled respectively as films -2, -3 and -4.

At first sight, one can observe the presence of the two morphotropic phases in the θ-2θ scans of all the films, denoted as ✝-1 and ✝-2 in **Figure 5. 46**.

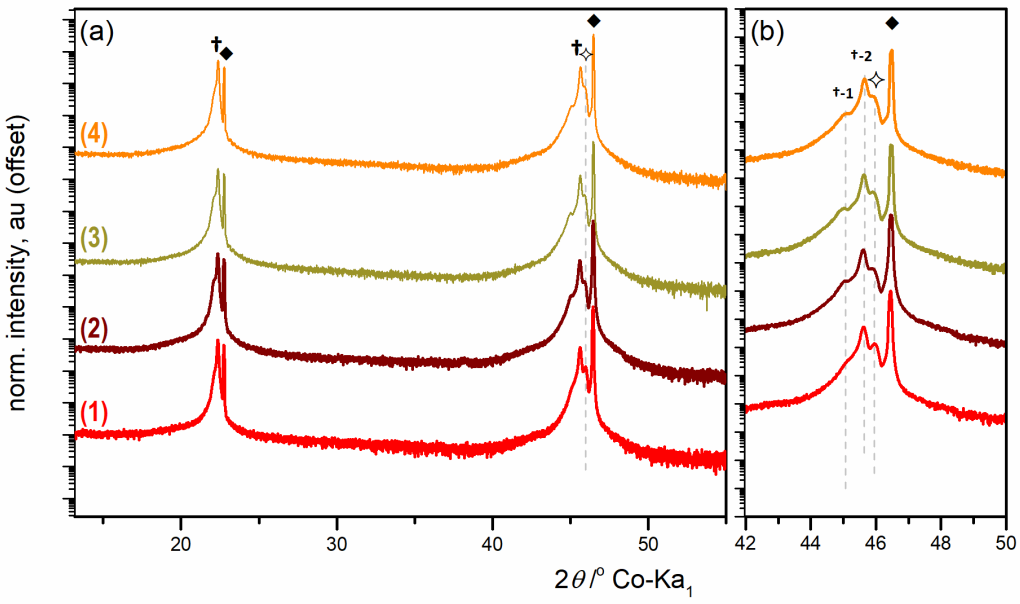

Figure 5. 46: (a) Out-of-plane θ/2θ scans and (b) magnified view around the $(002)_{PC}$ peak position of 13,000 laser shots BTFM-CTO/SRO films grown for studying the reproducibility of their ferroelectric properties. Growth conditions as described in **section 5.3.1.1**. Symbols (✝-1) and (✝-2) are marking, respectively, the orthorhombic and rhombohedral component of the BTFM-CTO films in the MPB region. Reflections of buffer SRO layer are highlighted with (◊) and substrate reflections with (◆).

Moreover, the RC measurements performed around the $(002)_{PC}$ reflection peak of the studied films have also confirmed: (a) the well-distinct separation of the orthorhombic and rhombohedral peak components, (b) a further improvement in the crystallinity of the two phases in comparison to the initial film growth (film -1) and finally (c) an increased presence of the orthorhombic (minority) phase as indicated in the relative intensity of the two phases.

A smooth surface with a root-mean-square roughness (R_{rms}) smaller than 2.5 nm was shown in all the films although in some cases the topology of the films did not exhibit the characteristic square-like texture of the first film, in **Appendix F**. The roughness and the mosaicity of all the films have been tabulated in **Table 5. 11**.

Overall, the following BTFM-CTO films (films -2, -3, -4) were found to demonstrate a better crystal quality and more well-defined boundaries of the two-phase coexistence region.

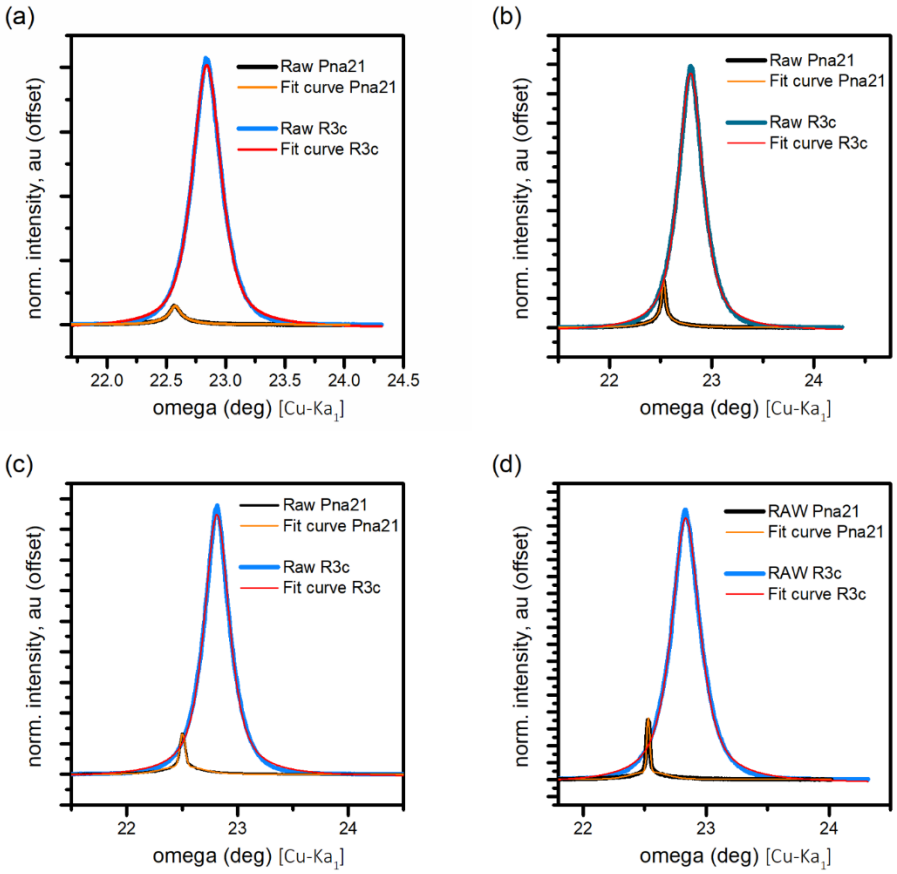

Figure 5. 47: Rocking curve (raw data and fit curve) around the $(002)_{PC}$ peak splitting of 13,000 pulses BTFM-CTO/SRO film of **Figure 5. 46**: (a) film -1, (b) film -2, (c) film -3 and (d) film -4.

Table 5. 11: Mosaicities of $SrRuO_3$-buffered epitaxial BTFM-CTO thin for PE measurements (films of 13,000 laser shots thick).

Film	Roughness		Mosaicity							
			Peak -1 (Pna21)				Peak -2 (R3c)			
	RSM (nm)	Peak-to-Valley (nm)	FHWM (deg.)	Adj. R-Square	Model	c-axis	FHWM (deg.)	Adj. R-Square	Model	c-axis
(1)	2.50	30.3	0.130(1)	0.996	Gauss	4.016	0.291(1)	0.999	PsdVoigt1	3.972
(2)	1.94	16.1	0.039(1)	0.998	Gauss	3.947	0.290(1)	0.998	PsdVoigt1	3.901
(3)	2.07	18.2	0.048(1)	0.995	Gauss	3.951	0.275(1)	0.999	PsdVoigt1	3.898
(4)	2.22	19.1	0.026(1)	0.992	Gauss	3.946	0.279(1)	0.999	PsdVoigt1	3.894

5.3.3.2 PE measurements

The dielectric measurements of the films were conducted using an Agilent E4980 Precision LCR meter E4980 and applying an AC voltage of 0.2 V in the frequency range 0.1 kHz to 1 MHz. The geometry of the capacitor used in these measurement is illustrated in **Figure 5. 35b**. Preliminary measurements under a $-0.03 < V < 0.03$ bias field have shown the ohmic character of the sputtered Pt contacts and the insulating nature of all the films with resistances in the order of $\sim 10^9\ \Omega$cm.

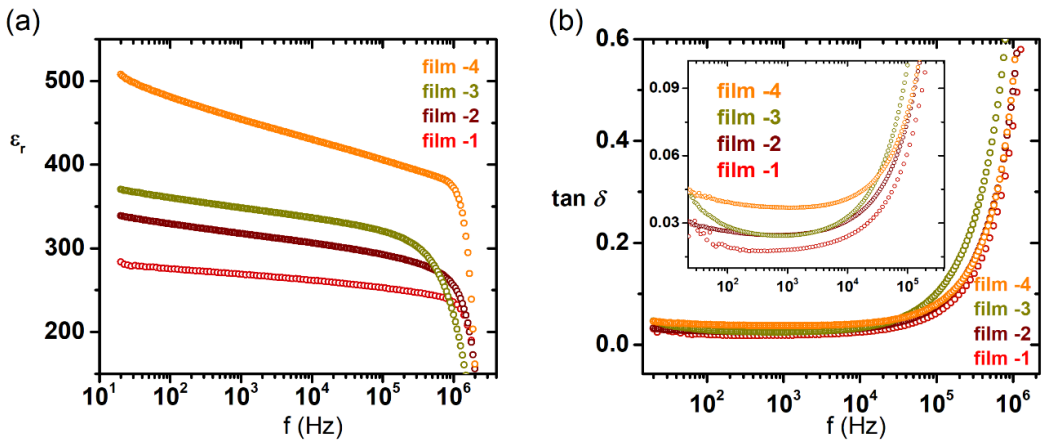

Figure 5. 48: Frequency dependent (in log scale) of (a) real part of dielectric constant (ε_r) and (b) dielectric loss (tan δ) for repeated BTFM-CTO films (13,000 laser shots).

The dielectric constant $\boldsymbol{\varepsilon}$ and dielectric loss tan$\boldsymbol{\delta}$ of the films, shown in **Figure 5. 48**, confirmed the insulating character of the samples with losses lower than 0.05 (for frequencies up to 30 kHz).

The room temperature polarization versus electric field hysteresis measurements (*PE* loop) of the films were performed using a commercial aixPES workstation (aixACCT Systems GmbH, Germany) and are shown in **Figure 5. 49**.

All the loops were measured using a range of driving voltages from 5 V to a maximum up to 25 V at frequency ranges of 1 and 2 kHz. The applied field was calculated after dividing the applied voltage with the thickness of the films, for d = 240 nm, according to:

$$E = \frac{V}{d}$$

while the coercive field (E_c) was calculated from the relation:

$$E_c = \frac{\left|V_c^{(+)} + V_c^{(-)}\right|}{2d}$$

where V_c is the nominal voltage required for switching and d the film thickness.

When comparing the *PE* response of the examined films, in **Figure 5. 49**, one can note that the films demonstrating a well-distinct morphotropic boundary (films: -2, -3, -4) were also found to present more symmetric and rectangular-shaped ferroelectric loops of a significantly higher remanent polarization (P_r). On the contrary, the film with the worst crystallographic quality (film-1) was also found to display a more tilted ferroelectric loop of a lower maximum remanent polarization.

A summary of the ferroelectric properties of the films is shown in **Table 5. 12**. The maximum measured polarization (P_{max}), remanent polarization (P_r), nominal switching voltage (V_c) and coercive field (Ec) for the maximum possible applied voltage (V_{max}) of each film have been listed in **Table 5. 12**. There, it can be clearly seen that a polarization as high as 130 μC/cm^2 was possible to be obtained under an applied field of 700 – 800 kV/cm. This is an enhanced ferroelectric performance in comparison to the bulk BTFM-CTO (66 μC/cm^2) due to the preferential crystallographic orientation of the films.

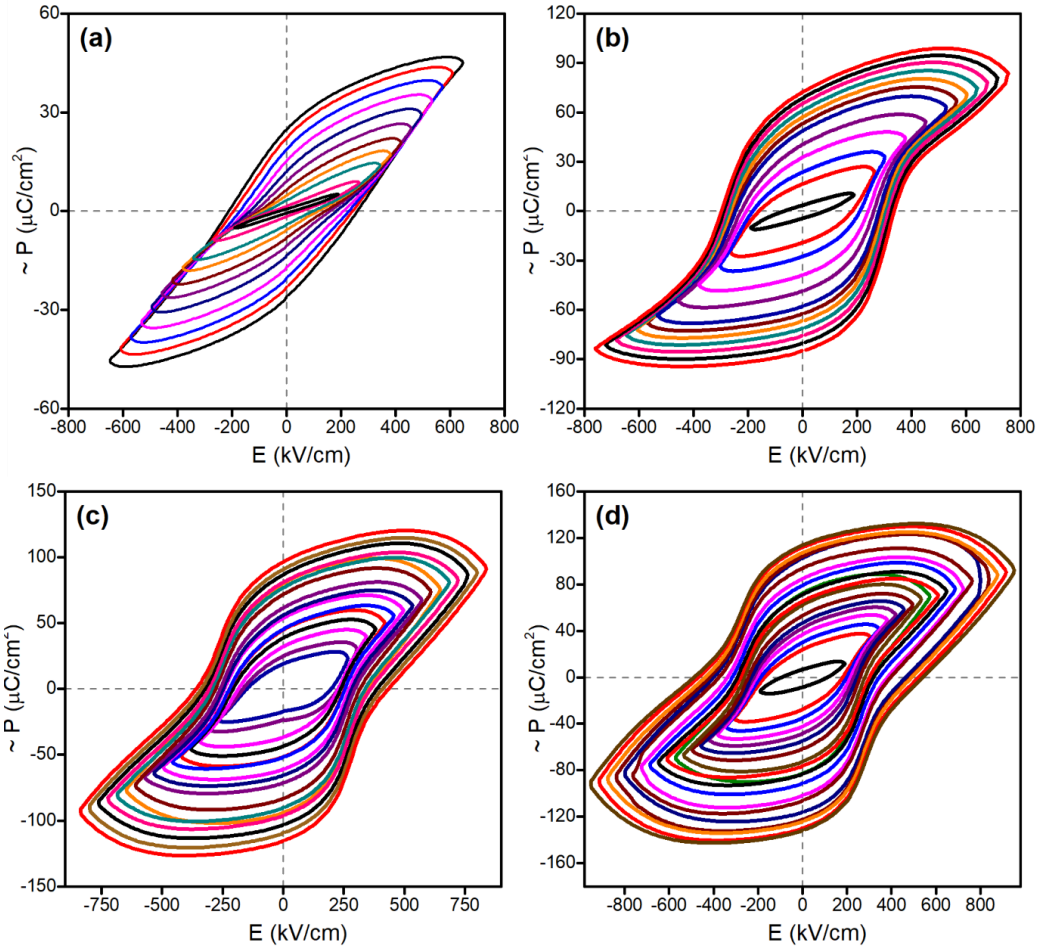

Figure 5. 49: Room temperature *PE* hysteresis loops of the BTFM-CTO films in **Figure 5. 44** at 2 kHz: (a) film -1, (b) film -2, (c) film -3, (d) film -4.

Table 5. 12: Summary of maximum measured polarization $\left(P_{max}^{(001)}\right)$, remanent polarization (P_r), nominal switching voltage (V_c), coercive field (E_c) and the calculated polarization $\left(P_{max}^{(111)}\right)$ for BTFM-CTO films grown on SRO-buffered STO substrates. Data recorded with a frequency of 2 Hz at the maximum applied voltage (*Max. Volt*).

	V_{max}	$P_{max}^{(001)}$	P_r		V_c		E_c	$P_{max}^{(111)}$
Film	(V)	(μC/cm²)	(μC/cm²)		(V)		(kV/cm)	(μC/cm²)
			$P_r^{(+)}$	$P_r^{(-)}$	$V_c^{(+)}$	$V_c^{(-)}$		
n1	17	45.06	24.80	-25.53	6.76	-5.51	258.86	78.04
n2	20	83.45	72.26	-84.44	8.77	-7.73	348.103	144.53
n3	22	91.21	96.46	-114.68	11.31	-9.36	436.08	157.98
n4	25	92.19	113.75	-130.92	14.08	-12.67	564.35	159.97

To compare the ferroelectric response of the films under the same applied field, their *PE* hysteresis loops at a driving voltage of 11V have been summarized in **Table 5. 13** and **Figure 5. 50a**. As can be seen in **Figure 5. 50a**, film-1 is showing an inferior ferroelectric performance of a narrower, more tilted and hardly saturated loop with a remanent polarization reaching below the one third of the other films. Under the same applied field (11 V), the rest of the films have demonstrated broader, more rectangular-shaped and well-saturated loops of a higher remanent polarization. The improved ferroelectricity of these films (2, 3, 4) is also evident in an increased external electric field required to depolarized, as seen in **Figure 5. 50b**.

Table 5. 13: Summary of maximum measured polarization $\left(P_{max}^{(001)}\right)$, remanent polarization (P_r), nominal switching voltage (V_c), coercive field (E_c) and the calculated polarization $\left(P_{max}^{(111)}\right)$ for BTFM-CTO films grown on SRO-buffered STO substrates. Data recorded at 11 V driving voltage at 2 Hz**.**

Film	$P_{max}^{(001)}$	P_r		V_c		E_c	$P_{max}^{(111)}$
	(μC/cm²)	(μC/cm²)		(V)		(kV/cm)	(μC/cm²)
		$P_r^{(+)}$	$P_r^{(-)}$	$V_c^{(+)}$	$V_c^{(-)}$		
n1	20.84	6.47	-7.81	3.69	-2.56	131.85	36.10
n2	44.62	32.56	-38.59	6.25	-5.37	245.15	77.28
n3	50.21	44.75	-51.23	6.59	-5.75	260.34	86.97
n4	54.97	42.76	-50.56	6.07	-5.55	245.78	95.21

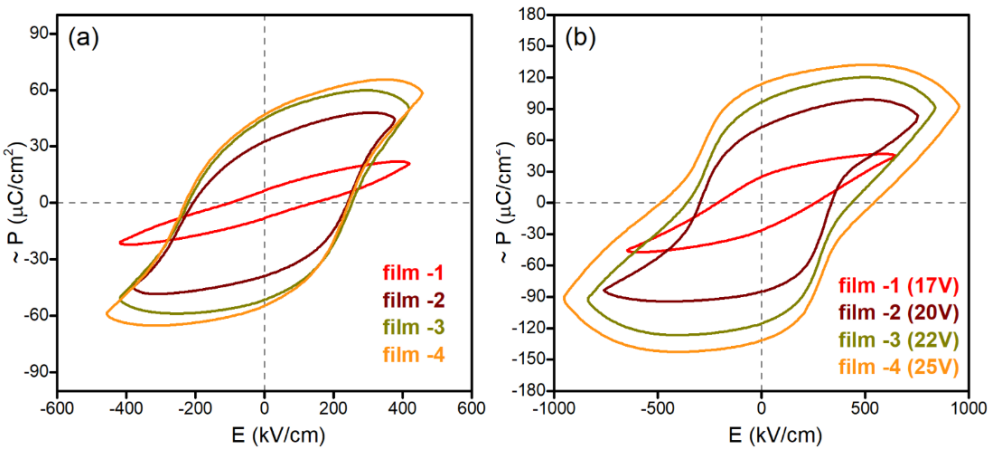

Figure 5. 50: Comparison of the room temperature *PE* hysteresis loops of the BTFM-CTO films in Figure 5. 49 t 2 kHz under: (a) 11 V driving voltage and (b) the maximum applied voltage before capacitor's leak failure.

To evaluate the losses of the examined BTFM-CTO films we have also studied the ferroelectric response of the films as a function of the measurement frequency. Room temperature *PE* hysteresis loops were obtained in a range of frequencies between 50 Hz and 2 kHz in one of the samples (film -4) and the obtained PE loops are presented in **Figure 5. 51**. As can be seen, the film retained a rectangular-shaped, saturated loop for frequencies as low as 500 Hz where its PE response start to become lossy. These results confirmed the insulating character of the BTFM-CTO films but also highlighted the relatively more lossy character of the film compared to the bulk BTFM-CTO (in **Figure 2.25**).

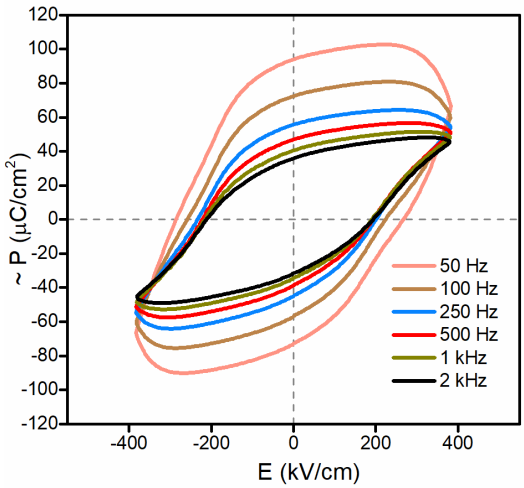

Figure 5. 51: Room temperature *PE* hysteresis loops of BTFM-CTO for film -4 of **Figure 5. 46** as a function of the measured frequency at driving voltage of 9 V.

In summary, our study on the ferroelectric properties of BTFM-CTO films have shown a strong correlation between the structural characteristics and the ferroelectric properties of the films. BTFM-CTO films of high crystal quality, demonstrating a well-separated morphotropic boundary between the two phases, resulted in samples exhibiting superior ferroelectric properties. These remarks also underline the need of further work on the structural analysis of the samples and the effect of film inhomogeneities and growth discontinuities in the MPB region in their ferroelectric properties.

A substantial increase in the polarization was observed in BTFM-CTO films compared to bulk samples due to the preferential crystallographic orientation of the films. However, the non-

completely tetragonal PE loops of the BTFM-CTO films and the comparably inferior dielectric nature of the films (for frequencies lower than 250 Hz) might also suggest a conductivity contribution[305] to the ferroelectric response of the examined BTFM-CTO films that needs to be further investigated.

5.4 Magnetic properties of BTFM-CTO films

The magnetic properties of BTFM-CTO films were examined on a thick (13,000 pulses) BTFM-CTO film deposited on a plain STO substrate using commercial magnetometers (MPMS XL-7 and MPMS3 of Quantum Design, USA). Prior to the measurements, the epitaxial growth of the studied BTFM-CTO film sample in the morphotropic phase boundary region was confirmed by XRD.

At first, the temperature-dependent magnetisation *M*(T) of the film was recorded between 5 and 400 K under zero field cooled (ZFC) and field cooled (FC) conditions according to the following procedure: initially, the sample was cooled down to the lowest temperature (2 K) in the absence of any magnetic field and the zero field cooled magnetisation (M_{ZFC}) was measured by heating up the sample up to 400 K under an in-plane applied magnetic field of 1 kOe. For the field cooled measurement, the sample was again cooled down to 2 K under an applied in-plane magnetic field of 1 kOe and the field cooled magnetisation (M_{FC}) was re-measured was temperature increased under the same field.

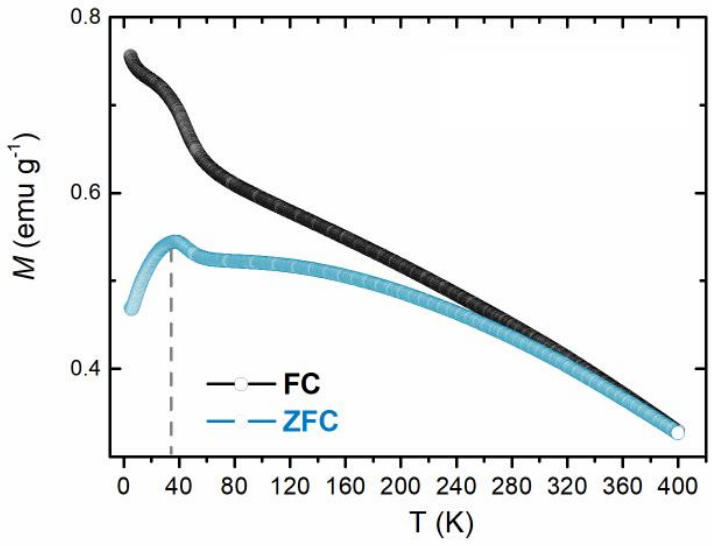

Figure 5. 52: Temperature dependent magnetisation *M(T)* of BTFM-CTO film (13,000 laser shots thick) measured at zero field cooling (ZFC) and field cooling (FC) conditions under an in-plane applied field of 1 kOe.

The collected ZFC-FC magnetization curves of the BFTF-CTO film, in **Figure 5. 52**, showed a different from the bulk magnetic behaviour. Contrary to the bulk BTFM-CTO, where a room temperature weak ferromagnetic ordering was observed, the BTFM-CTO films have not shown any sign of a ferro/paramagnetic transition across the examined range of temperatures (2 - 400 K). The measured magnetization of the film (in ZFC and FC conditions) was found to be significantly higher than that of the bulk BTFM-CTO (0.4 against 0.04 emu/g at 300 K) which indicates the presence of a magnetic phase of a much larger magnetization.

Moreover, the exponential decrease of zero field cooled magnetisation, M_{ZFC}, as well as the presence of a local peak at 40 K (blocking temperature, T_b) as temperature is lowered suggest a magnetic response similar to the behaviour of superparamagnetic nanoparticles [306].

To further investigate the magnetic behaviour of the examined BTFM-CTO film, extensive field-dependent magnetization *M*(H) measurements were conducted in a wide range of temperatures under an in-plane applied field of ±7 T. Magnified patterns of these *M*(H) isotherms in the range of ±0.7 T and ±0.25 T are respectively presented in **Figure 5. 53a** and **Figure 5. 53b**. Based on these figures, it can be seen that the sample undergoes a paramagnetic transition at temperatures above 700K, where the relation between field strength *H* and magnetization *M* is becoming linear. The negative gradient of the isotherms at higher fields is attributed to the strong diamagnetic interference of the substrate. However, as the temperature of the measurements is decreasing to 500 and 400 K, the *H* dependence of *M* is losing its linearity and an emerged "S" shape response of a long-range ferroelectricity is observed. As temperature is further reduced, a low-coercivity loop is starting to take shape reaching at 5 K a coercivity ($2H_c$) of 1.2 kOe.

Similarly to the temperature-dependent magnetization measurements of **Figure 5. 52**, isothermal remanent magnetization of the film was found significantly larger than that of the bulk sample.[307] These findings, in correlation with the absence of a room temperature ferro/paramagnetic transition, are strongly suggesting the presence of a strongly magnetized ferromagnetic phase, on the film making the observation of the possible weak ferromagnetic BTFM-CTO not feasible. The exact nature of this phase can only be identified with further measurements of Mossbauer spectroscopy.

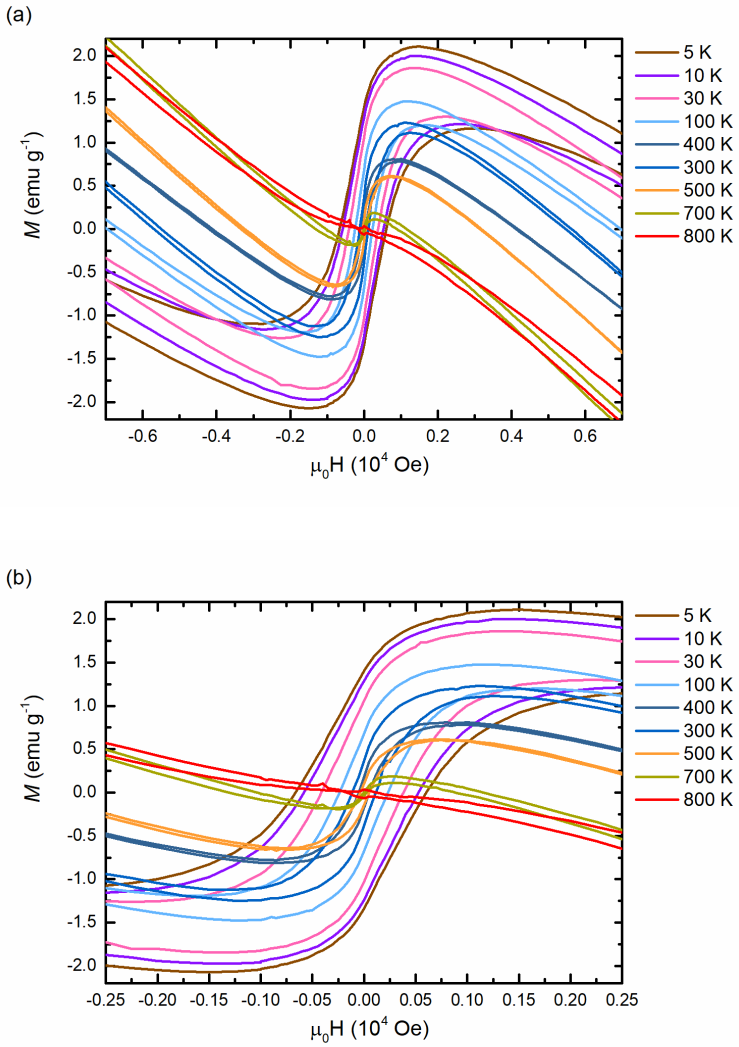

Figure 5. 53: (a) Isothermal field-dependent magnetization *M*(H) measurements in the range of ±0.7 T along the out-plane [110] direction of BTFM-CTO film (13,000 laser shots thick) and (b) magnified view focusing in the range of ±0.30 T.

The temperature-dependent coercivity of the BTFM-CTO film, obtained from the field-dependent magnetization *M*(H) measurements of **Figure 5. 53**, is also summarized in **Figure 5. 54** where some additional findings are revealed. Firstly, an exponential temperature-dependence of film's coercivity can be clearly seen. This dependence seems to be in good agreement with Kneller's law describing the temperature dependence of coercivity in nanoparticles:

$$H_c = H_o * \left[1 - \left(\frac{T}{T_b}\right)^{a_k}\right]$$

where T_b the superparamagnetic blocking temperature of the nanoparticles, H_o the coercivity at T = 0 K and a_k is a constant related to the magnetocrystalline anisotropy of the material which in the case of single-domain and non-interacting nanoparticles is equal to 0.5[308].

However, it is also known from the literature that the application of this law is only confined to lower temperatures where most of the nanoparticles are blocked while in real systems the particle-size distribution and interparticle interactions of nanoparticles induce a further divergence between experimental data and theoretical calculations[309].

Furthermore, the observation of a relatively high coercivity at temperatures well above the expected blocking temperature (estimated in **Figure 5. 52** at about 40 K) indicates the additional presence of a long-range magnetic ordering. One way of addressing these findings could have been fitting the coercivity data with two components: one describing the low temperature superparamagnetic response of film nanoparticles and a second component for the observed in **Figure 5. 53** long-range ferromagnetic ordering at higher temperatures.

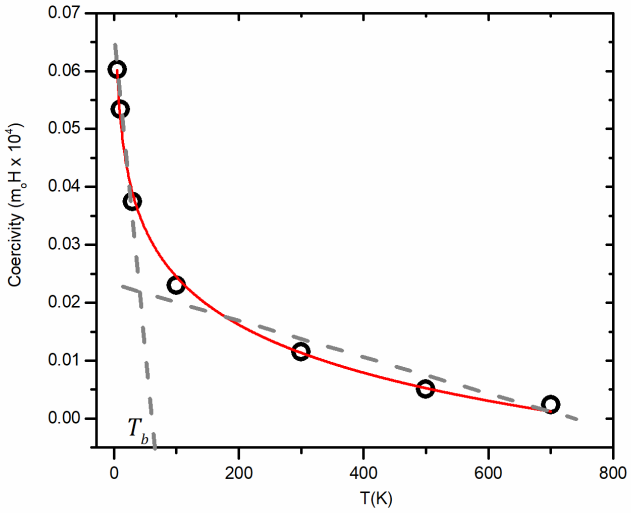

Figure 5. 54: Temperature-dependent coercivity of nanoparticles in BTFN-CTO film (13,000 laser shots thick). The red and grey dot lines added to act as guide to eyes. The coercivity field was measured by averaging the positive and negative field axis values of the hysteresis loops and the red and grey dot lines have been added to act only as guide.

With the completion of the isothermal field-dependent magnetization *M*(H) measurements of **Figure 5. 53**, temperature-dependent magnetisation measurements were repeated at temperatures between 300 and 900 K. We performed those measurements two times, in field

heating (FH) and field cooling (FD) conditions under an in-plane applied magnetic field of 1 kOe, in **Figure 5. 55**. Interestingly, when these measurements were extended to higher temperatures this time, a clear magnetic transition point close to 800 K was observed indicating the presence of a ferromagnetic iron spinel phase (possibly Fe_3O_4).

Two further remarks can be made about the obtained magnetization curves of **Figure 5. 55**. The first one is the significant increase in the measured magnetization of the system by almost an order of magnitude when temperature-dependent magnetisation measurements repeated at temperatures of 300 – 900 K which should be attributed to the magnetic history of the sample and the strong magnetic orientation of a fraction of superparamagnetic nanoparticles caused by the preceding isothermal field-dependent measurements. The second point is the difference between measured magnetization in FH and FC conditions, a sign of thermally induced fluctuations in the magnetic moments of superparamagnetic particles.

In conclusion, the performed magnetic measurements confirmed the inclusion of magnetically-strong iron impurities in the BTFM-CTO film which was not previously detected by in-house and synchrotron XRD studies.

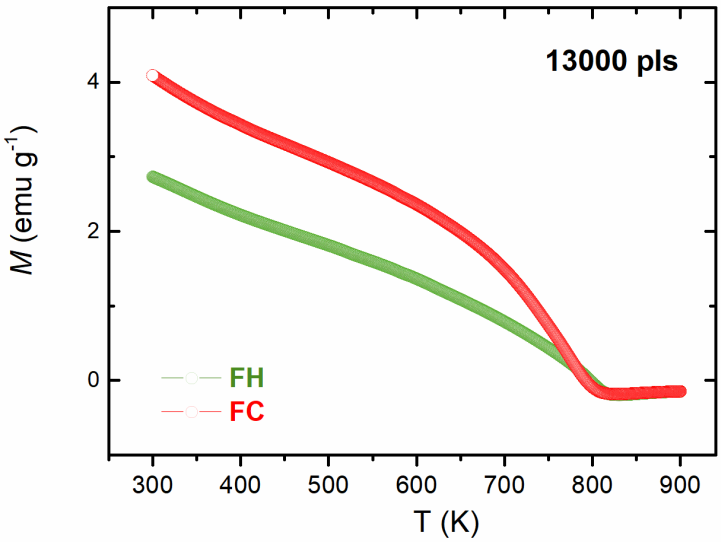

Figure 5. 55: Repeat of temperature dependent magnetisation, *M(T)*, measurements for BTFM-CTO film (13,000 laser shots thick) on field heating (FH) and field cooling (FC) conditions under an in-plane applied field of 1 kOe. The higher magnetization values observed this time is due to the magnetic history of the sample.

To investigate the possible inclusion of iron impurities during the film growth we also conducted cross-sectional EDX measurements (depth profile scans) on the studied BTFM-CTO film, in **Figure 5. 56**.

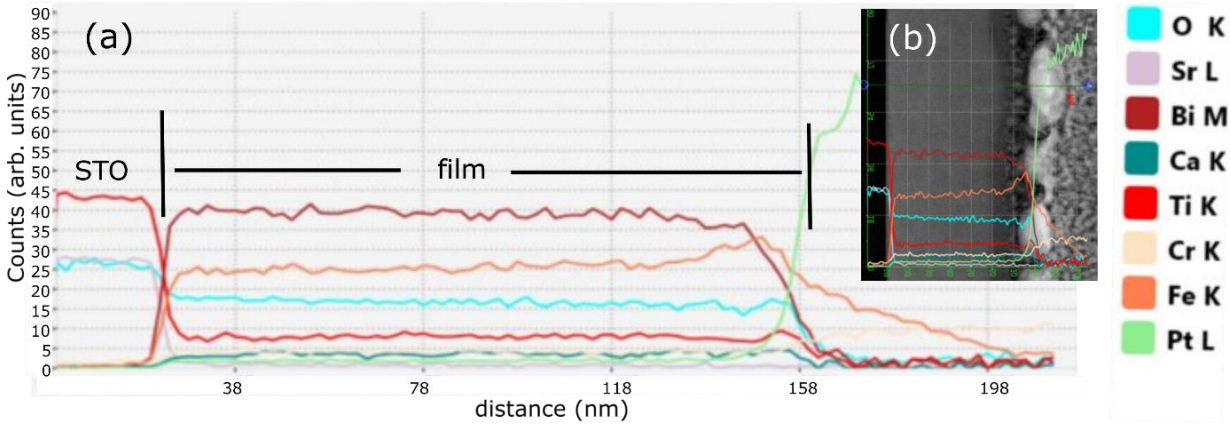

Figure 5. 56: EDX on a FIB-prepared BTFM-CTO film: (a) In-depth EDX line scan on a BTFM-CTO film deposited in STO. In x-axis, the distance (nm) is measured along the growth direction starting from the substrate surface (starting from an arbitrary point) and moving to the top layers of the deposited film. (b) Low magnification dark-field SEM cross-section micrograph of the same sample is shown overlaid with EDX line scan profiles of the constituent elements. In both sub-figures, the high Ti and Pt concentrations are respectively highlighting the STO substrate and the coated Pt surface coating areas of the examined sample. The sample was prepared by low kV FIB thinning.

As seen in the in-depth EDX line scan of **Figure 5. 56a,** three different film areas can be distinguished in the received in-depth profiles of BTFM-CTO film cation concentrations: (i) the substrate, where Ti concentration reaches its maximum, (ii) the main phase of the film with a reasonably uniform distribution of the constituent cation elements and finally (iii) the Pt surface coating of the films. However, as we are reaching the outermost oxide region (~ 20 nm thickness), an increase in the Fe concentration is observed at the expense of Bi concentration which is decreased.

These observations were also confirmed by high magnification SEM cross section images where an area of high Fe-content was observed in the outer layers of the BTFM-CTO film in contrast to the main volume of the film (inner film layers) in **Figure 5. 57b**.

These in-depth variations in the composition of the films can possibly be correlated with the volatility of bismuth during the film growth and may be responsible for the formation of minor iron-related impurity phases.

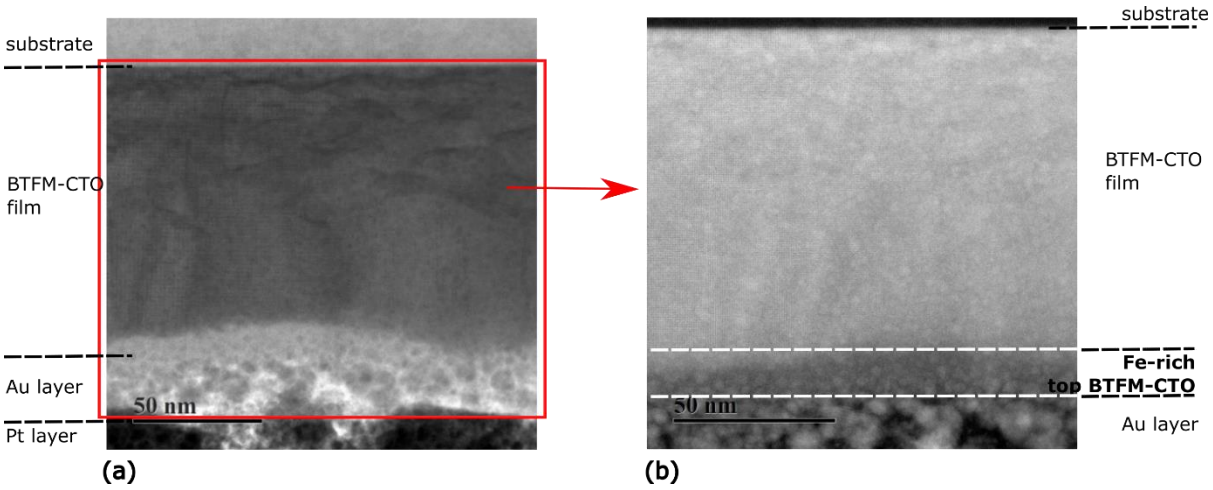

Figure 5. 57: SEM cross-sections images on FIB-prepared BTFM-CTO film: (a) Low magnification bright field and (b) Zoomed detail of sub-figure (a) in high magnification dark field image. In sub-figure (a) can be seen the substrate (top up), BTFM-CTO film, sputtered Au layer and deposited Pt layer (bottom down).

In summary, the magnetic measurements on this chapter have shown the substantially different magnetic behaviour of bulk and thin film BTFM-CTO. Our study showed the absence of a room temperature long-range magnetic ordering in BTFM-CTO film and the presence of an iron-related impurity phase with a Curie temperature close to 800 K. The presence of the magnetically strong iron-impurity did not allow us to identify the possible presence of a weak ferromagnetic BTFM-CTO response. Our findings have also provided strong evidences of the superparamagnetic, nanoparticle nature of the iron-related impurity.

In the future, a more conclusive characterization of the magnetic properties of BTFM-CTO films will require an extensive investigation of iron magnetic state in our samples. The Mössbauer spectroscopy is a powerful technique towards this direction to study the local nuclear spin moment iron experiences on the local environment of the as-grown films and further our understanding of the long-range magnetic order of BTFM-CTO in the future.

5.5 Conclusions

The work presented in this chapter focused in the morphotropic growth of single-oriented $0.85BiTi_{0.1}Fe_{0.80}Mg_{0.1}$ - $0.15CaTiO_3$ (BTFM-CTO) films and the comparative study of their multiferroic properties to those of bulk BTFM-CTO.

For the deposition of BTFM-CTO, a Bi-rich target was used to compensate for losses of the volatile bismuth. The stoichiometric growth of single-oriented BTFM-CTO films was found to be highly dependent on a narrow window of growth conditions at a temperature of 710 °C, oxygen partial pressure of 15 mTorr and a laser fluence of 1.5 J/cm^2. Small change of the oxygen pressure resulted on films containing bismuth- or iron-impurities, with higher oxygen pressures favouring Fe-rich films. In a similar way, films grew on higher or lower temperatures than the optimum temperature of 710 °C were seen to contain Fe impurities or demonstrate a worst crystal quality.

The crystalline structure of BTFM-CTO films was also found to be sensitive to epitaxial constrains. A higher lattice mismatch in the growth of ultra-thin (~ 20 nm) BTFM-CTO films in LAO substrates led to the growth of a single tetragonal-like phase, relaxed to a mixture of tetragonal-like and morphotropic (O+R) phases only at higher thickness.

On the contrary, the epitaxial stabilization of a morphotropic BTFM-CTO was obtained in films deposited on STO substrates, in agreement with bulk data[290]. Given the close d_{space} parameters of the coexisting rhombohedral and orthorhombic phases, the MPB growth of the as-grown films has been uncovered as a peak splitting of their out-of-plane $(00l)_{PC}$ reflections. Detailed XRD studies on films of different thicknesses revealed the presence of two well-distinct crystalline phases as well as the progressive relaxation of the morphotropic phase towards the rhombohedral phase as film thickness is increasing. Reciprocal space maps on a relative thick BTFM-CTO film (13,000 laser shots) verified its coherent morphotropic growth along different in-plane crystallographic directions confirming its epitaxial in-plane stretching to the substrate.

Ferroelectric measurements performed on epitaxially grown morphotropic BTFM-CTO films on SRO-buffered STO substrate have shown a room temperature ferroelectricity with a remanent $\boldsymbol{P}_{max}^{(001)_{PC}}$ polarization exceeding 130 μC/cm^2, for a maximum applied voltage up to 25 V. These values were found to be much larger than those measured on bulk BTFM-CTO due to the preferential orientation of the films. However, the slightly tilted and not fully

saturated *PE* loops of the BTFM-CTO films highlight the inferior to the bulk BTFM-CTO dielectric nature of the films and indicate a conductivity contribution to their ferroelectric response that needs to be further investigated.

The room temperature ferroelectricity of BTFM-CTO films was found to depend greatly on the structural properties of the as-grown films and films failed to stabilise in the MPB composition have also shown a lossy, non-ferroelectric behaviour.

In the future, additional work is essential to acquire a better understanding between the crystal structure and the ferroelectric properties of the as-grown films. Advanced x-ray techniques of characterization such as SAED, HRTEM and nano- (or micro-) focused synchrotron X-ray beam spectroscopy can offer a fine control over the local topology and elemental composition of the films and unveil the role of inhomogeneities or growth discontinuities at the MPB region to the ferroelectric response of the films. In-situ synchrotron diffraction measurements as a function of electric field could give an insight on the evolution of the crystalline structure around the morphotropic phase boundary of films in conjunction with studies of their structural response under an applied electric field. In addition, PFM measurements (switching spectroscopy, SS-PFM) can offer tremendous opportunities on studying the correlation between the polarization distribution, the evolution of domain arrangements and local switching mechanisms of the films with their local microstructure at the MPB and their poling-induced electromechanical properties.

When it comes to the magnetic properties of BTFM-CTO films, a substantially different behaviour from the bulk material was observed. A strongly magnetized ferromagnetic iron-based impurity, with a Curie temperature at about 800 K, was found to dominate the overall magnetic response of the films. Additional measurements of the field-dependent magnetization of BTFM-CTO films at different temperatures have also indicate the presence of superparamagnetic nanoparticles in the film samples.

Cross-sectional EDX measurements (depth profile scans) on a thick (13,000 laser shots) BTFM-CTO film revealed an increased Fe concentration together with a decrease of Bi content in the outer film region (~ 0.20 nm thickness). These observations highlight the difficulty of controlling the stoichiometric deposition of the highly volatility Bi in the outer film layers and may possibly outline routes on improving the film growth protocol and eliminating the presence of secondary impurities. The possible presence of crystalline impurities in the top

layers of the as-deposited films, which has not been seen in out XRD studies, could also be investigated with grazing-incident angle diffraction studies (GIXD).

Nevertheless, a detailed magnetic characterization of BTFM-CTO films is far from completed and essential information on the magnetic ordering of the as-deposited films is still needed to obtain. In this direction, Mössbauer measurements at variable temperatures could offer an insight on the local atomic structure and the long-range magnetic order of the films allowing us to distinguish different magnetic phases and assess the iron content in the perovskite environment of BTFM-CTO.

References

[290] P. Mandal, M.J. Pitcher, J. Alaria, H. Niu, M. Zanella, J.B. Claridge, M.J. Rosseinsky, *Adv. Funct. Mater*. **26**, 2016, 2523

[291] H. Béa, M. Bibes, S. Fusil, K. Bouzehouane, E. Jacquet, K. Rode, P. Bencok, A. Barthélémy, *Phys. Rev. B* **74**, 2006, 020101(R)

[292] Z. Luo, Z. Chen, Y. Yang, H.J. Liu, C. Huang, H. Huang, H. Wang, M.M. Yang, C. Hu, G. Pan, W. Wen, X. Li, Q. He, T. Sritharan, Y.H. Chu, L. Chen, G. Gao, *Phys. Rev. B* **88**, 2013, 064103

[293] S. Nakashima, T. Uchida, K. Doi, K. Saitoh, H. Fujisawa, O. Sakata, Y. Katsuya, N. Tanaka, M. Shimizu, *Jpn. J. Appl. Phys.* **55**, 2016, 101501

[294] Y. Zhou, L. Fang, L. You, P. Ren, Le Wang, J. Wang, *Appl. Phys. Lett.* **105**, 2014, 252903

[295] T. Ohnishi, H. Koinuma, M. Lippmaa, *Appl Surf Sci*. **252**, 2006, 2466

[296] I. Kojima, B. Li, *The Rigaku Journal* **16**, 1999, 31

[297] SmartLab Studio Software for SmartLab, Ver 1.4.1.0, Rigaku, 2016

[298] W. Eerenstein, F.D. Morrison, F. Sher, J.L. Prieto, J. P. Attfield, J.F. Scott, N.D. Mathur, *Philos. Mag. Lett*. **87**, 2007, 249

[299] X.D. Wu, S.R. Foltyn, R.C. Dye, Y. Coulter, R.E. Muenchausen, *Appl. Phys. Lett*. **62**, 1993, 2434

[300] G. Rijnders, D.H.A. Blank, J. Choi, C.B. Eom, *Appl. Phys. Lett*. **84**, 2004, 505

[301] Q. Gan, R.A. Rao, C.B. Eom, L. Wu, F. Tsui, *J. Appl. Phys*. **85**, 1999, 5297

[302] J. Meng, Z. Chen and A. Jiang, Jpn. *J. Appl. Phys*. **54**, 2015, 055502

[303] X.Y. Zhang, Q. Song, F. Xu, C.K. Ong, Appl Phys Lett **94**, 2009, 022907

[304] C. Chauhan, R. Jotania *Adv. Mater. Res.* **665,** 2013, 210

[305] L. Mitoseriu L.P. Curecheriu, in *Nanostructured Barium Titanate Ceramics: Intrinsic versus Extrinsic Size Effects* In: M. Algueró, J. M. Gregg, L. Mitoseriu (eds.), *Nanoscale Ferroelectrics and Multiferroics*, *Volume I & II*, John Wiley & Sons, 2016

[306] D. Ortega, *Structure and Magnetism in Magnetic Nanoparticles* In: N. Thanh (ed.), *Magnetic nanoparticles: from fabrication to clinical applications*, CRC Press, 2012

[307] P. Mandal, M. J. Pitcher, J. Alaria, H. Niu, P. Borisov, P. Stamenov, J. B. Claridge, M. J. Rosseinsky, *Nature* **525**, 2015, 363

[308] C. Nayek, K. Manna, G. Bhattacharjee, P. Murugavel, I. Obaidat, *Magnetochemistry* **3**, 2017, 19

[309] E.C. Mendonc, C.B.R. Jesus, W.S.D. Folly, C.T Meneses, J.G.S. Duque, A.A.Coelho, *Appl. Phys.* **111**, 2012, 053917

Appendices

Appendix A: PDOS calculations of $SrZnO_2$ doping

Partial density of states (PDOS) of $SrZnO_2$, $SrZn_{(31/32)}Na_{(1/32)}O_2$, $Sr_{(31/32)}K_{(1/32)}ZnO_2$, $Sr_{(31/32)}Ag_{(1/32)}ZnO_2$ and $SrZn_{(31/32)}Ag_{(1/32)}O_2$ were calculated using spin polarized DFT calculations by Gupta et al.[iv]

Figures of the calculated PDOS versus energy relative to the valence band maximum (E_{VBM} – determined from the energy of the highest occupied eigenstate) of $SrZnO_2$, $SrZn_{(31/32)}Na_{(1/32)}O_2$, $Sr_{(31/32)}K_{(1/32)}ZnO_2$, $Sr_{(31/32)}Ag_{(1/32)}ZnO_2$ and $SrZn_{(31/32)}Ag_{(1/32)}O_2$ (x = 1/32) are presented in **Figure App. 1** to **Figure App. 5**.

The marked dashed lines in subfigures b indicate the E_F . The occupied states of the studied systems are shaded in grey with the remaining unoccupied states left unshaded. The presence of the empty states above E_F is indicative of p-type doping.

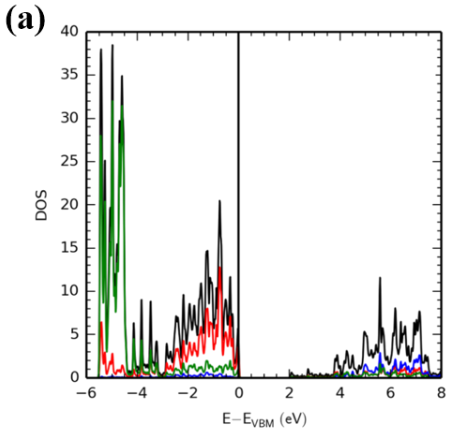

Figure App. 1: Partial density of states (PDOS) of $SrZnO_2$ calculated using spin polarized DFT calculations. Taken from[iv].

[iv] C.A. Tzitzeklis, J.K. Gupta et al. *Inorg. Chem.*, 2018, 57 (19), 11874

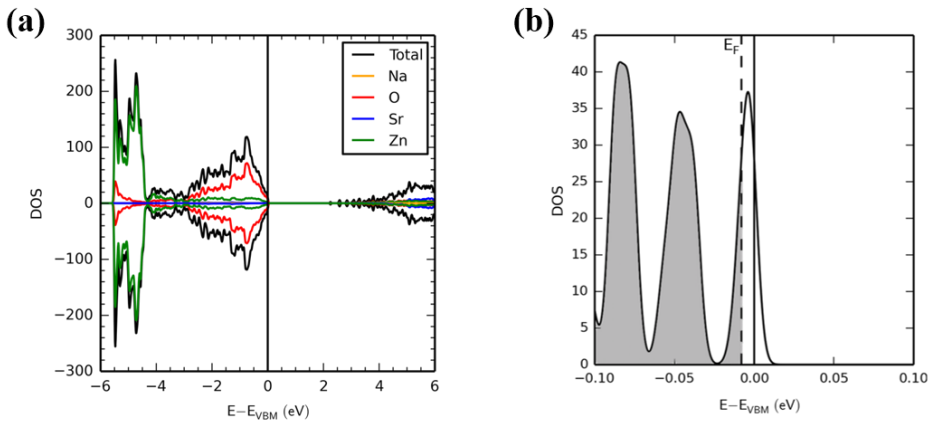

Figure App. 2: Partial density of states (PDOS) of $Sr_{(31/32)}Na_{(1/32)}ZnO_2$ by spin polarized DFT calculations. Taken from[iv].

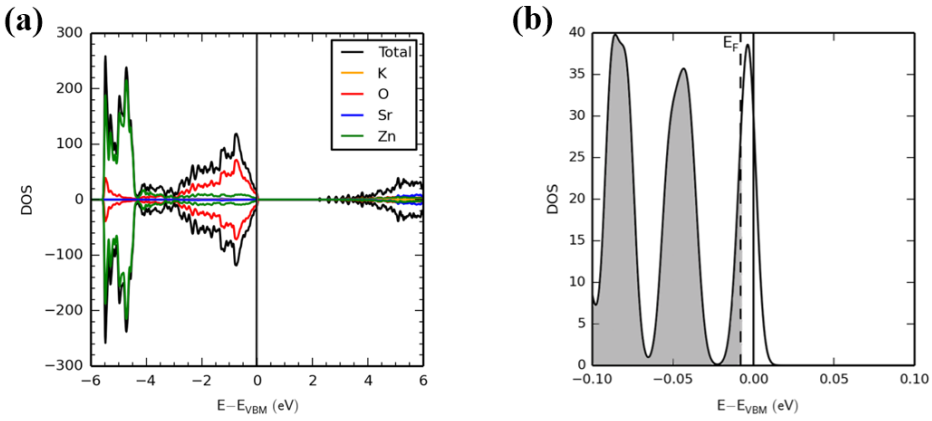

Figure App. 3: Partial density of states (PDOS) of $Sr_{(31/32)}K_{1/32)}ZnO_2$ by spin polarized DFT calculations. Taken from[iv].

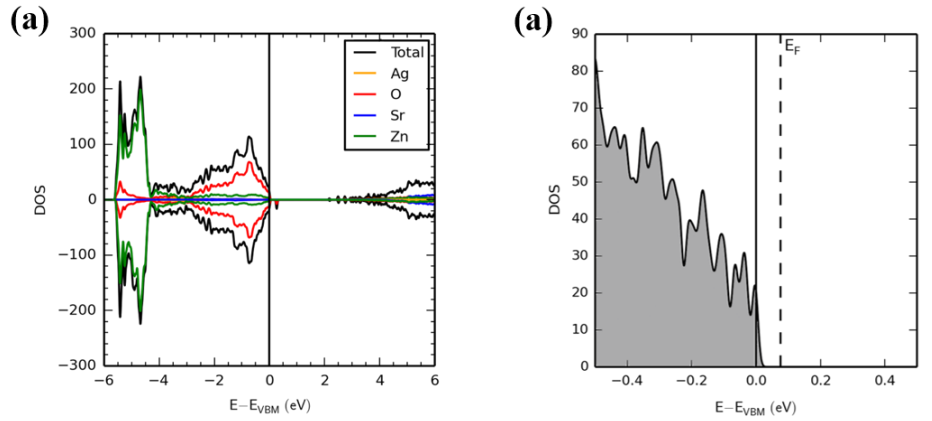

Figure App. 4: Partial density of states (PDOS) of $Sr_{(31/32)}Ag_{1/32)}ZnO_2$ by spin polarized DFT calculations. The unsymmetrical PDOS with a calculated net magnetization of 0.46μB is characteristic of Ag^{2+}, due to the presence of an unpaired electron Taken from[iv].

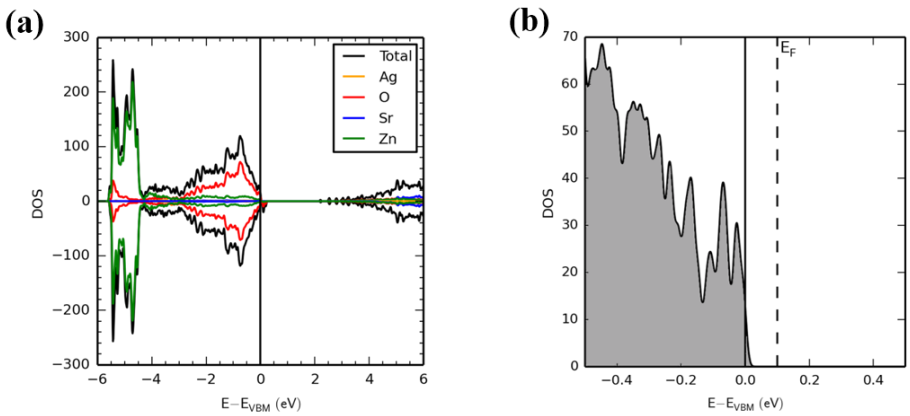

Figure App. 5: Partial density of states (PDOS) of $SrZn_{(31/32)}Ag_{(1/32)}O_2$ by spin polarized DFT calculations. Taken from [iv].

Appendix B: X-ray powder diffraction data on the ICDD database

Table App. 1: X-ray powder diffraction data of ZnO, $SrCO_3$ and $SrZnO_2$ on the ICDD database.

ZnO

hkl	*2Theta*	*d-spacing*	*F*
010	37.02	2.8176	31.69
002	40.125	2.6075	51.83
011	42.304	2.4789	34.85
012	55.732	1.9138	23.17
-120	66.717	1.6267	49.38
013	74.403	1.4795	38.03
020	78.831	1.4088	22.45
-122	80.798	1.3802	38.68

$SrCO_3$ – Pmcn (62)

hkl	*2Theta*	*d-spacing*	*F*
011	21.157	4.8725	4.37
110	23.748	4.3473	19.27
020	24.719	4.179	18.47
111	29.445	3.5198	99.88
021	30.246	3.4286	106.25
002	34.713	2.9985	80.14
121	36.669	2.8437	19.71
012	36.955	2.8224	64.07
102	40.514	2.5835	55.31
200	41.155	2.545	114.07
031	41.468	2.5267	37.07
112	42.495	2.4683	75.7
130	42.941	2.4439	111.79
022	43.082	2.4363	76.74
131	46.563	2.2632	3.22
211	46.723	2.2558	27.34
122	48.04	2.1975	1.97
220	48.601	2.1736	80.6
040	50.693	2.0895	64.86

$SrZnO_2$

hkl	*2Theta*	*d-spacing*	*F*
002	18.11	5.685	22.76
011	19.83	5.1948	12.68
012	25.37	4.0736	7.58
101	32.33	3.2134	3.2
013	32.68	3.1792	12.13
020	35.68	2.92	179.14
004	36.68	2.8425	180.28
021	36.88	2.8282	88.73
111	37.05	2.8154	117.2
022	40.29	2.5974	30.84
112	40.45	2.5874	74.62
014	40.97	2.5558	24.55
103	41.76	2.51	55.73
023	45.5	2.3131	95.86
113	45.65	2.306	172.84
120	47.96	2.2012	41.42
121	48.9	2.1611	27.08
015	49.94	2.119	12.42
122	51.67	2.0527	13.23
024	52.1	2.0368	161.04
114	52.24	2.032	12.78
031	55.58	1.9187	22.04
123	56.06	1.9034	0.31
006	56.33	1.895	27.41
105	56.77	1.8815	17.99
032	58.117	1.8417	22.1
016	59.51	1.8025	32.96
025	59.81	1.7941	109.91
115	59.93	1.7908	109.11

Appendix C: Fittings of $SrZn_{1-x}Li_xO_2$ impedance spectroscopy data

The AC impedance spectra of the x_{ICP} = 0.027, $SrZn_{1-x}Li_xO_2$, sample at 500 ºC and 600 ºC under 1 atm of O_2, presented in **Figure 4.18**, were fitted to the conventional equivalent circuit of **Figure App. 6**. by Dr. Stanislav Savvin.

The C_b and C_b capacitance values for the impedance spectra at 500 ºC were according of the (C_b = 1.25×10^{-11} F). A second smaller semicircle, emerging at low frequencies in the spectra of both temperatures, has been assigned to the electrode response ($C_{el} \sim 10^{-5}$ F).

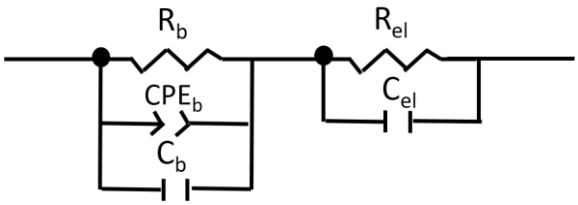

Figure App. 6: Conventional equivalent circuit of the AC impedance spectra of the x_{ICP} = 0.027, $SrZn_{1-x}Li_xO_2$, sample.

Table App. 2: Fitting parameters for the AC impedance spectra of Figure 4.18**.**

	R_b (Ω cm)	C_b (F)	CPE_b (F)	R_{el} (Ω cm)	C_{el} (F)
500 ºC	57,167	1.25×10^{-11}	5.51×10^{-8}	1,415	2.63×10^{-5}
600 ºC	816,270	1.18×10^{-11}	3.11×10^{-10}	57,656	2.54×10^{-7}

Appendix D: Ex-situ annealing treatment of BTFM-CTO films

The ex-situ annealing of the as-grown mixture of tetragonal and pseudocubic BTFM-CTO film phases deposited on LAO, in section 5.2.1.1, was investigated here using a rapid thermal annealing (RTA) vacuum furnace. Our aim was here to study the reproducibility of the partially uncontrollable in-situ, heat treatment of films grown on LAO, of **section 5.2.1**, by ex situ processes.

Films of different thicknesses were deposited under the same conditions (temperature: 650 ^{o}C, chamber pO_2 pressure: 0.5 mTorr, laser fluence: 1 J/cm^2 with the use of a stoichiometric BTFM-CTO target) and cooled down to room temperature without any post deposition treatment. Following this, the films were placed inside a rapid thermal annealing (RTA) vacuum furnace and were subjected to different annealing conditions by a rapid (50 ^{o}C/min) IR heat treatment under a high oxygen overpressure (150 Torr) as summarized in

. XRD patterns of the films, before and after the ex-situ rapid thermal annealing treatment, have been collected and changes in the crystal structure of the obtained films were assessed.

To ensure the sameness of samples prior their ex-situ post deposition heat treatment, the films were deposited on 5x10 mm LAO substrates and were subsequently cut in two (resulting in 2 samples of 5x5 mm).

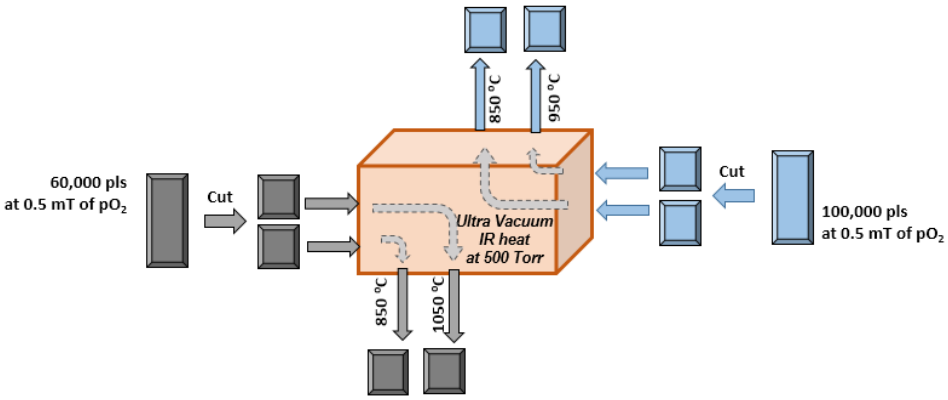

Figure App. 7: Heat treatment of BTFM-CTO films (of 60,000 and 100,000 laser shots) in a rapid thermal annealing (RTA) vacuum furnace. The films were treated at different temperatures under 150 Torr of pO_2. The resulting XRD patterns of the films, for 60,000 and 100,000 laser shots, are shown in **Figure App. 8** and **Figure App. 9**, respectively.

Table App. 3: Examined post deposition, ex-situ, annealing treatment of BTFM CTO films grown on LAO substrates. The films were subjected to a 15 min rapid (50 ºC /min) IR heat treatment, under 150 Torr of oxygen pressure inside a RTA vacuum furnace.

Film	sample	Treatment temperature (oC)	pO_2 (Torr)	Duration (min)
60,000	A-1	850	150	15
	A-2	1050	150	15
100,000	B-1	850	150	15
	B-2	950	150	15

At first sight, the as-grown films (for 60,000 and 100,000 laser shots) were found to crystallized in a mixture of a pseudocubic and tetragonal phases regardless of their thickness, in **Figure App. 8a** and **Figure App. 9a**.

When it comes to the as-treated films, a number of observations are revealed. Firstly, the as-treated films have shown a phase transformation from the mixed (pseudocubic and tetragonal) phases towards the pseudocubic phase. Secondly, this phase transition to the pseudocubic phase was also found to be temperature- and thickness-dependent. For a given film thickness there is a temperature threshold below which the phase transformation is thermodynamically unfavourable. In addition, stabilizing the crystal structure of the as-treated BTFM-CTO films at the MPB was found to emerge as a metastable equilibrium state between the mixed (pseudocubic and tetragonal) phases and the pseudocubic phase. Lastly, it should be noted that none of the obtained heat-treated films was free of impurities.

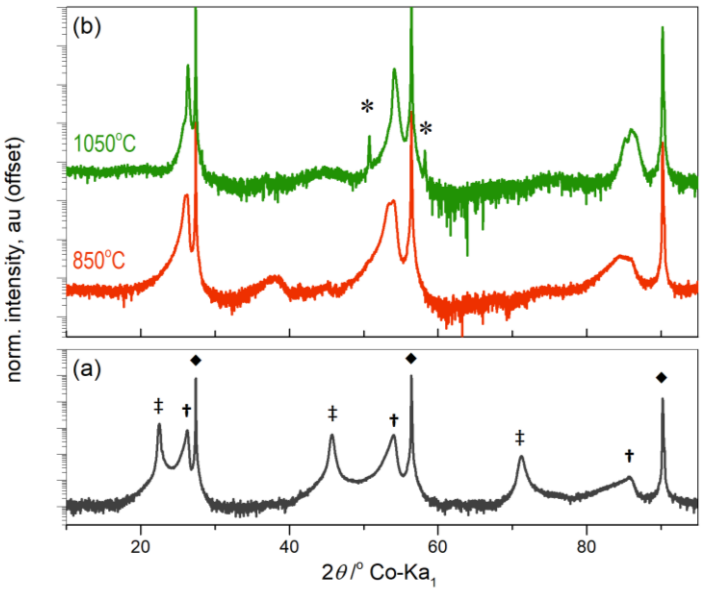

Figure App. 8: Out-of-plane θ/2θ scans showing the ex-situ post-deposition heat-treatment of a 60,000 laser shots BTFM-CTO films deposited in a rapid thermal annealing vacuum furnace under 150 Torr of pO_2: (a) as-deposited films, before heat treatment, (b) the resulted, as-treated, films subjected to different ex-situ heat treatments as described in **Table App. 3**. Peaks denoted with (†) indicate the $(00l)_{PC}$ film peaks and with (‡) the extra set of reflections of the tetragonal BTFM-CTO. The (◆) symbol highlights the LAO substrate peaks and (*) Fe_2O_3 impurities.

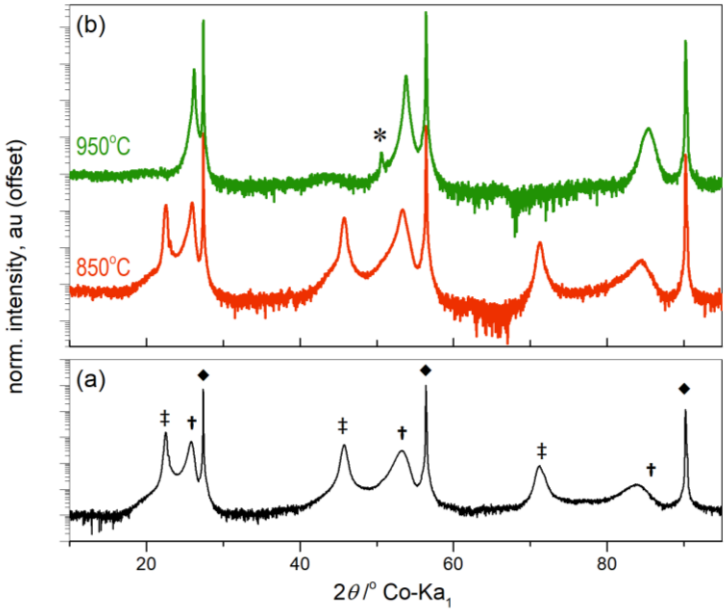

Figure App. 9: Out-of-plane θ/2θ scans showing the ex-situ post-deposition heat-treatment of a 100,000 laser shots BTFM-CTO films in rapid thermal annealing vacuum furnace under 150 Torr of pO_2: (a) as-deposited films, before heat treatment, (b) the resulted, as-treated, films subjected to different ex-situ heat treatments as described in **Table App. 3**. Peaks denoted with (†) indicate the $(00l)_{PC}$ film peaks and with (‡) the extra set of reflections of the tetragonal BTFM-CTO. Symbol (◆) highlights the LAO substrate peaks and (*) Fe_2O_3 impurities.

Appendix E: EDX/TEM measurement on BTFM-CTO films

The EDX/TEM data of BTFM-CTO films deposited at various growth conditions are presented in diagrams as it follows: (a) Ternary diagram of Fe-Ti-Mg (B-site cations, in atoms %) where the red filled cycle is highlighting the average composition of a number of measurements (in black) and the green filled cycle the nominal composition of the films, (b) inset in subfigure-(a) is shown a magnified area of the collected data, (c) Bi/Ca and (d) Bi/Fe ratios on the measured composition (coloured in opaque yellow) where with dark yellow and green colour are marked the average and the expected nominal composition. The uncertainty of the calculated Bi/Ca and Bi/Fe ratio is given with black error bars as $\pm 1\sigma$ on the calculated average composition (dark yellow column).

E.1: BTFM-CTO films at various laser fluences

BTFM-CTO films deposited at 0.50, 0.66 and 1.15 J/cm^2 with the use of stoichiometric target. The rest of the growth conditions as follows; deposition temperature: 650 ^{o}C; chamber pO_2 pressure: 0.5 mTorr, for 180000 pulsed laser shots on LAO substrates.

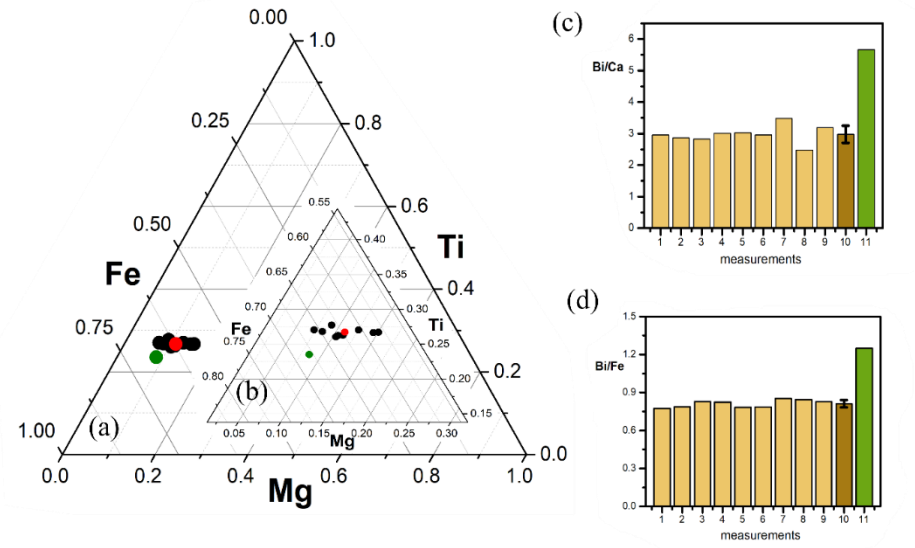

Figure App. 10: EDX/TEM data for the BTFM-CTO film at 0.50 J/cm^2 on nine randomly chosen positions.

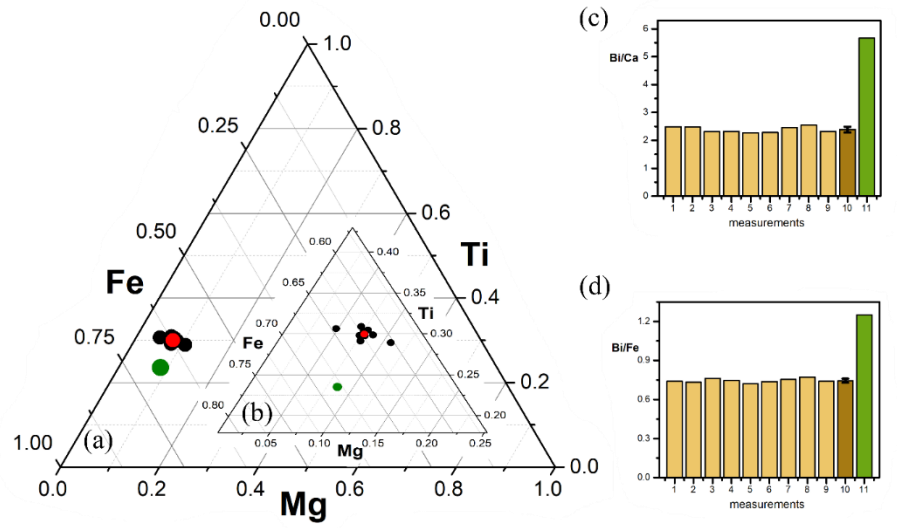

Figure App. 11: EDX/TEM data for the BTFM-CTO film at 0.66 J/cm^2 on nine randomly chosen positions.

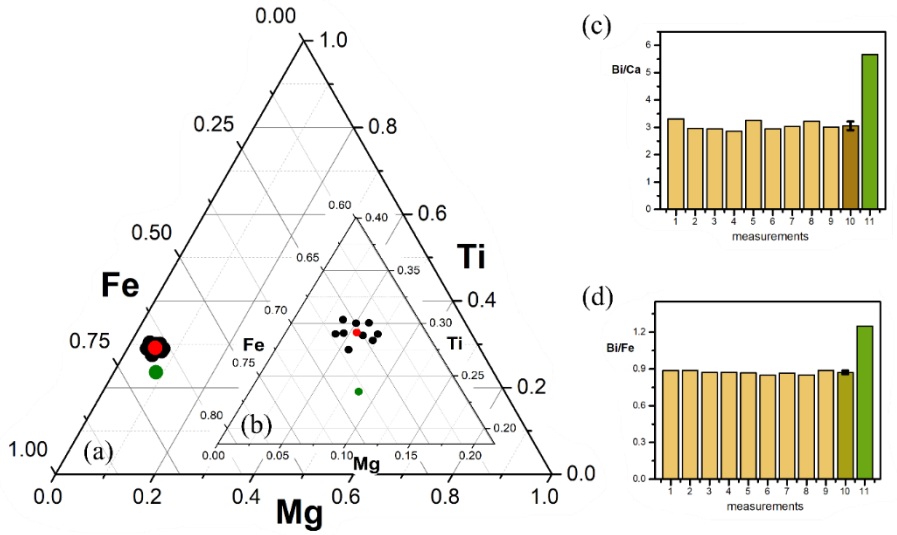

Figure App. 12: EDX/TEM data for the BTFM-CTO film at 1.15 J/cm^2 on nine randomly chosen positions.

E.2: BTFM-CTO films at various pO_2

BTFM-CTO films deposited at pO_2 of: 5, 70 and 100 mTorr with the use of the Bi-rich target. The rest of the growth conditions as follows; deposition temperature: 650 ^oC; laser fluence: 1.5 $J.cm^{-2}$, for 180,000 pulsed laser shots on LAO substrates.

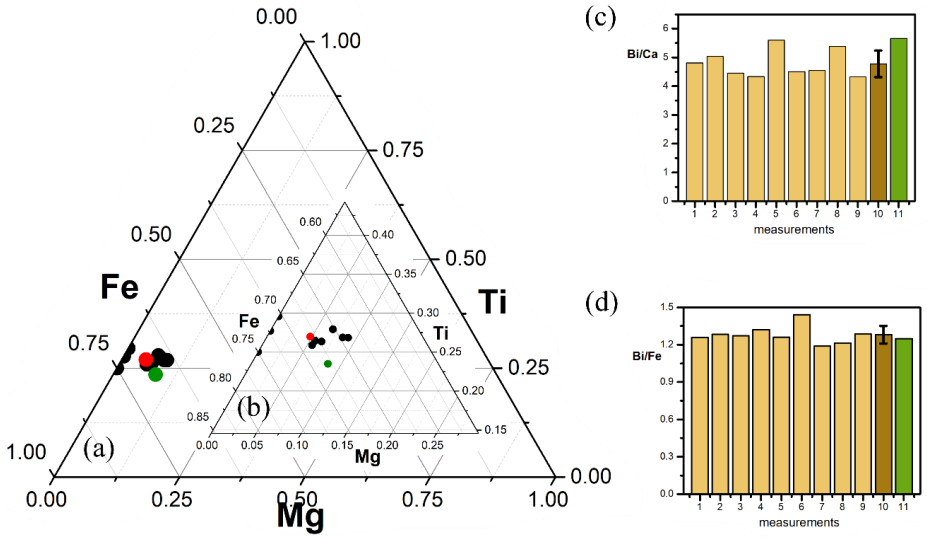

Figure App. 13: EDX/TEM data for the BTFM-CTO film at 5 mTorr on nine randomly chosen positions.

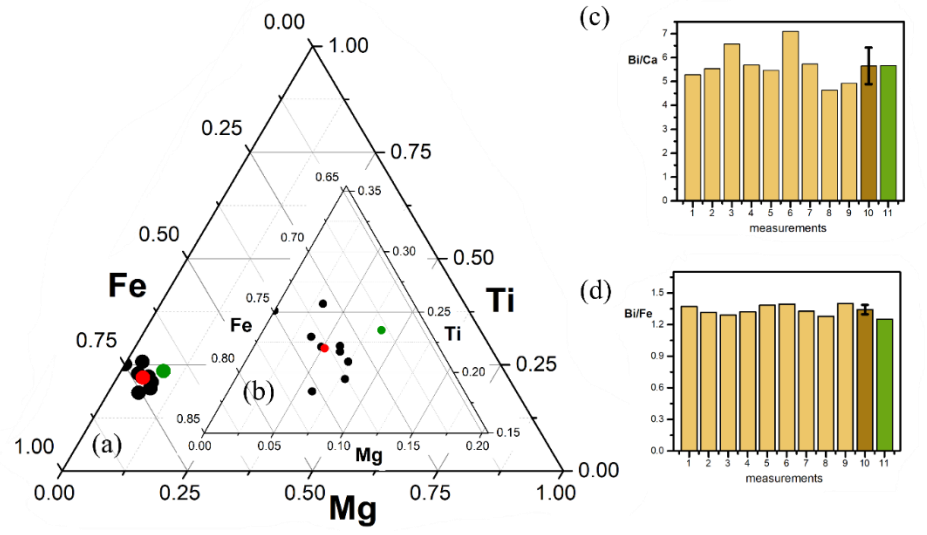

Figure App. 14: EDX/TEM data for the BTFM-CTO film at 70 mTorr on nine randomly chosen positions.

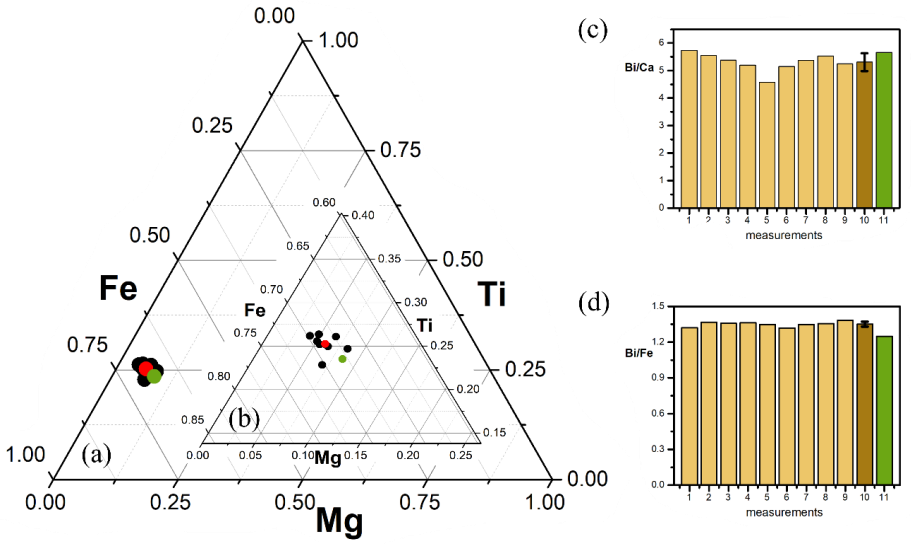

Figure App. 15: EDX/TEM data for the BTFM-CTO film at 100 mTorr on nine randomly chosen positions.

E.3: BTFM-CTO films at 10 mTorr and 50 mTorr of pO_2

BTFM-CTO films deposited at pO_2 of: 10 and 50 mTorr with the use of the Bi-rich target. The rest of the growth conditions as follows; deposition temperature: 650 ^{o}C; laser fluence: 1.5 J.cm^{-2}, for 180,000 pulsed laser shots on STO substrates.

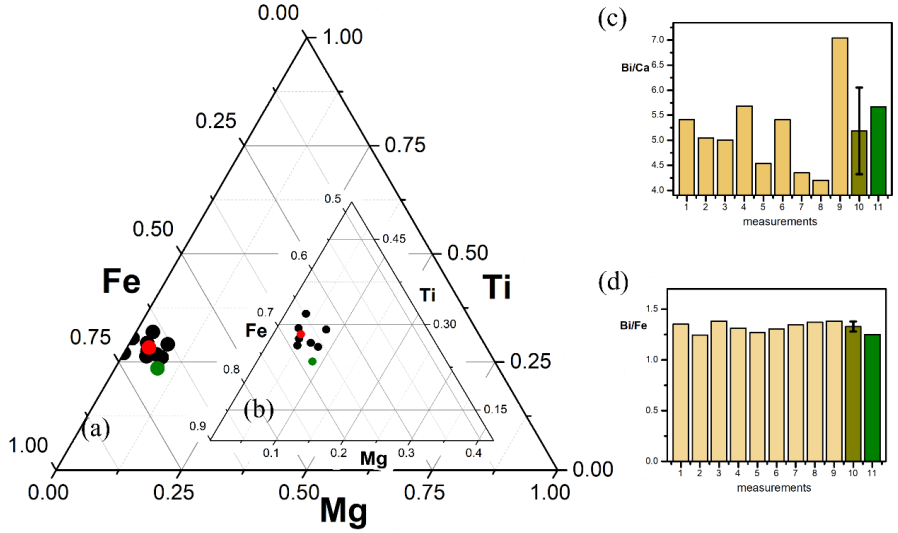

Figure App. 16: EDX/TEM data for the BTFM-CTO film at 10 mTorr on nine randomly chosen positions.

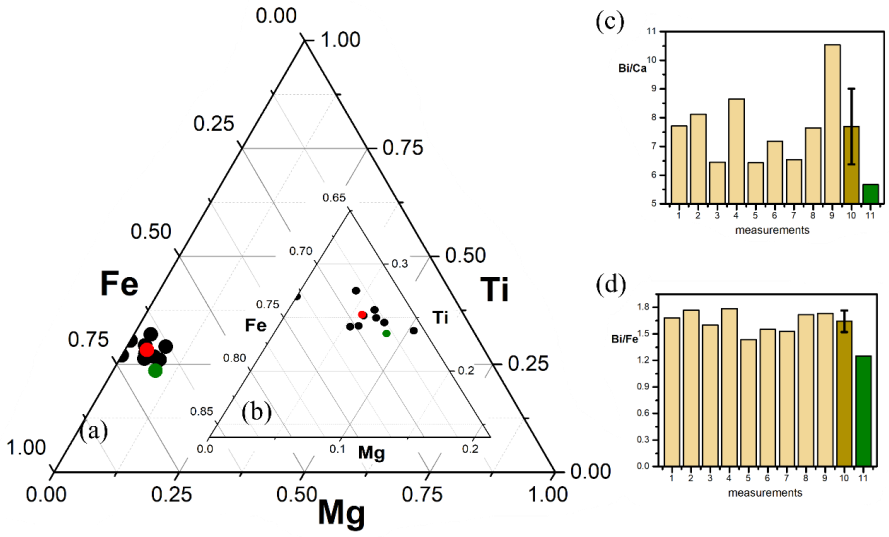

Figure App. 17: EDX/TEM data for the BTFM-CTO film at 50 mTorr on nine randomly chosen positions.

Appendix F: Topology of SRO-buffer BTFM-CTO films

Figure App. 18 to **Figure App. 21** are showing the AFM images of SRO-buffered BTFM-CTO grown for *PE* measurements. All the films were 13,000 pulsed laser shots thick and were grown at 710 ^{o}C, under 15 mTorr of oxygen pressure, as described in **section 5.3.3.1**.

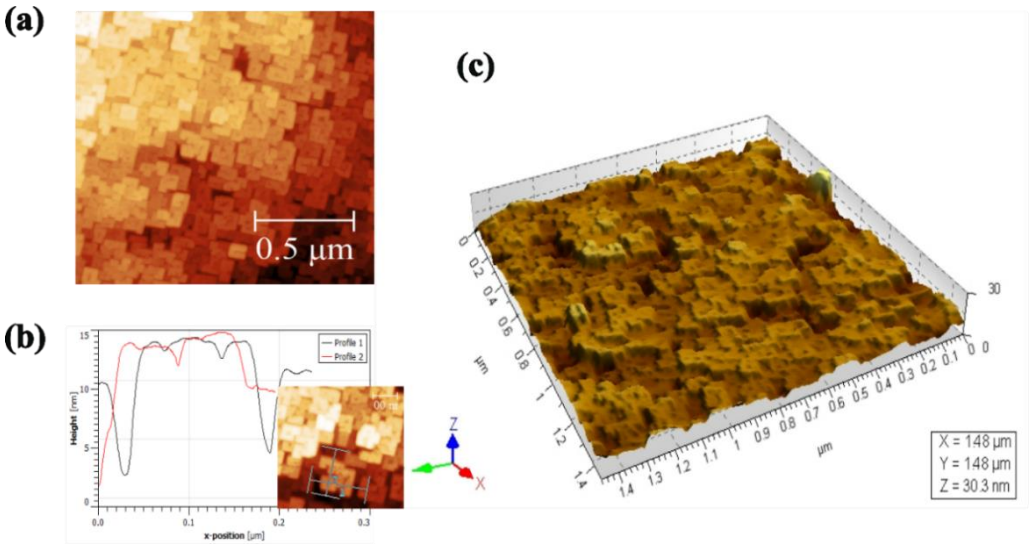

Figure App. 18: (a) AFM plain view image (1 x 1 µm), (b) line profile and (c) 3D projection of a 2 x 2 µm area of film -1 in **Figure 5. 46** of **section 5.3.3.1**.

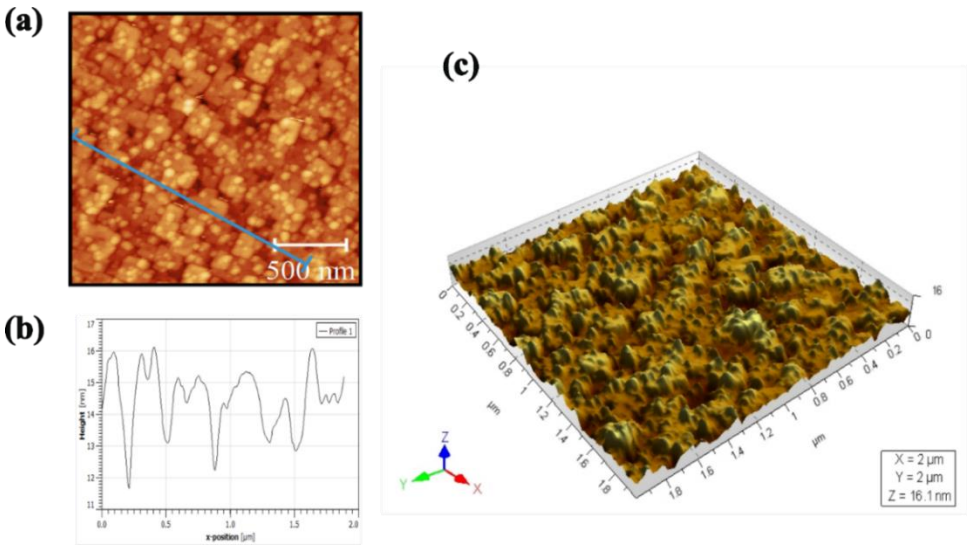

Figure App. 19: (a) AFM plain view image (1 x 1 µm), (b) line profile and (c) 3D projection of a 2 x 2 µm area of film -2 in **Figure 5. 46** of **section 5.3.3.1**.

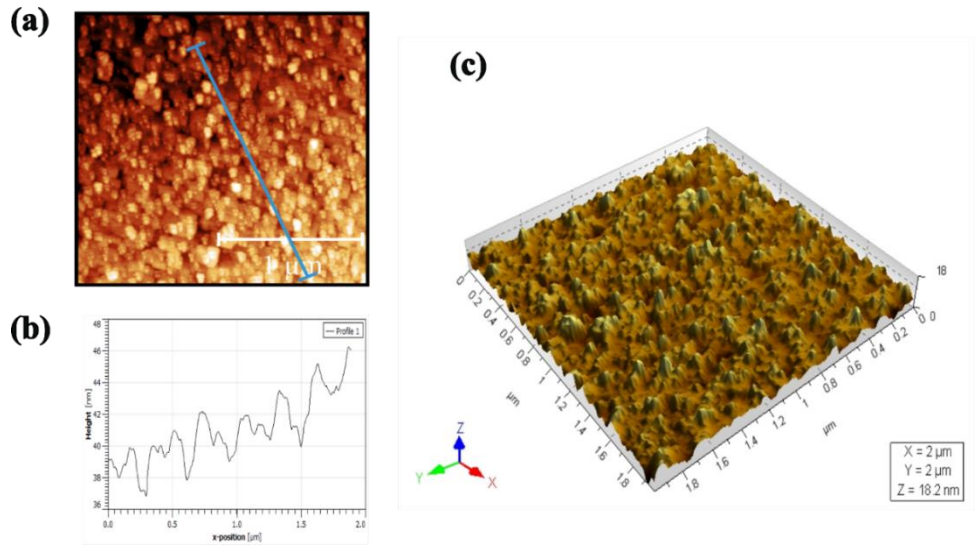

Figure App. 20: (a) AFM plain view image (2 x 2 µm), (b) line profile and (c) 3D projection of a 2 x 2 µm area of film -3 in **Figure 5. 46** of **section 5.3.3.1**.

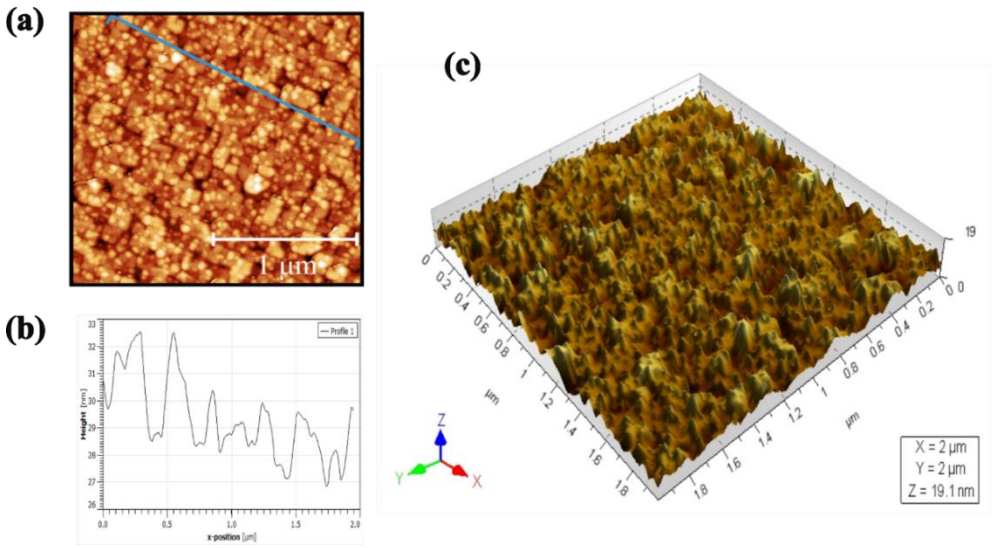

Figure App. 21: (a) AFM plain view image (2 x 2 µm), (b) line profile and (c) 3D projection of a 2 x 2 µm area of film -4 in **Figure 5. 46** of **section 5.3.3.1**.